



HAL
open science

Innovative methods for background rejection in next-generation neutrinoless double beta decay bolometric experiments

Antoine Armatol

► **To cite this version:**

Antoine Armatol. Innovative methods for background rejection in next-generation neutrinoless double beta decay bolometric experiments. Instrumentation and Detectors [physics.ins-det]. Université Paris-Saclay, 2023. English. NNT : 2023UPASP105 . tel-04327156

HAL Id: tel-04327156

<https://theses.hal.science/tel-04327156>

Submitted on 6 Dec 2023

HAL is a multi-disciplinary open access archive for the deposit and dissemination of scientific research documents, whether they are published or not. The documents may come from teaching and research institutions in France or abroad, or from public or private research centers.

L'archive ouverte pluridisciplinaire **HAL**, est destinée au dépôt et à la diffusion de documents scientifiques de niveau recherche, publiés ou non, émanant des établissements d'enseignement et de recherche français ou étrangers, des laboratoires publics ou privés.

Innovative methods for background rejection in next-generation neutrinoless double beta decay bolometric experiments

Méthodes innovantes pour le rejet du bruit de fond dans les expériences bolométriques de recherche de la désintégration double bêta sans émission de neutrino de prochaine génération

Thèse de doctorat de l'université Paris-Saclay

École doctorale n° 576, Particules, hadrons, énergie et noyau : instrumentation, imagerie, cosmos et simulation (PHENIICS)
Spécialité de doctorat: Physique des Particules
Graduate School : Physique, Référent : Faculté des sciences d'Orsay

Thèse préparée dans les unités de recherche **Département de Physique des Particules** (Université Paris-Saclay, CEA) et **IJClab** (Université Paris-Saclay, CNRS), sous la direction de **Claudia NONES**, Chercheuse, CEA-Saclay (DPhP).

Thèse soutenue à Paris-Saclay, le 21 septembre 2023, par

Antoine ARMATOL

Composition du jury

Membres du jury avec voix délibérative

Corinne AUGIER

Professeure des universités, IP2I, Université Claude Bernard Lyon 1

Olivier DRAPIER

Directeur de recherche, LLR, Institut Polytechnique de Paris

Cécile JOLLET

Maître de conférences HDR, LP2I, Université de Bordeaux

Jean Antoine SCARPACI

Directeur de recherche, IJCLab, Université Paris-Saclay

Karoline SCHAEFFNER

Chargée de recherche, MPI for physics, München

Présidente

Rapporteur & Examineur

Rapporteur & Examinatrice

Examineur

Examinatrice

Titre: Méthodes innovantes pour le rejet du bruit de fond dans les expériences bolométriques de recherche de la désintégration double bêta sans émission de neutrino de prochaine génération

Mots clés: Bolomètres, Rejet du bruit de fond, Désintégration double bêta sans neutrino, Physique du neutrino, Basse radioactivité.

Résumé: La recherche de la désintégration double bêta sans émission de neutrino ($0\nu 2\beta$) est un enjeu majeur de la physique contemporaine car son observation démontrerait que le neutrino est une particule de Majorana. La demi-vie du processus étant reliée à la masse effective de Majorana $m_{\beta\beta}$, cela fournirait aussi une mesure de l'échelle de masse du neutrino et une information sur la hiérarchie de masse. L'expérience de prochaine génération CUPID vise à atteindre une sensibilité suffisamment grande pour explorer complètement l'espace des valeurs pour $m_{\beta\beta}$ dans le cas de la hiérarchie inversée de masse. Elle utilisera pour cela des bolomètres scintillants constitués d'un cristal de Li_2MoO_4 (LMO), contenant du ^{100}Mo comme isotope candidat à la 2β , couplé à un détecteur de lumière bolométrique en Ge. Grâce à la méthode de double mesure lumière/chaleur, CUPID va pouvoir rejeter le bruit de fond dû aux particules α qui est la principale source limitant la sensibilité de CUORE, l'expérience précédente, et vise à obtenir un bruit de fond de 10^{-4} coups/kg/keV/an (ckky) dans sa région d'intérêt (ROI). Si après CUPID la $0\nu 2\beta$ nous échappe toujours, il faudra pousser la réduction du bruit de fond à un niveau encore meilleur pour maintenant explorer le spectre des valeurs pour $m_{\beta\beta}$ possibles seulement dans le cas de la hiérarchie normale de masse. C'est dans ce contexte que s'inscrivent BINGO (Bi-Isotope $0\nu 2\beta$ Next Generation

Observatory) et les travaux de cette thèse. Ce projet vise à tester des méthodes innovantes pour atteindre un bruit de fond de 10^{-5} ckky dans la ROI du ^{100}Mo mais aussi du ^{130}Te respectivement dans des cristaux de LMO et de TeO_2 . Tout d'abord, un assemblage innovant des bolomètres réduisant la quantité de matériel passif autour des détecteurs a été développé et validé. Deuxièmement, une R&D sur l'implémentation d'un veto cryogénique actif composé de scintillateurs autour du volume contenant les bolomètres a été faite pour rejeter les événements γ provenant de l'extérieur par coïncidence. Une étude des candidats potentiels a mené à la sélection du BGO pour le matériel composant le scintillateur. Un test cryogénique d'un module prototype du veto contenant deux BGO est aussi reporté dans cette thèse. D'autres mesures relatives à la collection de lumière ont aussi été réalisées à température ambiante. Finalement, pour utiliser les cristaux de TeO_2 comme bolomètres scintillants, il est nécessaire de booster les performances des détecteurs de lumière. Pour cela, BINGO va utiliser des détecteurs utilisant l'effet de Neganov-Trofimov-Luke (NTL) pour amplifier le signal. Une campagne de R&D a été réalisée pour tester une nouvelle méthode de dépôt des électrodes d'aluminium ainsi que différentes géométries pour celles-ci.

Title: Innovative methods for background rejection in next-generation neutrinoless double beta decay bolometric experiments

Keywords: Bolometers, Background rejection, Neutrinoless double beta decay, Neutrino physics, Low radioactivity.

Abstract: The search for neutrinoless double beta decay ($0\nu 2\beta$) is a major challenge in contemporary physics, as its observation would demonstrate that the neutrino is a Majorana particle. The half-life of the process being related to the effective Majorana mass $m_{\beta\beta}$, it would also provide a measure of the neutrino mass scale and information on its mass hierarchy. The next-generation experiment CUPID aims to reach a sensitivity high enough to explore completely the region of possible values for $m_{\beta\beta}$ in the case of the inverted hierarchy. It will use scintillating bolometers made of a Li_2MoO_4 (LMO) crystal, containing ^{100}Mo as the $\beta\beta$ candidate isotope, coupled to a Ge bolometric light detector. Thanks to the dual light/heat readout, CUPID will be able to reject the background due to α particles, which is the main source limiting the sensitivity of CUORE, its predecessor, and aims to achieve a background level of 10^{-4} counts/kg/keV/year (ckky) in the region of interest (ROI). However, if the $0\nu 2\beta$ still eludes us after CUPID, we will have to push the background reduction even further to explore the spectrum of values for $m_{\beta\beta}$ possible in the case of the normal mass hierarchy. It is in this context that BINGO

(Bi-Isotope $0\nu 2\beta$ Next Generation Observatory) and the work of this thesis lay. This project aims to test innovative methods for achieving a background of 10^{-5} ckky in the ROI of ^{100}Mo but also of ^{130}Te , respectively embedded in LMO and TeO_2 crystals. Firstly, an innovative assembly of bolometers reducing the amount of passive material around the detectors has been developed and validated. Secondly, R&D on implementing a cryogenic active veto composed of scintillators around the volume containing the bolometers was done to reject external γ by coincidence. A study of potential candidates led to the selection of the BGO for the material. A cryogenic test of a prototype veto module containing two BGOs is also reported in this thesis. Other light collection measurements have also been done at room temperature. Finally, to use TeO_2 crystals as scintillating bolometers, it is necessary to boost the performance of the light detectors. To achieve this goal, BINGO will operate light detectors using the Neganov-Trofimov-Luke (NTL) effect to amplify the signal. An R&D campaign has been conducted to test a new method for depositing aluminum electrodes and different electrode geometries.

To my grandfather Jean

Résumé en français

Le Modèle Standard est l'un des accomplissements majeurs de la physique de l'infiniment petit. Il a permis de grandes avancées dans la compréhension de notre Univers et de son fonctionnement. Cependant, nous savons aujourd'hui qu'il n'est pas complet car il n'est pas capable d'expliquer les propriétés de la plus énigmatique des particules fondamentales : le neutrino. Ce lepton existant en trois saveurs (ν_e , ν_μ et ν_τ) est la particule la plus abondante de l'Univers, mais aussi la plus insaisissable car elle n'interagit qu'au travers de l'interaction faible. Il a été découvert à la fin du XX^{ème} siècle que lorsqu'ils se propagent, les neutrinos oscillent d'une saveur à une autre. Cette propriété est possible seulement s'il existe trois états propres de masses ayant une différence de masse, bien que très petite, non-nulle, impliquant donc que deux de ces masses le sont aussi. Le Modèle Standard prédisant les neutrinos non-massifs, cela fut donc le premier indice de ces limites et de la nécessité d'une extension. L'une des plus prometteuses pour inclure la masse du neutrino serait de considérer qu'il s'agit d'une particule de Majorana, c'est-à-dire que le neutrino et l'antineutrino sont identiques. Cela violerait la conservation du nombre leptonique et pourrait apporter des explications sur l'asymétrie matière/anti-matière de notre Univers. Pour démontrer que le neutrino est une particule de Majorana et non de Dirac comme les autres leptons, le seul moyen serait d'observer un phénomène uniquement possible dans ce premier cas : la double désintégration bêta sans émission de neutrino.

La double désintégration bêta sans émission de neutrino ($0\nu 2\beta$) est une transition nucléaire hypothétique qui serait possible pour les 35 isotopes pouvant déjà réaliser la double désintégration bêta avec émission de neutrino ($2\nu 2\beta$) dans le cas où le neutrino serait une particule de Majorana. Cependant, la recherche expérimentale n'est possible qu'avec 11 d'entre eux. Il s'agirait du processus le plus rare de la physique nucléaire avec des limites actuelles sur sa demi-vie supérieures à 10^{26} ans. Le signal expérimental recherché est un pic à l'énergie de transition $Q_{\beta\beta}$ dans le spectre de l'énergie sommé des deux électrons émis. Observer ce pic serait donc la preuve que les neutrinos sont des particules de Majorana. De plus, dans le cas où la désintégration est médiée par l'échange d'un neutrino léger de Majorana, la demi-vie est inversement proportionnelle au carré de la masse effective de Majorana $m_{\beta\beta}$, un paramètre nous donnant une mesure de l'échelle de masse. Les valeurs théoriquement possibles pour ce paramètre dépendent de la hiérarchie de masse du neutrino et les expériences recherchant ce paramètre sont capables aujourd'hui, de rejeter les valeurs supérieures à 36-156 meV en fonction de l'élément de matrice nucléaire. L'objectif pour leurs successeurs sera donc d'atteindre une sensibilité assez grande pour explorer totalement le spectre des valeurs pour $m_{\beta\beta}$ inférieur à environ 20 meV, correspondant à la valeur minimale pour laquelle la hiérarchie inversée reste possible.

La recherche de ce processus est un défi expérimental. Due à son extrême rareté, un très faible nombre d'événements est attendu. Afin de le maximiser, une importante masse de l'isotope candidat doit être observée sur une longue période. De plus, il est aussi nécessaire de minimiser le nombre d'événements de bruit de fond attendus dans la région d'intérêt autour de l'énergie de transition. Ce dernier est généralement quantifié par un paramètre nommé l'index de bruit de fond b , qui donne leur nombre attendu par kg par keV et par an (ckky) dans la région d'intérêt. Le choix de l'isotope à observer n'est donc pas anodin. Il doit avoir une grande abondance naturelle ou une technique d'enrichissement doit exister. De plus, il doit avoir une $Q_{\beta\beta}$ élevée, car la demi-vie est inversement proportionnelle à la puissance 5 de ce paramètre. Au final, 9 isotopes sont vraiment prometteurs d'après ces contraintes

comme par exemple le germanium, le xenon ou le molybdène. Parmi ces derniers, ceux avec une $Q_{\beta\beta} > 2.615$ MeV sont d'autant plus intéressants puisque leur signal est attendu dans une région d'énergie supérieure à la plus haute raie en énergie du spectre de la radioactivité γ naturelle, donc avec moins de bruit de fond attendu. En plus de cela, l'isotope doit être compatible avec une méthode de détection permettant la recherche de la $0\nu 2\beta$. Il est nécessaire de l'utiliser dans un environnement à très basse radioactivité (par exemple dans des laboratoires souterrains pour réduire le flux des rayons cosmiques). Il est également souhaitable pour celle-ci d'avoir une fonctionnalité permettant d'identifier les événements de bruit de fond et donc de les rejeter activement. Cela permet de minimiser le paramètre b , qui est l'un des points clés pour une expérience afin d'augmenter sa sensibilité à $m_{\beta\beta}$. Il s'agit aussi du principal sujet du travail présenté dans ce manuscrit. Les bolomètres scintillants, qui sont les détecteurs utilisés et étudiés au cours de cette thèse, sont parmi les méthodes de détection les plus prometteuses.

Un bolomètre est un calorimètre opéré à des températures proches du zéro absolu (~ 10 mK) qui est composé grossièrement de trois éléments : un matériel absorbeur, un thermomètre couplé à sa surface et un bain thermique auquel sont reliés les deux premiers composants afin de les maintenir à basse température. Lorsqu'une particule interagit dans l'absorbeur, elle provoque une élévation de température proportionnelle à l'énergie déposée, qui est ensuite mesurée par le thermomètre (dans le cadre de cette thèse, ce dernier est un NTD Ge dont la résistance varie avec la température). La force de ces détecteurs réside dans le fait qu'il est possible de choisir comme absorbeur un cristal diélectrique contenant l'isotope candidat à la $0\nu 2\beta$, assurant une grande efficacité de détection ($> 80\%$). De plus, ils peuvent atteindre une excellente résolution en énergie inférieure à 0.2% dans la région d'intérêt. L'expérience CUORE (Cryogenic Underground Observatory for Rare Event), actuellement en période de prise de donnée physique au laboratoire souterrain du Gran Sasso en Italie, utilise cette méthode de détection. Elle recherche la $0\nu 2\beta$ du ^{130}Te contenue dans environ 1000 cristaux naturels de TeO_2 . En figurant parmi les expériences les plus sensibles de la génération actuelle (elle a récemment exclu les valeurs de $m_{\beta\beta}$ supérieures à 90-305 meV) et grâce à son excellente résolution en énergie, elle a démontré le potentiel des bolomètres pour cette recherche et la faisabilité d'une expérience à grande échelle les utilisant. Cependant, l'index de bruit de fond obtenu par CUORE dans sa région d'intérêt est d'environ 10^{-2} ckky, ce qui l'empêche d'atteindre les objectifs fixés pour la prochaine génération d'expérience.

CUORE va donc avoir un successeur qui s'appelle CUPID (Cuore Upgrade with Particle Identification). CUPID va cette fois, utiliser des bolomètres scintillants pour lesquels l'absorbeur est un cristal scintillant. Ainsi, en associant à chacun d'eux un autre bolomètre auxiliaire en Ge, qui sera utilisé en détecteur de lumière, chaque événement donnera lieu à un signal de chaleur et à un signal de lumière. Cette caractéristique va permettre d'identifier et de rejeter les particules α , sources dominantes de bruit de fond pour CUORE, puisqu'elles émettent une quantité différente de lumière que les événements γ ou β . De plus, CUPID va changer d'isotope candidat et étudier le ^{100}Mo contenu dans des cristaux scintillants Li_2MoO_4 . Celui-ci a une $Q_{\beta\beta}$ à 3034 keV, soit supérieur à la limite de la radioactivité naturelle, contrairement au ^{130}Te . Ces deux améliorations vont permettre à CUPID de réduire par deux ordres de magnitudes le bruit de fond dans sa région d'intérêt et d'atteindre $b \sim 10^{-4}$ ckky, lui permettant ainsi d'explorer complètement le spectre des valeurs possibles pour $m_{\beta\beta}$, dans le cas de la hiérarchie inversée de masse.

Si CUPID ne découvre pas la $0\nu 2\beta$, il faudra pousser encore plus loin la sensibilité des expériences. Pour cela, il est crucial de réduire davantage le bruit de fond, tout en augmentant en parallèle l'exposition expérimentale totale (masse et temps de prise de données). C'est donc pour préparer cette éventualité, que BINGO (Bi-Isotope $0\nu 2\beta$ Next Generation Observatory),

un projet financé par l'ERC (European Research Council) en tant que Consolidator Grant, a vu le jour. Il propose des innovations sur la détection bolométrique afin d'atteindre un index de bruit de fond de l'ordre de 10^{-5} ckky dans les régions d'intérêt du ^{100}Mo mais aussi du ^{130}Te . Ce dernier est, malgré la position non-favorable de sa $Q_{\beta\beta}$, extrêmement prometteur dû à sa grande abondance isotopique naturelle (30%) et les excellentes performances bolométriques atteintes par les cristaux de TeO_2 . Trois piliers pour la réduction du bruit de fond sont proposés. Le premier consiste en une nouvelle façon d'assembler les bolomètres qui utilise de manière ingénieuse la position du détecteur de lumière ainsi qu'un fil en nylon afin de minimiser la surface des cristaux exposée au matériel passif. Cela permet une importante réduction de la contribution des événements de radioactivité de surface au bruit de fond comparé aux assemblages qui seront utilisés dans CUPID. Le second est l'implémentation d'un veto cryogénique actif autour des bolomètres. Il est composé de scintillateurs (BGO ou ZWO) dont la lumière de scintillation émise lors du passage d'une particule en leur sein sera détectée par des détecteurs bolométriques en Ge. Ce veto actif va ainsi permettre de rejeter les événements de bruit de fond γ provenant de l'extérieur de la zone des bolomètres par coïncidences entre le veto et les cristaux. Cette source de bruit de fond sera alors particulièrement réduite, ce qui permettra d'atteindre des niveaux de bruit de fond très bas même dans la région d'intérêt du ^{130}Te . Finalement, BINGO propose d'utiliser des détecteurs de lumière en Ge exploitant l'effet Neganov-Trofimov-Luke (NTL) afin d'amplifier leur signal. Ces derniers ont des électrodes en aluminium déposées sur leur surface qui permettent, lorsque l'on applique entre elles une différence de potentiel, de mettre en mouvement les porteurs de charges créés lors de l'interaction d'une particule dans le détecteur. Ce mouvement induit alors de la chaleur supplémentaire et permet donc d'obtenir une amplification du signal. Ce boost du ratio signal sur bruit va avoir plusieurs avantages. Du point de vue des bolomètres, il va permettre de détecter la lumière Cerenkov émise par les cristaux de TeO_2 lors de l'interaction d'une particule et donc de les utiliser comme bolomètres scintillants. De plus, cela permettra aussi un meilleur rejet des coïncidences aléatoires entre deux signaux, qui constitue une source de bruit de fond pour les cristaux contenant du ^{100}Mo dû à la courte demi-vie de sa $2\nu 2\beta$ (7.1×10^{18} ans). Ce type de détecteurs de lumière sera aussi utilisé pour détecter la lumière de scintillation émise par le veto actif. Ils vont permettre d'atteindre un seuil en énergie très bas, nécessaire pour une efficacité de rejet optimale des événements γ extérieurs. L'objectif est de pouvoir détecter une déposition d'énergie de 50 keV dans le veto.

C'est dans le cadre de la campagne de R&D menée sur les innovations de BINGO que s'inscrit les travaux de cette thèse. Les premiers tests cryogéniques de ces nouveautés ont été réalisés et ont permis des avancées significatives pour ces trois technologies, ainsi que la validation de certaines de leurs propriétés. Ils ont permis un pas un avant vers la construction du démonstrateur MINI-BINGO, qui sera installé dans le futur, au laboratoire souterrain de Modane. Il inclura toutes les innovations de BINGO et contiendra une tour de 12 LMO et une autre de 12 TeO_2 . L'objectif est de démontrer un index de bruit de fond de 10^{-4} ckky dans les deux régions d'intérêt après une année de prise de données, ce qui en ferait l'expérience bolométrique avec le plus bas bruit de fond jamais construite. MINI-BINGO aura ainsi un grand impact sur le futur de cette méthode de détection notamment pour les expériences post-CUPID.

Concernant l'assemblage avec le fil de nylon, les premiers prototypes ont été testés dans cette thèse. En passant par différentes étapes (d'un assemblage à petite échelle jusqu'au test d'une tour composée de deux modules contenant des cristaux de LMO de $45 \times 45 \times 45$ mm³), nous avons conçu un assemblage permettant de tenir robustement les détecteurs avec les fils en nylon. Nous avons également développé un protocole d'assemblage simple et rapide assurant une bonne reproductibilité des contraintes mécaniques de chaque module. De

plus, nous avons démontré qu'un tel assemblage ne présente pas de différence comparé à un autre plus standard (dans le style de CUPID) au niveau des performances que les détecteurs obtiennent. Cela a permis une première validation du concept pour les cristaux de LMO, et les tests seront poursuivis à l'avenir pour vérifier que les conclusions sont les mêmes pour les cristaux de TeO_2 , ceux-ci étant plus grands ($50 \times 50 \times 50 \text{ mm}^3$) et plus massifs.

Les premiers résultats de la R&D menée pour le veto actif cryogénique sont aussi présentés dans ce manuscrit. Nous avons identifié deux candidats potentiels pour le veto : le ZWO et le BGO. Une première comparaison à basse température a été réalisée afin de s'assurer de leur performance dans de telles conditions. De plus, un premier prototype de veto cryogénique a été testé. Il était composé de deux BGO trapézoïdaux de 12 cm de hauteur, chacun lu par deux détecteurs de lumière en Ge. Nous avons placé devant lui un cristal de TeO_2 avec une source d'uranium liquide déposée sur la surface faisant face aux scintillateurs pour simuler une contamination de surface. Ce test nous a permis de concevoir un premier support potentiel pour le veto final, d'étudier l'impact du refroidissement lent du BGO sur son environnement, ainsi que de développer un algorithme pour regarder les coïncidences entre le TeO_2 et les détecteurs de lumière du veto. Nous avons aussi réalisé une estimation du seuil en énergie atteint par chacun de ces derniers. Finalement, nous avons mis en place un banc de test de collection de lumière utilisant un tube photo-multiplicateur afin de comparer différentes configurations des BGOs. Nous avons pu tester deux matériaux réflecteurs dans lesquels le BGO peut être enveloppé ainsi que différents polissages du cristal pour voir leurs effets sur la collection de lumière.

Finalement, un test important a été réalisé sur les détecteurs de lumière NTL. Dans le passé, des amplifications de 10 sur le ratio signal sur bruit ont été obtenues sur des substrats de Ge circulaire avec des électrodes en forme d'anneaux. L'objectif pour BINGO est donc de reproduire, et surtout de faire mieux que ces résultats, mais avec des substrats carrés. Dans cette thèse, une nouvelle méthode d'évaporation des électrodes, plus simple et rapide pour le prototypage des détecteurs, a été testée. Elle nous a permis d'essayer trois nouvelles géométries d'électrodes qui optimisent la collection de charges pour les détecteurs carrés. Il s'est avéré cependant que cette nouvelle méthode produisait des détecteurs de lumière avec de moins bonnes performances que celle utilisée dans le passé. Nous avons donc aussi réalisé un test, cette fois avec l'ancienne méthode d'évaporation ainsi que l'ancienne géométrie des électrodes en anneaux, mais sur les substrats carrés. Cette fois, les détecteurs ont montré des résultats prometteurs malgré la géométrie non-optimale pour leur dimension. Deux des trois nouvelles géométries des électrodes imaginées dans cette thèse, vont donc être dans le futur testées à nouveau, mais avec cette ancienne méthode, afin de conclure sur leur performance.

Ce manuscrit est divisé en 7 chapitres : les chapitres 1, 2, 3 et 4 constituent une introduction aux notions importantes et une mise en contexte des travaux réalisés dans cette thèse. Les trois chapitres suivants (5, 6 et 7) contiennent les résultats obtenus et leur discussion. Finalement, une conclusion et les perspectives de ce travail peuvent être trouvés à la fin.

Le premier chapitre est une introduction à la physique du neutrino. Il présente un bref historique de sa prédiction à ce que l'on sait aujourd'hui. Ce chapitre expose les grandes questions encore non résolues de cette particule, comme sa nature, son échelle de masse ou la hiérarchie de ses masses. Il permet de souligner l'importance de la recherche de la désintégration double bêta sans émission de neutrino pour y répondre.

Le second chapitre décrit la recherche de la désintégration double bêta sans émission de neutrino. Après une introduction théorique sur ce processus, le défi expérimental de sa détection est expliqué dans les détails. Finalement, l'état de l'art des expériences la recherchant est présenté.

Le troisième chapitre décrit la détection des particules avec les bolomètres, la technologie

utilisée dans cette thèse. Leurs propriétés sont discutées ainsi que celles des NTD Ge, qui servent de senseur de température. De plus, le principe de fonctionnement des bolomètres scintillants y est détaillé. Le chapitre se clôt sur une brève description des cryostats, permettant d'opérer ces détecteurs à très basses températures.

Le quatrième chapitre introduit BINGO et les problématiques auxquelles le projet vise à répondre. Les trois innovations proposées y sont détaillées ainsi que leurs principales caractéristiques. Ce chapitre contient aussi une description du démonstrateur MINI-BINGO et de ses objectifs.

Le cinquième chapitre est le premier des trois chapitres de résultats. Il se concentre sur les tests effectués pour l'assemblage novateur avec le fil en nylon. Chaque étape de validation du concept y est décrite, jusqu'au test de la première tour de BINGO contenant 2 modules dans un laboratoire souterrain. La comparaison des performances obtenues avec celles des assemblages plus standards nous a démontré qu'un tel assemblage convenait pour les mesures bolométriques, ce qui est prometteur au vu de la réduction de la surface des cristaux exposés aux matériaux passifs qu'il offre.

Le sixième chapitre est consacré aux tests réalisés pour les vetos qui seront utilisés dans MINI-BINGO. Il est divisé en deux parties. La première partie se concentre sur le veto cryogénique actif et présente les différents résultats que nous avons obtenus. La comparaison des deux scintillateurs candidats, le premier prototype avec des cristaux de BGO ainsi que les tests de collection de lumière à température ambiante y sont décrits. La seconde partie est dédiée à la mesure de radioactivité d'un échantillon de plomb qui sera utilisé comme matériel d'un bouclier passif contre la radioactivité γ à l'extérieur de la zone expérimentale. Nous avons réalisé une mesure bolométrique de cet échantillon afin de déterminer son niveau de contamination en ^{210}Pb .

Le septième chapitre décrit le travail réalisé sur les détecteurs de lumière NTL. Il présente la nouvelle méthode d'évaporation testée (la photo-lithographie) ainsi que les trois nouvelles géométries d'électrodes pensées pour optimiser l'amplification des signaux sur les substrats carrés. Les résultats obtenus avec ces nouveaux détecteurs sont présentés et semblent montrer que cette méthode ne donne pas les résultats escomptés. Un nouveau test contenant des détecteurs produits avec l'ancienne méthode utilisant un masque mécanique pour évaporer les électrodes y est alors décrit. Celui-ci démontre qu'avec cette dernière, les détecteurs ont obtenus des performances plus prometteuses malgré la géométrie en anneaux qui n'est pas optimisée pour leur forme. Finalement, le lecteur trouvera à la fin, une discussion sur le potentiel des détecteurs NTL pour rejeter les coïncidences de signaux aléatoires qui constituent l'une des sources de bruit de fond dominante dans l'expérience de prochaine génération CUPID.

Cette thèse présente ainsi les premiers résultats obtenus et avancements réalisés dans chacune des innovations proposées par BINGO depuis le début du projet. Ce travail a apporté de précieuses informations pour la construction du démonstrateur MINI-BINGO, et va être poursuivi dans le futur. BINGO se place ainsi comme un projet précurseur cherchant à repousser le bruit de fond à un niveau de 10^{-5} ckky, soit un ordre de magnitude inférieur à celui de CUPID. Avec un tel index de bruit de fond, l'exploration du spectre de valeurs pour $m_{\beta\beta}$ inférieur à 10 meV et au-delà devient possible. Les innovations testées dans cette thèse pourraient ainsi devenir le standard des expériences bolométriques de demain.

Acknowledgements

I would like to express my profound gratitude to all those who have contributed to the successful completion of my PhD. Without their support, guidance, and encouragement, this achievement would not have been possible.

First of all, I would like to thank the members of my thesis jury: Corinne Augier, Olivier Drapier, Cécile Jollet, Jean-Antoine Scarpaci and Karoline Schaeffner. Thank you for your careful evaluation of my work and for the comments you provided to improve the quality of this manuscript.

I would like to express my immense gratitude to my supervisor Claudia Nones. Thanks to her guidance and encouragement, I always felt supported in my activities. Working under her supervision was a pleasure and I learned a lot from her. I could not have hoped for a better advisor.

I extend my sincere gratitude to my colleagues at CEA and IJCLab. I had the pleasure of working in two really dynamic and friendly groups. In particular, I would like to thank Edoardo Mazzucato for his help in many aspects of this thesis and for the time he always took to discuss with me and answer my questions (often around a coffee). I want to thank also Hawraa Khalife, with whom I worked a lot during these three years. She has contributed to almost all the work I am presenting in this manuscript and she taught me many things, always with patience and kindness. I also want to express a special thanks to Anastasiia Zolotarova, Emiliano Olivieri, David Baudin, Denys Poda, Benjamin Schmidt, Stefanos Marnieros and Andrea Giuliani for their help and support, their expertise has greatly assisted my work.

I would like to thank my family, especially my parents and my sister, for their unconditional support. I am conscious that without them and their dedication, I could not have succeeded. For that, I am infinitely grateful.

I want to thank also my lifelong friends, Bastien, Cindy, Maxime, Lucas, Pierre and Simon. We grew up together and they have always been really encouraging throughout these years, helping me also to take my mind off things when I needed it. I believe that they have contributed a lot to the achievement of my studies.

Last but not least, I would like to thank my wife Sarah, for always being so supportive. She helped me a lot during the writing of this manuscript, and I am really lucky to have her by my side.

Je sais que les souvenirs de ces trois années de thèse m'accompagneront durant toute ma carrière, ainsi que ceux des personnes qui ont participé à les créer.

Contents

| | | |
|----------|---|-----------|
| 1 | The neutrino, a vector of discovery | 9 |
| 1.1 | Once upon a time the neutrino | 9 |
| 1.2 | I oscillate... | 13 |
| 1.3 | ... so I have a mass | 16 |
| 1.4 | Conclusion | 20 |
| 2 | Searching for $0\nu 2\beta$ | 22 |
| 2.1 | What is $0\nu 2\beta$? | 22 |
| 2.2 | The experimental challenge | 25 |
| 2.3 | An overview of the background sources | 29 |
| 2.4 | $0\nu 2\beta$ experiments | 32 |
| 2.4.1 | High-Purity Germanium detectors (HPGe) | 32 |
| 2.4.2 | Xe Time-Projection Chamber (Xe TPC) | 34 |
| 2.4.3 | Large liquid scintillator | 36 |
| 2.4.4 | Cryogenic calorimeters | 38 |
| 2.4.5 | Tracking calorimeters | 41 |
| 2.4.6 | Summary and discussion | 42 |
| 3 | The bolometric technique | 44 |
| 3.1 | Working principle | 44 |
| 3.1.1 | The absorber choice | 45 |
| 3.2 | Thermal sensors | 46 |
| 3.2.1 | Neutron Transmutation Doped Ge | 47 |
| 3.2.2 | NTD operation and load curves | 50 |
| 3.3 | Detector response | 51 |
| 3.3.1 | Electronics and signal | 51 |
| 3.3.2 | Intrinsic and extrinsic noises | 52 |
| 3.3.3 | Analysis tools | 54 |
| 3.3.4 | Heaters and stabilization | 55 |
| 3.4 | Double read-out method | 56 |
| 3.4.1 | About the scintillation process | 57 |
| 3.4.2 | Bolometric light detectors and α rejection | 58 |
| 3.5 | Dilution cryostats | 59 |
| 3.5.1 | Working principle | 59 |
| 3.5.2 | The example of Ulysse: an above ground pulse-tube cryostat | 61 |
| 4 | BINGO: Bi-Isotope $0\nu 2\beta$ Next Generation Observatory | 64 |
| 4.1 | From CUORE to CUPID to BINGO | 64 |
| 4.2 | The Bi-Isotope approach | 65 |

| | | |
|----------|--|------------|
| 4.3 | Solutions brought by BINGO to the background puzzle | 66 |
| 4.3.1 | Enhancing the light signal with Neganov-Trofimov-Luke effect | 66 |
| 4.3.2 | The revolutionary detector assembly | 68 |
| 4.3.3 | The cryogenic active veto | 69 |
| 4.4 | On the way to MINI-BINGO | 71 |
| 5 | The BINGO nylon assembly | 73 |
| 5.1 | First prototype using $20 \times 20 \times 20$ mm ³ LMO crystals | 73 |
| 5.1.1 | The module description | 73 |
| 5.1.2 | Bolometric measurements | 75 |
| 5.2 | Second prototype using $45 \times 45 \times 45$ mm ³ LMO crystals | 79 |
| 5.2.1 | Design and assembly improvements | 79 |
| 5.2.2 | Cryogenic tests | 80 |
| 5.3 | Underground measurement with two modules | 84 |
| 5.3.1 | New mounting procedure and tower assembly | 84 |
| 5.3.2 | Tower installation and operations in LSC | 86 |
| 5.3.3 | Th calibration | 87 |
| 5.3.4 | Background measurements | 90 |
| 5.3.5 | Conclusion | 91 |
| 6 | The passive and active vetoing | 92 |
| 6.1 | First part: the BINGO cryogenic active veto | 92 |
| 6.1.1 | The scintillator choice | 92 |
| 6.1.2 | First veto prototype with two 12 cm high BGOs | 97 |
| 6.1.3 | Room temperature BGO light output measurements | 112 |
| 6.2 | Second part: Lead screening with bolometric measurements | 120 |
| 6.2.1 | Context of the measurement | 122 |
| 6.2.2 | Samples preparation | 123 |
| 6.2.3 | Cryogenic measurements and ²¹⁰ Pb contamination estimation | 124 |
| 7 | Neganov-Trofimov-Luke light detectors | 128 |
| 7.1 | Preliminary considerations | 128 |
| 7.2 | NTL light detector fabrication | 129 |
| 7.3 | Three new electrode designs | 131 |
| 7.3.1 | Edge geometry | 132 |
| 7.3.2 | Concentric geometry | 132 |
| 7.3.3 | Meander geometry | 133 |
| 7.4 | Cryogenic test and results | 134 |
| 7.5 | Back to the basics | 139 |
| 7.6 | Discussion on random coincidences rejection using NTL light detectors | 142 |
| | Conclusions and perspectives | 145 |
| | Bibliography | 151 |

Chapter 1

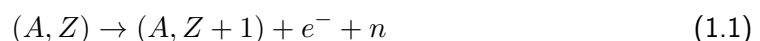
The neutrino, a vector of discovery

With its unique properties, the neutrino is surely one of the most enigmatic particles in the Universe. For decades, physicists have tried to build theories and experiments to unravel the mysteries surrounding it: why is its mass so light compared to other fermions? Are the neutrino and the anti-neutrino the same particle? And many others. Even though the puzzle is far from being completely solved, the neutrino has already led to a cascade of groundbreaking revelations in physics and it has given first hints about the limitations of the Standard Model. In this chapter, we will explore the history and the properties that make the most elusive of the fermions so special.

1.1 Once upon a time the neutrino

The prediction of a new particle

In 1927, C.D. Ellis and W.A. Wooster published an article [1] about their measurement of the energy spectrum of the emitted electron during the beta decay of Radium E (^{210}Bi). The result confirmed the concerns of the physicist risen since 1914 by previous experiments: the spectrum is continuous. Indeed, at that time, the beta decay was assumed to be a nuclear transition of the nucleus (A, Z) into $(A, Z+1)$, leading to the emission of an electron with a fixed kinetic energy equal to $Q = (M_{A, Z} - M_{A, Z+1}) - m_e$. However, the observation of a continuous energy spectrum for the electron is not compatible with such a description. To explain this contradiction, the nuclear physics community had to come up with new ideas that went as far as the non-conservation of the total energy in β -decay. This was not accepted by everyone, and in 1930, in an attempt to save one of the most fundamental principles of physics, W. Pauli sent a famous letter addressed to participants of a nuclear conference in Tübingen [2]. He proposed the existence of a new neutral and light particle, which he called "neutron", that would be part of the nuclei along protons and electrons and also emitted during the β -decay. This courageous assumption was turning the decay into a three-body process:



The released energy is in this case shared between the emitted electron (e^-) and the "neutron" (n), explaining the electron continuous energy spectrum without violating the energy conservation. Two years later, J. Chadwick discovered the neutron which appeared to have almost the same mass as the proton [3]. It was accepted later that nuclei are bounded states

between protons and neutrons but that these latter are not the particle emitted with the electron in the final state.

Nevertheless, when building the first β -decay theory in 1934, E. Fermi used the concept of a new spin 1/2, neutral and light particle created and emitted in addition to the electron [4] as suggested by Pauli. He called it "neutrino" which means in Italian "little neutral one." We know today that in the case of the β^- decay, it is actually an anti-neutrino ($\bar{\nu}$) that is emitted. The equation 1.1 can now be rewritten:

$$(A, Z) \rightarrow (A, Z + 1) + e^- + \bar{\nu} \quad (1.2)$$

In particular, Fermi understood that the process was due to the disintegration of a neutron into a proton in the mother nucleus leading to the creation of an electron and a neutrino:

$$n \rightarrow p + e^- + \bar{\nu} \quad (1.3)$$

First experimental detection

Fermi's β^- decay theory was really successful when applied to nuclear problems of that time, and it soon became one of the strongest arguments in favor of neutrino existence. To definitely state it, only an experimental observation was missing, but the challenge was tough. H. Bethe and R. Peierls were the first to estimate the cross-section of the neutrino with nucleons [5]. They found an extremely small value and concluded their paper by "*one can conclude that there is no practically possible way of observing the neutrino.*" This appeared to be true until the clever experiment idea proposed by B. Pontecorvo in 1946 [6]. His proposal was to use the namely inverse beta decay which corresponds to the interaction of a neutrino with a neutron which creates a proton and an electron ($\nu + n \rightarrow p + e^-$) to detect the neutrino. He also suggested nuclear reactors or the Sun as possible high-flux neutrino sources.

Based on the new hope brought by Pontecorvo and after a preliminary hint obtained in 1953 [7], the first confirmation of a neutrino detection occurred in 1956 by F. Reines and C.L. Cowan [8]. They used the anti-neutrino flux coming from the Savannah River power plant in the USA to observe the reaction:

$$\bar{\nu} + p \rightarrow n + e^+ \quad (1.4)$$

The experiment was placed in an underground room of the reactor building to shield it against the reactor neutrons and gammas but also against the cosmic rays. The set-up was composed of two water tanks with CdCl_2 diluted inside. They were surrounded by liquid scintillator layers for which the scintillation light was measured using photo-multiplier tubes. The sequence of detection was as follows: the anti-neutrino is interacting with a proton from the water, creating a positron and a neutron simultaneously. The positron annihilates with an electron from the water tank and emits two gammas at 511 keV that are detected in the liquid scintillator layers. On the other hand, the neutron diffuses and is captured by the cadmium which is an excellent neutron absorber. This capture produces a gamma thanks to the following reaction:

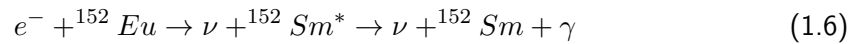
$$n + {}^{108}\text{Cd} \rightarrow {}^{109}\text{Cd}^* \rightarrow {}^{109}\text{Cd} + \gamma \quad (1.5)$$

This gamma is also detected in the liquid scintillator several microseconds later than the annihilation gammas, providing a really clear experimental signal of anti-neutrino detection. After three months of data-taking, they found around three anti-neutrinos interactions per hour in their detector, and finally measured a cross-section of $\sigma = 6.3 \times 10^{-44} \text{ cm}^2$ really close to the predictions. A few decades later, in 1995, Reines was awarded with a Nobel prize for neutrino detection.

The investigation of neutrino properties

After its detection, the neutrino was, without any doubt possible, a part of the particle physics landscape. Several studies about its characteristics started to understand exactly its role.

In 1957, Wu et al. [9] and Ledermann et al. [10] observed a large non-conservation of the parity in two different weak processes, confirming the hypothesis of T.D. Lee and C.N. Yang [11]. This surprising discovery was followed by several efforts to include this feature in the theory leading to the development of a massless two-component neutrino description. In this representation, the neutrino field can only be left-handed ($\nu_L(x)$) or right-handed ($\nu_R(x)$) while the anti-neutrino must have the opposite chirality. To answer which one of these two scenarios is true, Goldhaber et al. measured the helicity of the neutrino in 1958 [12]. The experiment was looking at the electron capture of Europium:



The beauty of this process is that, due to the total angular momentum conservation, the neutrino helicity is equal to the circular polarization of the gamma emitted in the direction of the ${}^{152}\text{Sm}^*$ momentum. By measuring the latter, the results were clear: the two-components theory is successful and the neutrino has a negative helicity, so is left-handed (the anti-neutrino is right-handed). This conclusion, along with the proof of the parity non-conservation in weak processes, paved the way to more elaborated theories such as V-A interaction with, so far, only one kind of neutrinos.

However, in 1962 the Brookhaven experiment [13] discovered a second type of neutrino associated with the weak processes involving muons, the muon-neutrino (ν_μ). It used for the first time a particle accelerator to produce an intense neutrino beam. Foremost, a beam of π^+ was produced by the bombardment of a Be target with 15 GeV protons. These π^+ were decaying, producing almost a pure ν_μ beam. By interacting in a target, the neutrino beam should have produced the same amount of μ^- and e^- if $\nu_e = \nu_\mu$. Nevertheless, twenty-nine μ^- events while only six e^- events, explainable with the background model, were observed. This important experiment showed that ν_e and ν_μ are two different particles and brought to L.M. Lederman, M. Schwartz and J. Steinberger a Nobel Prize in 1988.

Finally, the last flavor of neutrino, the ν_τ , was observed for the first time in 2000 by the DONUT (Direct Observation of the Neutrino Tau) experiment [14] at FermiLab. This direct measurement took place 25 years after the discovery of the tau lepton, which was the first hint of a third lepton generation. We know since 1989 that there is no more than three lepton families with a light neutrino ($< \sim 45.5 \text{ GeV}.c^2$) thanks to the results of LEP experiments at CERN that measured the decay widths of Z^0 [15–17].

By virtue of the intense experimental efforts of the 20th century second half, the neutrino revealed some of its mysteries. It was well described by the Standard Model as a two-component neutral and massless particle, interacting only through the weak force. However, there was a cloud on the horizon: a problem that kept the neutrino physicists in suspense for almost 30 years and that shook this picture.

The solar neutrinos problem

In 1968, the famous Homestake experiment developed by R. Davis observed for the first time the Solar neutrinos (i.e. neutrinos produced in the nuclear fusion reactions taking place in the Sun core). It was inspired by B. Pontecorvo idea [6] to use the neutrino capture of chlorine to detect them:



This process is advantageous for three main reasons. C_2Cl_4 can be used as a large volume target since it is cheap. The ^{37}Ar is a rare gas and the few nuclei produced can be easily extracted from the C_2Cl_4 by purging it with helium gas. Finally, ^{37}Ar is unstable and decays through electronic capture (EC). It has a convenient half-life of 35 days: this gives enough time to extract it, isolate it and count it using a gas-filled proportional counter to determine the number of neutrinos that have been captured. The 615-tonne of tetrachloroethylene-filled tank was placed in the Homestake gold mine in the US at 1474 m underground to shield it from cosmic rays. The experiment was a success since they managed to detect solar neutrinos. However, since the first results they obtained in 1968 [18], they measured a clear deficit between the measured solar neutrino flux and the one calculated by J. Bahcall who participated in establishing the Standard Solar Model (SSM). It was the beginning of the so-called "solar neutrino problem."

At first, there were attempts to modify the SSM to explain the deficit. For example, the solar neutrino flux could have been lower if the pressure and the temperature were lower in the Sun core than what was believed. However, other observations like helioseismology discarded this kind of hypothesis and confirmed the veracity of the SSM.

The second way to explain the discrepancy between measurements and predictions was to find a problem with the measurements themselves. To answer this, other experiments were needed to observe solar neutrinos. The first to confirm the deficit was KAMIOKANDE-II in 1989 [19] which was an imaging water Cherenkov detector that detected 8B solar neutrinos by neutrino-electron scattering $\nu_e e^- \rightarrow \nu_e e^-$. It was followed later on by GALLEX [20] in 1992 and SAGE [21] in 1994 which used a radiochemical method, as in the Homestake experiment, but with the neutrino capture of ^{71}Ga . The solar neutrino problem was confirmed and not dependent on the experiments or the solar model. Hence, the last possible solution to solve it was related to neutrino physics and the way they propagate...

In 1968, a few months after the publication of the Homestake experiment first results, B. Pontecorvo and V. Gribov proposed that the solar neutrino problem could be explained by a flavour oscillation of the neutrino [22]. Based on the oscillation between K^0 meson and \bar{K}^0 its antiparticle, Pontecorvo was thinking already since many years about a possible neutrino oscillation [23, 24]. They described the oscillation between ν_e and ν_μ in the case where only two flavours existed. This mechanism implies that neutrinos are massive particles, so a different picture compared to what was assumed at that time. However, with the increasing amount of experiments confirming the discrepancy between the measured solar neutrino flux and the predicted one, this theory started to be more and more under the spotlights over the years. In particular because the same kind of anomaly was remarked with atmospheric neutrinos: KAMIOKANDE in 1988 [25] and IMB-3 in 1991 [26] observed less muon-neutrinos produced by the interaction of cosmic rays in the upper atmosphere than expected.

Finally, the solar neutrino problem ended in 1998, when SUPER-KAMIOKANDE [27] brought the proof of neutrino oscillation. It measured an asymmetry between the flux of atmospheric neutrinos coming from above the detector and the one coming from below, which have to cross the Earth before being detected. It demonstrated the existence of neutrino oscillations and their dependency on the traveled distance since the flux is supposed to be 2π homogeneous without flavour oscillations. To close definitely the chapter, the solar neutrino experiment SNO in 2002 [28] obtained an evidence of the disappearance of ν_e thanks to its capability to detect all solar neutrino flavours through Charged Current (CC) and Neutral Current (NC) reactions. T. Kajita and A.B. McDonald earned in 2015 the physics Nobel Prize for their contribution in respectively SUPER-KAMIOKANDE and SNO.

Today's picture

The discovery of neutrino oscillations has solved the solar neutrino problem but it has also opened a new chapter for neutrino physics. This mechanism implies that neutrinos are massive, which is not the case in the current Standard Model of particle physics. Therefore, we will explore in the next section the consequences of such a modification and what it could imply for the nature of the neutrino itself. Let's first summarize what the current knowledge about neutrinos is.

Three flavours of neutrino are known ν_e , ν_μ , and ν_τ . Each of them has a charged lepton partner, respectively e^- , μ^- , and τ^- . They can interact with them and with six quarks u, d, c, s, b, and t only through the weak interaction and the exchange of a W^\pm or Z boson. Neutrino is really a special particle compared to the other fermions since it is the only one to interact solely with the weak interaction. Its interaction probability is many orders of magnitude smaller than for other leptons, making it a really elusive particle. Moreover, it is the lightest and most abundant fundamental particle.

More than 80 years after the first experimental detection, a lot of interrogations are still surrounding the neutrino. What is its fundamental nature? What is its mass? Does a sterile neutrino exist? Current experiments are trying to answer these questions, making neutrino physics one of the most promising fields to explore physics Beyond the Standard Model (BSM).

1.2 I oscillate...

Neutrino oscillation formalism

The neutrino oscillation is a complex quantum mechanism induced by lepton mixing. Indeed, neutrino flavours $|\nu_\alpha\rangle$ are superpositions of three neutrino mass eigenstates $|\nu_i\rangle$ which are the ones propagating. We can write:

$$|\nu_\alpha\rangle = \sum_{i=1}^3 U_{\alpha i}^* |\nu_i\rangle \quad (1.8)$$

where $\alpha=e, \mu, \tau$.

U corresponds to the 3x3 lepton mixing matrix known as the Pontecorvo-Maki-Nakagawa-Sakata (PMNS) matrix that can be parameterized as:

$$U = \begin{pmatrix} U_{e1} & U_{e2} & U_{e3} \\ U_{\mu1} & U_{\mu2} & U_{\mu3} \\ U_{\tau1} & U_{\tau2} & U_{\tau3} \end{pmatrix} \quad (1.9)$$

$$= \begin{pmatrix} c_{12}c_{13} & s_{12}c_{13} & s_{13}e^{i\delta} \\ -s_{12}c_{23} - c_{12}s_{23}s_{13}e^{i\delta} & c_{12}c_{23} - s_{12}s_{23}s_{13}e^{i\delta} & s_{23}c_{13} \\ s_{12}s_{23} - c_{12}c_{23}s_{13}e^{i\delta} & -c_{12}s_{23} - s_{12}c_{23}s_{13}e^{i\delta} & c_{23}c_{13} \end{pmatrix} \begin{pmatrix} 1 & 0 & 0 \\ 0 & e^{i\lambda_1} & 0 \\ 0 & 0 & e^{i\lambda_2} \end{pmatrix} \quad (1.10)$$

where $c_{ij}=\cos(\theta_{ij})$, $s_{ij}=\sin(\theta_{ij})$ with $\theta_{12}, \theta_{13}, \theta_{23}$ the three mixing angles. δ corresponds to the Dirac-CP-violation phase and could introduce a difference between ν and $\bar{\nu}$ oscillations. λ_1, λ_2 are the Majorana phases. They are not involved in neutrino oscillation and participate only in lepton number violation processes in which Majorana nature plays a role. In the case of a Dirac neutrino, they can be absorbed by the neutrino state. The relation 1.8 means that the probability for the flavour α to have the mass m_i is given by $|U_{\alpha i}^*|^2$. Inversely, when

ν_i interacts in a detector and produces a charged lepton, $|U_{\alpha i}|^2$ is the probability that the charged lepton will be of flavor α .

Each mass eigenstate propagates with a different phase factor leading to a modification of their coherent superposition. This provokes the flavour oscillation that is observed. The probability for the flavour α to change in the flavour β in vacuum and in the three flavours scenario is given by:

$$P(\nu_\alpha \longrightarrow \nu_\beta) = \delta_{\alpha\beta} - 4 \sum_{i < j} \text{Re}[U_{\alpha i} U_{\beta i}^* U_{\alpha j}^* U_{\beta j}] \sin^2\left(\frac{\Delta m_{ji}^2 L}{4E}\right) + 2 \sum_{i < j} \text{Im}[U_{\alpha i} U_{\beta i}^* U_{\alpha j}^* U_{\beta j}] \sin\left(\frac{\Delta m_{ji}^2 L}{2E}\right) \quad (1.11)$$

Where L corresponds to the distance traveled by the neutrino ($\sim ct$ since it is ultra-relativistic), E its energy, and $\Delta m_{ji}^2 = m_j^2 - m_i^2$. It is important to notice that only the squared-mass difference of neutrino is involved in the oscillation, making impossible the exact measurement of each of them through this process. From this equation, it is also clear that the observation of oscillation implies that Δm_{ji}^2 can not be null, so that the masses can not be degenerated and that at least two are different from zero. In total, the probability of oscillation depends on six parameters: the three mixing angles ($\theta_{12}, \theta_{13}, \theta_{23}$), the CP-phase δ and two independent squared-mass differences (one can choose Δm_{13}^2 and Δm_{12}^2 , hence, Δm_{23}^2 can be obtained by a calculation).

It exists a simpler approach where only a two flavours oscillation is considered. The oscillation probability becomes:

$$P(\nu_\alpha \longrightarrow \nu_\beta) = \sin^2(2\theta) \sin^2\left(\frac{\Delta m^2 L}{4E}\right) \quad (1.12)$$

This approximation works in many experimental scenarios. For example, it fits well atmospheric neutrino experiments where the oscillation is mainly $\nu_\mu \longrightarrow \nu_\tau$ and solar neutrino experiments since only ν_e are produced in fusion reactions and that they have a really small ν_3 component. In this case, the probability depends only on one mixing angle and on one squared-mass difference. Atmospheric and solar neutrino experiments are sensitive to different mass splitting that we can identify as $\Delta m_{atm}^2 \simeq \Delta m_{13}^2$ and $\Delta m_{sol}^2 = \Delta m_{12}^2$ respectively.

Nowadays, it exists various neutrino oscillation experiments that measure oscillation parameters using the two or three-flavour equation. Each one is sensitive to its own sub-set of parameters depending on the neutrino source, the energy region they observe, the distance L between the detector and the production point but also if they are looking to the appearance $P(\nu_\alpha \longrightarrow \nu_\beta)$ or disappearance $P(\nu_\alpha \longrightarrow \nu_\alpha)$ channel. No ν α [29], T2K [30], RENO [31], or in the future JUNO [32] and DUNE [33] can be cited as experiments participating to this effort. By combining all their results, more and more precise values are obtained. The parameter values determined from a global analysis are summarized in Table 1.1.

Neutrino mass hierarchy

As already discussed, neutrino oscillations only give access to the squared-mass difference. Although we know that it exists a narrow splitting and a much larger one, only the sign of Δm_{12}^2 is known. Three instances are possible for the mass pattern depending on the sign of Δm_{13}^2 :

| Parameter | Best fit $\pm 1\sigma$ | 3σ range |
|--|---------------------------|-----------------|
| Δm_{12}^2 (IO or NO) [10^{-5} eV ²] | $7.50^{+0.22}_{-0.20}$ | 6.94-8.14 |
| $\sin^2\theta_{12}$ (IO or NO) [10^{-1}] | 3.18 ± 0.16 | 2.71-3.69 |
| $ \Delta m_{13}^2 $ (IO) [10^{-3} eV ²] | $2.45^{+0.02}_{-0.03}$ | 2.37-2.53 |
| $ \Delta m_{13}^2 $ (NO) [10^{-3} eV ²] | $2.55^{+0.02}_{-0.03}$ | 2.47-2.63 |
| $\sin^2\theta_{23}$ (IO) [10^{-1}] | $5.78^{+0.10}_{-0.17}$ | 4.33-6.08 |
| $\sin^2\theta_{23}$ (NO) [10^{-1}] | 5.74 ± 0.14 | 4.34-6.10 |
| $\sin^2\theta_{13}$ (IO) [10^{-2}] | $2.225^{+0.064}_{-0.070}$ | 2.018-2.424 |
| $\sin^2\theta_{13}$ (NO) [10^{-2}] | $2.200^{+0.069}_{-0.062}$ | 2.000-2.405 |

Table 1.1 – Neutrino oscillation parameters determined from a global analysis. IO stands for Inverted Ordering and NO for Normal Ordering. Table adapted from [34].

- The Normal Ordering (NO) $m_1 < m_2 \ll m_3$. It is called "normal" since the neutrino ν_1 has the largest component of ν_e and ν_3 the smallest, it reproduces the charged lepton mass scenario.
- The Inverted Ordering (IO) $m_3 \ll m_1 < m_2$. In this case, m_3 is the smallest neutrino mass.
- The Quasi degenerated ordering $m_1 \simeq m_2 \simeq m_3$ is a special case where masses are much larger than the mass splittings (NO or IO still hold if respectively m_1 or m_3 is the lightest).

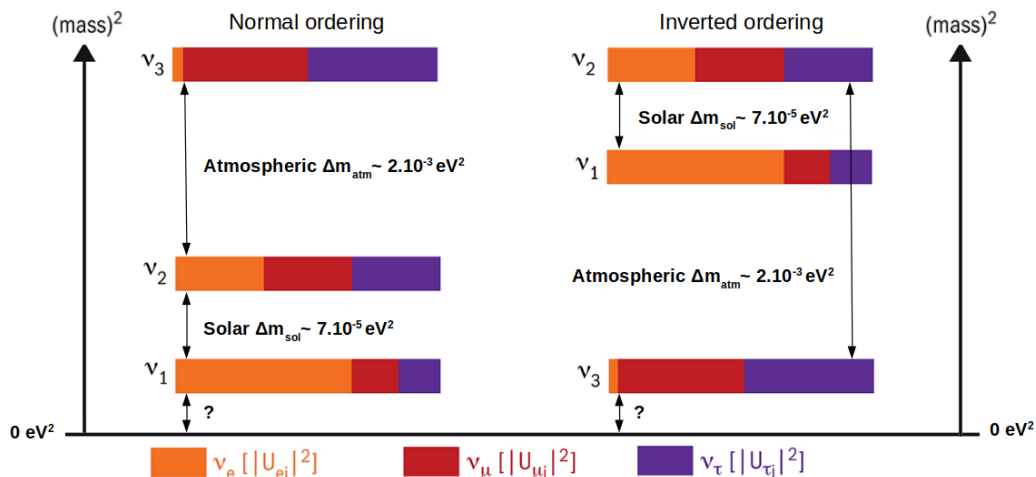


Figure 1.1 – Neutrino mass hierarchy in the case of the normal and inverted ordering.

The mass patterns are illustrated in Fig.1.1. It also shows to which mass-splitting solar and atmospheric experiments are the most sensitive in the case of the two flavour oscillation

approximation. In any case, the absolute mass scale remains unknown.

It is crucial to find which one of the neutrino mass hierarchy scenarios is the right one and therefore to measure the sign of Δm_{13}^2 . It would have implications not only for neutrino physics [35] but also for astrophysics [36], and cosmology [37]. This could be done for example using atmospheric neutrinos with an experiment that can observe matter effects on their oscillation when they are crossing the Earth. However, the current generation of experiments is not sensitive enough and is only able to favor the NO up to 2.7σ [38]. The effort will be pursued by next-generation experiments and the probability of having an answer in the decade has never been higher [39].

1.3 ... so I have a mass

The neutrino mass in the Standard Model

Neutrino oscillations imply a non-zero neutrino mass which is in contradiction with the current neutrino picture in the Standard Model. Indeed, since the Yukawa coupling requires a left-handed f_L and a right-handed f_R field component, the Higgs mechanism that generates the mass of the other fermions is incompatible with the only left-handed neutrino ν_L and right-handed antineutrino $\bar{\nu}_R$. Therefore, an extension of the model in which the neutrino becomes a massive particle is required. Three main approaches are possible depending on the neutrino nature.

Dirac mass term - The first way is just to consider the existence of a right-handed neutrino ν_R which would be called "sterile" since it would not interact through the weak interaction. In this case, the lepton number would be conserved and the neutrino described by four components ν_L , ν_R , $\bar{\nu}_R$ and $\bar{\nu}_L$ as any so-called "Dirac" particle. The Dirac mass term to add to the Lagrangian would be:

$$\mathcal{L}^D = -m_D(\bar{\nu}_R\nu_L + \bar{\nu}_L\nu_R) \quad (1.13)$$

$$m_D = \frac{y_\nu \times v}{\sqrt{2}} \quad (1.14)$$

where m_D is the Dirac neutrino mass, y_ν is the Yukawa coupling constant for neutrino, and v is the vacuum expectation value of the Higgs field. However, in this case, the Yukawa coupling has to be really tiny to give a small mass to the neutrino ($y_\nu \sim 10^{-12}$ for $m_D \sim 0.1$ eV), raising a new question: Why is neutrino mass so small compared to other fermions?

Majorana mass term - The second way is to consider a so-called "Majorana" neutrino. In 1937, E. Majorana proposed a new formalism for neutral fermions in which the lepton number conservation could be violated since a neutral particle could be identical to its antiparticle [40]. In this case, the neutrino field would satisfy the following:

$$\nu_R = \nu_L^c \quad (1.15)$$

where the index c corresponds to the charge conjugate. From eq.1.15, we can build a Majorana mass term to add to the Lagrangian using only the left-handed neutrino component:

$$\mathcal{L}_L^M = -\frac{m_L}{2}(\bar{\nu}_L\nu_L^c + \bar{\nu}_L^c\nu_L) \quad (1.16)$$

The factor $\frac{1}{2}$ appears to avoid double-counting since the hermitian conjugate is equal. This term creates two left-handed neutrinos out of vacuum and so it violates the lepton number

conservation by two units. Since it contains only left-handed components, it requires a coupling with a Higgs weak triplet to be gauge invariant. However, the Standard Model includes only one Higgs weak doublet, preventing the existence of this term in the Lagrangian without implying considerable additions to the model. If we want to stay in a minimal extension of the Standard Model, i.e. $m_L=0$, it seems mandatory to consider the existence of the right-handed sterile neutrino also in this case. The new Majorana mass term using this component would be written:

$$\mathcal{L}_R^M = -\frac{m_R}{2}(\bar{\nu}_R\nu_R^c + \bar{\nu}_R^c\nu_R) \quad (1.17)$$

But then, nothing prevents having the Dirac mass term as well. Such a combination is called the "See-Saw mechanism."

The See-Saw mechanism - This interesting approach consists in staying in the framework of the Majorana neutrino formalism but combining eq.1.17 with 1.13 to obtain the most general mass term possible. In addition to eq.1.13, we can now also create another Dirac mass term using the charge conjugate fields ν_L^c and ν_R^c . We can write:

$$\begin{aligned} \mathcal{L}^{M+D} &= \mathcal{L}_R^M + \mathcal{L}_1^D + \mathcal{L}_2^D \\ &= -\frac{m_R}{2}\bar{\nu}_R\nu_R^c - \frac{m_D}{2}\bar{\nu}_R\nu_L - \frac{m_D}{2}\bar{\nu}_L^c\nu_R^c + h.c. \end{aligned} \quad (1.18)$$

where h.c. means hermitian conjugate. We can simplify to:

$$\mathcal{L}^{M+D} = \frac{1}{2}(\bar{\nu}_L^c \quad \bar{\nu}_R) \mathcal{M} \begin{pmatrix} \nu_L \\ \nu_R^c \end{pmatrix} + h.c. \quad (1.19)$$

$$\mathcal{M} = \begin{pmatrix} 0 & m_D \\ m_D & m_R \end{pmatrix} \quad (1.20)$$

Since the matrix \mathcal{M} is not diagonal, the chiral eigenstates ν_L and ν_R do not have a definite mass. In other words, we have to diagonalize \mathcal{M} using an invertible matrix \mathcal{U} in order to obtain the mass eigenstates ν and N that correspond to the physical particles. We can write:

$$\mathcal{U}^{-1}\mathcal{M}\mathcal{U} = \tilde{\mathcal{M}} = \begin{pmatrix} m_\nu & 0 \\ 0 & m_N \end{pmatrix} \quad (1.21)$$

$$m_{\nu,N} = \frac{1}{2}(m_R \mp \sqrt{m_R^2 + 4m_D^2}) \quad (1.22)$$

If we choose as a constrain $m_D \ll m_R$ we obtain for the two neutrino masses:

$$m_\nu = \frac{m_D^2}{m_R} \quad (1.23)$$

$$m_N = m_R(1 + \frac{m_D^2}{m_R^2}) \simeq m_R \quad (1.24)$$

Consequently, in the case where m_R (and so m_N) is taken huge, m_ν becomes tiny. One can also express the mass eigenstates using the chiral eigenstates:

$$\nu \simeq (\nu_L + \nu_L^c) - \frac{m_D}{m_R^2}(\nu_R + \nu_R^c) \quad (1.25)$$

$$N \simeq (\nu_R + \nu_R^c) - \frac{m_D}{m_R^2}(\nu_L + \nu_L^c) \quad (1.26)$$

An interpretation is that ν corresponds to the light Majorana neutrino, mostly left-handed, that we observe in the weak interactions while N is a heavy sterile mostly right-handed neutrino. This is the so-called "Type I See-Saw mechanism." It provides a really elegant answer on the smallness of neutrino masses compared to other fermions due to their Majorana nature. If $m_D \sim 1$ MeV like for the other leptons, it would mean that m_R must be of the order of 10^9 MeV to obtain a light Majorana neutrino mass $m_\nu \sim 1$ meV. Moreover, the existence of such a heavy neutrino in the early universe could give clues on matter-antimatter asymmetry if it exists a CP violation in its decay. Of course, also in this case, the lepton number is not conserved.

We can summarize our three cases and their implications as follows:

- The neutrino is a **Dirac particle**, meaning that $m_{L,R} = 0$. It exists however a right-handed sterile component to the neutrino field. The lepton number is conserved.
- The neutrino is a **Majorana particle**. There is no need to add a right-handed component to the neutrino field, but the mass mechanism implies BSM Higgs physics. The lepton number conservation is violated.
- The neutrino is a **Majorana particle** but has a **non-zero Dirac mass**. A right-handed component exists, and the neutrino acquired its mass through the See-Saw mechanism. It must exist a heavy sterile neutrino. The lepton number conservation is violated.

One can understand the importance of finding out the nature of the neutrino, i.e. if it is a Dirac or a Majorana particle. However, it is a tough task since there is only one way within the current experimental scope to answer this question: the detection of neutrinoless double beta decay ($0\nu 2\beta$). It will be widely discussed in Chapter 2 since it is the topic on which the work done in this thesis takes place. But first, let's finish our exploration of the neutrino properties by interesting us to one of the big unknowns of neutrino physics: the absolute mass scale.

The absolute mass scale and its measurement

Although we have access to squared-mass differences of neutrino masses with oscillation experiments, their absolute mass scale stays a mystery. Several experiments are trying to measure it through different methods. The search for $0\nu 2\beta$ is one of them but it will not be mentioned in this section since the next chapter will be devoted to it. Some of the other efforts in this direction will be presented here.

Direct measurements with the β -decay spectrum - The shape of the emitted electron energy spectrum is sensitive to the mass of the electron-neutrino. According to the β -decay theory, the distribution of the electron energy in the final state is proportional to:

$$\frac{dN}{dE_e} \propto p(E + m_e)(E_0 - E_e)\sqrt{(E_0 - E_e)^2 - m_\nu^2} \quad (1.27)$$

where E_e is the electron energy, E_0 the maximum energy available, m_e the electron mass and m_ν the anti-neutrino mass.. One can clearly see that in the case of a massive neutrino, the distribution shape is modified, especially the position of the end-point compared to the

total available energy Q_β (Fig.1.2). Indeed, if $m_\nu \neq 0$, it is shifted negatively by $m_\nu c^2$ which corresponds to the rest energy of the neutrino. Hence, by measuring this shift, one should be able to measure in a model-independent way the neutrino mass. In reality, since the current experiments do not reach an energy resolution good enough to discriminate the three neutrino masses, they are sensitive to an effective value equal to:

$$m_\beta = \sqrt{\sum_{i=1}^3 |U_{ei}|^2 m_i^2} \quad (1.28)$$

However, the discrepancy between the spectrum for the non-massive and the massive neutrino is extremely small and constitutes an experimental challenge to be measured. The electron has a tiny probability of landing near the endpoint, making the statistics really low in this region. Consequently, isotopes with a small Q_β value and a short half-life are preferred to be used since it allows a higher rate in the Region Of Interest (ROI). Moreover, the endpoint region of the spectrum can be affected by many nuclear or atomic effects. It is important to choose an isotope which is not showing too many of these alterations to ensure maximum sensitivity to the effective neutrino mass.

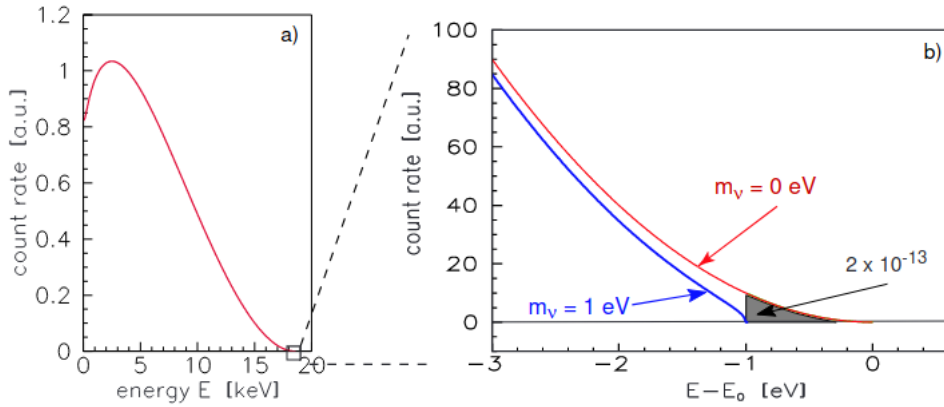


Figure 1.2 – Example of the beta decay of the tritium (left). Zoom on the end-point region (right). One can see the effect on the spectrum of a massive neutrino. The shaded region corresponds to only a 2×10^{-13} fraction of the total number of events. Figure from [41].

Since it is full-filling these requirements, tritium in a gaseous form is one of the most promising isotopes. It decays through the reaction:



with a $Q_\beta = 18.6$ keV and a half-life of $T_{1/2} = 12.32$ yr. It is used by the KATRIN experiment which is based on electrostatic spectrometers using a MAC-E filter [41]. It has obtained the most stringent limit of $m_\beta < 0.8$ eV. c^{-2} at 90% Confidence Level (CL) [42] and aims to reach a sensitivity at $m_\beta \sim 0.2$ eV. c^{-2} . In the future, the use of the Cyclotron Radiation Emission Spectroscopy (CRES) to measure the electron energy could eventually reach a sensitivity down to $m_\beta \sim 0.04$ eV. c^{-2} . The Project-8 collaboration has demonstrated the efficacy of the technique and has very recently obtained its first tritium β -decay spectrum [43].

Cosmological measurements - Since they are massive, neutrino density in the Universe affects various cosmological observables and the evolution of matter perturbations. This density depends on the neutrino mass sum defined by:

$$\sum m_\nu = m_1 + m_2 + m_3 \quad (1.30)$$

Hence, any measurement of spatial matter distributions and its power spectrum serves as a method of constraining $\sum m_\nu$, although it stays strongly model-dependant. One can cite for example the analysis of the CMB (Cosmic Microwave Background) lensing [44] or the use of the Lyman- α forest power spectrum [45] as methods to do so. The most recent limit has been obtained by the Dark Energy Survey (DES) and gives $\sum m_\nu < 0.13$ eV at 95% CL in the Λ CDM context by combining its data with the Planck telescope ones [46].

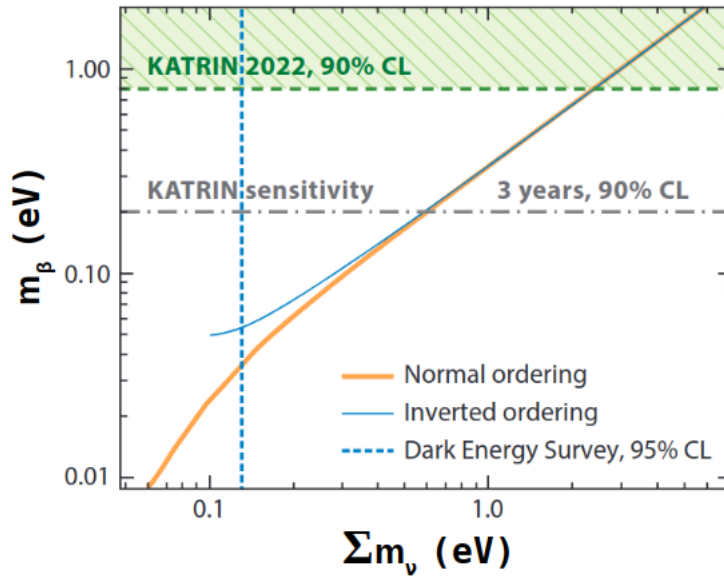


Figure 1.3 – m_β as a function of $\sum m_\nu$ depending on the mass ordering. The most recent limit obtained by KATRIN on m_β and by DES on $\sum m_\nu$ are shown. Figure from [47].

Different neutrino mass observables can be accessed using numerous direct or indirect detection methods. Due to its apparent smallness, it represents challenging measurements. However, by combining their results with the ones of oscillations experiments, the spectrum of possible values becomes smaller (Fig.1.3). This ongoing effort is crucial to obtain answers on the neutrino mass mechanism.

1.4 Conclusion

From a hypothetical particle to a key player in the field of particle physics, the neutrino is without a doubt a fascinating particle. Its elusive nature and the difficulty in detecting it have made it a challenge for physicists, but it has also provided unique opportunities for uncovering new physics. The discovery of neutrino oscillations, for example, was one of the first pieces of evidence for physics beyond the Standard Model and has led to a better understanding of neutrinos.

Many questions are still pending such as the fundamental neutrino nature (Majorana or Dirac particle), the mass ordering and the absolute mass scale, the existence of a sterile neutrino, or the CP violation in the lepton sector. The experimental efforts pursued to answer them are stimulating the research in this domain since many years and are making the neutrino a vector of discovery. Furthermore, they could provide valuable insights into other areas of physics, such as cosmology and the early universe.

The search for neutrinoless double beta decay could shed light on most of these mysteries in case of observation and is moreover the only accessible way to assess the Majorana nature of the neutrino. This underlines the importance of this process and places it at the center of neutrino physics. The interest in it is growing year by year along with the experimental progress to detect it. It is the main subject of this thesis, and it will be described in the next chapter.

Chapter 2

Searching for $0\nu 2\beta$

The work presented in this thesis has been realized in the framework of the search for neutrinoless double beta decay ($0\nu 2\beta$). With the questions raised by the discoveries on neutrinos made in the last decades, this topic has been propelled to one of the most important of contemporary experimental physics. Its observation would state the Majorana nature of neutrinos and the lepton number violation. However, it involves reaching stringent experimental conditions such as almost zero background events in the ROI. This chapter will describe the requirements to search for the rarest nuclear weak process.

2.1 What is $0\nu 2\beta$?

The two neutrino double beta decay

Before speaking about the $0\nu 2\beta$, it is essential to introduce the two neutrino double beta decay ($2\nu 2\beta$) since its existence is a prerequisite for the former to happen. The $2\nu 2\beta$ allows a nucleus (A, Z) to transform into $(A, Z+2)$ thanks to the simultaneous emission of two electrons and two anti-neutrinos:

$$(A, Z) \longrightarrow (A, Z + 2) + 2e^- + 2\bar{\nu}_e \quad (2.1)$$

It was initially proposed in 1935 by M. Goeppert-Mayer [48] who estimated a half-life higher than 10^{17} years for this disintegration using the Fermi's β decay formalism. It is a second-order process of weak interaction, making it extremely rare but possible.

Naturally, the nucleus $(A, Z+2)$ must have a smaller mass than (A, Z) for this decay to happen. In addition, the single β decay is required to be energetically forbidden or strongly suppressed so its half-life is in the experimental scope and its observation possible. The best candidates to undergo such a decay are the nuclei with an even number of protons and neutrons called even-even nuclei. The Bethe–Weizsäcker semi-empirical formula giving the mass $M(A, Z)$ of the nucleus (A, Z) is written as follows:

$$M(A, Z) = Zm_p + (A - Z)m_n - a_V A + a_S A^{2/3} + a_C \frac{Z^2}{A^{1/3}} + a_A \frac{(A - 2Z)^2}{A} + \delta(A, Z) \quad (2.2)$$

$$\delta(A, Z) = \begin{cases} +\delta_0, & \text{for even-even nuclei (A even)} \\ 0, & \text{for odd A nuclei} \\ -\delta_0, & \text{for odd-odd nuclei (A even)} \end{cases} \quad (2.3)$$

where m_p and m_n are, respectively, the proton and the neutron mass. The coefficients a_V , a_S , a_C and a_A are empirically determined and represent the effect on the binding energy of,

respectively, the volume of the nucleus, its surface, the Coulomb repulsion and the asymmetry neutrons/protons. Finally, $\delta(A, Z)$ is the pairing term that captures the spin pairing effect. From eq.2.2 and eq.2.3 it is clear that plotting $M(A, Z)$ as a function of the atomic number Z for isobaric nuclei gives one parabola for odd- A nuclei and two for even- A nuclei (Fig.2.1). In the latter case, due to the large mass difference between odd-odd and even-even nuclei introduced by the pairing term, it is often possible that the single β decay for the (A, Z) nucleus is forbidden since the $(A, Z+1)$ one has a higher mass. Consequently, the only way for it to decay to a more energetically favorable state is to simultaneously realize two beta decays to transform into the $(A, Z+2)$ isobaric state.

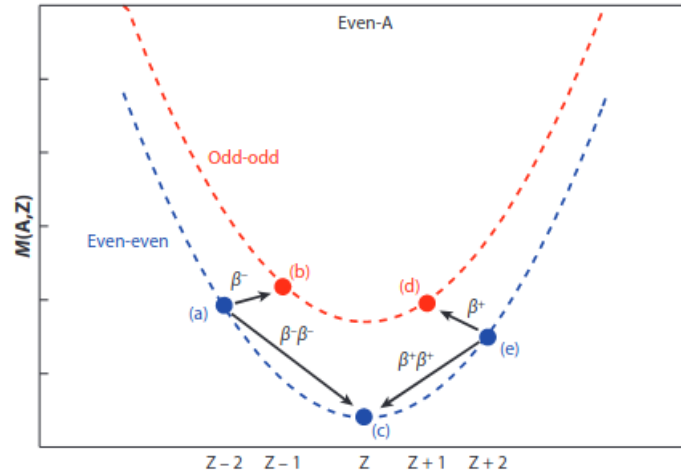


Figure 2.1 – $M(A, Z)$ as a function of Z in the case of even- A nuclei. The β^- decay from (a) to (b) is forbidden due to energy conservation. However, the $2\nu 2\beta$ from (a) to (c) is possible. Similar behavior is observed with electron capture or β^+ decay. Figure from [49].

The Standard Model authorizes this process since it does not violate any conservation law and it was detected for the first time in 1950 in ^{130}Te for which a half-life of 1.4×10^{21} years was measured [50]. Today, it has been observed for 11 nuclei over the 36 for which this decay is technically feasible with a half-life between 10^{18} and 10^{24} years [51]. These isotopes are summarized in Table 2.1.

The neutrinoless double beta decay

In the scenario where neutrinos are Majorana particles, the neutrinoless double beta decay becomes realizable. In 1939, W.H. Furry was the first to propose that a double beta decay without neutrino emission could occur through the emission and re-absorption of virtual Majorana neutrinos [52]. The reaction can be simply written:



Two electrons are created in the process, violating the lepton number conservation by two units. Hence, it is a BSM process that has never been observed.

It can be mediated by various BSM mechanisms, such as R-parity violation in supersymmetric models or the exchange of a right-handed W boson. However, the one requiring the most minimal extension of the Standard Model is the exchange of a light Majorana neutrino. It is usually the one studied and considered by most of the experiments searching for $0\nu 2\beta$: it

| Isotope | $Q_{\beta\beta}$ (keV) | $T_{1/2}^{2\nu 2\beta}$ (yr) |
|-------------------|------------------------|---------------------------------------|
| ^{48}Ca | 4272 | $5.3_{-0.8}^{+1.2} \times 10^{19}$ |
| ^{76}Ge | 2039 | $1.88 \pm 0.08 \times 10^{21}$ |
| ^{82}Se | 2995 | $0.87_{-0.01}^{+0.02} \times 10^{19}$ |
| ^{96}Zr | 3350 | $2.3 \pm 0.2 \times 10^{19}$ |
| ^{100}Mo | 3034 | $7.06_{-0.13}^{+0.15} \times 10^{18}$ |
| ^{116}Cd | 2813 | $2.69 \pm 0.09 \times 10^{19}$ |
| ^{128}Te | 865.87 | $2.25 \pm 0.09 \times 10^{24}$ |
| ^{130}Te | 2527 | $7.91 \pm 0.21 \times 10^{20}$ |
| ^{136}Xe | 2457 | 2.18×10^{21} |
| ^{150}Nd | 3371 | $9.34 \pm 0.65 \times 10^{18}$ |
| ^{238}U | ~ 1100 | $2.0 \pm 6 \times 10^{21}$ |

Table 2.1 – Nuclei for which the $2\nu 2\beta$ has been observed [51]. Their Q-value and measured two neutrino double beta decay half-life are indicated.

links the half-life of the decay to clear neutrino physics parameters and allows us to compare their sensitivity despite their technological differences. In any case, the detection would state the Majorana nature of neutrinos since it is impossible in the Dirac neutrino case [53].

For the light Majorana neutrino exchange, the $0\nu 2\beta$ rate can be written as follows:

$$(T_{1/2}^{0\nu 2\beta})^{-1} = G^{0\nu} g_A^4 |M^{0\nu}|^2 \frac{m_{\beta\beta}^2}{m_e^2} \quad (2.5)$$

Where we have:

$m_{\beta\beta}$, **The Majorana effective mass** - The experimental observable $T_{1/2}^{0\nu 2\beta}$ allows to constraint this important neutrino physics parameter. It is defined by:

$$m_{\beta\beta} = \left| \sum_{i=1}^3 U_{ei}^2 m_i \right| \quad (2.6)$$

It depends on the three neutrino mass eigenstates $m_{1,2,3}$, the two mixing angles θ_{12} and θ_{13} , the Dirac CP violation phase δ and the two Majorana phases $\lambda_{1,2}$ (see sec.1.2). It clearly gives information on the neutrino absolute mass scale as mentioned in section 1.3. Figure 2.2 shows the possible values for $m_{\beta\beta}$. Two regions are obtained depending on the neutrino mass ordering and the uncertainties of oscillations parameters and Majorana phases.

$G^{0\nu}$, **The phase-space factor** - This term embeds the kinematic of the decay and depends on the total energy of it ($G^{0\nu} \sim Q_{\beta\beta}^5$). The larger it is, the lower the expected $0\nu 2\beta$ half-life. It is determined with high accuracy, and a good summary of recent calculations for the isotopes of Table 2.1 can be found in [55].

g_A , **The weak axial coupling vector** - This parameter describes the strength of the weak interaction between nucleons. It is usually taken equal to $g_A \simeq 1.27$, which is the value in the case of free nucleon approximation measured in neutron beta decay. However, it could exist a quenching of this factor ($g_A < 1$) in $0\nu 2\beta$ due to nuclear medium and many-body

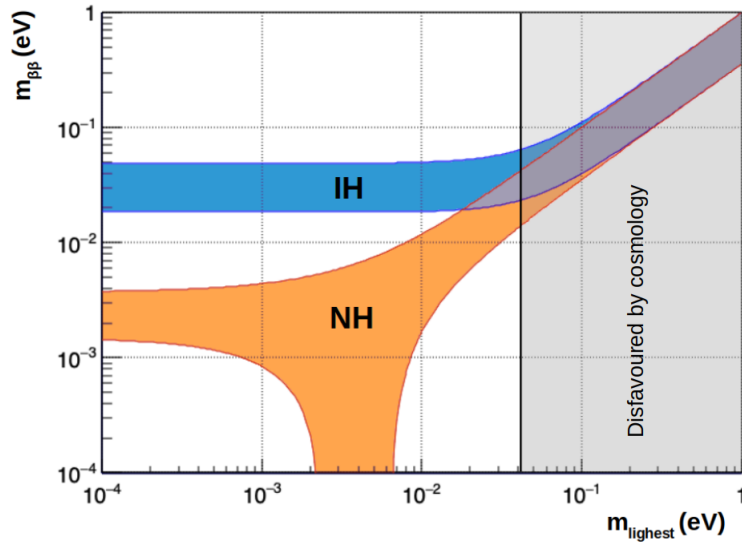


Figure 2.2 – Possible values for $m_{\beta\beta}$ as a function of the lightest neutrino mass. The blue region corresponds to values in the Inverted Hierarchy (IH) case, while the orange region is for the Normal Hierarchy (NH). The shaded part region shows the region disfavoured by the last results in cosmology [54] (see section 1.3).

nuclear effects that could negatively impact the $0\nu 2\beta$ rate [56]. This is still an open question and experimental aside theoretical efforts to answer it are ongoing.

$|\mathbf{M}^{0\nu}|$, **The Nuclear Matrix Element (NME)** - In addition to g_A , this term is the main source of uncertainties on eq.2.5 and therefore inevitably on $m_{\beta\beta}$ measurement. It describes all the nuclear physics aspects of the process. Its calculation implies complex many-body interactions, and theoretical models must be used. Various ones exist with their own advantages and limitations, but they are not always available for all the isotopes. One can cite, for example, the Nuclear Shell Model (NSM), the Quasi-particle Random Phase Approximation (QRPA), the Interacting Boson Model (IBM), or the Energy Density Functional (EDF). As it is well represented in Figure 2.3, these models give spreaded values that are not often compatible with each other. Consequently, when a constraint is put by an experiment on $m_{\beta\beta}$, an interval is given by considering the two extreme NME values for the observed isotope.

2.2 The experimental challenge

The experiments searching for $0\nu 2\beta$ measure at least the summed energies of the two emitted electrons. When anti-neutrinos are emitted along the electrons, they all share the available energy, leading to a continuous energy spectrum from 0 to $Q_{\beta\beta}$ with a maximum around 1/3 of $Q_{\beta\beta}$. In the case of the $0\nu 2\beta$ where only electrons are emitted, they should have a fixed energy equal to $Q_{\beta\beta}$, hence giving a mono-energetic peak at that position in the spectrum. The typical expected energy spectrum is given in Figure 2.4.

Observing this $0\nu 2\beta$ signature is challenging since this process half-life is expected to be much longer than the Universe age. To understand what are the main difficulties, we can estimate the sensitivity of a potential experiment. Given the exponential probability distribution of nuclear decays, the number of expected $0\nu 2\beta$ counts for a mass M of the

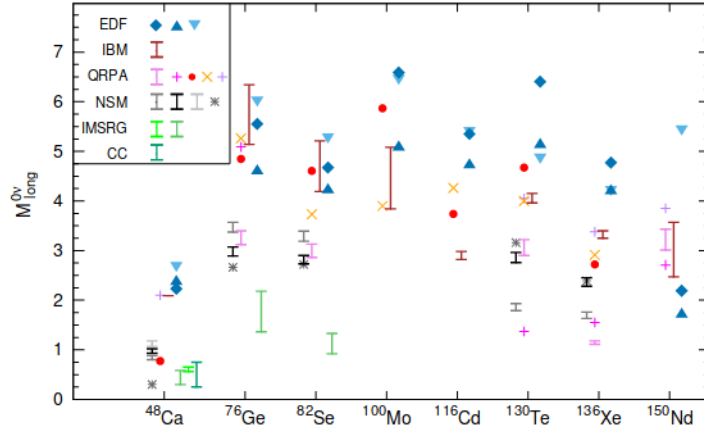


Figure 2.3 – The NME in case of the light Majorana neutrino exchange calculated using different nuclear many-body models for some of the $2\nu 2\beta$ isotopes. Figure taken from the recent $0\nu 2\beta$ review [57].

active detector and a time of exposure t is:

$$N = \log(2) \times a \times \epsilon \times \frac{M \times t}{T_{1/2}^{0\nu 2\beta}} \quad (2.7)$$

where a is the number of $0\nu 2\beta$ nuclei per kg in the active detector and ϵ the detection efficiency. In the case where n_b background events are expected without any uncertainty, the total number of events in the ROI N_{obs} follows this Poisson distribution:

$$Po(N_{obs}, N + n_b) = \frac{(N + n_b)^{N_{obs}}}{N_{obs}!} e^{-(N+n_b)} \quad (2.8)$$

It is possible to define an upper (lower) limit N_{up} (N_{low}) as the value of the parameter N such that, if we conduct numerous experiments that adhere to the Poisson distribution $Po(n; N_{up})$ ($Po(n; N_{low})$), no more than a fraction β (α) of them will result in a number that is greater than (less than) N_{obs} . The β and α values give the confidence level (CL). For example, a 95% CL corresponds to $\alpha + \beta = 0.05$. To estimate the sensitivity of our experiment, we consider that no observation is made (i.e., $N = 0$ and $n_b \neq 0$). In this case, only an upper limit has a meaning and is given by [58]:

$$S(n_b) = \sum_{n=0}^{\infty} Po(n|n_b)U(n|n_b) \quad (2.9)$$

with $U(n|n_b)$ the upper limit obtained in the unified approach [59]. In the large background approximation $S(n_b)$ becomes:

$$N_{up} \equiv S(n_b) \approx \kappa \sqrt{n_b} \quad (2.10)$$

with $\kappa = 1.64(1.96)$ for a 90%(95%) CL. Using eq.2.7 and eq.2.10, we can write for the experimental sensitivity to $T_{1/2}^{0\nu 2\beta}$:

$$T_{1/2}^{0\nu 2\beta} \propto a \times \epsilon \times \frac{M \times t}{\sqrt{n_b}} \quad (2.11)$$

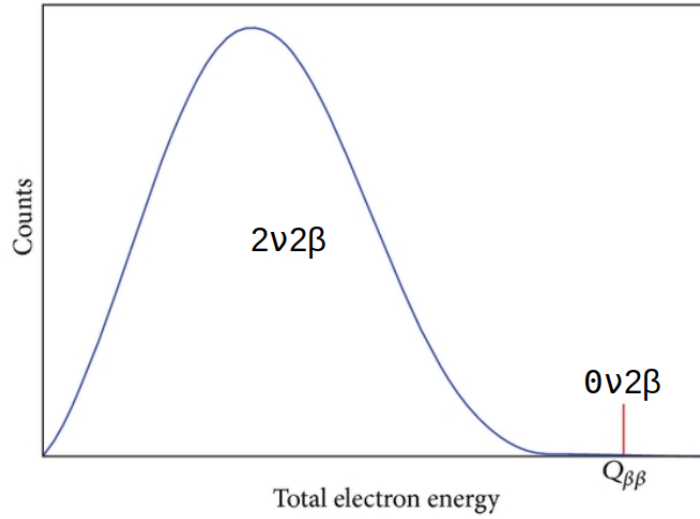


Figure 2.4 – $2\nu 2\beta$ and $0\nu 2\beta$ energy spectrum. In reality, the mono-energetic line due to $0\nu 2\beta$ is broadened by the detector energy resolution. The relative amplitude of the two spectra is exaggerated for better visualization.

We can introduce a new variable called the background index b that represents the number of background events expected in the region of interest per kilogram, per keV, per year in counts/kg.keV.yr (ckky) defined as:

$$b = \frac{n_b}{M \times t \times \Delta E} \quad (2.12)$$

Where ΔE corresponds to the width of the ROI related to the detector energy resolution. Finally, we obtain:

$$T_{1/2}^{0\nu 2\beta} \propto a \times \epsilon \times \sqrt{\frac{M \times t}{b \times \Delta E}} \quad (2.13)$$

This formula allows a good overview of the critical parameters. It is explicit that the total exposure $M \times t$ has to be maximized while b and ΔE have to be minimized. To do so, there are several parallel approaches that will now be described.

The isotope choice

In order to optimize the observation probability, both equations 2.13 and 2.5 must be considered. One can remark that several parameters in these depend on the isotope itself. The latter has to be chosen wisely among all the possible $0\nu 2\beta$ candidates presented in Table 2.1. Selecting an isotope with favorable matrix element predictions and the highest phase space increases the expected rate. Hence, it is usually interesting to aim for candidates with a large $Q_{\beta\beta}$ value. Moreover, it permits searching for the signal at higher energy in a region with fewer background events, as it will be discussed in Section 2.3. However, one has to deal with other constraints related to the feasibility and the cost of the experiment. Indeed, the $2\nu 2\beta$ isotope fraction in the active detector total mass must be maximized. It implies that the candidate already has a sufficient natural abundance or that it exists an enrichment technique at a reasonable cost. Nine "golden" isotopes are commonly considered the most promising since they fulfill these requirements. They are presented in Table 2.2 with some

of their relevant parameters. Naturally, the chosen isotope must also be compatible with a detection method. This leads us to the next point.

| $2\nu 2\beta$ isotope | Isotopic abundance (%) | $Q_{\beta\beta}$ (keV) | Phase space factor $G^{0\nu}$ (yr^{-1}) | Enrichable by centrifugation |
|-----------------------|------------------------|------------------------|--|------------------------------|
| ^{48}Ca | 0.19 | 4272 | 6.05×10^{-14} | No |
| ^{76}Ge | 7.73 | 2039 | 5.77×10^{-15} | Yes |
| ^{82}Se | 8.73 | 2995 | 2.48×10^{-14} | Yes |
| ^{96}Zr | 2.8 | 3350 | 5.02×10^{-14} | No |
| ^{100}Mo | 9.82 | 3034 | 3.89×10^{-14} | Yes |
| ^{116}Cd | 7.49 | 2813 | 4.08×10^{-14} | Yes |
| ^{130}Te | 34.08 | 2527 | 3.47×10^{-14} | Yes |
| ^{136}Xe | 8.86 | 2457 | 3.56×10^{-14} | Yes |
| ^{150}Nd | 5.64 | 3371 | 1.54×10^{-13} | No |

Table 2.2 – The nine "golden" isotopes with some of their parameters. Centrifugation is a method widely used and available at an industrial level for a reasonable cost. If this method is unavailable for a candidate, its enrichment is more complicated. This table is adapted from [60] in which a discussion about enrichment methods can be found.

The detection method

The choice of a suitable detector is an essential part since it participates in increasing the experiment sensitivity. Indeed, in equation 2.13, some parameters are closely related to it. First of all, the best way to maximize the detection efficiency ϵ is to use the calorimetric method, where the source is also the detector. It ensures a high probability of interaction for the electrons inside the detector. Secondly, the energy resolution must be high since the width of the ROI depends directly on it. Moreover, one should be able to disentangle a $2\nu 2\beta$ event in the endpoint region of the spectrum from an actual $0\nu 2\beta$ event. This requires an energy resolution around or below 1% to keep this background at a reasonable rate. Finally, the detection method must be easily scalable since a large mass of active material ($> \sim 100$ kg) is needed to enhance the number of candidate nuclei and the probability of a $0\nu 2\beta$ decay. With the "source=detector" method, it can usually be done relatively easily with a limitation more economical than technological.

Hence, one can identify two categories of experiments searching for $0\nu 2\beta$: the experiments with an embedded or dissolved source (source=detector) and those using an external source. The first category is the most popular and among it another discrimination can be made between those with a high energy resolution and those with a poor one. This paragraph is summarized on Figure 2.5 where the main current and future experiments are shown. A more detailed description of these experiments will also be given in Section 2.4.

The background reduction

The events that can mimic $0\nu 2\beta$ events by, for example, landing in the ROI or that add dead time to the detector constitute the $0\nu 2\beta$ experiment background. Understanding and

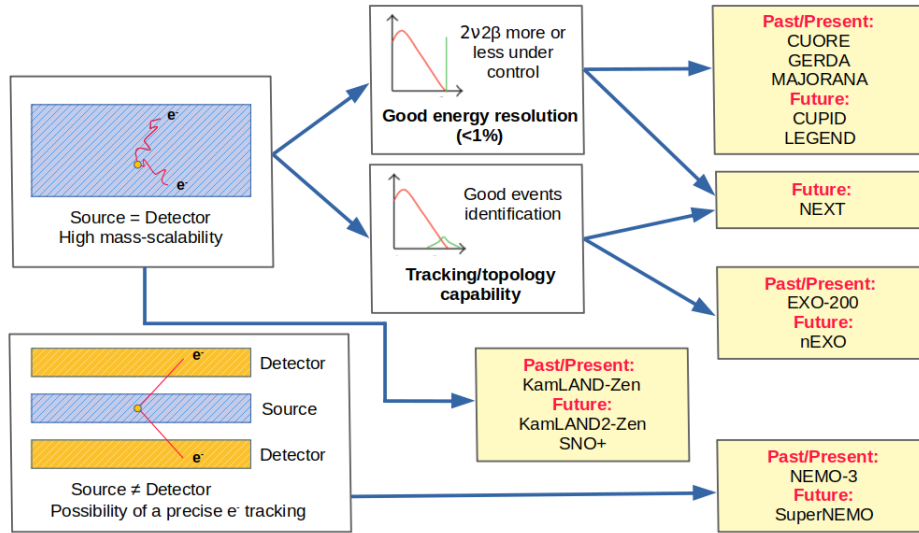


Figure 2.5 – The different categories to which belong the experiments searching for $0\nu 2\beta$. A detailed description of the experiments shown can be found in Section 2.4.

reducing them as much as possible is a crucial point. Indeed, in the ideal case of a "zero-background" experiment, the equation 2.13 would become:

$$T_{1/2}^{0\nu 2\beta} \propto a \times \epsilon \times M \times t \quad (2.14)$$

The sensitivity would scale linearly with the total exposure. Therefore, this experiment could run indefinitely without reaching any asymptotic limit in its maximum sensitivity (Fig.2.6). Hence, the experiments make a major effort to get as close as possible to this regime. The background index b (eq.2.12) is an excellent parameter to compare the background level reached by each of them since it is independent of the isotope and the detection method used. Currently, the lowest value was demonstrated by the GERDA experiment (see Section 2.4) with a background index of $b = 5.2 \times 10^{-4}$ ckky [61].

Although the isotope choice and the detection method can help to reduce or reject the background, additional efforts have to be provided, such as using extremely radiopure material or operating the experiment underground to shield it from cosmic rays. The main background sources to fight for $0\nu 2\beta$ experiments will be explicated in the next section.

2.3 An overview of the background sources

Cosmic rays

Cosmic-ray showers produced in Earth atmosphere can constitute a significant source of background in $0\nu 2\beta$ experiments if no action is taken against them. While most of the produced particles are quickly absorbed by a small amount of material, muons can cross several kilometers of material without being stopped. Unfortunately, they represent 75% of the total cosmic-ray interaction products at sea level and their flux is estimated around $2.10^{-2} \text{ cm}^{-2} \cdot \text{s}^{-1}$ in average. They contribute to the background directly by depositing an amount of their energy inside the detector and indirectly by producing other particles, such as protons or neutrons, during their interaction in the surrounding materials.

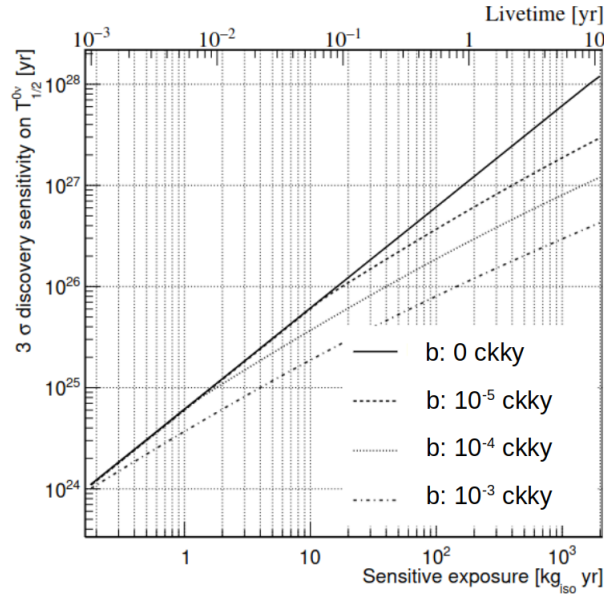


Figure 2.6 – 3σ discovery sensitivity on $T_{1/2}^{0\nu 2\beta}$ as a function of the sensitive exposure for different background index b . This plot is taken from the CUPID pre-CDR [62], an experiment using ^{100}Mo as the candidate isotope. A 5 keV FWHM energy resolution is assumed.

Therefore, operating $0\nu 2\beta$ experiments in underground laboratories is mandatory. The rock acts as a natural shield and reduces the muon flux drastically by around one order of magnitude for each additional 0.5 km depth, i.e., the probability of having a muon-induced background event. Some of the existing underground laboratories around the world are shown in Figure 2.7. A common way to compare them is by giving their depth in meter water equivalent (m.w.e), corresponding to the amount of water required to reach the same muon flux depletion. In addition, most of the experiments also have an active muon veto to mitigate the residual flux. It can consist of immersing the experimental setup into a water tank equipped with PMTs to detect the Cerenkov light produced by muons crossing it or surrounding it with plastic scintillators. It helps as well to reject by coincidences potential muon-induced particles.

Moreover, secondary particles created by cosmic-ray interactions can provoke spallation in materials and produce long-lived radionuclides inside. The latter are dangerous since they can undergo β decays with high Q-values and potentially land in the ROI. To mitigate this effect, materials that are part or will be in proximity to the detector are stored and sometimes even made underground before experiment assembly [63].

Natural radioactivity

One of the most harmful background contributions is natural radioactivity. Due to their very long half-life, ^{232}Th and ^{238}U are present in most of the materials and their decay chain constitutes the primary source of unwanted events. They produce α , β and γ radiations that can lead to signals in the ROI depending on their energy. α particles are produced between 4 and 9 MeV while γ 's are below 2.615 MeV, corresponding to the energy of the most energetic γ ¹ from ^{232}Th decay chain emitted during the de-excitation of ^{208}Tl . Finally, most of β 's are

¹In principle, higher energy γ are possible but have a very low branching ratio.

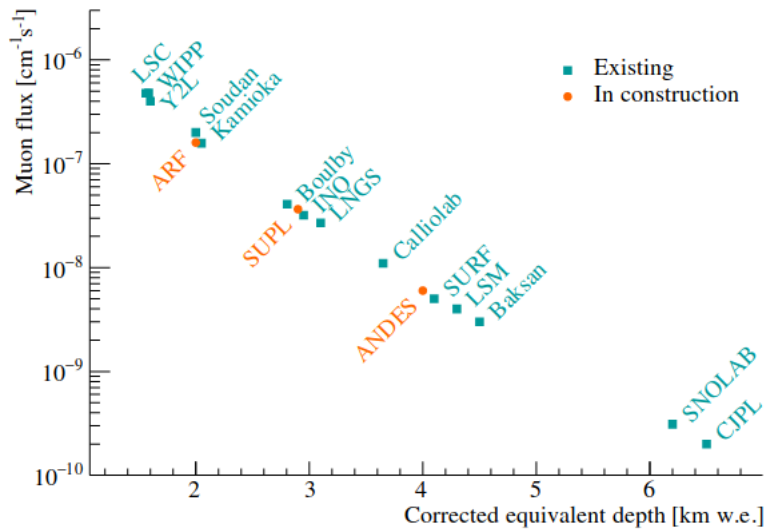


Figure 2.7 – Muon flux as a function of the depth in km.w.e for different underground laboratories.

emitted below 2 MeV except for the ^{214}Bi beta decay, which has a Q-value at 3.272 MeV.

From the material far away from the detector, only γ radiations can reach the latter. This contribution is called external radioactivity. A dense passive shield that can stop γ 's, such as lead², is usually implemented around the detector to reduce it at acceptable levels.

However, contamination in the detector or the material close to it can lead to partial or complete energy deposition in the detector by any radiation, even short-range α 's. A careful selection of suitable materials and monitoring of their radiopurity are essential, as well as meticulous surface cleaning. Event topology, particle identification, or delayed coincidences can also help further to reduce this contribution to the background. Moreover, it is crucial to stock and to do any operation, such as the detector assembly, in a clean environment with radon-free air to avoid additional contamination.

In general, the overall contribution of natural radioactivity depends on the isotope choice since the candidates with a $Q_{\beta\beta} > 2.615$ MeV (Table 2.2) have an expected signal in an energy region with naturally less expected background counts coming from this source.

Neutrons

As mentioned, materials are usually stored underground before the experiment installation to minimize spallation from neutrons produced in cosmic-ray showers. However, neutrons can also be produced underground due to residual muon spallation, (α, n) reactions and spontaneous fission decay of mainly ^{238}U present in the rock walls of the laboratory. These neutrons can induce secondary spallation, undergo inelastic scatterings, or be captured by nuclei, resulting in γ -ray emission during de-excitation. A neutron veto has to be implemented to keep the ones coming from outside the experiment to reach it. A possible approach can consist in surrounding the experiment with a bi-layer veto, including a thick layer of neutron moderator (e.g., polyethylene) and an inner layer with a high neutron absorption cross-section (e.g., boric acid or borated polyethylene).

²Archeological lead, which shows ultralow radioactivity [64], is often used in parts the closest to the detectors.

$2\nu 2\beta$ decay

The tail of the $2\nu 2\beta$ spectrum is an irreducible source of background when searching for $0\nu 2\beta$. It can populate the ROI (Fig. 2.4) and even mimic the topology of a $0\nu 2\beta$ event. A high energy resolution is crucial to minimize the amount of these events in the vicinity of the $0\nu 2\beta$ expected peak. The amplitude of this contribution depends on the detector technology but also on the chosen isotope: an experiment using an isotope with a relatively fast $2\nu 2\beta$ (e.g., ^{100}Mo) will have to face a higher rate of this kind of events. Moreover, when the detection method is relatively slow, it can lead to more probable random coincidences of two signals, also called pile-ups, whose energy can sum up and give a signal in the ROI.

Neutrinos

A flux of neutrinos from different sources, such as the atmosphere or the Sun, constantly crosses the Earth. They can interact within the detector through electron scattering ($\nu + e^- \rightarrow \nu + e^-$) or induce an inverse β -decay of the (A, Z) $\beta\beta$ isotope. In the latter case, the $(A, Z+1)$ produced can capture an electron and go back to the original isotope (A, Z) or undergo a β^- decay to the $(A, Z+2)$ state. These phenomena can lead to undesired events in the ROI, but their rate is so small that the current generation of $0\nu 2\beta$ experiments is not sensitive to them except for massive liquid scintillator ones. However, it might be a source that the next-to-next generations will have to deal with.

2.4 $0\nu 2\beta$ experiments

A broad experimental program is deployed to search for $0\nu 2\beta$ with a variety of detection methods and studied isotopes. Each of them has its advantages and limitations, but all share the same goal: detecting this extremely rare decay. It is crucial to explore these different directions since an observation in different isotopes is the only way to obtain the whole picture of $0\nu 2\beta$ and the mechanism which drives it. This section will describe the experimental landscape with the current and future generations of experiments.

2.4.1 High-Purity Germanium detectors (HPGe)

HPGe detectors are well-known and widely used devices in experimental physics. It consists of an ultrapure Ge diode, usually p-type, which is completely depleted of charge carriers when polarized inversely and cooled down to cryogenic temperature (~ 77 K). Hence, the e^- /hole(h^+) pairs created when a particle deposits its energy in the depleted zone are drifted to the electrodes and collected, producing a pulse. Since their number is proportional to the energy deposition, it allows measuring the latter with an excellent energy resolution ($< 0.2\%$ at 2 MeV) due to the small amount of energy needed to create a single pair (~ 2.9 eV). Their high efficiency, good linearity, and outstanding energy resolution make them promising detectors for $0\nu 2\beta$ search in ^{76}Ge .

GERDA

The GERmanium Detector Array (or GERDA) experiment was installed in the underground Laboratori Nazionali del Gran Sasso (LNGS) in Italy. During its last configuration, it was composed of 41 HPGe detectors (6 Closed-End Coaxial (CEC), 5 Inverted Coaxial Point Contact (ICPC) [65] and 30 Broad Energy Ge (BEGe) [66]) isotopically enriched to $\sim 87\%$ in ^{76}Ge . They were immersed in a 63 m^3 Liquid Argon (LAr) bath at 77K, acting as the cooling

liquid and as a shield against external radiations. Moreover, it was used as an active veto since it was equipped with Photo-Multiplier Tubes (PMTs) and Silicon Photo-Multiplier (SiPM) to read the scintillation light produced by the interaction of these radiations and reject them in case of coincidence with the HPGe detectors. The LAr cryostat was also immersed inside a huge water tank (590 m³ of purified water) equipped with PMTs (see Figure 2.8). It provided an additional shield against external radiations and acted as an active Cerenkov veto against the residual muons reaching the experiment. For events occurring in Ge crystals, cuts based on their timing, pulse shape (see [67, 68]) or position were also used to push further the background reduction.

GERDA took data in two phases: Phase-I from November 2011 to September 2013 and Phase-II from December 2015 to November 2019. By combining the two phases, it reached a final total exposure of 127.2 kg.yr. It demonstrated a background index of $b = 5.2^{+1.6}_{-1.3} \times 10^{-4}$ ckky, which is the lowest value ever achieved by a $0\nu 2\beta$ experiment, and an average energy resolution of 3.4 keV FWHM at $Q_{\beta\beta} = 2039$ keV. Finally, it has put the most stringent limit on ^{76}Ge $0\nu 2\beta$ half-life of $T_{1/2}^{0\nu 2\beta} > 1.8 \times 10^{26}$ yr (90% C.L.) corresponding to a Majorana effective mass of $m_{\beta\beta} < 79 - 180$ meV [61].

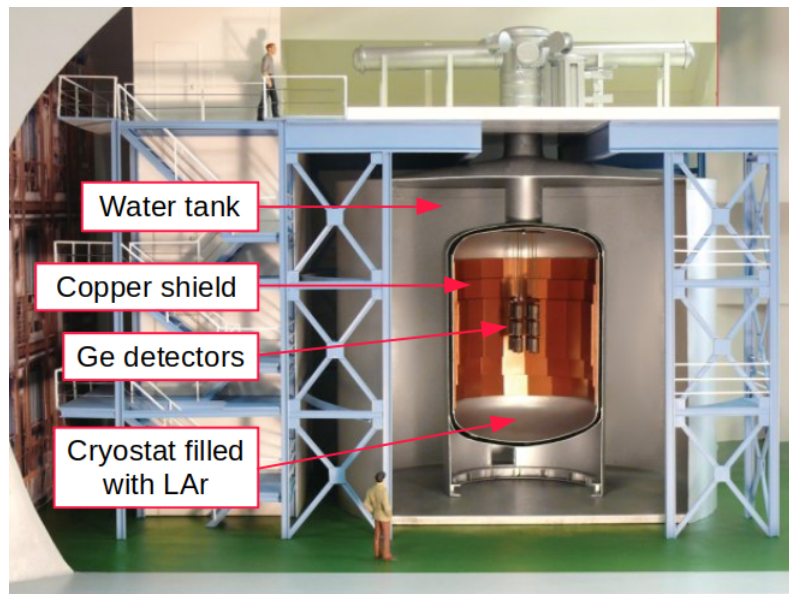


Figure 2.8 – 3D rendering of the section of the GERDA experiment.

MAJORANA

The MAJORANA demonstrator was located at the Sanford Underground Research Facility (SURF) in the USA. It used different types of HPGe detectors during its existence: P-type Point Contact (PPC) [69], ICPC, and BEGe. They were contained in a conventional vacuum radiopure copper cryostat. In addition to the 5 cm inner electroformed underground copper layer [70], another 5 cm of commercially obtained copper, followed by 45 cm of high-purity lead, acted as a shield against external radiations. Moreover, scintillating plastic panels were deployed in a 4π coverage around the experiment as an active muon veto, and the whole assembly was enclosed in a two layers borated and polyethylene shield against neutron.

From 2015 to 2021, MAJORANA has achieved a 64.5 kg.yr total exposure thanks to its up to 40.4 kg of detectors (27.2 kg enriched to $\sim 88\%$ in ^{76}Ge and 13.2 kg natural). It has

obtained the best energy resolution ever for $0\nu 2\beta$ experiments with 2.52 keV (0.12%) FWHM at $Q_{\beta\beta} = 2039$ keV. It allowed putting a limit on ^{76}Ge $0\nu 2\beta$ half-life $T_{1/2}^{0\nu 2\beta} > 8.3 \times 10^{25}$ yr (90% C.L.) which gives a range of upper limits for $m_{\beta\beta}$ of (113 – 269) meV [71]. Even though the limit is not as good as the one given by GERDA, the strength of the MAJORANA demonstrator lies in the obtained energy resolution and in the huge efforts put in finding and developing the most radiopure materials to build the experiment [72].

LEGEND

Based on the success of their respective experiments, the MAJORANA and GERDA collaborations have merged to build the next-generation $0\nu 2\beta$ ton-scale experiment LEGEND (Large Enriched Germanium Experiment for Neutrinoless $\beta\beta$ Decay) [73]. The first phase LEGEND-200, which will deploy 200 kg of active detectors in the previously GERDA LAr cryostat in LNGS, is in commissioning phase. It will benefit from the excellent background level reached in GERDA setup and even improve it using the high radiopurity of MAJORANA materials. Indeed, the dominant background sources in GERDA were close to the detectors and will be reduced by using, for example, the underground electroformed copper developed by MAJORANA. It will reuse the 70 kg of detectors enriched in ^{76}Ge used in GERDA and MAJORANA with, in addition, 130 kg of larger-mass ICPC detectors (~ 2.6 kg) newly produced. The latter can obtain an excellent energy resolution as demonstrated by MAJORANA ($\sim 0.12\%$ FWHM at $Q_{\beta\beta}$), allow really efficient background discrimination using pulse shape analysis [74] and can be made more massive implying fewer detectors (reduction in the number of cables and passive materials.) These upgrades should allow LEGEND-200 to reach a background index of $b \sim 2 \times 10^{-4}$ ckky and after five years of data taking a half-life sensitivity of 10^{27} yr. The second phase, LEGEND-1000, should take place later in a new cryostat capable of handling 1000 kg of active detectors. With further improvements in background reduction, it aims to reach a background index of $b \sim 1 \times 10^{-5}$ ckky. After 10 years of existence, it should come to an exclusion sensitivity of $T_{1/2}^{0\nu 2\beta} > 1.6 \times 10^{28}$ yr (90% C.L.) corresponding to $m_{\beta\beta} < (8.5 - 19.4)$ meV depending on the nuclear matrix element.

2.4.2 Xe Time-Projection Chamber (Xe TPC)

A Time-Projection Chamber (TPC) is a particle detector composed of a liquid or gas medium in which a high static electric field is applied through a cathode and a segmented anode. When an ionizing particle crosses the volume, the electrons liberated drift toward the anode equipped with a readout system that can reconstruct their number and position in the perpendicular direction of the field. Moreover, using the drift duration, one can also determine the position of their emission along the electric field. They can offer an excellent spatial resolution that helps to reject background. However, they usually struggle to reach energy resolution competitive with HPGe, for example. Since ^{136}Xe is a noble, reusable, and easily purified element, it can be used in its gas or liquid phase in TPC, allowing searching for its $0\nu 2\beta$ with this type of detector. However, since the $Q_{\beta\beta}$ of this isotope is 2457.8 keV, the ^{214}Bi gamma line at 2447.7 keV from natural radioactivity represents a challenging source of background.

EXO-200 and nEXO

EXO-200 (Enriched Xenon Observatory) is a Liquid Xe (LXe) TPC experiment that was located underground at the Waste Isolation Pilot Plant (WIPP) in the US. The cylindrical TPC was split into two drift regions with a common cathode at the center and filled with 200

kg of LXe enriched to 80.6% in ^{136}Xe (see Figure 2.9). Crossed wire planes were used on the anode sides to measure ionization. In addition, arrays of Large Area Avalanche PhotoDiode (LAAPD) [75] situated behind the wire planes were detecting the ^{136}Xe scintillation light emitted in response to an energy deposition. Since an anti-correlation exists between the measured ionization and scintillation energies, this dual readout improves the experiment energy resolution [76]. By using the xy position given by the anode planes, the drift duration and the time difference between light and charge signals, it was possible to achieve an excellent 3D reconstruction of the event positions and an efficient background rejection. To reduce the external radiations, the TPC was enclosed in several layers of passive shielding and an active muon veto was deployed around the installation. Moreover, the LXe provides an additional self-shielding, but consequently, the experiment sensitivity relies heavily on the detector fiducial innermost region.

EXO-200 took data during two phases (PHASE-I from 2011 to 2014 and PHASE-II from 2016 to 2018) with technical improvements in between and achieved a total exposure of 234.1 kg.yr. Thanks to a careful analysis based on event energy and topology, it reported a background index of 1.8×10^{-3} ckky in the fiducial volume and an energy resolution of 73 keV FWHM at the Q-value (2.97%) in average on the full dataset. Finally, it has put a lower limit on ^{136}Xe $0\nu 2\beta$ half-life of $T_{1/2}^{0\nu 2\beta} > 3.5 \times 10^{25}$ yr at 90% C.L. giving an upper limit on the Majorana effective mass of $m_{\beta\beta} < (93 - 286)$ meV [77].

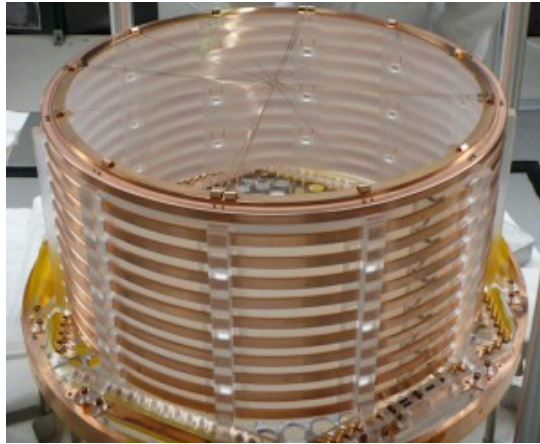


Figure 2.9 – Picture of one half of the EXO-200 TPC.

nEXO is the proposed ton-scale next-generation $0\nu 2\beta$ experiment based on EXO-200 technology. Its TPC will contain 5000 kg of LXe enriched to 90% in ^{136}Xe . Thanks to advancements achieved in understanding the generation of scintillation light and charges and their reconstitution within the detector as well as a new readout system (electrode tiles for the ionization, SiPM for the light), it aims to reach an energy resolution of ~ 46 keV FWHM at $Q_{\beta\beta}$ (1.88 %). nEXO should obtain a ^{136}Xe $0\nu 2\beta$ half-life exclusion sensitivity of $T_{1/2}^{0\nu 2\beta} > 1.35 \times 10^{28}$ yr (90% C.L.) after 10 years of data-taking which represents a Majorana effective mass of $m_{\beta\beta} < (4.7 - 20.3)$ meV [78].

NEXT

The NEXT (Neutrino Experiment with a Xenon TPC) collaboration uses electroluminescent (EL) TPCs filled with High-Pressure Gaseous Xe (HPGXe) to search for ^{136}Xe $0\nu 2\beta$. HPGXe TPCs can, in principle, reach better energy resolution than LXe ones since there are fewer

fluctuations in the production of ionization pairs [79]. In addition, a moderately higher electric field is applied close to the anode, accelerating ionization electrons. The latter excite but do not ionize the Xe atoms in this region, leading to a secondary scintillation light emission called electroluminescence during the atomic de-excitation. When measured, the EL signal provides a precise count of ionization electrons, enhancing further the energy resolution. Moreover, if the light collection has a sufficiently precise spatial resolution, it can also be used to reconstruct tracks.

The NEXT-White detector was a demonstration of the NEXT technology. It was installed in the Laboratory Subterr neo de Canfranc (LSC) from 2016 to 2021. Its cylindrical asymmetric EL TPC contained 4.3 kg of HPGXe at 10 bar. The anode and the cathode were placed at both ends, with a dense array of SiPMs behind the former (the tracking plane) and about ten PMTs behind the latter (the energy plane), measuring the primary scintillation and the EL light. It showed an excellent energy resolution of 1% at the Q-value [80] with excellent tracking reconstruction [81] validating the technology in a large-scale radiopure detector.

The NEXT-100 detector, a direct follow-up of NEXT-White, is now under construction and will be installed in LSC. It will contain 100 kg of HPGXe enriched in ^{136}Xe at 15 bar. A background index of 4×10^{-4} c/kg is expected, and after 3 years of lifetime a half-life exclusion sensitivity of $T_{1/2}^{0\nu 2\beta} > 6 \times 10^{25}$ yr (90% C.L.) [82].

Finally, a ton-scale concept called NEXT-HD exists. It will use only SiPMs for light readout, removing the undesired events induced by PMTs ceramic, the expected leading source of background in NEXT-100. However, it requires operating at a lower temperature to reduce SiPMs dark count rate (Usually, a 30 K temperature drop allows a reduction by one order of magnitude of the dark count rate). The foreseen design of the experiment is also different with respect to NEXT-100, with a symmetric TPC containing a central cathode along with an anode and an EL region at both extremities. A low-diffusion mixture, such as Xe-He, is envisaged to improve the position and energy resolution [83]. A half-life exclusion sensitivity of $T_{1/2}^{0\nu 2\beta} > 2.7 \times 10^{27}$ yr (90% C.L.) is expected for such an experiment after 10 years of data taking [84] and could be improved to 10^{28} yr using single- ^{136}Ba ($0\nu 2\beta$ ^{136}Xe daughter atom) tagging technology [85].

2.4.3 Large liquid scintillator

Liquid-loaded scintillator detectors comprise a liquid scintillator in which the $0\nu 2\beta$ isotope is diluted. After an energy deposition inside, scintillation light is emitted and measured by photo-detectors seeing the experimental volume. They usually allow, in addition to the energy reconstruction, to determine the position and the topology of the event based on the number and timing of the detected photons. The main advantage of this technology is the easiness of the mass-scalability: kton of liquid scintillator can be deployed with only a few percent of $0\nu 2\beta$ isotope mass-loading to achieve ton-yr exposure. However, since the scintillation yield is usually rather low, its energy resolution is limited to values that keep the $2\nu 2\beta$ spectrum as a worrying source of background. Moreover, since this kind of experiment implies huge masses of liquid scintillator, the irreducible neutrino background described in Section 2.3 can also become a non-negligible contribution.

KamLAND-Zen

KamLAND-Zen is exploiting the ultralow background setup of the underground neutrino oscillation experiment KamLAND (Kamioka Liquid Scintillator Antineutrino Detector) [86] situated in the Kamioka mine in Japan to search for $0\nu 2\beta$ in ^{136}Xe . The Xe-loaded liquid

scintillator (XeLS) is contained in a spherical inner nylon balloon which is itself inside an outer balloon filled with 1 kton of liquid scintillator (LS). This outer LS acts as an active shield. PMTs are used to detect scintillation light and are placed on the surface of the stainless steel containment vessel providing a 34% solid-angle coverage (see Figure 2.10). Finally, everything is surrounded by a 3.2 kton Cerenkov-water tank also equipped with PMTs, providing further shielding and active background rejection. The first phase, KamLAND-Zen 400, took place from 2013 to 2015 and used up to 387 kg of enriched Xe. Since 2019 and after installing a bigger and less radioactive inner balloon containing 745 kg of enriched Xe, the second phase KamLAND-Zen 800 is in data taking period. As expected within large liquid scintillators, the energy resolution is only 4% in the region of interest, which is relatively high compared to other detection methods. However, thanks to its huge mass, combining the entire data set of the first phase with the data taken so far by the second allows the KamLAND-Zen collaboration to reach a total exposure of 970 kg·yr and to put a lower limit on ^{136}Xe $0\nu 2\beta$ half-life of $T_{1/2}^{0\nu 2\beta} > 2.3 \times 10^{26}$ yr at 90% C.L [87]. This value corresponds to an upper bound on the Majorana effective mass of $m_{\beta\beta} < (36 - 156)$ meV, which is currently the most stringent limit for this parameter.

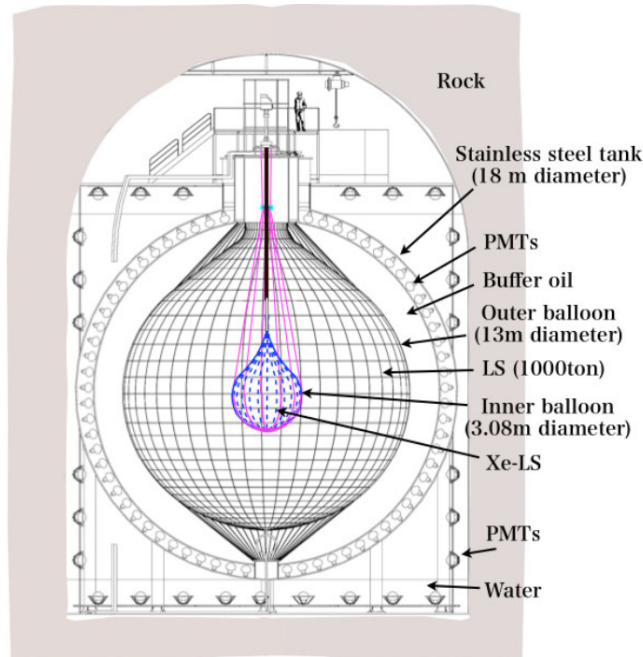


Figure 2.10 – Schematic view of the KamLAND-Zen detector. Taken from [88].

A proposed next-generation follow-up called KamLAND2-Zen (KL2Z) is already in preparation where, in total, around 1 ton of ^{136}Xe will be deployed. A significant improvement from 4% to 2% at the $Q_{\beta\beta}$ is foreseen for the energy resolution by working, for example, on the PMTs or by using a scintillator with a higher light yield. This, in addition with other improvements on background rejection, should permit KL2Z to reach a sensitivity to $m_{\beta\beta}$ values around 20 meV [88].

SNO+

SNO+ utilizes the infrastructure of the famous solar neutrino experiment SNO (Sudbury Neutrino Observatory) [89] located underground at SNOLAB in Sudbury, Canada. It has

been upgraded mainly to search for $0\nu 2\beta$ in ^{130}Te , but it can explore a vast physics program. It is composed of a spherical acrylic vessel (AV), hosting the target medium, inside an external volume filled with 7000 tons of ultra-pure water. A geocentric mechanical structure equipped with almost 9500 inward-facing PMTs and light concentrators surrounds the AV. In addition, around one hundred of outward-facing PMTs are detecting the light coming from the region external to this support structure and tag cosmic rays. In the first phase of SNO+, from May 2017 to July 2019 - called the water phase - the AV was filled with 905 tons of ultra-pure water. It allowed, in addition to the commissioning of the detector, to measure for example the solar ^8B neutrino flux [90] or to search for invisible nucleon decays [91, 92]. The second phase, the scintillator phase, is now ongoing with the AV filled with ~ 780 tons of the new liquid scintillator developed by the collaboration [93]. Finally, the tellurium phase will take place right after where the LS will be loaded with natural Te. Initially, a 0.5% ^{nat}Te loading (~ 1.3 ton of ^{130}Te) will be used and should lead to ^{130}Te $0\nu 2\beta$ half-life exclusion sensitivity of $T_{1/2}^{0\nu 2\beta} > 2 \times 10^{26}$ yr (90% C.L.) after 3 years of data taking. Finally, by increasing the loading in ^{nat}Te to 2.5%, the SNO+ experiment could put a lower limit on the half-life of $T_{1/2}^{0\nu 2\beta} > 1 \times 10^{27}$ yr (90% C.L.) [94] after 4 years of data taking, giving a $m_{\beta\beta}$ range of 16-39 meV .

2.4.4 Cryogenic calorimeters

Cryogenic calorimeters, or bolometers, are the main subject of this PhD thesis. Since they will be widely described in Chapter 3, only their essential features will be summarized here. They are composed of an absorber, usually a dielectric crystal, embedding a $0\nu 2\beta$ candidate isotope cooled down to tens of mK. A thermistor is coupled to it to measure the temperature rise induced by a particle interaction occurring inside. They are ideal for $0\nu 2\beta$ search due to the flexibility in the absorber material choice, the excellent energy resolution they can achieve ($< 0.5\%$ FWHM at $Q_{\beta\beta}$) and their high detection efficiency ($\sim 80\text{-}90\%$).

CUORE

CUORE (Cryogenic Underground Observatory for Rare Events) is the largest bolometric experiment ever built and is located at LNGS in Italy. It uses an array of 988 TeO_2 crystals arranged in 19 towers to search for $0\nu 2\beta$ in ^{130}Te (see Figure 2.11). The 750 kg (206 kg of ^{130}Te) of detectors are cooled down to 15 mK thanks to an enormous dry dilution cryostat [95], also referred to as the coldest cubic meter in the known Universe. Energy depositions in the crystals are measured using NTD (Neutron Transmutation Doped) Ge [96] glued directly on one of their surfaces. Special care has been taken in surrounding material choice, its cleaning, and crystal radiopurity to minimize the amount of internal contaminations. A passive lead shield surrounding the detector array placed directly inside the cryostat and one outside are used to mitigate the external radioactivity. Finally, a 20-cm layer of polyethylene and a thin layer of boric acid suppress neutron contribution. This shielding and additional cuts on the pulse shape of the signal or multi-crystal events allow CUORE to reach a background index of $b = (1.49 \pm 0.04) \times 10^{-2}$ c/ky. The dominant remaining contribution comes from the energy-degraded α s from surface contamination in the materials constituting the detector. CUORE is taking data since 2017 and has recently reached a total ^{130}Te exposure of 288.8 kg·yr. Thanks to an excellent energy resolution of 7.8 keV FWHM ($\sim 0.31\%$) at $Q_{\beta\beta} = 2527.5$ keV, it has put the most stringent limit on ^{130}Te $0\nu 2\beta$ half-life of $T_{1/2}^{0\nu 2\beta} > 2.2 \times 10^{25}$ yr (90% C.L.) corresponding to a limit on the Majorana effective mass of $m_{\beta\beta} < (90 - 305)$ meV [97]. The important message to take away from CUORE

is that a ton-scale bolometric experiment is technically feasible, opening the path to the next-generation $0\nu 2\beta$ experiment CUPID.

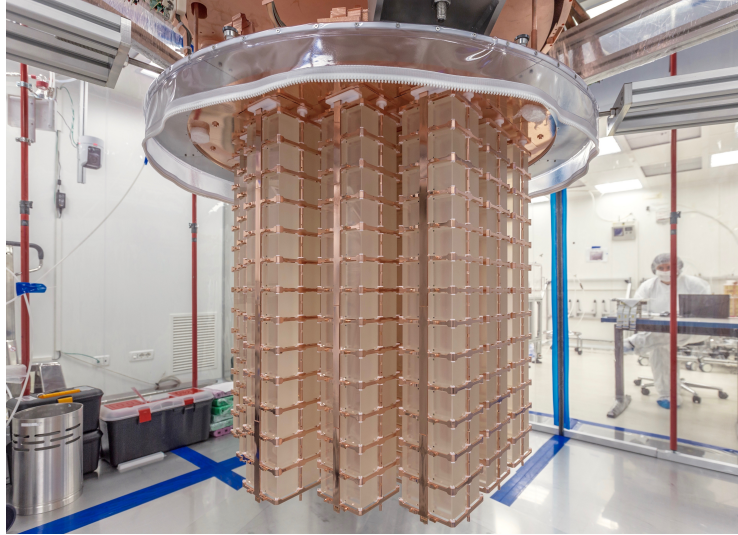


Figure 2.11 – Cuore towers inside the opened cryostat.

CUPID and its demonstrators

The direct successor of CUORE is CUPID (Cuore Upgrade with Particle IDentification). It will be installed in the same, but upgraded, cryostat at LNGS after the end of CUORE and aims to reach a sensitivity $> 10^{27}$ yr. To achieve its goal, CUPID will increase the total mass of the candidate isotope and will reduce by a factor of 100 the background index in the ROI compared to its predecessor. Firstly, it will use the so-called scintillating bolometers: the absorber will be a scintillating crystal, meaning that in addition to the heat signal produced during an energy deposition, scintillation light will also be emitted. This scintillation will be measured by deploying an auxiliary Ge bolometer acting as a light detector (Ge-LD) next to the main absorber. This dual readout method allows the identification and rejection of the α events, dominant background contribution in CUORE, since they emit a different amount of light than γ s and β s when interacting in the crystal. Secondly, CUPID will move to the study of another isotope, the ^{100}Mo , which has a $Q_{\beta\beta}$ higher than 2.615 MeV, the endpoint of the natural γ radioactivity, and so with a region of interest containing fewer background counts. In the past years, two CUPID demonstrators have been built to demonstrate the efficiency of the scintillating bolometer technology against α events but also to choose the best isotope and the best crystal.

The first demonstrator, CUPID-0 was using 26 ZnSe scintillating crystals embedding ^{82}Se ($Q_{\beta\beta} = 2997.9$ keV) as the candidate isotope coupled to Ge-LDs. Among them, 24 were enriched to 95% in ^{82}Se and 2 with natural isotopic abundance, leading to a total mass of 5.13 kg of ^{82}Se . Bolometers were placed in a shielded cryostat at LNGS, and the demonstrator took data from 2017 to 2020 in two phases with a 6 months break for an upgrade in between. CUPID-0 demonstrated an excellent α rejection thanks to the dual readout method and reached a background index of $b = 4.5 \times 10^{-3}$ ckky on average for the two phases, which is 3.3 times better than the CUORE one. However, ZnSe crystals showed a poor energy resolution compared to TeO_2 with 21.8 keV FWHM (0.73 %) at the Q-value due to a high internal contamination [98] which limits their performance. By combining

the two phases, a total exposure of 8.82 kg·yr in ^{82}Se has been reached, allowing to put a lower limit on its $0\nu 2\beta$ half-life of $T_{1/2}^{0\nu 2\beta} > 4.6 \times 10^{24}$ yr (90% C.L.) (corresponding to $m_{\beta\beta} < (263 - 545)$ meV) [99], still today the most competitive result for this isotope. ZnSe crystals were finally not chosen for CUPID due to their not really good energy resolution and the difficulties of their crystallization.

In parallel, another demonstrator called CUPID-Mo was testing Li_2MoO_4 (LMO) crystals embedding ^{100}Mo ($Q_{\beta\beta} = 3034$ keV) at Laboratoire souterrain de Modane (LSM) in France. In total, 20 LMO crystals enriched to $\sim 97\%$ in ^{100}Mo coupled to Ge-LDs were operated around 20 mK for a total isotope mass of 2.3 kg. The experiment ran between 2019 and 2020, corresponding to a total ^{100}Mo exposure of 1.47 kg·year. It also demonstrated a $>99.9\%$ α rejection thanks to the heat and light signal detection and a background level of $b = 3.9_{-1.6}^{+1.7} \times 10^{-3}$ ckky. It obtained an excellent energy resolution in the ROI of 7.4 keV FWHM ($\sim 0.24\%$), that allowed CUPID-Mo to put the most stringent limit on ^{100}Mo $0\nu 2\beta$ half-life of $T_{1/2}^{0\nu 2\beta} > 1.8 \times 10^{24}$ yr (90% C.L.) [100]. Moreover, LMO crystals showed, in addition to their excellent performance (high energy resolution and efficiency), an extremely good radiopurity and a relatively easy enrichment in ^{100}Mo at a reasonable cost [101]. This placed them as the perfect candidates for the next-generation experiment CUPID.

The baseline design for CUPID is to use about 1600 LMO crystals with a $>95\%$ enrichment to ^{100}Mo coupled to Ge-LDs inside CUORE cryostat, representing around 240 kg of ^{100}Mo . Based on CUORE, CUPID-0, and CUPID-Mo background models, a background index of $b \sim 10^{-4}$ ckky is expected with a dominant contribution coming from the fast $2\nu 2\beta$ of ^{100}Mo (see Section 2.3) for which rejection techniques are still under study to keep it at a safe level. Assuming an energy resolution of 5 keV at the $Q_{\beta\beta}$, CUPID can reach a half-life exclusion sensitivity of $T_{1/2}^{0\nu 2\beta} > 1.5 \times 10^{27}$ yr (90% C.L.), corresponding to $m_{\beta\beta} < (10 - 17)$ meV [62] after 10 years of data taking.

Furthermore, some projects are also trying to push the boundaries of background level in bolometric experiments and prepare the next-to-next generation of $0\nu 2\beta$ experiments. This is the case for example of BINGO (Bi-Isotope Next Generation $0\nu 2\beta$ Observatory), which will be presented in Chapter 4. It aims to demonstrate that a background index of 10^{-5} ckky is reachable by bolometric experiments using clever and innovative methods and technologies. The work accomplished in this thesis is mainly for BINGO R&D, and the objectives will be discussed later.

AMoRE

AMoRE (Advanced Molybdenum-based Rare process Experiment) is another experiment using ^{100}Mo embedded inside scintillating bolometers to search for $0\nu 2\beta$. AMoRE is coupling a MMC (Metallic Magnetic Calorimeter) [102] as a thermistor to the absorbers of both light and heat channels. Between 2016 and 2018, AMORE-pilot demonstrated that the MMC-based readout was working well and was suitable for larger experiments [103]. The next phase of the experiment, AMoRE-I is now installed and takes data at YangYang underground Laboratory (Y2L) in Korea. It contains 13 $^{48\text{depl.}}\text{CaMoO}_4$ crystals and 5 LMO crystals for a total of 6.2 kg inside a dilution cryostat shielded from external radioactivity. It aims to demonstrate a background level of $b \sim 10^{-2}$ ckky and reach a half-life limit for ^{100}Mo $0\nu 2\beta$ of $\sim 10^{24}$ yr [104]. Finally, the last phase AMoRE-II will follow. It will use ~ 200 kg of enriched molybdate-crystals (LMO is the considered candidate but other crystals are under study) corresponding to around 100 kg of ^{100}Mo . It expects to reach a background index of $b < 10^{-4}$ ckky with the objective to reach a sensitivity to the Majorana effective mass of

$$m_{\beta\beta} = (20 - 50) \text{ meV [105].}$$

2.4.5 Tracking calorimeters

Tracking calorimeters is the only approach presented here where the source differs from the detector. It implies that the source has to be contained in an extremely thin foil to minimize the inevitable energy loss inside of emitted electrons, making the mass scalability difficult and impacting the energy resolution. Nevertheless, it allows a complete reconstruction of the decay topology using tracking in three dimensions as well as calorimetric and timing information. Hence, it can give answers on the process driving $0\nu 2\beta$ and efficiently reject background events. For all these reasons, it is usually assumed that the optimal use of this technology is not for the brute search of $0\nu 2\beta$ which requires enormous detector mass, but more once it will be discovered to test the different possible mediating processes by knowing already where to look at.

NEMO-3 and SuperNEMO

The NEMO-3 (Neutrino Ettore Majorana Observatory) [106] was a tracking experiment located at LSM in France that took data from 2003 to 2013. It consisted of a cylinder composed of different layers (see Figure 2.12). In the middle, a thin foil containing the isotope of interest was sandwiched between two cylindrical tracking chambers made of wire cells. The innermost and outermost layers of the detector were made of plastic scintillators acting as the calorimeter thanks to PMTs measuring the scintillation light. In addition, a 25 Gauss magnetic field inside the tracking volumes and parallel to the foil axis was generated by a solenoid surrounding the detector to identify the emitted particle charge using the curvature of their track. It was possible to recognize electrons, positrons, photons, and α particles. NEMO-3 was a multi-isotope experiment since its source foil comprised seven different $0\nu 2\beta$ candidates: ^{100}Mo (6.9 kg), ^{82}Se (932 g), ^{130}Te (454 g), ^{116}Cd (405 g), ^{150}Nd (36.6 g), ^{96}Zr (9.4 g), ^{48}Ca (7.0 g). Measurements of the $2\nu 2\beta$ half-life of all of them were performed, and limits were put on their $0\nu 2\beta$ rate. For ^{100}Mo , it has reached a total isotopic exposure of 34.3 kg·yr with a background index of $b \sim 10^{-3}$ ckky in the ROI limited by ^{100}Mo $2\nu 2\beta$. A $0\nu 2\beta$ half-life limit of $T_{1/2}^{0\nu 2\beta} > 1.1 \times 10^{24}$ yr (90% C.L.) has finally been obtained [107].

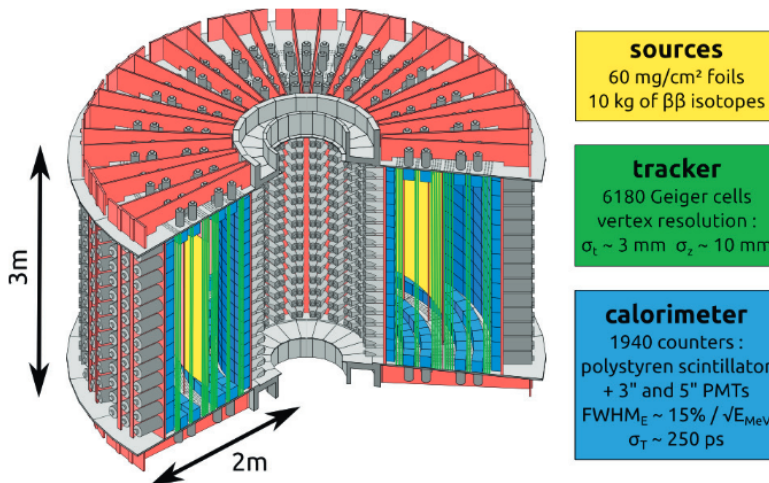


Figure 2.12 – Schematic view of the NEMO-3 experiment. Taken from [108].

The next step, SuperNEMO [109], is based on the same detector concept as NEMO-3. It will study ^{82}Se , which has a longer $2\nu 2\beta$ half-life than ^{100}Mo , reducing this contribution to the background. The goal is to improve energy resolution (from 8% to 4% at 3 MeV) by enhancing the light collection and using PMTs with higher quantum efficiency. Moreover, work has been done on the detector design and its radiopurity. The first demonstrator, SuperNEMO-D is under commissioning at LSM. It will contain 7 kg of ^{82}Se with the objective to validate the detector improvements and that a background index of $b \sim 10^{-4}$ c/ky is reachable. It aims to reach a half-life exclusion sensitivity of $T_{1/2}^{0\nu 2\beta} > 6 \times 10^{24}$ yr (90% C.L.) after 2.5 years of data taking [110]. An experiment using this technology and deploying 100 kg of ^{82}Se could aim to reach an exclusion sensitivity of $T_{1/2}^{0\nu 2\beta} > 1 \times 10^{26}$ yr (90% C.L.) thanks to further improvements on the background.

2.4.6 Summary and discussion

| Experiment | detection technique | isotope | lim $T_{1/2}^{0\nu}$ (yr) | lim $m_{\beta\beta}$ (meV) | exposure (kg yr) | Ref. |
|-----------------|--------------------------|-------------------|------------------------------|-------------------------------|---------------------|-------|
| GERDA | HPGe | ^{76}Ge | 1.8×10^{26} | 79-180 | 127.2 | [61] |
| MAJORANA | HPGe | ^{76}Ge | 8.3×10^{25} | 113-269 | 64.5 | [71] |
| EXO-200 | Liquid TPC | ^{136}Xe | 3.5×10^{25} | 93-286 | 234.1 | [77] |
| KamLAND-Zen 400 | Liquid scintillator | ^{136}Xe | 1.07×10^{26} | 61-165 | 504 | [88] |
| KamLAND-Zen 800 | Liquid scintillator | ^{136}Xe | 2.3×10^{26} | 36-156 | 970 | [87] |
| CUORE | Bolometers | ^{130}Te | 2.2×10^{25} | 90-305 | 288.8 | [97] |
| CUPID-0 | Scintillating bolometers | ^{82}Se | 4.6×10^{24} | 263-545 | 8.82 | [99] |
| CUPID-Mo | Scintillating bolometers | ^{100}Mo | 1.8×10^{24} | 280-490 | 1.47 | [100] |
| NEMO-3 | Tracking calorimeter | ^{100}Mo | 1.1×10^{24} | 330-620 | 34.3 | [107] |

Table 2.3 – Previous and current generation $0\nu 2\beta$ experiments.

| Experiment | detection technique | isotope | mass (kg) | lim $m_{\beta\beta}$ (meV) | Ref. |
|----------------|--------------------------|-------------------|--------------|-------------------------------|-------|
| LEGEND-200 | HPGe | ^{76}Ge | 200 | 35-73 | [111] |
| LEGEND-1000 | HPGe | ^{76}Ge | 1000 | 8.5-19.4 | [73] |
| nEXO | Liquid TPC | ^{136}Xe | 5000 | 4.7-20.3 | [78] |
| NEXT-100 | Gaseous TPC | ^{136}Xe | 100 | 80-160 | [82] |
| NEXT-HD | Gaseous TPC | ^{136}Xe | ~ 1000 | 13-57 | [111] |
| KamLAND2-Zen | Liquid scintillator | ^{136}Xe | ~ 1000 | ~ 20 | [88] |
| SNO+ (Phase I) | Liquid scintillator | ^{136}Xe | 1300 | 41-99 | [112] |
| CUPID | Scintillating bolometers | ^{100}Mo | 253 | 10-17 | [62] |
| AMoRE II | Scintillating bolometers | ^{100}Mo | 200 | 20-50 | [105] |
| SuperNEMO | Tracking calorimeter | ^{82}Se | 100 | 40-100 | [110] |

Table 2.4 – Next-generation $0\nu 2\beta$ experiments.

The experimental landscape searching for $0\nu 2\beta$ has been presented in this section. The various experiments and their sensitivity are summarized in Table 2.3 and Table 2.4. When we have a look to the possible values of the Majorana effective mass as a function of the

lightest neutrino mass, we can see that the current generation is able to exclude the region above the inverted hierarchy mass scenario as illustrated in Figure 2.13. The objective of the next-generation experiments is to reach sensitivities high enough to explore this area fully and, in the case of no discovery, discard the inverted ordering. The discovery potential of experiments such as nEXO or CUPID is high since they will also investigate a non-negligible part of the normal hierarchy spectrum of values in addition to the inverted hierarchy region. However, in case of no discovery, the sensitivities may have to be pushed further in the future in order to start also the exploration of the normal hierarchy region band below 3 meV. It is with that goal in mind that BINGO, the project in which the work of this thesis lies, has proposed to prepare the next-to-next generation of bolometric experiments (see Chapter 4).

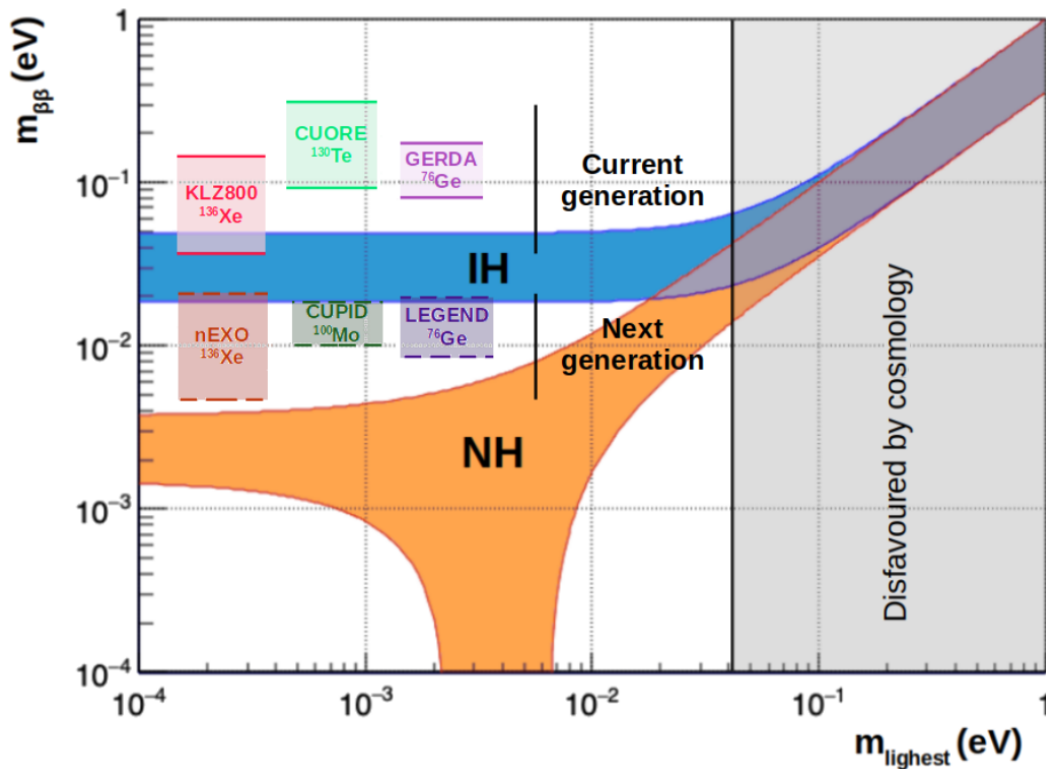


Figure 2.13 – Majorana effective mass as a function of the lightest neutrino mass. Some limits on $m_{\beta\beta}$ put by the current generation of experiments (solid lines) and foreseen by the next generation experiments (dashed lines) are shown.

Chapter 3

The bolometric technique

The term "bolometers" refers nowadays usually to cryogenic calorimeters, which can detect particles and measure their energy through the temperature variation induced by their interaction in the detector. S. P. Langley invented it in 1878 and gave this name to a room-temperature device sensitive to the energy of electromagnetic radiations by measuring the resistance variations they were provoking in thin Pd strips thanks to an $R(T)$ dependence [113]. Around 50 years after, in 1935, F. Simon proposed that the sensitivity of such detectors could be increased by several orders of magnitude if they were used at low temperatures [114] thanks to the absorber heat capacity diminution. From that moment, the development of cryogenic bolometers started and it was raising more and more interest in the particle physics community. For example, in 1949, the first detection of single α particles from a polonium source with a superconductive NbN layer at 15.5 K was successfully performed [115]. It is finally in 1983 that E. Fiorini and T.O. Niinikoski proposed to use cryogenic bolometers for rare-event searches as the neutrinoless double beta decay [116], which led more than 30 years later to the construction of one of the most sensitive experiment to this process: CUORE.

Indeed, these detectors are really ideal for the search of $0\nu 2\beta$ since they gather almost all the required features explained in Chapter 2. Moreover, many developments over the years have allowed overcoming some of their limits, such as the dual heat and light readout of scintillating bolometers introduced to reject α background that will be used in the next generation experiment CUPID. The R&D is still ongoing now to push even further the possibilities of these detectors and the work presented later in this thesis is a good illustration of it. But before, this Chapter will summarize the main features of cryogenic bolometers and how they are operated.

3.1 Working principle

The operation principle of bolometers is rather simple: when an incoming particle deposits its energy inside a crystal, it is absorbed by the lattice and almost completely converted into vibrations, i.e. phonons. This conversion induces a rise of temperature ΔT in the absorber proportional to the original deposited energy ΔE as it is shown by equation 3.1.

$$\Delta T = \frac{\Delta E}{C} \quad (3.1)$$

where C is the heat capacity of the detector. By coupling a thermometer to the crystal, it is possible to measure this temperature variation and access the energy of the impinging particle.

A bolometer is never completely isolated from the external world but it is weakly coupled to what is called a heat bath (usually a mechanical holder made of copper for example), which has a base temperature T_0 . It means that after the rise of temperature provoked by the particle energy deposition, the detector relaxes back to T_0 within a characteristic time τ , also referred to as the pulse decay time. Equation 3.1 becomes:

$$\Delta T(t) = \frac{\Delta E}{C} \exp\left(-\frac{t}{\tau}\right) \quad \text{with} \quad \tau = \frac{C}{G} \quad (3.2)$$

where G corresponds to the thermal conductance between the detector and the heat bath. This equation gives the time scale on which the thermal signal takes place. A simplified drawing of a typical bolometer can be found in Figure 3.1, where all the components described in this paragraph are present.

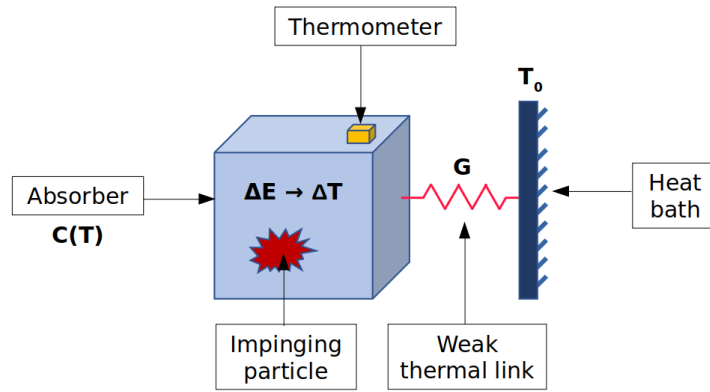


Figure 3.1 – Simplified schema of a bolometer.

From equation 3.2 and since the heat capacity of solids drops at low temperatures, it is clear that operating these detectors at cryogenic temperatures allows the obtention of thermal signals within the scope of detection. Moreover, the choice of the material absorber is also playing an important role.

3.1.1 The absorber choice

The specific heat $c(T)$, defined as the heat capacity divided by the mass of the sample, depends on the temperature and for solids can be expressed as follows:

$$c(T) = c_l(T) + c_e(T) \quad (3.3)$$

where $c_l(T)$ corresponds to the contribution to the specific heat from the solid lattice while $c_e(T)$ corresponds to conduction electron one.

In the case of a dielectric and diamagnetic crystal, $c_e=0$ and only the lattice plays a role. If the temperature is well below the Debye temperature θ_D thus, the specific heat of such material becomes:

$$c_l(T) = \frac{12}{5} \pi^4 \frac{N_A}{M} k_B \left(\frac{T}{\theta_D}\right)^3 \quad (3.4)$$

with N_A the Avogadro number, M the molar mass of the crystal and k_B the Boltzmann constant.

In the case of a metal, the conduction electron contribution scales linearly with the temperature and is dominating at low temperatures. However, for a superconductor, when the temperature is well below its critical one T_c , the contribution becomes exponentially decreasing with T . This behavior is described by the following equations:

$$c_e(T) = \begin{cases} aT, & \text{if } T > T_c \\ 8.5 \cdot \gamma \cdot T_c \cdot \exp\left(-1.44 \cdot \frac{T_c}{T}\right), & \text{if } T \ll T_c \end{cases} \quad (3.5)$$

Therefore, dielectric and diamagnetic crystals seem to be the best candidates to be used as absorbers in bolometers since they can reach really low heat capacity if they are operated at temperatures well below their Debye one. Moreover, such crystals embedding $0\nu 2\beta$ isotope candidates exist which makes them perfect for the search of this rare process using the source=detector approach. Single crystals are usually better since poly-crystals can lead to multi-Compton scattering within them, giving anomalies on the heat signal. It is important to recall also that the quality and radiopurity of the absorber still have to be controlled since it can have an impact on their performance (impurities can lead to energy loss and bad energy resolution) and on the experiment background. On the other hand, superconductor metals can also make good bolometers (see Chapter 6) if they are operated in the right circumstances (well below T_c and θ_D). Table 3.1 gives some of the properties of the absorbers that have been used in the framework of this thesis.

| Physical property | TeO ₂ | Li ₂ MoO ₄ | Ge |
|--|---------------------------------|----------------------------------|---------------------------------|
| Crystal type | Dielectric | Dielectric | Semiconductor |
| θ_D (K) | 232 | 316 | 374 |
| c (J.K ⁻¹ .cm ⁻³) | $1.8 \cdot 10^{-5} \text{ T}^3$ | $7.5 \cdot 10^{-6} \text{ T}^3$ | $2.7 \cdot 10^{-6} \text{ T}^3$ |
| ρ (g.cm ⁻³) | 6.04 | 3.07 | 5.32 |

Table 3.1 – Main characteristics of some absorbers discussed in this thesis.

3.2 Thermal sensors

In order to measure the energy deposited in the absorber, a sensor sensitive to the induced temperature variation is coupled to it. It must have a property directly depending on the temperature and it can be, for example, the electrical resistance. At low temperatures, the two main devices using this feature are:

NTD (Neutron Transmutation Doped) Ge - They are semiconductor chips doped at a level such that their resistance depends strongly on the temperature [96]. They can be glued on the surface of the absorber and are sensitive only to thermal phonons. They have a high impedance and give, therefore, quite slow signals ($\mathcal{O}(\text{ms})$). They have been successfully operated in large-scale $0\nu 2\beta$ experiments such as CUORE or CUPID-Mo. A further description can be found in this section since they are the sensors used in all the tests presented in this thesis.

TES (Transition Edge Sensor) - They are low impedance superconductive thin films operated in a small region around their transition temperature T_c [117]. They show at this temperature a steep variation of their resistance due to the superconductor transition. They

can be deposited directly on the absorber offering faster signals ($\mathcal{O}(\mu\text{s})$) than NTD Ge and can detect athermal phonons. However, they imply a more sophisticated low-impedance readout at low temperatures using SQUIDs [118]. They have never been yet used in a large-scale $0\nu 2\beta$ bolometric experiment but are an option for CUPID light detectors [119].

For sensors having an $R(T)$ dependence, we can evaluate their performance by writing their sensitivity, such as:

$$A = \left| \frac{d \ln R(T)}{d \ln T} \right| \sim \frac{\Delta R}{R} \frac{T}{\Delta T} \quad (3.6)$$

This parameter expresses how much the resistance varies as a function of the temperature variation. It characterizes the ability of the sensor to transform the temperature signal into an electrical one. Typically, an NTD Ge gives a negative value of order unity, while a TES sensor gives a positive value of order hundreds but can be operated only on a small range of temperatures. As already mentioned, we will focus here on the NTD-Ge since they were the thermal sensor used during every test that will be described in this thesis.

3.2.1 Neutron Transmutation Doped Ge

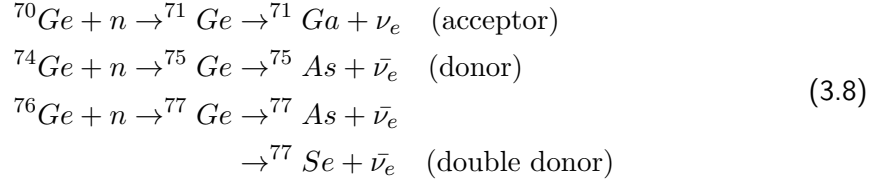
Pure semiconductors become too highly resistive at low temperatures to be used as thermistors. However, by doping them, one can tune their resistivity in order to reach a regime allowing their operation as thermal sensors. Indeed, the introduction of impurities in the perfect crystal lattice creates a disordered system changing its electron transport properties. P.W. Anderson [120] and N.F. Mott [121] described the properties of such doped materials. They showed that it exists a critical dopant concentration below which the Ge conductivity goes to zero at zero temperature and above which there is always a finite conductivity. It can be referred to as the "Metal-Insulator Transition" (MIT). It appeared that a Ge crystal doped just below this MIT acquires a strong resistance dependence on the temperature, which is perfect for a high-sensitivity thermal sensor. Indeed, in that particular case, charge carriers are considered trapped in three-dimensional potential minima, and conduction takes place thanks to the quantum tunneling effect between two dopant sites following the absorption or the emission of a phonon. If the temperature is sufficiently high, electrons from an impurity site hop to the closest unoccupied one, and the mechanism is called the Nearest Neighbor Hopping (NNH). However at low temperatures ($\ll 10$ K), due to the lack of high-energy phonons, longer hops are favored to find an unoccupied impurity site closer to the energy of the available phonons. This is the Variable Range Hopping (VRH) regime [122]. In the latter situation, the resistivity of the material can be written as:

$$\rho(T) = \rho_0 \exp\left(\frac{T_0}{T}\right)^\gamma \quad (3.7)$$

where γ was found equal to 1/2 by I.B. Shklovskii and A.L. Efros [123].

Therefore, the dopant concentration and its homogeneity are the critical factors in making the best and most reproducible thermistor that can be operated in the VRH regime. It appeared that irradiating high-purity thin Germanium wafers with an intense flux of thermal neutrons generated by a nuclear reactor was giving extremely good results. With this method, called Neutron Transmutation Doping, neutron captures occur on the stable Germanium atoms ($A=70,74,76$ with the respective isotopic abundance 20.5%, 36.5% and 7.8%), forming donor and acceptor sites randomly distributed throughout the crystal lattice with the reactions presented in equation 3.8. After exposition to a neutron flux, the concentration of Se can be considered as negligible while a concentration of $2.94 \times 10^{-2} \text{ cm}^{-3}$ per neutron/ cm^2/s for Ga

and $8.37 \times 10^{-3} \text{ cm}^{-3}$ per neutron/cm²/s for As is expected for natural Ge. It is thus possible to fine-tune the total dopant concentration and predict the resistivity of the obtained p-type gallium-doped material 32% compensated with arsenic.



It was shown that thanks to the quite low cross-section of neutron capture in Germanium, the neutron flux remains constant inside the wafers, ensuring very homogeneous doping. Therefore, they can be cut afterward in the required dimensions for the thermistors and each sample shows really similar resistance properties [124]. Before cutting, some additional steps are required to prepare the wafers for electrical contacts: after irradiation, the crystal structure is repaired by annealing at 400°C for 6 hours. The surface of the two wafer sides is made metallic by boron ions implementation before the sputtering of a thin layer of Pd and Au making the electrical contacts. Finally, the wafer is annealed again at 200°C for 1 hour before being cut in the desired thermistor dimensions, making sure that two electrical contacts are present on both sides of it. This procedure ensures low noise ohmic contacts. Usually, the NTD Ge originating from the same production batch are labeled with a reference and shows similar properties (during this thesis, for example, 41B NTDs have been used and were produced during the CUORE NTD fabrication process). A photo of an NTD Ge can be seen on the left side of Figure 3.2.

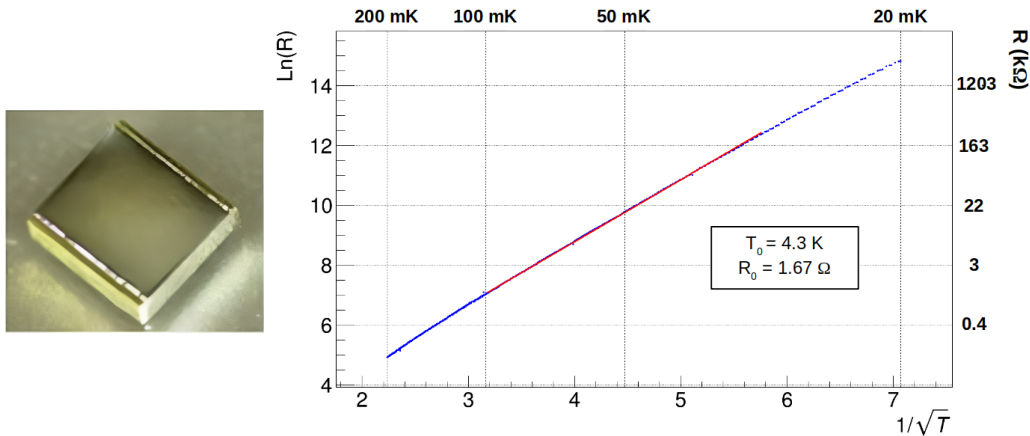


Figure 3.2 – *left*: Photo of $3 \times 3 \times 1 \text{ mm}^3$ 41B NTD Ge. One can see the Au contacts on the sides. *right*: $R(T)$ plot (linearized) of a 41B NTD Ge of the same dimension. The curve have been fitted with a first-order polynomial function (red line) to extract the R_0 and T_0 parameters.

These devices exhibit a strong resistance dependence on the temperature and from equation 3.7, we can write:

$$R(T) = R_0 \exp\left(\frac{T_0}{T}\right)^{1/2} \tag{3.9}$$

Where T_0 is a constant depending on the doping concentration while R_0 depends on the geometry of the NTD. Both can be determined experimentally by measuring the NTD

resistance as a function of the temperature. From that, it is possible to fit the obtained curve and extract the value of these two parameters as shown in the right side of Figure 3.2.

The NTD gluing procedure

Another crucial point is the coupling of the NTD Ge to the absorber. Usually, it is done using a bi-component epoxy Araldite® glue that showed good properties at low temperature and low radioactivity [125] and a fast drying (~ 1 hour). However, this part has to be realized carefully because it can induce mechanical stress on the NTD sensor, changing its constant values and, therefore, potentially raising too much its resistance and affecting its performance. To avoid this effect as much as possible, it is in principle better to use a matrix of non-overlapping glue spots instead of a veil. Moreover, a reproducible procedure has been developed to keep this step as much as possible under control due to the negative impact it can have on the NTD performance.

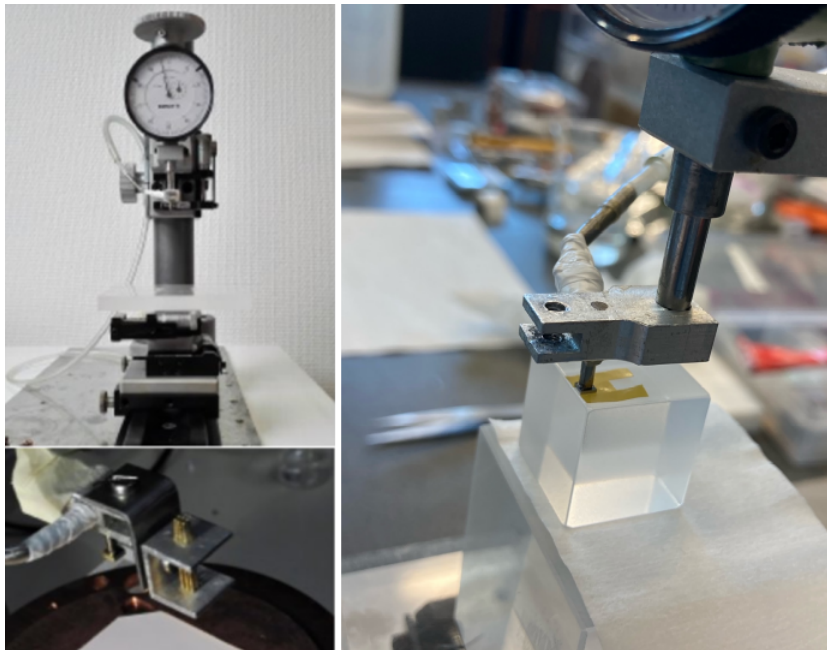


Figure 3.3 – *top left*: Photo of the gluing tool. *bottom left*: Photo of the pogo pin matrix to make nine glue spots. *right*: An NTD Ge being glued on an LMO crystal. One can see the mylar mask used to keep a fixed gap between the sensor and the absorber surface.

We used a gluing tool shown in Figure 3.3. It is composed of a plate on which the crystal to be glued is placed. This plate can move along the X and Y axis thanks to lateral screws. On the top of the tool, there is a metallic "arm" that can move along the Z-axis. We can attach to this arm a pogo pin matrix made of 9, 6, or 3 pogo pins depending on the desired number of glue spots. After deepening the matrix in the glue, we can put it in contact with the crystal top surface to deposit the glue spots. Finally, the arm also has a small tube facing downward linked to a vacuum pump. We can, by suction, place the NTD at the bottom of the tube and use the movement of the arm to deposit the NTD on the glue spots and apply a known pressure during the drying. Usually, for relatively big NTDs ($3 \times 3 \times 1 \text{ mm}^3$), a $50 \text{ }\mu\text{m}$ mylar mask is placed upstream to surround the glue spots and allow a gap between the NTD and the crystal surface to avoid the spots merging. For smaller NTDs

($3 \times 1 \times 1 \text{ mm}^3$) like the one used for Ge light detectors, the mask is not used and the spots are making a veil after the NTD deposition. This procedure was developed for the NTD gluing of CUPID-Mo detectors, which has demonstrated its reliability for obtaining good and reproducible bolometric performance [126].

To connect the NTD to the outer readout electronics and once the bolometer is mounted in its assembly, gold wires are bonded on the NTD gold pads to gold pads situated on a Kapton[®] foil generally glued on the copper holder. From that, Cu twisted wire pairs are soldered with tin for the adaptation to the cryostat wiring. In addition to the electrical connection, these bonded Au wires provide the main thermalization of the bolometer to the heat bath.

3.2.2 NTD operation and load curves

In order to convert the temperature variation of the bolometer after an energy deposition into an electrical signal, the NTD Ge has to be biased. This can be done through the circuit shown in Figure 3.4 (left). A constant direct current I_{bol} is injected to read the voltage difference V_{bol} between the two Au pads of the NTD through two load resistors at room temperature which have a resistance R_L typically one order of magnitude higher than the sensor ($R_L \gg R_{NTD}$). This condition ensures a constant current despite the NTD resistance variation. Therefore, registering continuously the voltage drop $V_{bol} = I_{bol} \cdot R_{NTD}$ across the NTD allows one to measure the energy deposition during particle interactions inside the bolometer.

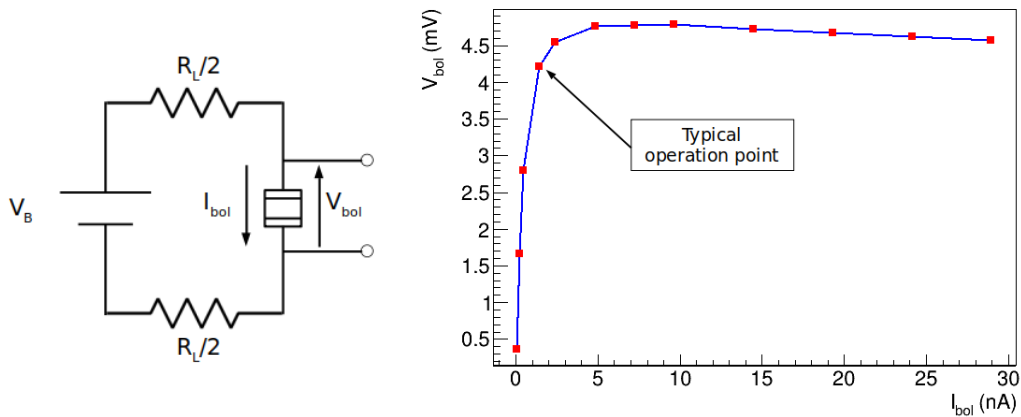


Figure 3.4 – *left*: Schema of the NTD Ge bias circuit. *right*: Load curve at 15 mK of an NTD Ge glued on a TeO_2 crystal.

An electrical power $P = I_{bol} \cdot V_{bol}$ is dissipated through the NTD. It increases, in principle, its temperature to $T = T_0 + P/G$ if we stay in the simple model described in section 3.1 and therefore decreases its resistance according to equation 3.9. This effect is known as the electrothermal feedback. Looking at a typical NTD $V(I)$ for a given T_0 , also referred to as the load curve, shown on the right side of Figure 3.4, one can see that for low bias, the slope is quite linear. After a high enough bias value, known as the inversion point, the behavior changes: the slope decreases and becomes non-linear due to the high contribution of the electrothermal feedback.

Each red point in Figure 3.4 is a potential working point. However, it exists an optimum bias to inject through the NTD where the signal-to-noise ratio is maximum. To find it, a common method is to inject in the bolometer a known energy E (using the heater for example,

see section 3.3.4) and search for the point where the induced ΔV is maximum, i.e. where the sensitivity defined as $\Delta V/E$ (often expressed in nV/keV in this thesis) is the maximum. Usually, this point is situated just before the inversion point on the load curve and is chosen as the working point.

3.3 Detector response

3.3.1 Electronics and signal

In most of the tests presented in this thesis, the room-temperature electronics design that was used to read and save the NTD voltage variations is described in Ref. [127]. A schematic and simplified view of it is shown in Figure 3.5. It is composed of a room-temperature low-noise Differential Voltage Pre-amplifier (DVP) which is the first stage of the sensor voltage variation amplification. It has a high input impedance thanks to its JFET input and provides an amplification of 27V/V. It is followed by a Programmable-Gain Amplifier (PGA), constituting the second amplification stage. This gain can be set from 1 V/V to 50 V/V giving a total selectable gain between 27 V/V and 1350 V/V, which is necessary for adaptability to the detector sensitivities. The signal passes through a Bessel low-pass filter acting as an anti-aliasing one for which the cut-off frequency can be tuned and set at a value higher than the signal bandwidth. Finally, the signal is digitalized by a commercial 16bits National Instrument ADC card before being sent to our data acquisition software.

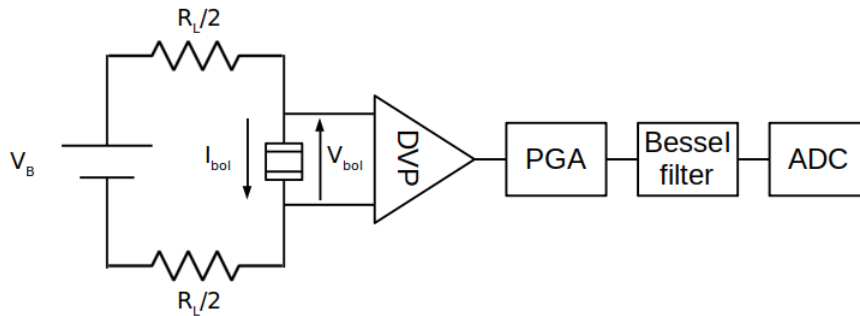


Figure 3.5 – Schematic view of the full electronics used during most of the tests presented in this thesis.

The typical voltage variation measured after a particle interaction in the bolometer is shown in Figure 3.6. From equations 3.6 and 3.1, the maximum amplitude ΔV is directly proportional to the energy deposited ΔE through the relation:

$$\Delta V = A \cdot g \cdot V_{bol} \frac{\Delta T}{T_0} = A \cdot g \cdot V_{bol} C \frac{\Delta E}{T_0} \quad (3.10)$$

With g , the gain applied by the electronics on the output signal. If we consider that the energy deposition and the rise of temperature in the absorber is instantaneous, the time that takes the signal to reach its maximum is related only to the time needed for the heat to diffuse to the NTD Ge. Thus, it is mainly associated to the thermal conductance of the coupling made with the glue. We define as the "rise-time" the time taken by the pulse to rise from 10% to 90% of its amplitude. After the maximum, the pulse starts to decay on a longer time scale. This component is related to the time that takes the NTD and so the absorber to relax back to the heat bath temperature, depending on their mutual thermal

couplings. We define the decay time as the time necessary for the signal to decay from 90% to 30% of its maximum amplitude. The determination of these two temporal constants is useful since it can provide non-physical pulse or event discrimination (see Chapter 6 for an example). However, the most crucial parameter to evaluate precisely is the pulse amplitude that carries the energy information, and its determination can be made harder by the noise contribution to the signal.

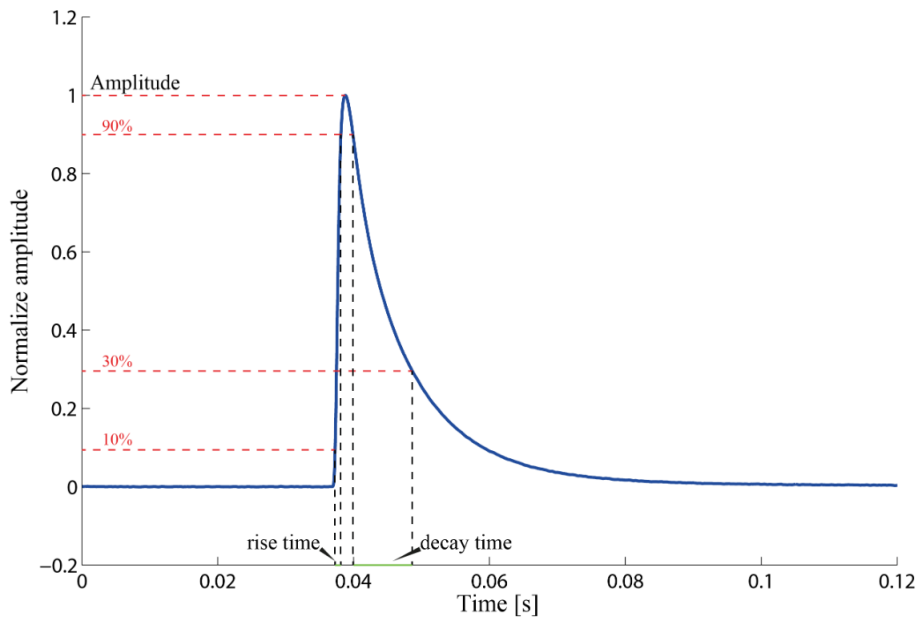


Figure 3.6 – Typical voltage signal obtained after a particle interaction in the bolometer. Figure from [128].

3.3.2 Intrinsic and extrinsic noises

The signal shown in Figure 3.6 was picked in an energy region with a really high signal-to-noise ratio. Therefore, the noise contribution is not seeable. However, it is present, and it can have a direct impact on the energy resolution achieved by the detector. The following function can describe the signal:

$$V(t) = a \cdot s(t - t_0) + n(t) \quad (3.11)$$

where a is the amplitude, $s(t)$ the signal shape with t_0 the starting time and $n(t)$ the noise contribution. It is important to understand from where the noise contributions are originated to minimize their impact on the amplitude determination. We can distinguish two categories of noise sources: the intrinsic sources and the extrinsic ones.

Intrinsic sources

It corresponds to the sources that depend on the physics behind the absorber and the NTD Ge themselves. They are unavoidable and thus are the contributions limiting the theoretical intrinsic energy resolution. In this category, we have:

- **Thermodynamic noise** - Bolometers can reach really good energy resolution compared to other detection methods. This is due in part to the fact that almost the totality of the

energy deposited by a particle in the absorber is converted into mediators of the detection, i.e. phonons. The intrinsic energy resolution limitation is mainly due to the statistical fluctuation of the number of phonons exchanged between the detector and the heat bath. If we consider that the average energy of phonons is $\langle e \rangle \simeq k_B T$, then the number of phonons created for an internal detector energy $E = C(T) \cdot T$ is $N = E/k_B T$. Assuming a Poisson distribution for N , we end up with an energy fluctuation due to this effect given by:

$$\Delta E = \sqrt{N} \cdot k_B T = \sqrt{k_B C(T) T^2} \quad (3.12)$$

It is completely independent of the amount of deposited energy during a particle interaction. Taking the values of Table 3.1, this contribution for a 250g LMO crystal at 15 mK would be of only $\Delta E \simeq 15.8$ eV. Of course, this is just a theoretical limit, and in reality, other noise contributions prevent reaching such a low energy resolution.

- **Johnson noise** - The NTD Ge can be considered as a resistor in a simple model. Therefore, it generates a Johnson noise arising from the thermal motion of electrons within it. It produced a white noise which has a power spectrum defined in a first approximation by:

$$\sqrt{e_n^2} = \sqrt{4k_B T R} \quad [V/\sqrt{Hz}] \quad (3.13)$$

Where R is the NTD resistance, and T is the temperature. It was shown in Ref. [129] that if the NTD is operated in the right conditions at the optimal working point, the two intrinsic noise contributions treated together give an ultimate energy resolution of the same order of magnitude as the thermodynamic noise alone.

Extrinsic sources

It includes the sources that come from the readout circuit or the environment of the detector. One can cite, for example, the Johnson noise induced by the load resistors. However, it is proven that if the condition $R_L \gg R_{bol}$ is satisfied, this contribution can be made negligible compared to the NTD Johnson noise, although they are operated at room temperature [129]. In general, the read-out electronic contributes at a low level to the general noise since it was built and optimized for bolometric measurements [127].

Therefore, the main contributions from these sources come from the environment where the detectors are operated. Indeed, bolometer signals develop in the low-frequency domain (a few Hz for large crystals and hundreds of Hz for the Ge light detectors). Therefore, they are really sensitive to microphonics induced by vibrations. Unfortunately, they have to be operated in cryostats which are not the quietest environment due to, for example, pulse-tube vibration or mixture circulation. Some decoupling methods have to be used to reduce as much as possible the propagation of these vibrations to the detectors [130, 131], in addition, of course, to fix the detectors tightly. Moreover, electromagnetic interference can constitute another harmful contribution. One has to carefully dispose of the electronic elements of the setup to avoid them as much as possible.

The two last contributions described are usually really difficult to quantify and are, most of the time, limiting the energy resolution, preventing the bolometer from reaching its ultimate energy resolution. Despite this, the bolometric technique stays the method with one of the best energy resolutions in the landscape of experiments searching for neutrinoless double beta decay (see Chapter 2).

3.3.3 Analysis tools

From our data acquisition software, we obtain binary files containing the full data stream of voltage variations across the NTD Ge. To process them, a MatLab-based software was developed at IJCLab in Orsay called Argonaut [128]. It takes care of the event triggering, the pulse amplitude determination and the estimation of several other relevant parameters, such as the rise time, the decay time, or the baseline value before the pulse trigger.

For a more accurate amplitude determination, it applies to the data an optimum Gatti-Manfredi filter [132]. The transfer function is designed to maximize the signal-to-noise ratio but does not change the amplitude value, improving the energy resolution of the detector. Let's consider the function $v(t) = a \cdot s(t)$ carrying the information on the pulse amplitude a , its filtered version could be written:

$$\tilde{v}(t) = \frac{a}{2\pi} \int_{-\infty}^{+\infty} H(j\omega)S(\omega)e^{-j\omega t} d\omega \quad (3.14)$$

where $S(\omega)$ is the Fourier transform of $s(t)$ and $H(j\omega)$ the filter transfer function. On the other hand, the noise RMS after filter application and assuming it is ergodic, would become:

$$\langle \tilde{n}^2 \rangle^{\frac{1}{2}} = \left(\frac{1}{2\pi} \int_{-\infty}^{+\infty} \mathcal{N}(\omega)|H(j\omega)|^2 d\omega \right)^{\frac{1}{2}} \quad (3.15)$$

Where $\mathcal{N}(\omega)$ is the spectral power density of the noise associated with the measurement. Therefore the SNR is given by:

$$\text{SNR} = \frac{\frac{a}{2\pi} \int_{-\infty}^{+\infty} H(j\omega)S(\omega)e^{-j\omega t} d\omega}{\left(\frac{1}{2\pi} \int_{-\infty}^{+\infty} \mathcal{N}(\omega)|H(j\omega)|^2 d\omega \right)^{\frac{1}{2}}} \quad (3.16)$$

From this equation, it exists a unique solution for $H(j\omega)$ which maximizes the SNR:

$$H(j\omega) = K \frac{S^*(\omega)}{\mathcal{N}(\omega)} e^{-j\omega t} \quad (3.17)$$

with K a constant. Therefore, two inputs are necessary before applying the filter to the data: the pulse shape function $s(t)$ and the noise power spectrum $\mathcal{N}(\omega)$.

For the determination of $s(t)$, the Argonaut software provides an interface to construct a representative pulse, also called a mean pulse, in which one can manually select a specific quantity of event pulses from a designated energy range (in our case, we are interested in the gamma energy region) and averaging them to minimize the contribution of the noise. Similarly, it provides another interface to build the mean noise power spectrum by averaging the power spectra from a collection of signal-free data windows. These two steps have to be realized carefully since the performance of the filter is quite dependent on them.

The data trigger can be realized on the filtered data, where an amplitude threshold is manually chosen by the user. To avoid any trigger in the baseline, we usually set a value corresponding to 5σ of the filtered baseline RMS Gaussian distribution. Moreover, another parameter based on the Pearson correlation factor, which we call here simply correlation, illustrates how similar in shape is the analyzed pulse compared to the mean pulse. The correlation can go from 0 if the shapes are completely different to 1 if they are exactly the same. During the trigger step, only pulses above a certain correlation (usually set to 0.8 or 0.9) are triggered to avoid the trigger of non-physical events. This is quite efficient for

low-rate data, but when a high rate of events is present in the data stream, this can affect the reconstruction efficiency (see Chapter 6.) We obtain at the end of the data processing an ASCII file where each line corresponds to a triggered event with all the determined parameters, including its amplitude. Among them, the correlation parameter is also present, allowing during the data analysis a more stringent cut if necessary.

3.3.4 Heaters and stabilization

Another factor can possibly degrade the energy resolution of the detectors: since the NTD Ge sensitivity depends on the temperature, it is quite sensitive to temperature instabilities in the cryostat. Thus, small temperature variations of the heat bath can induce slight variations in the pulse amplitude for the same energy deposition, enlarging the energy resolution. Therefore, to monitor and stabilize the detector response another device beside the NTD Ge is glued on the absorber surface. It consists of a heavily doped silicon resistive chip (Figure 3.7), called a heater, that is used to inject signals periodically at a fixed energy in the absorber by Joule effect [133]. It is connected to a room temperature pulse generator for which the parameters are tuned to obtain a pulse shape close - but not identical so they can be rejected during the analysis - to the physical events. The energy of the heater signals is usually chosen larger than the γ energy region to avoid any misinterpretation.

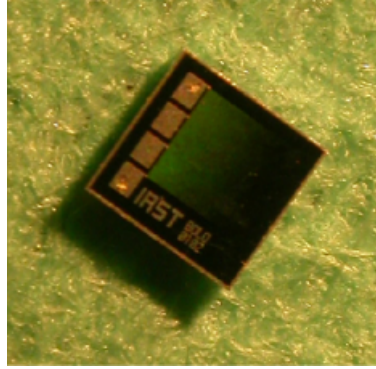


Figure 3.7 – Photo of a $2.33 \times 2.40 \times 0.52 \text{ mm}^3$ heater. Its bonding is done in a similar way to NTD Ge, on the external gold pads.

We can easily identify these events during the offline analysis thanks to their high energy and different correlation value. By looking at the amplitude of each pulse as a function of the baseline value b preceding it, which is a sort of measurement of the heat bath temperature, we observe a clear drift due to the temperature dependence of the detector response. We can fit this drift with a first-order polynomial function $f(x)$, which can be used to correct the amplitude a of every event - not only the heater ones - using the following formula [134]:

$$a_c = \frac{a_{\text{ref}}}{f(b)} \cdot a \quad (3.18)$$

with a_c the corrected amplitude and a_{ref} a reference amplitude value, usually taken as the average value of heater amplitudes before correction. The corrected amplitude of the heater pulses is distributed around a_{ref} . The stabilization process is illustrated in Figure 3.8. It is important to mention that in the case where the statistic in the γ region is high enough to observe clear peaks (during a calibration measurement for example), this stabilization procedure can be applied using one of the γ lines, sometimes giving better results to improve their energy resolution.

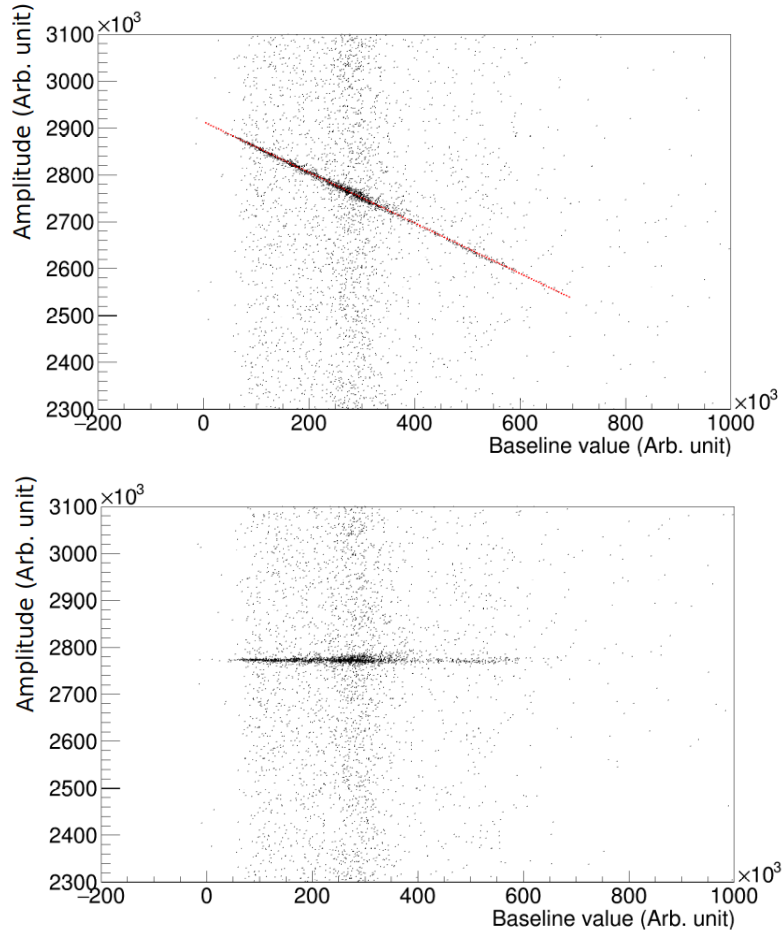


Figure 3.8 – *top*: Heater amplitudes as a function of the baseline value preceding the pulse during a TeO_2 crystal measurement. The dashed red line represents the first-order polynomial function used to fit and stabilize the data. *bottom*: Heater amplitude distribution after the stabilization process.

In addition, the heater can be used to search for the NTD optimum working point by looking at the amplitude of its pulses during pre-measurement parameter tuning. Indeed, the higher they are, the best is the NTD Ge sensitivity.

3.4 Double read-out method

The base features of bolometers described so far in this Chapter show how promising is this detection method for the search of $0\nu 2\beta$ and why CUORE is among the most sensitive experiment in the field. However, contrary to other detection methods like the ones used for GERDA or Kamland-Zen (see section 2.4), they do not allow event identification which is crucial for background rejection. This is one of the reasons preventing CUORE from reaching the objective of the next generation experiments. Indeed, the CUORE background in the ROI is dominated by energy-degraded α 's due to the contamination of the materials surrounding the detector or the surface of the bolometer itself without any solution to reject them.

To overcome this limitation, one can take advantage of the flexibility in the absorber material choice and select one which scintillates. The detection and quantification of this

scintillation light, in addition to the thermal signal, provide a supplementary piece of information for each event allowing, in our case, the rejection of the α background as it will be explained in this section. This type of dual read-out detector is called a scintillating bolometer and will be used in the CUPID experiment, the successor of CUORE.

3.4.1 About the scintillation process

The generation of scintillation light in inorganic crystals involves intricate mechanisms that are not yet fully comprehended. After an energy deposition, one of the primary mechanisms responsible for it is the de-excitation of electrons within the conduction band, which are associated with impurities that create energy levels between the valence and conduction bands. During this process, the electrons emit photons at low energies that are not reabsorbed by the crystal.

The light yield (LY) of an inorganic crystal, i.e. the amount of light emitted after an energy deposition, is defined as:

$$LY = \frac{dL}{dE} \quad [\text{keV/MeV}] \quad (3.19)$$

The interesting feature of this parameter is that it depends on the stopping power dE/dr of the impinging particle and so on its nature. J.B. Birks proposed a semi-empirical equation capturing this behavior in 1951 [135]:

$$\frac{dL}{dr} = \frac{S \frac{dE}{dr}}{1 + kB \frac{dE}{dr}} \quad (3.20)$$

Where S is the scintillation efficiency, k is the quenching parameter, and $B \frac{dE}{dr}$ is the density of impurity centers along the particle path. kB is also referred to as the Birks factor.

Therefore, we can rewrite equation 3.20 for particles with a high stopping power such as α 's:

$$\frac{dL}{dr} \simeq \frac{S}{kB} \quad (3.21)$$

While for the light ones with a lower stopping power like γ 's and β 's it can be approximated by:

$$\frac{dL}{dr} \simeq S \frac{dE}{dr} \quad (3.22)$$

We can define a quenching factor QF , which expresses this difference in light yield between α and β/γ particles:

$$QF = \frac{LY_{\alpha}}{LY_{\beta/\gamma}} \quad (3.23)$$

Due to the fact that α particles deposit their energy in a smaller volume than β/γ 's, they have access to fewer impurities. Thus, the quenching factor QF is inferior to 1 for most of the scintillating crystals, including LMO crystals used in this thesis. However, it is not possible to generalize since, in the unique case of ZnSe crystals, it appears to be superior to 1 for not yet explained reasons [136]. In any case, detecting this scintillation is the key to discriminating α events from β/γ in bolometric experiments.

3.4.2 Bolometric light detectors and α rejection

The cryogenic temperatures at which bolometers are operated limit the possible choice of devices to detect the scintillation light. Therefore, the easiest way to implement this idea is to use an auxiliary bolometer, also read by its own NTD Ge, that will act as a light detector. The first test of such configuration was successfully operated using a sapphire bolometric light detector to detect the scintillation light of a $\text{CaF}_2(\text{EU})$ crystal [137]. Thanks to the dual heat/light readout, a full α and β/γ discrimination was obtained, demonstrating the power of this method.

One of the best absorber materials for a bolometric light detector is definitely Germanium. This semiconductor presents a low heat capacity at low temperatures (see Table 3.1), can be highly radiopure, and have a short absorption length for scintillation photons. Ge crystals can also be produced in thin slabs ($\mathcal{O}(100 \mu\text{m})$), allowing the covering of large areas without having a too large Ge mass, keeping the light detector heat capacity low enough to be sensitive to this kind of photons. Furthermore, in order to enhance their light collection, it is common to evaporate on their surface a thin layer of SiO [138]. This description constitutes the basis of all the light detectors operated with scintillating bolometers in this thesis, and a simplified drawing of the basic setup can be found in Figure 3.9.

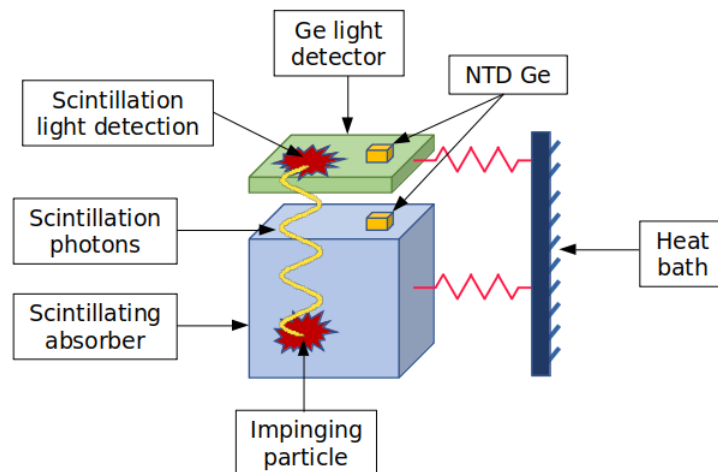


Figure 3.9 – Simplified drawing of the working principle of a scintillating bolometer operated with a Ge bolometric light detector.

With this configuration, each event depositing a high enough amount of energy in the main absorber will also be detected in coincidence by the Ge light detector. Therefore, we can plot the light signals as a function of the heat signals. The typical plots obtained are shown in Figure 3.10. One can see that we distinguish two regions of events: the γ/β band and the α band due to the scintillation properties described earlier. By using the light yield of each event, it is possible to identify α 's and completely reject them, getting rid of their background contribution. Real light yield plots can be found, for example, in Chapter 5.

We can quantify the ability of a scintillating bolometer to separate α events from γ/β ones using a parameter called the discrimination power (DP). After fitting the LY distribution of the two different bands using a Gaussian function, we can extract their respective mean value μ and standard deviation σ to calculate the DP using the following formula:

$$DP = \frac{|\mu_{\gamma/\beta} - \mu_{\alpha}|}{\sqrt{\sigma_{\gamma/\beta}^2 + \sigma_{\alpha}^2}} \quad (3.24)$$

The LUMINEU project first demonstrated the α rejection with LMO crystals coupled to Ge wafers [139]. It led to the construction of the CUPID-Mo experiment, which showed that a large-scale experiment searching for neutrinoless double beta decay with these detectors was feasible (see section 2.4). They will finally constitute the basis of the detectors that will be used in the next-generation experiment CUPID with the objective of exploring the inverted hierarchy region of possible values for $m_{\beta\beta}$ thanks to the background reduction they provide (see Chapter 4).

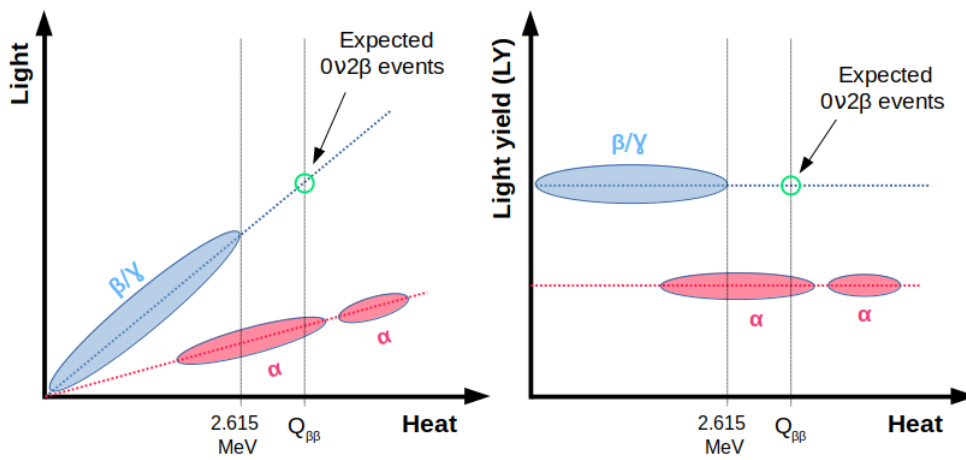


Figure 3.10 – *left*: Schema of the light signal as a function of the heat signal obtained for a crystal with a $QF > 1$. The $Q_{\beta\beta}$ shown corresponds to the one of ^{100}Mo . *right*: Light yield as a function of the heat signal.

3.5 Dilution cryostats

Cryostats are the name given to the setups hosting and keeping isolated from the external world the thermodynamic machines used to cool down the bolometers. They are an impressive piece of engineering and have allowed scientists for several decades now to explore the properties of matter at low temperatures. It exists different types which can cover different ranges of temperature. Since bolometers are usually operated between 10 and 50 mK, we are interested here in the so-called dilution refrigerator, which contains a dilution unit (DU) providing the cooling power to reach such temperatures. Their working principle will be presented in this section, and the cryogenic setup used for most of the tests performed in this thesis will be described.

3.5.1 Working principle

In general, a dilution refrigerator can be divided into several volumes, each being at a different temperature and shielded from the others with cylindrical copper screens to avoid black-body radiation in a sort of "Russian doll" configuration. The most external one at room temperature is referred to as the Outer Vacuum Chamber (OVC). It is pumped to a high

vacuum to prevent any heat conduction or heat convection with the outside world and the inner volumes. Inside the OVC, a first screen at 80 K can be found, and then more internally the Inner Vacuum Chamber (IVC) at 4 K. The latter hosts the DU, which has parts inside three other copper screens, one inside the other, at respectively 1 K, 50 mK and 10 mK. The coldest part of the DU and thus of the cryostat, called the Mixing Chamber (MC), is situated in the 10 mK screen and is the part to which the bolometers are thermally coupled. The cooling down is divided in roughly two steps.

The first one consists of pre-cooling at around 4.2K, necessary for reaching lower temperatures with the dilution unit, as it will be explained later. Depending on the type of cryostat it can be done differently. In a so-called "wet" cryostat, this temperature is reached by placing the OVC in a bath of liquid helium posterior to a liquid nitrogen one at 77K in some machines to reduce helium consumption. In any case, a periodical He refill is required during the cryostat operation to keep this temperature. On the other hand, in a "dry" cryostat, this temperature is obtained thanks to a thermodynamic cycle taking place in a device called a "pulse tube" (PT). In a naive approach, this cycle can be described by the four following steps. First, gaseous helium is compressed inside the pulse tube, increasing its temperature and pressure, making it flow to the warm end of the tube, where it exchanges heat. Then it is expanded adiabatically, reducing its temperature and provoking its flow to the cold end of the tube which is thermally connected to the cryostat. There, it picks up the heat. The cycle is then repeated all along the cryostat operation to reach and maintain a temperature around 4K. Both methods are used in dilution cryostat used for bolometric measurements. Wet cryostats usually induce less mechanical vibrations than PT ones during their functioning, which is better for bolometric measurements, but are way more expensive in the long term due to their continuous consumption of liquid helium.

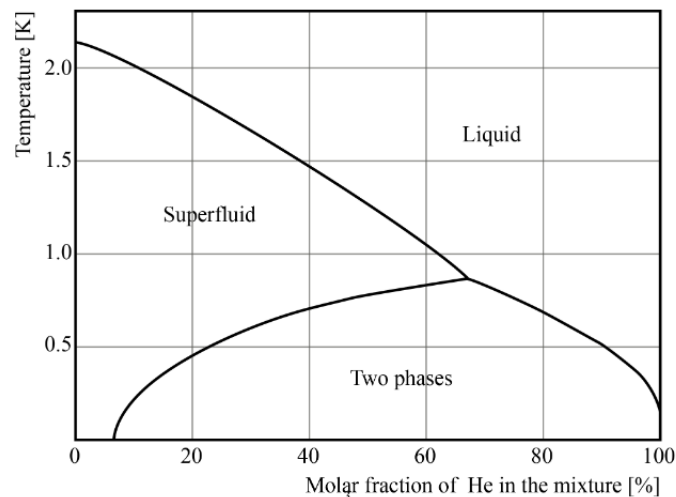


Figure 3.11 – Phase diagram of a ^3He - ^4He mixture with the temperature as a function of the ^3He content.

To reach temperatures lower than 4K, the dilution unit is used. It is a complex tube circuit where a ^3He - ^4He mixture can circulate. The cooling effect is based on a quantum phenomenon taking place in the mixture. At very low temperatures (below 870 mK) and if the ^3He concentration is larger than 6.5%, it separates in two phases as illustrated by the phase diagram shown in Figure 3.11. One containing almost pure ^3He floating at the top is called the concentrated phase, and the other one, the diluted phase, is composed of

mainly ^4He and a small percentage of ^3He . The content of ^3He in the diluted phase is well-defined at each temperature and tends to stay constant. Therefore, if some ^3He is removed from this diluted phase, the same amount of ^3He from the concentrated phase will cross the boundary between the two phases to reestablish equilibrium. Since the enthalpy of ^3He in the concentrated phase is lower than in the diluted phase, this reaction is endothermic and so provides a cooling power where it happens.

The dilution unit is designed to make this ^3He absorption by the diluted phase happen by pumping it out continuously. A scheme can be found in Figure 3.12. The diluted phase in the mixing chamber, where the ^3He absorption takes place, contains around 6.4% of ^3He while the one in the still, a part situated in a warmer part of the cryostat and connected by a pipe to the MC, contains around 1% of it. This leads to an osmotic pressure gradient that makes the ^3He flow from the MC to the still. Since the ^3He has a lower vapor pressure than ^4He in the still, it can be pumped out. The amount extracted can be re-injected in the MC to ensure continuous operation. To do so, the ^3He re-enters the cryostat by passing to tubes strongly thermally coupled to the pulse tube or to the LHe bath, so it cools back to around 4K. Then, it passes through a Joule-Thomson flow impedance in dry cryostats or through a pumped secondary liquid helium bath (called the 1K pot) in wet cryostats, reducing its temperature to 1K in both cases. Finally, it is further thermalized thanks to heat exchangers connected to the pumped line until it reaches the base temperature of the cryostat in the MC.

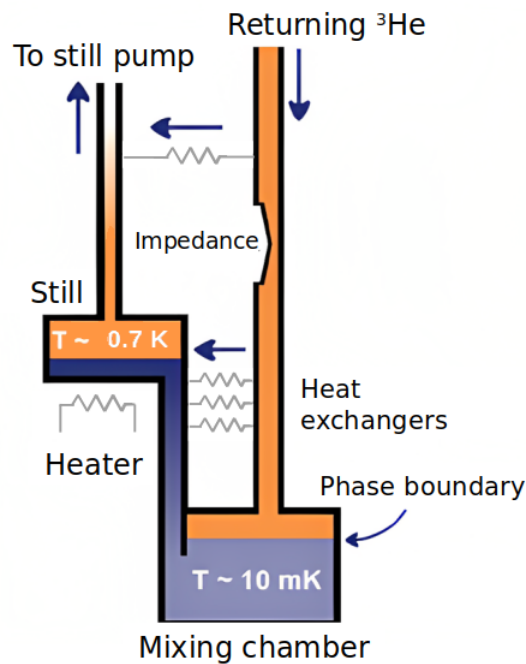


Figure 3.12 – Schema of the working principle of a dilution unit.

3.5.2 The example of Ulysse: an above ground pulse-tube cryostat

The Ulysse cryostat is a dry cryostat situated at IJCLab in Orsay where all the cryogenic measurements realized during my thesis were performed. The design of the system dates back to 1999 when CNRS and Air Liquide developed it. It became operational in 2003 at the Insubria laboratory located in Como, Italy. A brief description of it will be given in this

section.

The pulse tube at the top of the cryostat, used for the pre-cooling, is a commercial PT405 model produced by Cryomech [140]. This model is composed of two stages where the first one can achieve a cooling power of 25 W at 55 K while the second one can achieve a cooling power of 0.3 W at 3.5 K.

For cooling down below 4K, it contains a classical dilution unit with sintered silver heat exchangers and a large pumping system with a 40 m³/h rotary pump and a 400 l/s turbo pump in He. It provides the cooling power needed to cool down massive bolometers and can reach base temperatures at the level of 10 mK when loaded. The mixing chamber at the bottom of the DU overhangs the experimental volume consisting of a cylinder with a height of 20 cm and a 30 cm diameter. Since bolometers are sensitive to mechanical vibrations and since the PT can induce some, a decoupling system has been installed. It consists of a so-called floating plate attached to the still stage by four springs and thermalized to the MC by soft copper braids. The springs can be changed depending on the weight that will be attached to the floating plate in order to make sure that their total cut-off frequency is around 3 Hz. The PT frequency being at 1.4 Hz, it allows the reduction of the impact of its harmonics on the detectors. Due to the spring elongation when they are loaded, the effective experimental space is a bit smaller than announced. However, it is still sufficient to test several crystals at the same time. The temperature at the floating plate can be stabilized to a fixed chosen value by the use of a PID controller. It sends power to a heater in order to heat up the plate to the desired temperature and compensate for the fluctuations.

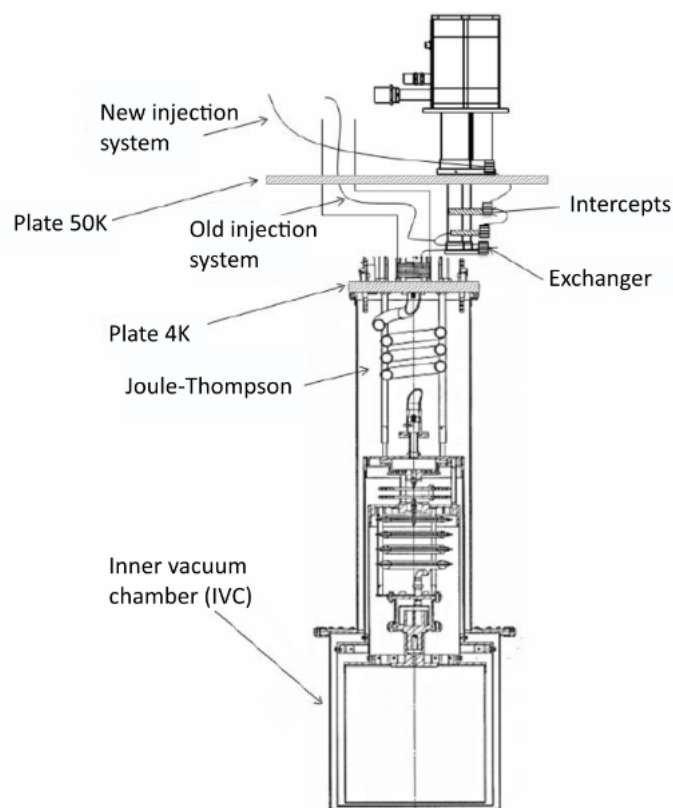


Figure 3.13 – Schematic view of the inner parts of Ulysse cryostat.

The cryostat design is based on the PT-DR1 one further described in Ref. [141], but some modifications were done in 2012. The number of sintered silver heat exchangers has been reduced from four to two without impacting the base temperature. Moreover, two copper heat exchangers were installed on the stainless steel tube connecting the two main stages of the pulse tube to profit from the cooling power available in the regenerator of the PT. It improved the mixture condensation process and in this configuration, it takes only around 3h instead of 20h before the modification.

In total, the cryostat has 18 electrical connections reaching the MC available for bolometric readout and heater pulse injection. Twelve channels reach two jaeger connectors outside the cryostat, and the six others a fisher one.

Since the cryostat is above-ground, the rate of events when measuring a bolometer is quite high due to environmental radioactivity and cosmic rays. This can prevent the measurement of large crystals. To reduce this effect, a 10 cm thickness shield of low-activity lead was placed around the OVC. In addition, the cryostat structure is placed on four dumper modules which isolate it from external vibrations. These two parts can be seen in the photo of Figure 3.14.

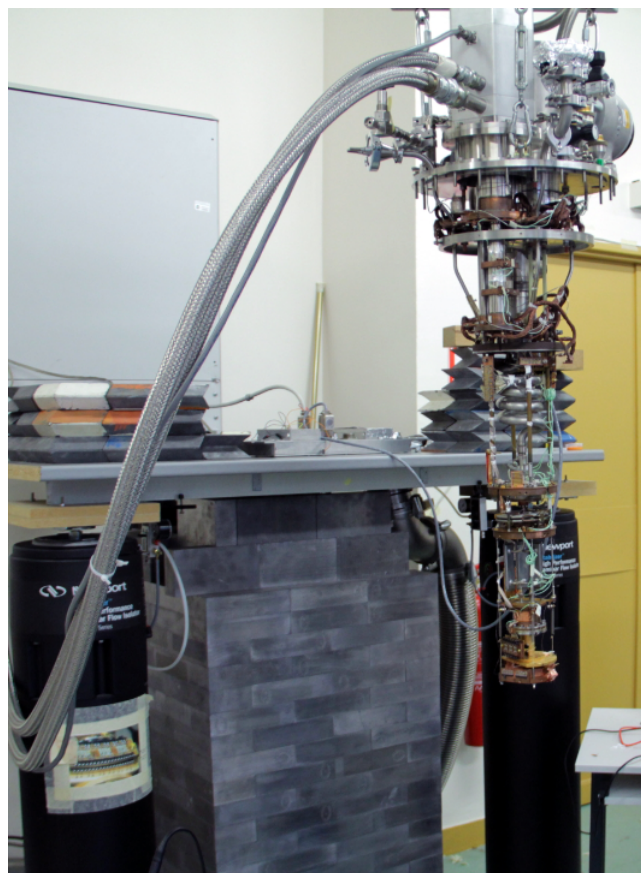


Figure 3.14 – Photo of Ulysses when opened and outside the OVC. One can see behind the lead shield surrounding the OVC and the dumper modules.

Chapter 4

BINGO: Bi-Isotope $0\nu 2\beta$ Next Generation Observatory

The work presented in this thesis has been realized in the framework of the BINGO project. The latter is funded by the European Research Council (ERC) as a Consolidator Grant. It proposes several innovations for bolometer operation to search for $0\nu 2\beta$, focusing on background reduction and a clever isotope combination to increase the sensitivity to the process of next-generation bolometric experiments. The final objective of BINGO is to demonstrate that implementing its ideas into a ton-scale experiment would allow starting to explore the region of possible values for $m_{\beta\beta}$ below 5 meV. In this chapter, the BINGO concepts will be detailed.

4.1 From CUORE to CUPID to BINGO

As already described in Chapter 2, CUORE is the largest bolometric experiment ever built. By observing 206 kg of ^{130}Te embedded inside TeO_2 crystals installed in a huge cryostat at LNGS, it is one of the most sensitive $0\nu 2\beta$ experiments of the current generation. Once its final exposure will be reached and along with the other current generation experiments which are using different detection methods, it will allow excluding the possible values for $m_{\beta\beta}$ above the edge of the inverted hierarchy region in the case where the process is mediated by a light Majorana neutrino exchange [142].

Nowadays, next-generation experiments are in preparation for several different detection techniques. They share a common goal: reaching a sensitivity to $0\nu 2\beta$ high enough to fully explore the region of possible values for $m_{\beta\beta}$ in case of the inverted ordering of neutrino masses (between 19 and 50 meV). The formula 2.13 shows that to do so, an increase of the total exposure along with a decrease of the background events in the ROI is necessary. In the case of CUORE, the main limiting parameter to achieve this goal is definitely the amount of background index in the ROI. In its last published results [97], it demonstrated a background index of around 1.5×10^{-2} c/ky. When looking at the background model in Figure 4.1, we see that it is mainly due to two contributions: the degraded-energy surface α s coming from surrounding materials which is the dominating one and the rather high amount of β and γ background coming from natural radioactivity decay chains due to the non-favorable expected position of ^{130}Te $0\nu 2\beta$ peak (below 2615 keV).

The successor of CUORE and next-generation experiment, CUPID, will overcome this limitation by implementing two main improvements. First of all, it will change the isotope studied and move to ^{100}Mo . This isotope has a Q-value above the natural radioactivity

endpoint, meaning that the region in which we expect the $0\nu 2\beta$ signal is naturally less populated by β/γ background events. Moreover, CUPID will embed this candidate in LMO crystals which have demonstrated their good performance in the CUPID-Mo demonstrator. They can be used as scintillating bolometers, which are described in Chapter 3, and completely get rid of the α background thanks to the particle identification they offer. Looking at the region of interest of ^{100}Mo in Figure 4.1, one can see that these upgrades will allow CUPID to reach a background index of $\sim 10^{-4}$ cky and, after 10 years of lifetime, put an upper limit on $m_{\beta\beta}$ between 17 and 20 meV, matching the objective of next-generation experiments.

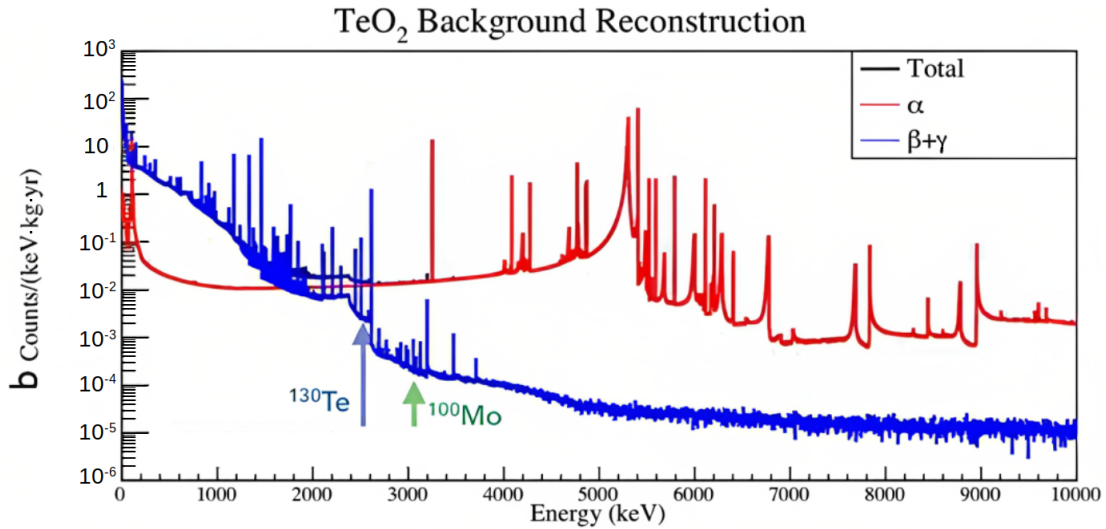


Figure 4.1 – CUORE background model. The contribution of α particles can be seen in red and the one of β/γ in blue. The ROI of ^{130}Te and ^{100}Mo are pointed out as well. Figure adapted from [143]

If at that point $0\nu 2\beta$ is still escaping us, the background reduction will have to be pushed even further. This requires a major technological improvement since current methods are limited by the $\beta + \gamma$ "floor" visible in the CUORE background model. To give an answer to this problem, the BINGO project has been created. It proposes innovative technologies and methods to reject the remaining β and γ background events and reach a background index of $\sim 10^{-5}$ in the ROI of ^{100}Mo but also of ^{130}Te as both isotopes will be studied with BINGO.

4.2 The Bi-Isotope approach

By moving to ^{100}Mo , CUPID is naturally reducing the β/γ background contribution. However, it is also discarding ^{130}Te which is nevertheless one of the most promising isotopes for $0\nu 2\beta$ search. Indeed, among all the candidate isotopes, it is the one that has the highest natural abundance ($\sim 34\%$ against only $\sim 9.8\%$ for ^{100}Mo), making the enrichment of the crystals and the mass scalability much cheaper. Moreover, CUORE has demonstrated the excellent bolometric performance of TeO_2 crystals, which can reach tremendous energy resolution and extremely high radiopurity. It would then be important to consider this isotope for the next-next bolometric $0\nu 2\beta$ experiments, for which \sim ton of isotope is needed.

Two requirements are indispensable to use TeO_2 crystals in a low background experiment. Firstly, it must be possible to operate them as scintillating bolometers to reject α particles.

Since these crystals are weak scintillators, one must be able to detect the Cerenkov light emitted during the interaction of a particle within it. Indeed, no Cerenkov light emission is expected for α interactions while some is emitted during a β or γ one [144]. This feature needs however light detectors having a really high signal-to-noise ratio since the expected Cerenkov yield is only 140 eV/MeV. Such a low light signal is out of detection for the usual Ge bolometric LDs used for example in CUPID-Mo. At this purpose, BINGO has a solution that will be explained in the next section. Secondly, new ways to reject or mitigate β and γ events must be implemented in order to clean the ROI of ^{130}Te and decrease by a factor 100 their contribution to the background. Thanks to its innovations, BINGO will also pursue this goal.

In addition, LMO crystals embedding ^{100}Mo are also meeting all the performance requirements for a next-generation experiment as demonstrated by CUPID-Mo. The idea of BINGO is then to use them as well along TeO_2 crystals. Since they are less sensitive to the β/γ background due to the higher Q-value of ^{100}Mo , they could be deployed all around TeO_2 crystals in order to provide an extra layer of active shielding against external radioactivity for the latter. Moreover, they will benefit also from the innovative background reduction techniques that will allow reaching as well a background index of around 10^{-5} ckky in ^{100}Mo ROI. Finally, this Bi-Isotope approach could allow us, in the case of a discovery in one isotope, to obtain a confirmation in the second one without building a new experiment.

4.3 Solutions brought by BINGO to the background puzzle

To reach its background reduction objectives, BINGO is based on three innovations that will be explained in this section.

4.3.1 Enhancing the light signal with Neganov-Trofimov-Luke effect

As already mentioned, Ge light detectors used in CUPID-Mo and based on an NTD Ge read-out are not showing the required sensitivity to detect the Cerenkov light emitted by TeO_2 crystals. It is then necessary to upgrade their way of functioning. The innovation proposed by BINGO is to use the so-called Neganov-Trofimov-Luke (NTL) [145, 146] light detectors to enhance the light signal.

Since Ge is a semiconductor, $N = E_0/\epsilon$ pairs of e^- and h^+ are created when it absorbs a particle of energy E_0 , where ϵ is the average energy required to create one pair, also called the quantum efficiency. This parameter can vary as a function of the incident particle energy, especially at low values as shown in Figure 4.2 [147]. In a regular Ge bolometer, these pairs are quickly recombining, restituting the total energy E_0 to the crystal lattice in form of phonons. However, if a voltage difference V is applied through the wafer thanks to Al electrodes deposited on the Ge surface, the charge carriers will drift before recombining and will be collected. This drift produces an additional contribution to the rise of temperature induced by the particle interaction due to the Joule effect and hence, an amplification of the measured signal. The total measured energy E is given by:

$$E = E_0 \left(1 + \eta \frac{Vq}{\epsilon} \right) = E_0 \cdot G \quad (4.1)$$

where q is the elementary charge, and G is the NTL gain. The parameter η is comprised between 0 and 1 and takes into account the possibility of an incomplete charge collection due to charge trapping by impurities or recombination. It depends mainly on the Ge purity but also on the distance between electrodes. In the case where the voltage difference value V is

high enough, the NTL thermal contribution is completely dominating the signal measured by the NTD, amplifying drastically the signal-to-noise ratio since baseline fluctuations are not affected. However, the trapping of charges, their recombination, or space charges can degrade the NTL gain G over time. To overcome this, a periodical "regeneration" is required to neutralize the space charges by sending an intense photon flux in the wafer using a LED [148].

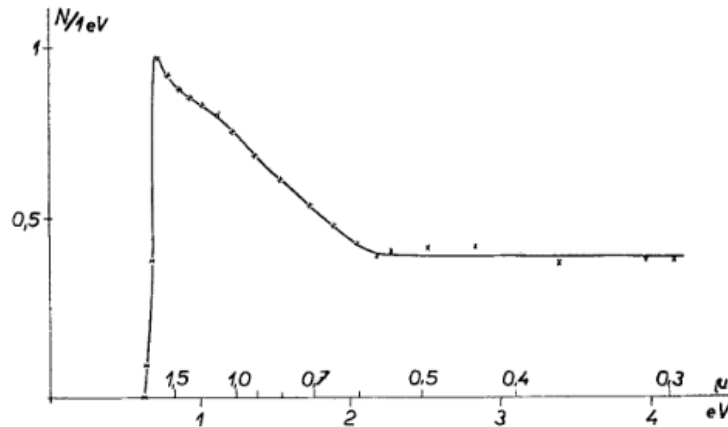


Figure 4.2 – Number of e^-/h^+ pairs created by the absorption of 1 eV in Ge as a function of the incident particle energy. After around 2.5 eV, the value stabilizes around 0.3 pairs/eV, corresponding to a threshold of around 3 eV for single-pair production. This figure comes from Ref. [147].

NTL light detectors allow amplification of the light signal implying only the evaporation of Al electrodes on the surface of the Ge wafer, without changing the "philosophy" of the detector or its readout. It makes them the perfect candidates to be used in experiments using scintillating bolometers. In addition, many of them have been already successfully operated [149, 150] and it has been shown that when coupled to TeO_2 crystals, they allow the detection of the Cerenkov light with a complete rejection of the α background events [151] (shown in Figure 4.3). In this case, the 44 mm diameter wafer had circular Al electrodes evaporated on its surface.

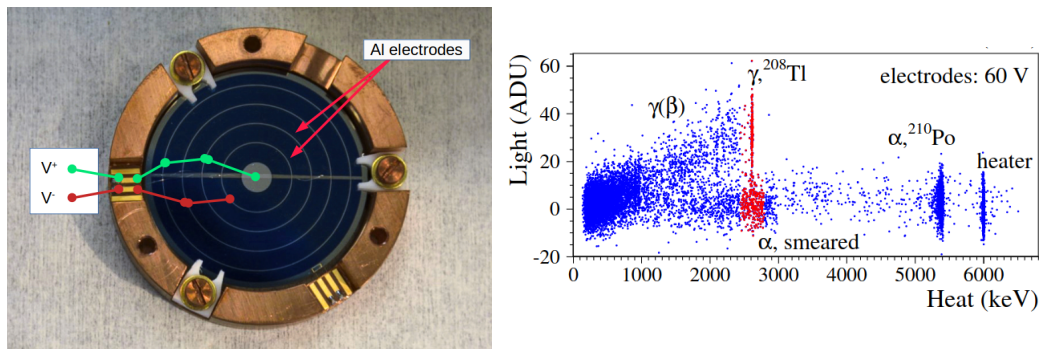


Figure 4.3 – *left*: An NTL light detector inside its copper holder used for the TeO_2 Cerenkov light measurement. A schematic view of the electrode bondings is shown. Photo from Ref. [150]. *right*: α discrimination obtained by detecting the Cerenkov light emitted by a TeO_2 crystal. The electrodes were biased with a 60 V voltage difference. A detailed description of this test can be found in Ref. [150, 151].

In addition to the α background rejection they will offer for both types of crystals, these detectors will also help to push down the background level induced by ^{100}Mo $2\nu 2\beta$ pile-up events. It is expected at a level around $\sim 3 \times 10^{-4}$ ckky for an LMO-based experiment using standard Ge light detectors [152] while it has been shown recently that NTL light detectors could help to reduce it considering an R&D work to improve the performance already demonstrated [153].

The main challenge for BINGO is to prove that their use is possible in large-scale $0\nu 2\beta$ experiments. It aims to confirm the NTL detector performance but also to study new electrode patterns and wafer shapes to maximize the NTL gain and the ease of assembly. Finally, the goal is to show their reproducibility and to develop a suitable mass-production procedure to prepare the implementation of this technology in a CUPID-like experiment. The work done in this direction during this thesis is presented in Chapter 7.

4.3.2 The revolutionary detector assembly

In bolometric experiments, the passive materials surrounding the detectors can be contaminated by nuclides of the natural radioactive chains that can lead to α , β , or γ radiations. Assuming a full α rejection, we expect a continuous contribution from γ and surface β in the ROI of $\sim 10^{-4}$ ckky of both ^{130}Te and ^{100}Mo (5×10^{-4} ckky and 3×10^{-4} respectively). For γ radiations, they can be kept under control and at a level of around $\sim 10^{-5}$ ckky simply by choosing extremely radiopure materials close to the detectors. For example, the so-called NOSV copper used in CUORE has a contamination $< 5 \mu\text{Bq/kg}$ in ^{238}U and ^{232}Th [154] and even lower values could be achieved - $< 0.1 \mu\text{Bq/kg}$ - for ^{232}Th (the most harmful for ^{130}Te) using electroformed copper [70]. The second contribution from surface β is more challenging to reduce. Even though most of the β spectrum from natural radioactive chains is concentrated below 2 MeV, there are two transitions from ^{214}Bi and ^{208}Tl at respectively 3270 and 4999 keV. By depositing a small amount of energy in their originated material before interacting in the crystal, they can lead to a continuous spectrum with an endpoint at their Q-value, populating our two ROI. In the case of CUORE, this gives a background level of around 10^{-4} ckky although meticulous surface cleaning have been performed on the materials close to the detectors. Since there is no real room for improvements of the cleaning procedure, a new innovation has to be implemented to mitigate this contribution down to values lower than 10^{-5} ckky.

To overcome this limitation, BINGO proposes simply to work on the way bolometers are assembled. The idea is based on two pillars: reducing the amount of passive materials surrounding the detector compared to for example the CUORE assembly and taking benefit of the Ge light detector presence. The former can be realized by using for the first time a nylon wire to hold laterally the crystals to a small copper structure situated in the middle. Since this nylon wire is thin, the surface of passive materials around the crystals is drastically reduced. Moreover, using specially designed PTFE pieces, it is possible to place NTL Ge light detectors vertically in between the crystal and the remaining surface of copper. In this configuration, the LD is acting as an active shield against the copper surface radioactivity since it has the same surface dimension as the crystal. A schematic view of a BINGO nylon assembly module is shown in Figure 4.4.

Moreover, this revolutionary detector assembly has another advantage: when the modules are arranged in a matrix as also shown in Figure 4.4, two different types of regions appear. The first one, which can be called "White" zone, is composed only - with the small exception of nylon wires and PTFE - of the main absorbers which are extremely radiopure as demonstrated by the previous bolometric experiments. In addition, thanks to the compactness of the

assembly, they are really close to each other, making the coincidences easier which allows an efficient multi-site events rejection. The second region, called in opposite the "Grey" zone, is situated between two light detectors and contains the copper holder. This region can be exploited to put the readout wiring, the Kapton foil for bondings, and all the other necessary materials. They have of course to be radiopure but usually, their surface radiopurity is less controlled. Therefore, they will be kept isolated from the crystals to keep their potential contribution to the background as low as possible.

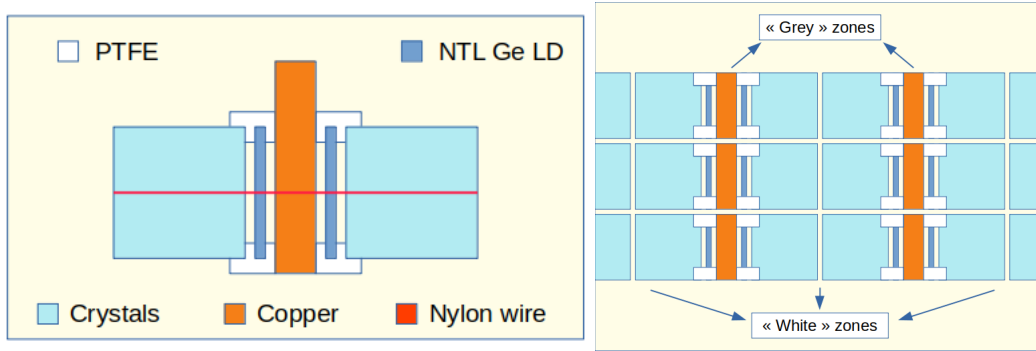


Figure 4.4 – *left*: Schematic view of the revolutionary BINGO nylon assembly
right: Top view of an array of crystals composed of nylon assembly modules.
 The "white" and "grey" zones are explained in the text.

With such a configuration of the detectors, we expect a reduction by two orders of magnitude of the inert material facing the detectors compared to CUORE. It will reduce the surface radioactivity contribution down to levels compatible with the BINGO objective of a 10^{-5} ckky background index. The work realized in the framework of this thesis with the test of the first prototypes and the validation of the concept is described in Chapter 5.

4.3.3 The cryogenic active veto

The last remaining source of background preventing reaching a background index lower than $b \sim 10^{-4}$ ckky is the external γ radioactivity coming for example from the cryostat or the shields. It has been shown by CUORE that it contributes at a level of 2.5×10^{-3} ckky in ^{130}Te ROI and only $\sim 2 \times 10^{-5}$ ckky in ^{100}Mo ROI. It is then essential to implement an innovation to mitigate this type of events, especially when using TeO_2 crystals.

The idea proposed by BINGO is to add, for the first time in a large array of macro-bolometers, a cryogenic active veto in a 4π coverage configuration all around the detector matrix. It will be made of several scintillators which will have an NTL light detector placed at both their extremities to detect the scintillation light emitted after a particle interaction within it. The material has to respect some requirements: It must be really dense with a relatively large thickness to absorb as many γ as possible; it must have a high radiopurity to not induce background or dead time; and finally, to flag as many events as possible, it must have a high scintillation yield and a low energy threshold. If an external γ from the ^{208}Tl transition at 2615 keV loses 80 keV in the surrounding material before interacting in a TeO_2 crystal, it can give an event in the ^{130}Te ROI. The veto should be able to detect such a low loss of energy in it, hence, a conservative energy threshold of around 50 keV is required. The NTL light detectors, thanks to the signal amplification they provide, will help to reach this threshold value. Two envisaged scintillator candidates are ZnWO_4 (ZWO) and $\text{Bi}_4\text{Ge}_3\text{O}_{12}$ (BGO) which both fulfill these requirements. Other considerations discussed in Chapter 6

have to be taken into account to make a final choice for the veto material.

By realizing coincidence cuts between the bolometers and the veto crystals, it will become possible to reject most of the external γ background to keep their contribution to the background at values lower than $b \sim 10^{-5}$ ckkY as presented in Figure 4.5. This drawing shows also the possibilities of β surface event rejection offered by the veto and the compact nylon assembly. Moreover, as already mentioned, putting the TeO_2 crystals in the inner part of the detector matrix surrounded by LMO crystals decreases even more this source of background. Indeed, the latter can also be used as an active veto due to the smaller impact of this type of event in ^{100}Mo ROI. A possible arrangement of the BINGO towers and cryogenic veto in the CUORE cryostat is shown in Figure 4.6.

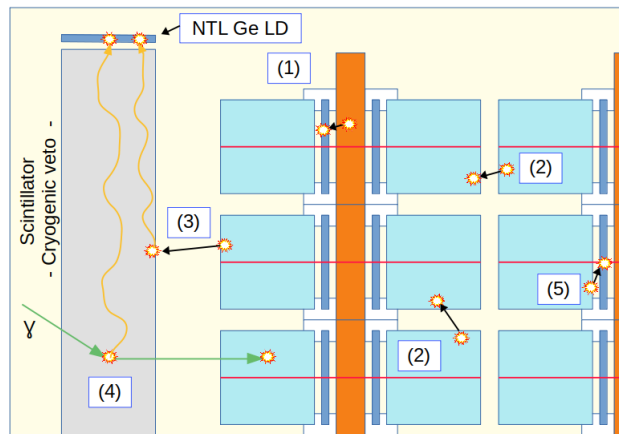


Figure 4.5 – Drawing showing different possible coincidences to reject external γ events and surface β events thanks to BINGO improvements. 1: Surface β event from the Cu holder rejected by coincidence with the Ge light detector. 2: Surface β event from a crystal rejected by coincidence with another crystal. 3: Surface β event rejected by coincidence with the cryogenic veto. 4: External γ interacting in a crystal and rejected by coincidence with the veto. 5: Surface β event from a crystal rejected by coincidence with the light detector.

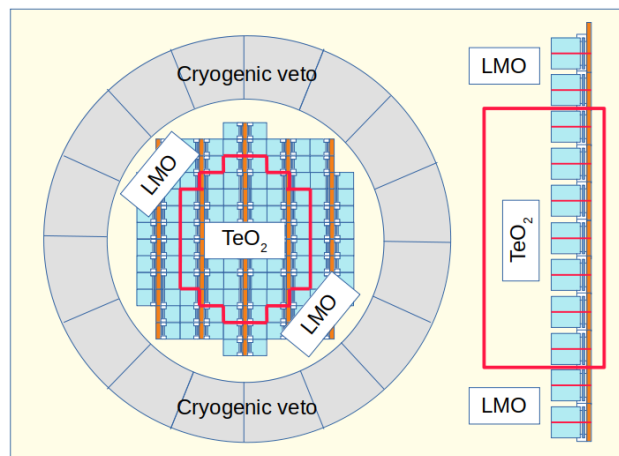


Figure 4.6 – Top view of a possible arrangement of BINGO improvements in the CUORE cryostat. The top and bottom parts of the veto are not shown.

The cryogenic active veto is obviously a promising innovation for background reduction

in bolometric experiments but is also a challenge. Indeed, implementing such a structure at low temperatures is not trivial and the goal of BINGO will be to demonstrate its working principle but also its feasibility. Some requirements are essential such as the low energy threshold and a proper mechanical assembly to hold it. Some tests have been realized in the framework of this thesis, including cryogenic measurements of the two veto candidates and a first prototype. This work is described in Chapter 6.

4.4 On the way to MINI-BINGO

The last step of the BINGO project will be the construction of a demonstrator called MINI-BINGO. It will aim to validate all the proposed technologies and open the path for their implementation in, for example, the successor of the CUPID experiment. It will be operated in a brand new dry dilution cryostat that will be purchased for this occasion and installed in the underground laboratory of Modane. This fridge will have all the features required for a low background experiment such as radiopure materials, external and internal lead shields, and an external neutron shield.

MINI-BINGO will be composed of two towers, each made of six nylon assembly modules. The first one will contain twelve $45 \times 45 \times 45 \text{ mm}^3$ natural LMO crystals which have been produced at the Nikolaev Institute of Inorganic Chemistry (NIIC, Novosibirsk, Russia) using the low-thermal-gradient Czochralski technique described in reference [155]. The second one will contain twelve $50 \times 50 \times 50 \text{ mm}^3$ natural TeO_2 spare crystals from the CUORE experiment. Each crystal will be faced by one NTL light detector. All the bolometric readouts will be done thanks to a NTD Ge glued on each detector.

The cryogenic veto will be made of BGO scintillators for the reasons explained in Chapter 6. The lateral side will be composed of two floors of sixteen $20 \text{ cm}^2 \times 22.5 \text{ cm}$ trapezoidal crystals facing one trapezoidal NTL light detector (at the bottom for the first floor and at the top for the second floor). The top and bottom parts of the veto will be a $\varnothing 150 \text{ mm} \times 50 \text{ mm}$ cylindrical crystal, to ensure a 4π coverage, with a cylindrical NTL Ge LD, on the top or at the bottom respectively, for the scintillation light detection.

A drawing of a preliminary prototype is shown in Figure 4.7 and the main components of MINI-BINGO are summarized in Table 4.1.

| Sections | Compound | Number of elements | Crystal volume | Total mass (kg) | Number of light detectors |
|-------------------|---------------------------------------|--------------------|--|-----------------|---------------------------|
| Molybdenum tower | Li_2MoO_4 | 12 | $45 \times 45 \times 45 \text{ mm}^3$ | ~ 3.4 | 12 |
| Tellurium tower | TeO_2 | 12 | $50 \times 50 \times 50 \text{ mm}^3$ | ~ 8.5 | 12 |
| Veto lateral side | $\text{Bi}_4\text{Ge}_3\text{O}_{12}$ | 32 | Trapeze $20 \text{ cm}^2 \times 22.5 \text{ cm}$ | ~ 102.6 | 32 |
| Veto top | $\text{Bi}_4\text{Ge}_3\text{O}_{12}$ | 1 | Cylinder $706.5 \text{ cm}^2 \times 5 \text{ cm}$ | ~ 25.1 | 1 |
| Veto bottom | $\text{Bi}_4\text{Ge}_3\text{O}_{12}$ | 1 | Cylinder $706.5 \text{ cm}^2 \times 5 \text{ cm}$ | ~ 25.1 | 1 |

Table 4.1 – Principal components of the MINI-BINGO demonstrator.

After one year of data taking, if no background counts are observed in the region between 2500 and 3500 keV containing the two isotopes ROI and since the total mass of detectors

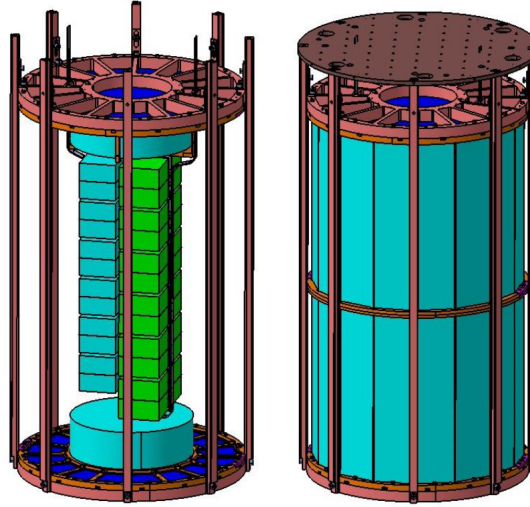


Figure 4.7 – *left*: Inner view of the MINI-BINGO prototype. One can see the mechanical copper structure designed to hold the detectors. At the center, the two towers are visible with in blue the LMO and in green the TeO_2 crystals. The top and the bottom part of the BGO veto can also be seen. *right*: Outer view of the prototype. The lateral part of the veto, composed of two floors of trapezoidal BGO crystals, is seeable.

is around 11.9 kg, the background index upper limit at 90% C.L. demonstrated should be $b < 2 \times 10^{-4}$ cky and could be even decreased by running for a longer period. If it succeeds, it will prove the accessibility of a background index of 10^{-5} cky for a ton scale bolometric experiment, which will have positive consequences on the search for $0\nu 2\beta$. Indeed, if we consider an experiment with such a low background and that contains 2 tons of ^{100}Mo with a 8 keV width ROI, a rough calculation gives that after 10 years of data-taking, it would come to an exclusion sensitivity of $T_{1/2}^{0\nu 2\beta} > 1.46 \times 10^{28}$ yr (90% C.L.) corresponding to $m_{\beta\beta} < (3 - 5.4)$ meV. Its sensitivity would be high enough to start the exploration of the region of possible values for $m_{\beta\beta} < 5$ meV, which hold only in the case of the normal ordering of neutrino masses (see Figure 2.13).

MINI-BINGO will be extremely important for the bolometric technique in general. Before its construction, we have to realize smaller-scale tests on BINGO innovations to validate the new technologies. They are explained and detailed in the three next Chapters. This one has presented an overview of the BINGO main objectives and allows the reader, I hope, to give meaning to the title of this thesis: "Innovative methods for background rejection in next-generation neutrinoless double beta decay bolometric experiments."

Chapter 5

The BINGO nylon assembly

This chapter will describe the steps we went through to validate the so-called nylon-wire assembly. As presented in Chapter 4, BINGO aims to employ a detector module where nylon wires keep fixed the main absorbers to the copper holder with the Ge light detectors sandwiched in between. To implement this idea, a clever design has been developed to ensure the mechanical robustness of the assembly but also the easiness of its mounting. Cryogenic tests have been performed to check its bolometric behavior and suitability for the $0\nu 2\beta$ large-scale experiments.

5.1 First prototype using $20\times 20\times 20$ mm³ LMO crystals

In a scintillating bolometer assembly, it is crucial to have both the main absorber and the Ge light detector well-fixed to avoid any parasitic movements that could induce thermal noise and destroy their performance. Our main challenge was finding a reliable way to attach the nylon wire to the copper holder while applying a force strong enough on the crystal. Although BINGO will use in fine $45\times 45\times 45$ mm³ crystals, the first design of the assembly was realized for smaller $20\times 20\times 20$ mm³ ones. It is better for testing the preliminary mechanical approach since such a smaller assembly is easier to manipulate and, in case of failure, cheaper and more effortless to modify.

5.1.1 The module description

The initial prototype is shown in Figure 5.1.(A) with the module containing two $20\times 20\times 20$ mm³ LMO crystals (named LMO2 and LMO4), each coupled with one $20\times 20\times 0.25$ mm³ Ge light detector (LD2 and LD4 respectively) and fixed with one nylon wire (for this first test, a simple commercial nylon wire was used). As shown in Figure 5.1.(B), we used on both sides of the Cu holder a screw on which there are three nuts separated by two washers to attach the nylon wires. Each of the latters is placed between a nut and a washer and fixed by crushing it while tightening the nut. Special polytetrafluoroethylene (PTFE, also called Teflon) pieces have been designed to position the Ge LD between the crystal and the copper. They are placed on the Cu holder at the corners of the crystal and contain a slot in their middle to host the light detector. Hence, when pressure is applied to the crystal by the nylon wire, the slot acts as a clamp for the light detector fixing it as well. A preliminary mounting was realized using dummy crystals in aluminum to ensure the design validity and to establish an assembly procedure. Moreover, this mock-up was immersed in liquid nitrogen to check how the nylon wires were reacting to cryogenic temperatures. We verified their tension and

the overall solidity of the module before and after the bath. Since no changes were observed, we moved to the real assembly.

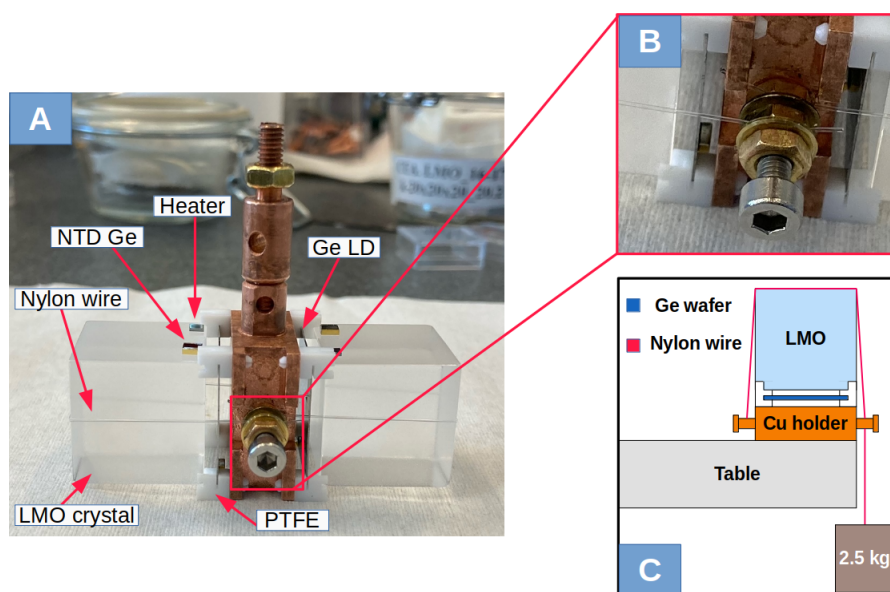


Figure 5.1 – (A) First prototype of the nylon assembly with $20 \times 20 \times 20 \text{ mm}^3$ LMO crystals. The main components are labeled. (B) Zoom on the part where the nylon wires are attached. (C) Schema of the method to put the wire in tension.

The protocol to assemble the module was the following: first, the copper holder is positioned horizontally. The four Teflon pieces are placed in their respective holes within it, the LMO crystal is positioned on them and the light detector is slipped into the slots. Secondly, one end of a nylon wire is fixed on one side of the copper holder while the other is attached to a 2.5 kg weight. The mass of 2.5 kg was determined empirically by trying different ones and seeing which was enough to apply a force on the crystal and clamp the light detector, completely fixing them. After making sure that the wire is well placed on the crystal and passes in between a washer and a nut on the other side of the Cu holder, the weight is suspended as illustrated in Figure 5.1.(C), putting in tension the wire and applying a force on the LMO crystal. Finally, the wire is fixed by tightening the nut, and its extra length is cut. The procedure is repeated for the second crystal but with this time the whole assembly resting on the first mounted crystal. This asymmetry can lead to a difference in the force applied between the two crystals with in principle the first better fixed. In our case, LMO4 was the first mounted crystal and LMO2 was the second one. In the end, we have not observed any obvious difference between the two and the obtained module was really rigid, with all the detectors composing it tightly fixed.

As also visible in Figure 5.1.(A), each crystal was equipped with a $3 \times 3 \times 1 \text{ mm}^3$ 41B NTD-Ge glued before the assembly on the top surface with 6 small spots of Araldite[®] Rapid (following the same procedure than the one described in Chapter 3) and one heater with one glue spot for temperature stabilization. For the light detectors, smaller $3 \times 1 \times 1 \text{ mm}^3$ (a 41B cut in 3) NTD-Ge were glued with a veil of Araldite[®] Rapid. After the mounting, they were all bonded with $25 \mu\text{m}$ diameter gold wires to Kapton[®] foils with gold pads located on the Cu holder. From here, copper twisted wires were soldered to connect everything to the cryostat wiring.

5.1.2 Bolometric measurements

The next step was to realize a cryogenic measurement to verify the bolometric performance of all the detectors. The assembly has been suspended in a copper structure (Figure 5.2, left) which was closed later using a reflecting foil (3M[®] Enhanced Specular Reflector Film) to enhance scintillation light collection and a copper foil. Another detector assembly, unrelated to this Chapter, has been also connected to optimize the use of the experimental space available inside the cryostat. The whole structure has been screwed to the floating plate of Ulysse cryostat (described in Section 3.5.2) above-ground in Orsay (Figure 5.2, right).

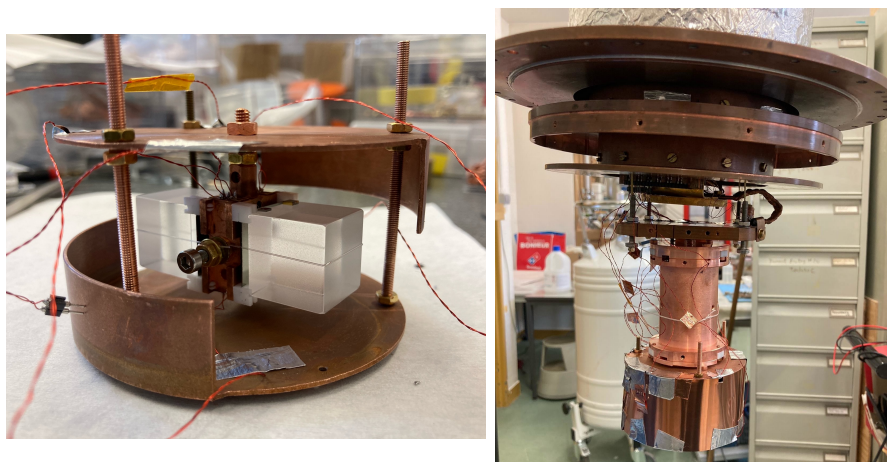


Figure 5.2 – *left*: The small prototype inside its copper structure. *right*: The cryostat configuration during the cryogenic measurement. The closed nylon assembly structure is at the bottom, attached to another detector unrelated to this Chapter.

We cooled down the cryostat to 15 mK and realized several measurements. The IV curves drawn for each detector are shown in Figure 5.3. The bias to inject in NTDs was chosen close to the inversion point for light detectors, while for the crystals, it corresponds to the point where the best signal-to-noise ratio (S/N) has been obtained (Table 5.1).

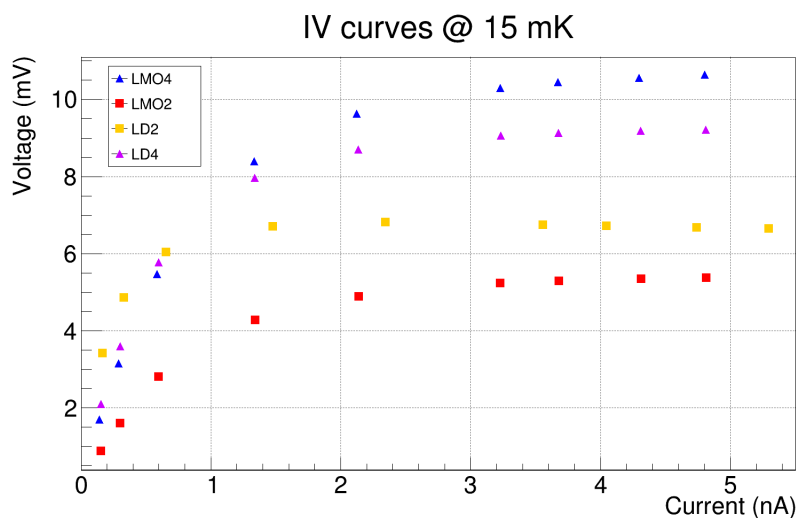


Figure 5.3 – IV curves at 15 mK for each detector.

| Detector | Current (nA) | V_{bol} (mV) | R_{NTD} (M Ω) |
|----------|--------------|----------------|-------------------------|
| LMO2 | 1.35 | 4.3 | 3.18 |
| LMO4 | 2.12 | 9.6 | 4.49 |
| LD2 | 0.66 | 6.0 | 9.19 |
| LD4 | 1.34 | 7.9 | 5.91 |

Table 5.1 – Best working points of the detectors at 15 mK.

The data acquisition was realized with the electronics described in Section 3.3.1 with a 5 kHz sampling frequency and a Bessel cut-off frequency of 675 Hz. The data processing was done using the Ithaca program described in Section 3.3.3, which applies a Gatti-Manfredi Optimum Filter and extracts the energy and the essential parameters of each pulse. During the measurements, a ^{232}Th source was placed between the external lead shield and the OVC of the cryostat. It produces the main γ lines of the decay chain in the energy spectra of the crystals, making the energy calibration easier. Pulse amplitudes were stabilized using the α peak of ^6Li neutron capture since it gave better results than using the heater pulses. A second-order polynomial function was finally used to calibrate. No energy calibration was done for light detectors since no clear peak or muon bump appeared in their energy spectra due to the short duration of the measurements, the relative smallness of their surface, and their vertical position.

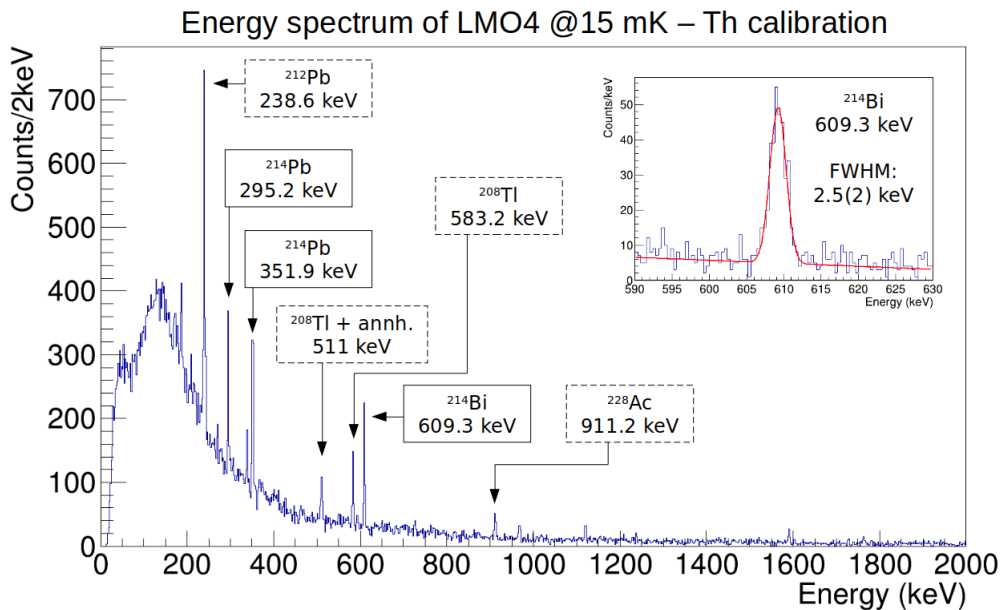


Figure 5.4 – Energy spectrum of LMO4 with a Th source after a 27.8h measurement. The most prominent γ lines from the ^{232}Th (dashed squares) and ^{238}U (solid squares) decay chains are labeled. The ^{214}Bi line at 609.3 keV has been fitted using a gaussian together with a linear background component.

The energy spectrum obtained for LMO4, after a cut on the correlation parameter (see Section 3.3.3) to keep only the physical events, is shown in Figure 5.4, where the peaks used for the detector calibration are pointed out. We can thus determine the sensitivity of the

bolometer in nV/keV defined as:

$$S[nV/keV] = \frac{D \times A}{2^n \times G \times E} \times 10^9 \quad (5.1)$$

where D is the dynamic range, A the amplitude of the pulse in ADU, n is the ADC digitization (16 bits in our case), G is the gain and E is the pulse energy in keV. It gives us the response in Volt of the detector before amplification to energy deposition in keV. Another important parameter to understand the bolometer performance is its baseline resolution, which describes the width of the baseline amplitude distribution. It offers a good estimation of the noise level during the measurement after applying the optimum filter and is the main parameter on which the S/N depends. Table 5.2 reports the two crystal sensitivities and their baseline resolutions. Promising baseline FWHM - below 1 keV - and γ peak energy resolutions have been obtained for both. The difference in sensitivity (even though not so problematic since both are rather high) can be explained either by the NTD gluing, which can be tricky to be perfectly reproducible or by the fact that LMO4 was the first mounted in the assembly so in principle subject to a higher force applied by its nylon wire.

| Detector | Sensitivity (nV/keV) | FWHM _{bsl} (keV) | FWHM at 609 keV (keV) | FWHM at ${}^6\text{Li}(n,t)\alpha$ (keV) |
|----------|----------------------|---------------------------|-----------------------|--|
| LMO2 | 178 | 0.95 | 2.4 | 10.1 |
| LMO4 | 300 | 0.85 | 2.5 | 6.0 |

Table 5.2 – Performance of the LMO crystals at their best working point at 15 mK.

No such parameters were calculated for light detectors since no energy calibration was possible. However, we could use them to look at coincidences with the heat channels and see if a α and β/γ discrimination was possible.

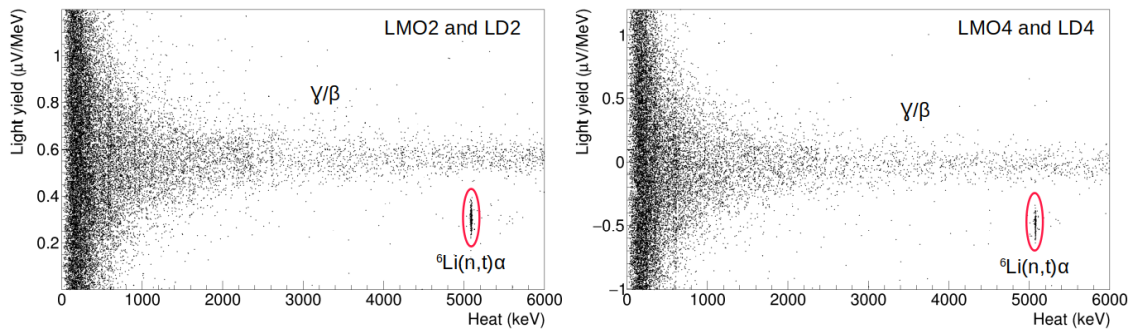


Figure 5.5 – Light yield vs Heat for both crystals. One can see the two separate bands of α and β/γ events

In Figure 5.5 the light yield (i.e. the light signal amplitude in μV divided by the heat signal in MeV) as a function of the heat signal in both crystals are represented. The ${}^6\text{Li}$ present in LMO crystals has a strong probability of capturing neutrons leading to an α emission, thus we observe a peak around 5 MeV coming from this process. It appears at an energy higher than the Q-value of the capture (4783.8 keV) because there is also a small quenching in the heat channel for α events compared to γ used for the calibration [155]. In any case, we can clearly distinguish the β/γ band from the α due to their difference in light yield. We have calculated a good discrimination power between 3 and 6 MeV of 4.9 and 5.2 for LMO2 and LMO4

respectively. Moreover, this difference in light output allows to isolate events of the ${}^6\text{Li}(n,t)\alpha$ peak and determine its energy resolution. The values are shown in Table 5.2. For LMO4 we have obtained an excellent energy resolution of 6.0 keV FWHM, which is the best ever obtained in an above-ground bolometric measurement. In the case of LMO4, the β/γ events are distributed around 0 while the α events give a negative value. This is due to cross-talks between the heat and light channels with this assembly: when an energy deposition occurs in the crystal, a part of the heat is transmitted directly to the Ge light detector through the Teflon pieces. Hence, it affects the pulse shape and the amplitude of the light signal, which gives negative values after the optimum filtering. This effect also happens in LMO2 and LD2 but at a lower magnitude, probably because it is less pressed against the Teflon pieces than LMO4. Since this small prototype was in a closed structure that allows a high light collection, these cross-talks were not preventing us from discriminating α s and β/γ s.

Finally, we wanted to compare the noise power spectra and pulse shapes obtained in this new assembly with a more conventional one used in the past with crystals of a similar size, with the same NTD gluing procedure, and tested in the Ulysse cryostat. We chose to compare with the so-called CROSS1 assembly used for R&D of the CROSS (Cryogenic Rare-event Observatory with Surface Sensitivity) experiment [156]. The assembly is explained in Ref [157], but what is important for us is that it contains a $20\times 20\times 10\text{ mm}^3$ LMO where two PTFE pieces on the top are pressing the crystal against two on the bottom, fixing it to the copper structure (Figure 5.6). This way of holding the bolometer is similar to what is generally used in experiments such as CUPID-Mo [100], or CUORE [97]. For a fair comparison, it is essential to have the crystal NTDs at a close resistance value; we had then to change the working point of LMO2. A performance summary can be found in Table 5.3, where the rise-time τ_r and the decay-time τ_d of a typical pulse are also specified.

| Detector | Temperature (mK) | Current (nA) | R_{NTD} (M Ω) | Sensitivity (nV/keV) | FWHM _{bsl} (keV) | τ_r (ms) | τ_d (ms) |
|------------|------------------|--------------|-------------------------|----------------------|---------------------------|---------------|---------------|
| LMO2 | 15 | 0.6 | 4.7 | 163 | 1.58 | 8 | 24 |
| LMO4 | 15 | 2.1 | 4.5 | 300 | 0.85 | 7 | 20 |
| CROSS1 LMO | 15.5 | 1.3 | 4.7 | 292 | 1.20 | 12 | 38 |

Table 5.3 – Comparison of the performance obtained by the LMO crystals in the nylon assembly and in the CROSS1 assembly

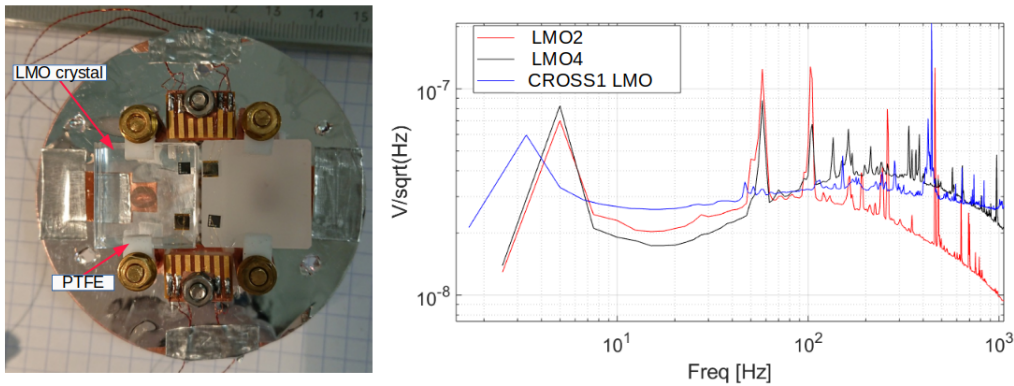


Figure 5.6 – *left*: CROSS1 assembly. *right*: Comparison of the noise power spectra obtained in both assemblies in the same experimental setup.

From Table 5.3, one can see that the crystals in the nylon assembly are showing similar performance than the one in the more conventional CROSS1 assembly. They have even obtained a faster signal than the CROSS LMO. Moreover, in Figure 5.6, the noise power spectrum of each detector is shown. The only difference between the nylon assembly spectra and CROSS1 spectrum is the presence of a peak at 57 Hz and its harmonic at 114 Hz. It could be due to vibrations induced by the nylon wire itself. Apart from that, no additional noise contribution can be seen in the signal bandwidth (between 5 and 50 Hz).

In conclusion, this first prototype has obtained good bolometric performance, close to what was obtained in the past with a more standard assembly. It showed that this innovative way of holding the detector is appropriate. This first prototype had some defaults, such as an asymmetry in the mounting of the two crystals or cross-talks between heat and light channels. However, it was convincing enough to move to a test with $45 \times 45 \times 45 \text{ mm}^3$ LMOs. Between the two measurements, we also improved the design and the assembly procedure, as it will be explained in the next section.

5.2 Second prototype using $45 \times 45 \times 45 \text{ mm}^3$ LMO crystals

After demonstrating the assembly principle with small crystals, we decided to pursue a new test with $45 \times 45 \times 45 \text{ mm}^3$ LMO crystals which is the size foreseen for MINI-BINGO and the next generation experiment CUPID [62].

5.2.1 Design and assembly improvements

Since we had to produce new copper and PTFE pieces for this bigger assembly, we worked on an improvement of the overall structure and the mounting procedure. We have reduced the copper holder mass to 100 g by removing unnecessary matter and we developed a tool to make the nylon wire installation easier. Moreover, instead of having 4 PTFE pieces with one at each corner of the crystal, we moved to only three with two on the bottom corners and one on the top at the center of the crystal edge. In addition to reducing the amount of passive material, it mitigates the potential cross-talks between the Ge wafers and the LMOs while it is still enough to fix them firmly. Regarding the nylon wire, we chose a 0.45 mm thickness one available commercially coated with fluorocarbon that can handle 16 kg at maximum (Caperlan® Resist).

Figure 5.7 shows a photo of the various elements used during the assembly. In particular, one can see the mounting tool that allowed us to have an easier and more reproducible way to place the nylon wires. It is composed of an aluminum structure in a U shape on which two pulleys with a black plastic screw in the middle are present at each lateral external face. The procedure is the following. First, the Cu holder is fixed at the center of the tool thanks to a screw underneath. The PTFE pieces are placed inside; the two LMO crystals are placed at their positions (marked by Teflon squares on the tool that are seeable in Figure 5.7); Ge wafers are slipped into the PTFE piece slots. The components are held together afterward by screwing the two black screws against the LMO crystals to start to apply pressure. To fix the first crystal, a nylon wire is first passed between its surface and the black screw. Both wire ends are going in a separate hole on the opposite lateral surface of the tool, each being in front of a small pulley. A weight of 4 kg is suspended at each end, taking care that the wire rests on the two pulleys (this step is shown in Figure 5.7). The pulleys permit a smooth change of direction to not damage the wire and convert the vertical force applied by the weights into a horizontal one. Since a mass of 4 kg is suspended at both ends of the nylon wire, a total mass of 8 kg is homogeneously put on the LMO crystal, pushing it against the

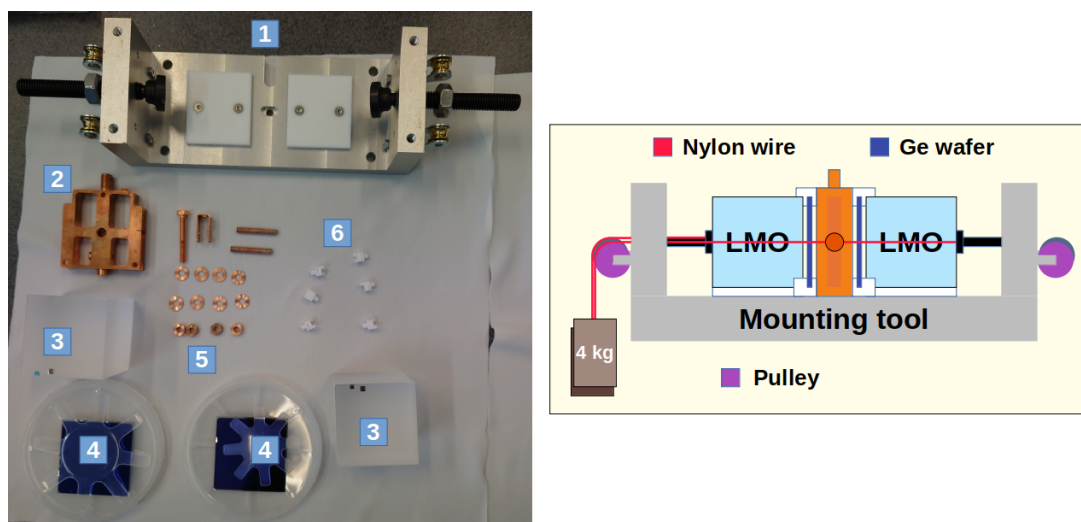


Figure 5.7 – *left*: All the elements used for the assembly. -1-: the mounting tool. -2-: the Cu holder. -3-: LMO crystals. -4-: Ge wafers. -5-: Cu pieces. -6-: PTFE pieces. *right*: Drawing representing the assembly procedure where the LMO on the right is the one being fixed. A detailed description can be found in the text.

Cu holder and clamping by the same occasion its light detector. Finally, the wire is fixed on each side of the copper holder, like for the small assembly, and the extra length is cut. This procedure is repeated symmetrically for the second crystal without any differences. This new method ensures that the two sides of the assembly are firmly fixed by their respective nylon wire and that the force applied by them is identical.

We first tested the procedure with aluminum dummy detectors and once again put this mock-up assembly in a liquid nitrogen bath to verify its behavior at cryogenic temperatures. No problem was seen, and we moved to assemble real detectors for bolometric measurements.

5.2.2 Cryogenic tests

To validate the $45 \times 45 \times 45 \text{ mm}^3$ assembly, we decided to use an already tested crystal, called LMO56b, coming from the CROSS crystal batch. This bolometer had already glued on its surface a 41B $3 \times 3 \times 1 \text{ mm}^3$ NTD using a veil of UV glue (a special glue, which dries once exposed to UV light, tested in the framework of CROSS) and two Si heaters. It was tested in the past for the CROSS experiment in an assembly using a more standard copper structure to hold the detectors, referred as CROSS assembly. Moreover, we also took the same $45 \times 45 \times 0.3 \text{ mm}^3$ Ge light detector that was used in this previous measurement called LD56b. It had a SiO coating on both its surfaces to enhance its light collection and a 1/3 41B NTD Ge glued on it. Hence, these two detectors were our reference to verify the big nylon assembly performance.

At that time, we received a set of six radiopure natural LMO crystals ordered by BINGO that will be used for the MINI-BINGO demonstrator. We took benefit of this measurement to test one, named LMO21-2, and glued on it a 41B $3 \times 3 \times 1 \text{ mm}^3$ NTD with 9 Araldite® Rapid spots and one heater following the usual procedure. We coupled to it a Ge wafer, named LD21-2 on which we also glued a 1/3 41B NTD Ge.

We assembled these 4 detectors with the above protocol and obtained the assembly

shown in Figure 5.8. Electrical contacts were made precisely in the same way that was already explained for the first prototype. Before mounting it to the cryostat, we attached to it another more conventional detector assembly - the one in which LMO56b was already measured - composed of other new crystals from BINGO batch to measure them in a more standard way. The whole structure was finally fixed to the floating plate of Ulysse cryostat, as also shown in Figure 5.8.

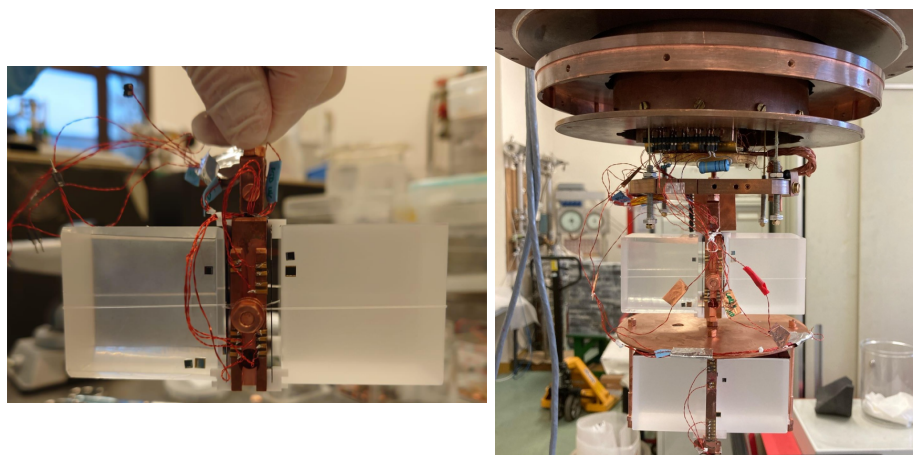


Figure 5.8 – *left*: The $45 \times 45 \times 45 \text{ mm}^3$ nylon assembly. LMO56b is the crystal on the left, while LMO21-2 is on the right. *right*: The assembly inside the cryostat. Under it, another more standard detector assembly is attached. A copper plate separates the two assemblies.

We cooled down the cryostat to several sub-20 mK temperatures and the results presented were obtained at 15 mK. As usual, the data were acquired with the same electronics as the small nylon assembly, with a sampling frequency of 5 kHz and a Bessel cut-off frequency of 675 Hz. Data analysis was also done in the same way.

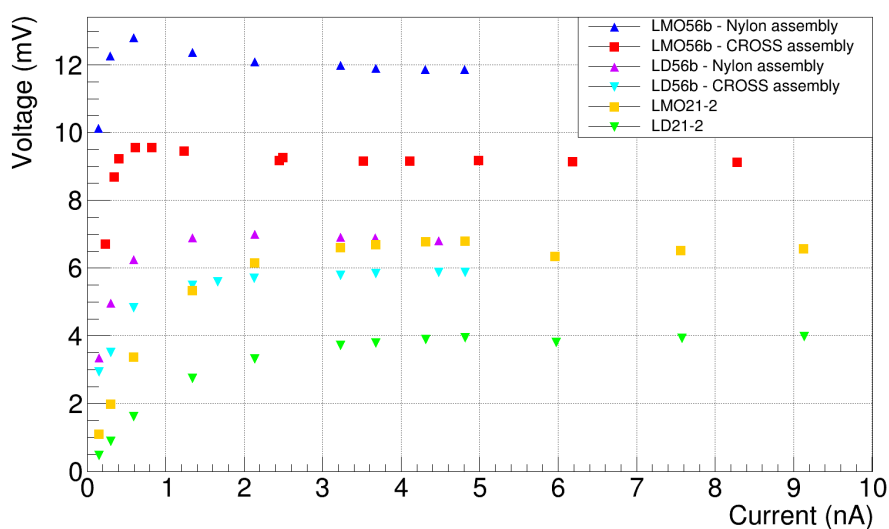


Figure 5.9 – Load curves at 15 mK for each detector present in the nylon assembly.

For each detector, we performed the load curves (Figure 5.9). It is interesting to compare the behavior of the two reference detectors, LMO56b and LD56b, in the two different assemblies. Both of their NTDs show a higher voltage (i.e, a higher resistance) in the nylon assembly than in the CROSS assembly for the same bias current value. In principle, it means that the detectors are colder. Since the load curves were measured at the same cryostat temperature, it seems that the two detectors were better coupled to the heat bath in the nylon assembly. The working points where the detectors showed the best performance are presented in Table 5.4.

| Detector | Current (nA) | V_{bol} (mV) | R_{NTD} ($M\Omega$) | Sensitivity (nV/keV) | $FWHM_{bsl}$ (keV) | τ_r (ms) | τ_d (ms) |
|----------------|--------------|----------------|-------------------------|----------------------|--------------------|---------------|---------------|
| LMO56b - Nylon | 0.32 | 12 | 41.2 | 66 | 13 | 19.5 | 56 |
| LMO56b - CROSS | 0.24 | 9.2 | 37.3 | 82 | 29 | 17.5 | 55 |
| LMO21-2 | 0.60 | 5.0 | 8.3 | 57.5 | 4.9 | 16 | 47 |
| LD56b | 4.5 | 6.8 | 1.5 | 563.8 | 0.39 | 3.2 | 11.5 |
| LD21-2 | 3.7 | 6.4 | 1.7 | 639.2 | 0.35 | 1.4 | 6 |

Table 5.4 – Best performance obtained by the detectors. The values for LMO56b in the CROSS assembly are obtained at a similar NTD resistance than in the nylon assembly. The same comparison for LD56b is not shown since such data do not exist.

Given the size of crystals in an above-ground measurement, we cannot put a Th source outside the cryostat for calibration. Since the rate of events would be too large, it would induce too many pile-up events due to the rather slow response of the bolometers and make the analysis too complicated. Hence, the energy calibration of crystals was done using the few γ lines from natural radioactivity visible in their spectrum (Figure 5.10). If no such peaks were present, we used the ${}^6\text{Li}(n,t)\alpha$ peak to realize a rough calibration, taking into account the α quenching factor. For the light detectors, we calibrated them using the muon bump, i.e. the distribution of energy deposition by muons inside the light detector. It can be fitted with a Landau function and, according to simulations, it has a maximum of around 260 keV for a 0.3 mm thickness vertical Ge wafer.

Results presented in Table 5.4 show a comparison of LMO56b performance in both assemblies. Although there are some slight differences, it is clear that no degradation of the bolometric performance was observed when moving to the nylon assembly. The mean pulse is a bit slower than in the CROSS assembly: this effect can be due to the higher resistance of the NTD. The sensitivity obtained for the second crystal, LMO21-2, is reasonably good and it shows a good baseline FWHM. One can say that it behaves as an average bolometer of this size. In addition, both light detectors have obtained similar performance and allow rather good particle discrimination (Figure 5.11). For example, above 3 MeV we obtained a discrimination power of 2.7 for LMO21.2 and LD21-2. This value could even be improved in the future since the noise conditions of this measurement were not ideal. Furthermore, we measured a relatively low light yield of around 0.15 keV/MeV for γ since the light collection was not the best due to the openness of the structure. There could be, in addition, some residual cross-talks between the heat and light channels through PTFE pieces that affect the energy measured in the latter. This effect was, in any case, not as strong as in the small assembly since we didn't observe a mean negative value for α 's light yield. The larger size of the detectors and the 3 PTFE pieces instead of 4 can explain why.

Finally, we can look at the noise power spectra (NPS), especially in the case of LMO56b,

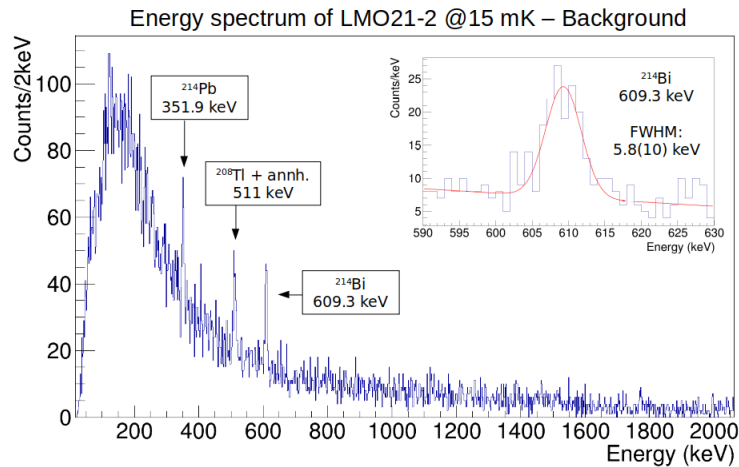


Figure 5.10 – Energy spectrum of LMO21-2 obtained at 15mK after a data-quality cut during a 9.25h background measurement where the crystal performed the best (See Table 5.4).

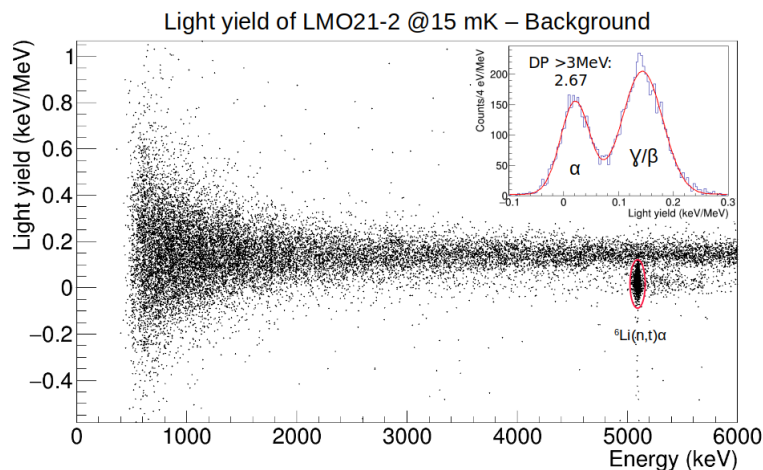


Figure 5.11 – Light yield of LMO21-2 measured by LD21-2 during a background measurement at 15 mK where the light detector obtained its best performance (See Table 5.4).

for which we can compare with the one obtained in the CROSS assembly. They are presented in Figure 5.12. We can see that the crystal has obtained an equivalent NPS in both assemblies, once again showing that the nylon assembly is not introducing additional noise or vibrations to the crystal in the signal bandwidth. In general, LMO56b has shown a relatively high noise level compared to LMO21-2 for no apparent reason. We believe that it is unrelated to the assembly since both crystals were mounted in the same way and it was a feature already present in the CROSS assembly.

In conclusion, this first test of a $45 \times 45 \times 45$ mm³ nylon assembly was successful. It demonstrated the suitability of the assembly for such a size of crystals and light detectors. They have obtained good bolometric performance, similar to what was obtained in the past in a more standard assembly for LMO56b. We were confident to move on to another step, getting closer to the MINI-BINGO demonstrator and validating this concept: the underground test of two nylon assembly modules.

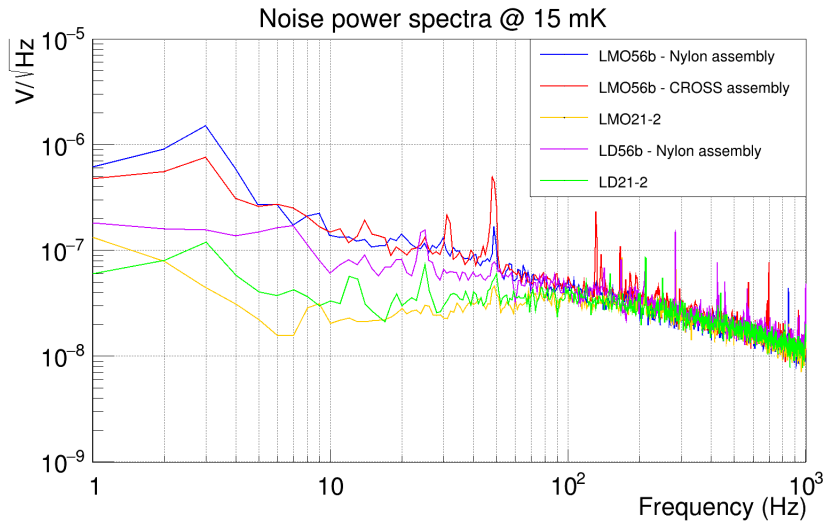


Figure 5.12 – Noise power spectrum of each detector at 15 mK.

5.3 Underground measurement with two modules

With the proof-of-concept assembly being validated by the previous step, we decided to continue with a new measurement, with two modules stacked in a small tower. Some further improvements were made to the assembly design, with an even lighter copper holder. The mounting tool was also ameliorated to eliminate the weights and simplify the assembly procedure. This small BINGO tower has been measured in the underground laboratory of Canfranc (LSC). This laboratory is situated 2450 m.w.e underground and allows a good muon flux reduction [158] for low background measurements.

5.3.1 New mounting procedure and tower assembly

For this test, new holders were produced with a further reduction of the copper mass (from 100 g to 78.5 g) by removing useless parts. The stacking into a tower was also foreseen by adding a hole at the top of the holder. A copper rod can be inserted inside the modules to make a "skewer." We also changed the way nylon wires are attached: instead of a vertical screw with nuts and washers on it between which the nylon wires were crushed one by one, we now use a horizontal one that allows, once screwed, to fix one end of each wire at the same time in between washers (Figure 5.13). It is more convenient since it requires fewer tools (no additional nuts to tight) and effort. This method became possible because we also modified the mounting tool. The use of weights to apply the force on the nylon wires was not optimum since it required having the mounting tool at the edge of a table which is potentially risky for the detectors. To get rid of them, we added a new part at both extremities of the aluminum structure. It contains a metallic screw on its two lateral sides with a hole in its body aligned with the nylon wire path in which we can pass it and make a node to block it inside (Figure 5.13). Once both ends are fixed in their respective screw, we can screw the latters to roll up the wire around them, putting it in tension. We use two torque screwdrivers tuned to apply a 4 kg force on each side of the wire equivalently to the previous method with weights. When the desired force is applied, we can fix the metallic screws in their position using a nut, keeping the proper tension on the wire. We can repeat this procedure on the other side of the mounting tool to attach the second crystal with another nylon wire. Finally,

we can fix both nylon wires simultaneously by screwing the horizontal copper screw on both sides of the holder, crushing the wires between washers.

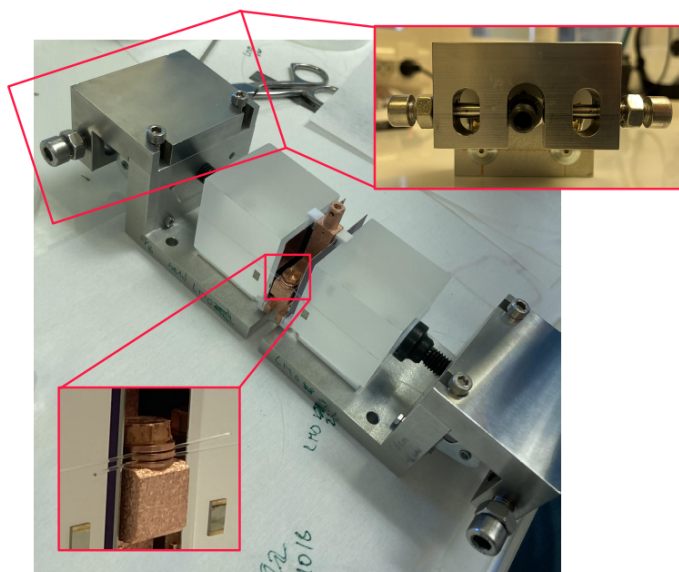


Figure 5.13 – One module in the new assembly tool.

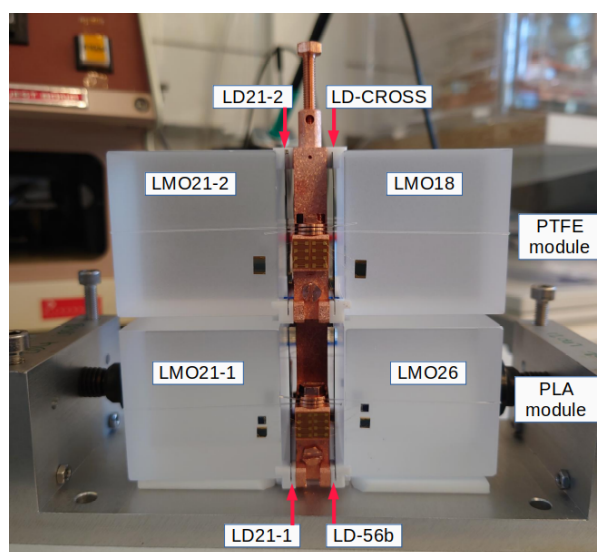


Figure 5.14 – The nylon assembly first tower composed of two modules. The detectors are labeled. The top module was assembled using PTFE pieces while we used PLA for the bottom one.

We assembled two modules using this procedure in the IJCLab clean room with special care given to materials cleaning and manipulation to avoid surface contaminations. For both, the same nylon wire as in the previous measurement was used. One module was assembled with the usual PTFE pieces while we tried for the second one to use 3D printed PLA pieces since it is simpler to produce them and this could be an interesting alternative. Each module was containing two $45 \times 45 \times 45 \text{ mm}^3$ and two $45 \times 45 \times 0.3 \text{ mm}^3$ SiO coated Ge light detectors. We decided to remeasure LMO21-2 from the previous measurement and its light detector

LD21-2 keeping the same NTDs glued on them. We assembled also two other crystals from the BINGO batch, LMO21-1 and LMO18, on which we glued with 9 spots of Araldite® Rapid a $3 \times 3 \times 1 \text{ mm}^3$ 41B NTD Ge. The former was facing LD21-1 while we used for the latter a light detector already measured in an underground CROSS measurement that we will call here LD-CROSS. We glued on both of them a $1/3$ 41B NTD Ge with 3 Araldite® Rapid spots of glue. The last crystal, LMO26, is also from the BINGO batch but had never been tested before. For this one, a 41B Ge NTD ($3 \times 3 \times 1 \text{ mm}^3$) was also glued with 9 spots. We used to measure its scintillation light LD56b which was already measured in the above-ground test. In addition, we glued a spare $3 \times 5 \times 1 \text{ mm}^3$ 605b Ge NTD on each crystal, using 18 spots of Araldite® Rapid and a Si heater. Finally, after fixing the two modules with a copper rod, we ended up with the configuration shown in Figure 5.14. Bondings of the NTDs and heaters were done with $25 \mu\text{m}$ diameter Au wires to Au pads on Kapton® foil glued on the holder from where we soldered twisted Cu wires to prepare for connexion to the cryostat.

5.3.2 Tower installation and operations in LSC

The tower was transported to LSC and installed in the CROSS Cryogenic Underground facility (C2U) [159]. It is a pulse-tube (PT) dilution cryostat equipped with the Ultra-Quiet Technology™ [160] that allows to mitigate the transmission of vibrations induced by the PT to the structure. Detectors are also suspended with a spring to the mixing chamber to reduce even further these vibrations.

In addition to the good muon flux reduction offered by the underground location of the cryostat, the detector volume is shielded from external γ -rays on the top by an internal 13 cm thick disk made of radiopure lead and copper layers and on the sides and bottom by an external radiopure lead shield with a 25 cm thickness.

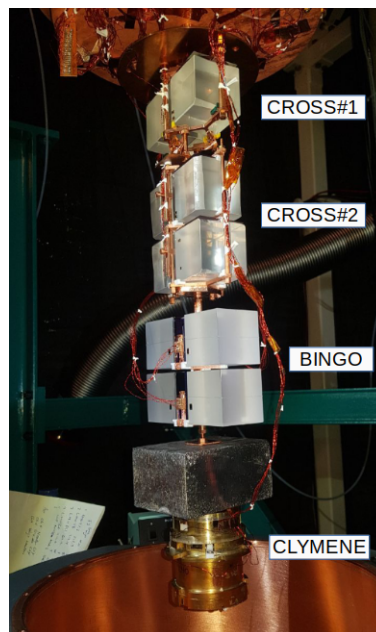


Figure 5.15 – Photo of the configuration inside the C2U during this measurement. The lead brick between the BINGO and CLYMENE assemblies was put to reach a total mass compatible with the spring elongation and vibration cut-off frequency.

To benefit from the whole cryostat detector volume, the BINGO tower was attached to three other detector assemblies: two for the CROSS experiment R&D on the top and one belonging to the CLYMENE project [161] on the bottom. A lead brick was also added to the configuration to reach the total mass for which the spring was optimized. The full setup inside attached to the cryostat can be seen in Figure 5.15.

The detector readout was performed using a low-noise room-temperature DC front-end electronics and the data was acquired with a 2 kHz sampling frequency and a 300 Hz low pass Bessel filter cut-off frequency. A wave-function generator was used during the run to inject pulses through the heaters inside the crystals for detector optimization and data stabilization. The same generator also served to send photon-burst with a room-temperature LED to shine the whole detector cavity through optical fibers going inside. Equivalently to pulses in heaters for crystals, this was used to optimize light detector response.

A total of 1862.2 hours of data were acquired at 16 mK among which 974h were dedicated to a ^{232}Th calibration using, as a source, a thoriated tungsten wire inserted inside the lead shield and 732 h to background measurement. The rest was mainly for neutron calibration and other studies which are not covered in this thesis.

5.3.3 Th calibration

The results of the Th calibration that will be presented here were realized with the detectors at the working points where they obtained the best performance. They are summarized in Table 5.5. The Th source is also helpful to calibrate light detectors: We observed in their energy spectrum a peak due to the γ s interacting with the Mo inside the crystals, producing x-rays at around 17.5 keV that are fully absorbed. It allowed us to do a linear calibration after determining the position of this peak with a Gaussian function and a linear background contribution fit.

| Detector | Current (nA) | R_{NTD} (M Ω) | Sensitivity (nV/keV) | FWHM _{bst} (keV) | τ_r (ms) | τ_d (ms) |
|----------|--------------|-------------------------|----------------------|---------------------------|---------------|---------------|
| LMO21-2 | 0.8 | 13.4 | 85 | 1.9 | 18 | 49 |
| LMO18 | 1 | 11.2 | 31 | 2.9 | 29 | 101 |
| LMO21-1* | 1 | 9.3 | 44 | 2.5 | 35 | 123 |
| LMO26* | 1 | 8.6 | 57 | 5.9 | 32 | 90 |
| LD21-2 | 1 | 8.8 | 1658 | 0.17 | 5 | 17 |
| LD-CROSS | 1 | 5.8 | 985 | 0.25 | 4 | 18 |
| LD21-1* | 1 | 9.2 | 1322 | 0.26 | 4 | 13 |
| LD56b* | 1 | 8.7 | 1788 | 0.21 | 8 | 23 |

Table 5.5 – Working points of the detectors during Th calibration. The detectors inside the PLA assembly are labeled with a star.

From Table 5.5, we can see that all the detectors behaved reasonably well. In particular, LMO21-2 appeared to be extremely well-performing with a high sensitivity and a baseline FWHM inferior at 2 keV. Its pulses were also the fastest among all the crystals for an unknown reason. On the other hand, LMO26 showed a higher noise than the other detectors but still under 6 keV. Regarding the light detectors, all of them exhibited performance convenient for α discrimination. We know for example that the CUPID experiment objective for light detector baseline FWHM is around 235 eV, and in our case two wafers - LD21-2 and LD56b - reached a lower value. However, their pulse constants were rather slow if we compare

with what was obtained above-ground. In general, we did not observe any major difference between the PTFE and PLA assemblies.

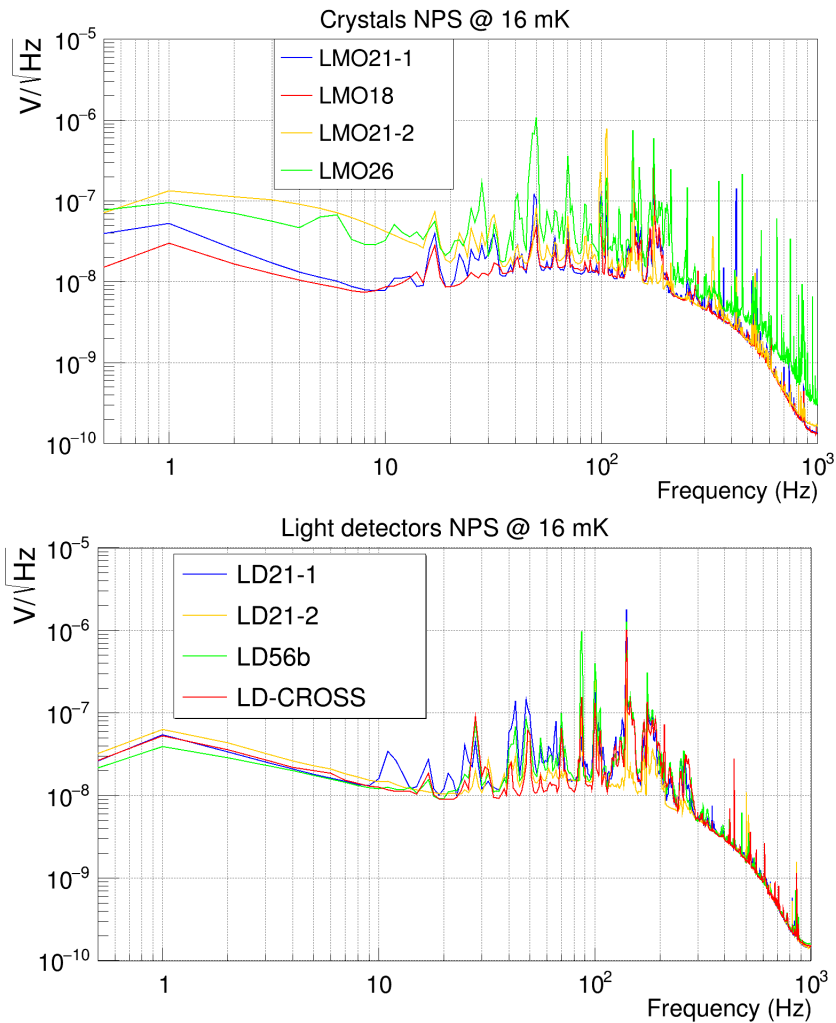


Figure 5.16 – *top*: Crystal noise power spectra obtained at 16 mK. *bottom*: Light detector noise power spectra obtained at 16 mK.

The noise power spectra acquired during this measurement are presented in Figure 5.16. All detectors show a high amount of peaks between 10 and 200 Hz that are mainly harmonics of the PT frequency at 1.4 Hz. Therefore, it seems that the spring-decoupling was not optimal, although we thought the lead weight would help. Their amplitudes are the highest for LMO26, which explains its higher noise level. Moreover, we see a peak at 50 Hz and its harmonics at 100 Hz and above due to the external electric configuration. This contribution is also present at room temperature and is not related to our detector setup. The noise conditions in this run were then not optimal, however, it did not prevent us to reach good bolometric performance, which is promising since by working on them we could even get better results.

The energy spectrum obtained with about 90h Th calibration measurement can be seen in Figure 5.17. In this plot, the energy spectra of the four LMO crystals have been merged into one. Using it, we determined the energy resolution at 2615 keV by fitting the ^{208}Tl peak. We found a value of 6.4 keV FWHM which is really good for LMO crystals of this size

and comparable to the recent measurement of LMO crystals in a more standard CUPID-like assembly [162]. The DE (Double Escape) and SE (Single Escape) peaks are due to the 2615 keV γ interaction in the crystal: if it interacts by creating an electron/positron pair, the latter can recombine and emits at its turn two γ s at 511 keV. If the two escape the crystal (DE), this gives a signal at 2615-1022 keV while if only one escapes and the other is captured (SE), it gives a signal at 2615-511 keV.

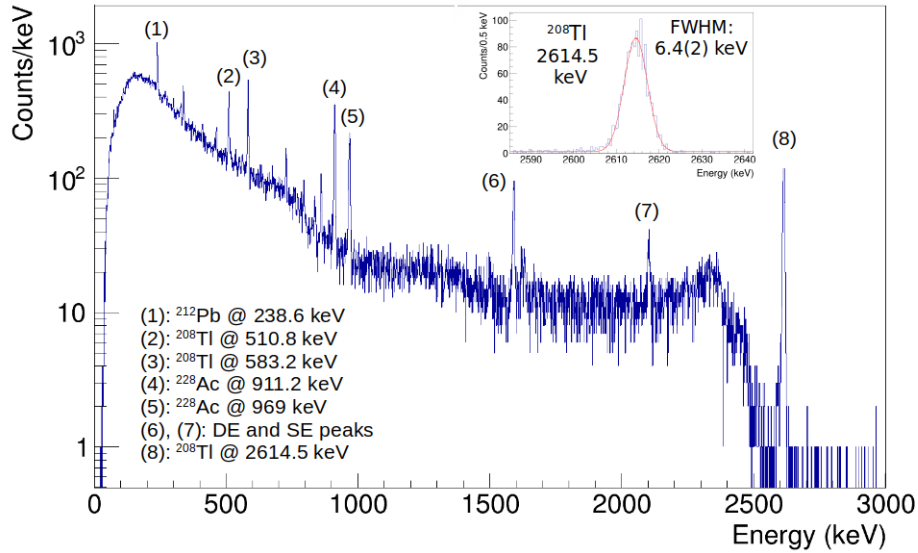


Figure 5.17 – Combined energy spectra of the four LMO crystals during an almost 90h Th calibration. The energy resolution at 2.615 MeV has been determined by fitting the peak with a gaussian and a linear background contribution. Other peaks coming from the ^{232}Th decay chain are shown.

We can take benefit of this calibration to evaluate the α rejection power. Thanks to the clear γ lines, we can easily determine the light yield and the discrimination power. The results obtained are shown in Table 5.6 and the light yield plots in Figure 5.18. We found values between 0.22 and 0.24 keV/MeV for the light yield which is compatible with what has been obtained with similar size and shape LDs in the past in CUPID module test [162] or in the 12 LMO tower in CROSS cryostat [163]. The discrimination power is calculated for the events with an energy superior at 2.5 MeV. We see that two of them meet the requirements to reach an α rejection higher than 99.9% ($\text{DP} > \sim 3.1$ [152]). The two others have a DP inferior at 3 probably because the LDs they were facing had the highest baseline FWHM. In any case, in the final BINGO configuration, NTL light detectors will ensure to reach the DP objective.

| Detector | Light yield (keV/MeV) | Discrimination power (σ) |
|----------|-----------------------|-----------------------------------|
| LMO18 | 0.22 | 2.64 |
| LMO21-2 | 0.24 | 5.05 |
| LMO26 | 0.24 | 3.86 |
| LMO21-1 | 0.22 | 2.83 |

Table 5.6 – Light yields and discrimination powers measured at 16 mK during the 90h Th calibration.

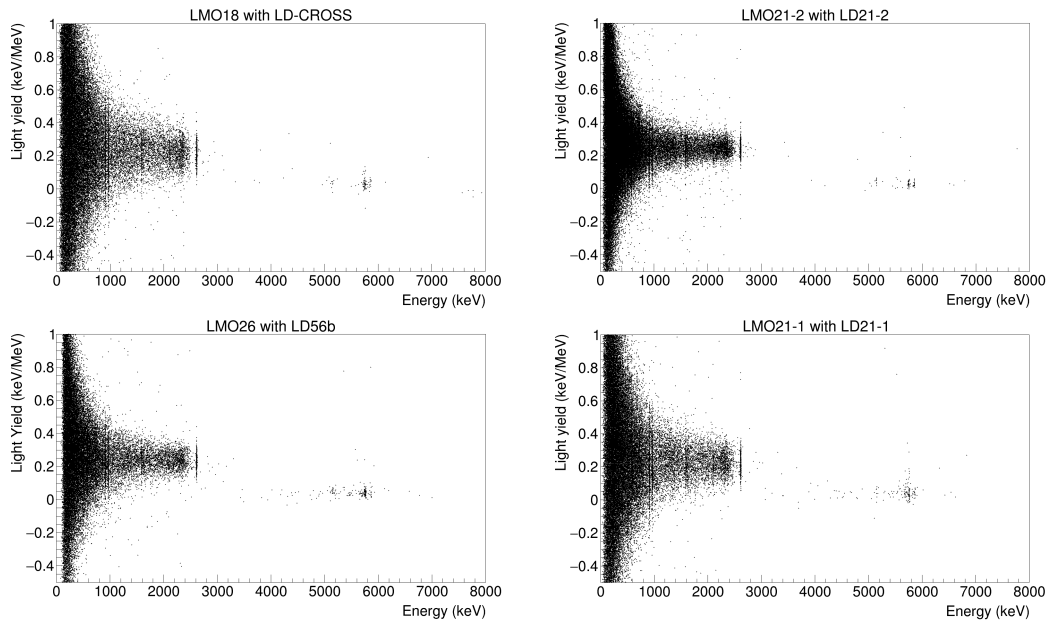


Figure 5.18 – Coincidences heat and light obtained for each LMO with its light detector during the Th calibration.

5.3.4 Background measurements

Among all the background data, we selected the best 300 hours with the same working points as in the Th calibration in order to estimate roughly the ^{210}Po contamination of the BINGO crystals. Considering only the events with a light yield lower than 0.15 keV/MeV, we have isolated α events above 3 MeV. The spectrum obtained between 4 MeV and 6 MeV, once the events of the four LMOs merged, is shown in Figure 5.19. It is recalibrated to take into account the α energy quenching.

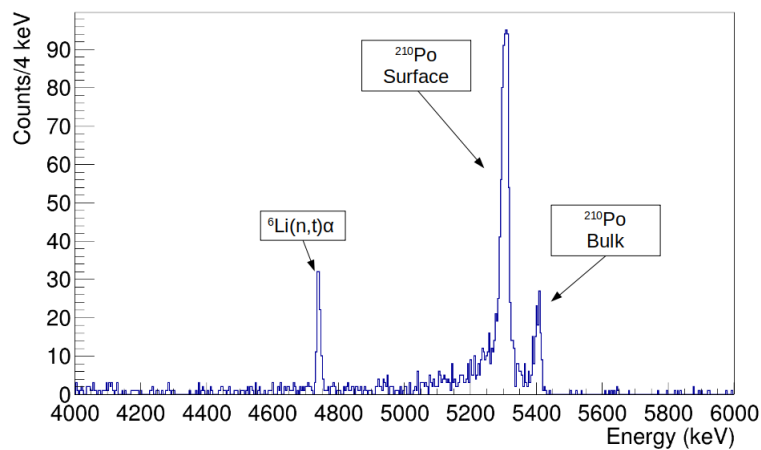


Figure 5.19 – α region obtained during a 300h background measurement for the four LMO together.

Three peaks are clearly visible. The first one corresponds to the neutron capture of ^6Li while the two others are what we call the ^{210}Po doublet. They correspond to the α decay

of ^{210}Po to ^{206}Pb which has a Q-value at 5407 keV. If this process happens in the bulk of the crystal, we measure the total energy which gives the peak that we call "Bulk". However, if it happens in the surrounding materials, we will not measure the nuclear recoil but only the emitted α energy at 5.3 MeV, giving the second peak called "Surface". The latter has a tail since the α can lose some of its energy in its original material before interacting in the crystal. Thus to estimate the internal contamination of the crystals, we are interested in the "Bulk" peak.

We just counted the number of events in an interval of ± 30 keV ($\sim \pm 3\sigma$) around the Q-value of the peak and normalized this value by the duration of the measurement and by the total mass of detectors (assuming 270 g per crystal). We find for the ^{210}Po a contamination of around $128(10)$ $\mu\text{Bq/kg}$. This result is coherent with what is usually measured for LMO crystals [155]. However, the goal was not to realize a precise contamination measurement of the crystals so we used a simple method just to have a rough estimation. A dedicated study could be done, especially because here we have considered a 100% selection efficiency after the analysis cut which is in principle not true. Although the selection efficiency is usually high ($>80\%$), the result may vary by a few percent depending on it. However, even in the worst case, the ^{210}Po contamination should not be higher than 186 $\mu\text{Bq/kg}$, confirming the high radiopurity of these crystals.

5.3.5 Conclusion

The underground measurement of the first small BINGO tower has been a success. We have shown that the crystals in the nylon assembly were performing in a similar way as when inside a more standard one. Stacking the module in a tower seems not to change this and the four crystals and four light detectors have obtained satisfying results. We tested also two types of soft pieces between the crystals and the Cu holder. We did not observe any major difference between PTFE and PLA which is promising since PLA is less expensive and easier to produce.

Through the different steps presented in this Chapter, we have proved that the nylon assembly is a suitable way to operate scintillating bolometers. It is promising for the next-generation $0\nu 2\beta$ bolometric experiments since it minimizes the surface of passive materials around the detectors. In the last configuration, we have a reduction of more than 2 orders of magnitude compared to the CUORE configuration. With the use of the LD as an additional active shield, it should be enough to mitigate the surface β contribution to the background to a level lower than 10^{-5} cky. In addition, we have developed a robust assembly procedure that comes with a cleverly designed mounting tool. Each module requires less than ten minutes and only two persons to be assembled which is appreciable for a ton-scale experiment.

In the framework of MINI-BINGO, a slightly bigger module containing two $50 \times 50 \times 50$ mm^3 TeO_2 crystals have to be tested to confirm also its performance, although we do not expect any difference with the LMO module. Moreover, the next planned measurements will include NTL light detectors to validate their operation in the nylon assembly and check the α rejection thanks to the detection of the Cerenkov light in the case of TeO_2 [144].

Chapter 6

The passive and active vetoing

Since BINGO requires an extremely low background environment, several layers of passive shields will be implemented around and inside the cryostat to mitigate external background events. In addition, as explained in Chapter 4, an active cryogenic veto will be deployed for the first time as close as possible to the area of detectors to reject the remaining γ events. This Chapter is divided into two parts. The first one will describe the different tests realized for the preparation of the BINGO cryogenic veto, from the material choice to the first prototype measurement. The second one will present the bolometric measurement of a lead piece that we made to evaluate its radiopurity since the same lead will be used for the internal shield of the MINI-BINGO cryostat.

6.1 First part: the BINGO cryogenic active veto

The BINGO cryogenic veto will be composed of an array of scintillators for which the scintillation light emitted after a particle interaction within it will be read thanks to NTL Ge light detectors. This innovation will allow rejecting efficiently the events coming from outside by looking at the coincidences with the crystals, keeping this source of background below 10^{-5} ckky. However, its implementation is challenging for several reasons since, for example, a clever structure allowing a 4π covering should be designed, which represents, once the scintillators are mounted inside, an additional mass that needs to be cooled down. MINI-BINGO will prove that this veto is feasible and that it reaches the performance needed such as an energy threshold of 50 keV. The purpose of the work done in this thesis was to open the path for the demonstrator, from a first comparison of the two principal scintillator candidate properties to the cryogenic test of the first veto prototype.

6.1.1 The scintillator choice

As already mentioned in Chapter 4, the material of the veto has to satisfy several requirements: It must be really dense to absorb as many γ 's as possible; it must have a high radiopurity to not induce background or dead time; and finally, it must have a high scintillation yield so we can detect an energy deposition as low as 50 keV within it with the NTL light detectors. Two scintillator candidates considered at the beginning were ZnWO_4 (ZWO) and $\text{Bi}_4\text{Ge}_3\text{O}_{12}$ (BGO) crystals.

ZWO and BGO properties

ZWO is a scintillator crystal with a high density of 7.81 g/cm^3 ensuring a good γ absorption with a reasonable thickness. It is a promising material for Dark Matter searches due to its anisotropic light output features [164] and its study has been mainly done in this framework. Scintillation light yield values between 5100 and 9500 photons/MeV are reported in the literature [165]. It makes it an excellent scintillator which is appreciable for the BINGO veto in order to reach the lowest possible energy threshold. Moreover, since the development of the material was done for low background experiments, it is available in very radiopure versions with for example an upper limit on ^{228}Th contamination as low as $0.17 \text{ }\mu\text{Bq/kg}$ [166] and it is actually one of the less radioactive scintillating materials. However, such radiopure ZWO crystals have never been grown in the large sizes required for the MINI-BINGO demonstrator and additional R&D might be required to do so. In addition, the procurement of this crystal became difficult due to the conflict between Ukraine and Russia, the only known producers being in these two countries. It was then necessary to envisage an alternative candidate for the MINI-BINGO veto.

A good alternative to ZWO is BGO. It is a scintillator material that has also excellent properties to be used as a veto for BINGO: Its density of 7.13 g/cm^3 and high Z allow a high gamma stopping power. It is also a good scintillator with measured light yield values between 2700 and 11000 photons/MeV [165]. The main advantage of BGO is that, since it is widely used for different applications, various producers exist and the sizes and shapes we need are commercially available. However, it is known BGO crystals have a ^{207}Bi contamination coming from the Bi raw material used to grow the crystal. The level of this contamination depends most likely on the content of lead in the ore from which it was extracted since ^{207}Bi is produced by the interaction of cosmic protons on ^{206}Pb ($^{206}\text{Pb} + \text{p} \rightarrow ^{207}\text{Bi}$) [167]. In literature, contamination values between 7 and 4000 mBq/kg can be found [168], motivating a careful choice of the BGO. Indeed, the ^{207}Bi undergoes an electron capture to transform into ^{207}Pb . The γ peaks that this process can produce (mainly at 570 keV, 1063 keV and 1770 keV) are not so harmful since their energy is below our ROI. However, the rate of events this contamination can induce in our veto could be a problem: if it is too high, the veto becomes less efficient as it would induce too many accidental coincidence with the detectors. For MINI-BINGO and its total BGO mass of around 150 kg, if we consider a typical event rejection time window of 5 ms in the bolometers after seeing an event inside the veto, we can expect that a contamination $>600 \text{ mBq/kg}$ would lead to an overall deadtime $>45\%$. This is why it is crucial to monitor this parameter if we want to use BGO, and we estimate that the maximum acceptable contamination would be $<100 \text{ mBq/kg}$. Finally, BGO, tested in the past in a bolometric measurement, appeared really slow to cool down [169]. Although in our case it will not be used as a bolometer, it could have an effect on the cooling down of the nearby materials, especially the other crystals and light detectors.

To check the features described in this section, we decided to realize a cryogenic test of one sample of both veto candidates. It allowed us to have a first comparison of their performance at cryogenic temperatures, and in the case of the BGO, see how its slow cooling down was affecting its environment.

Cryogenic tests for comparison

For this test, we received in 2021 one cylindrical ZWO crystal and one cylindrical BGO ($\varnothing 30 \times 60 \text{ mm}^2$), both polished and produced at NIIC in Russia before the beginning of the conflict in Ukraine. We designed a copper holder to host such a crystal shape. It is an open

cylinder with a smaller aperture on the bottom ($\varnothing 2.5$ cm instead of 3.3 cm on the top) and the inside covered with a VikuitiTM Enhanced Specular Reflector Film. The BGO or ZWO is placed inside, resting on 3 L-shape small PTFE pieces while it is blocked by 3 other rectangular pieces on the top which apply pressure by tightening the screws, as visible on the left photo of Figure 6.1. The bottom of the holder has a slot in which a circular 4.4 cm diameter and 0.175 mm thickness Ge wafer can be mounted, clamped by 3 PTFE pieces. This part can be closed with a copper cap. On the top, the configuration is slightly different: another light detector of the same dimension can be mounted directly inside the top cap also with 3 PTFE pieces clamping it (center photo of Figure 6.1). In this way, once the assembly is fully closed, the crystal is facing two light detectors (right photo of Figure 6.1). Finally, it is possible to attach this structure to the floating plate of Ulysse cryostat for cryogenic measurements as it can be seen in Figure 5.2.

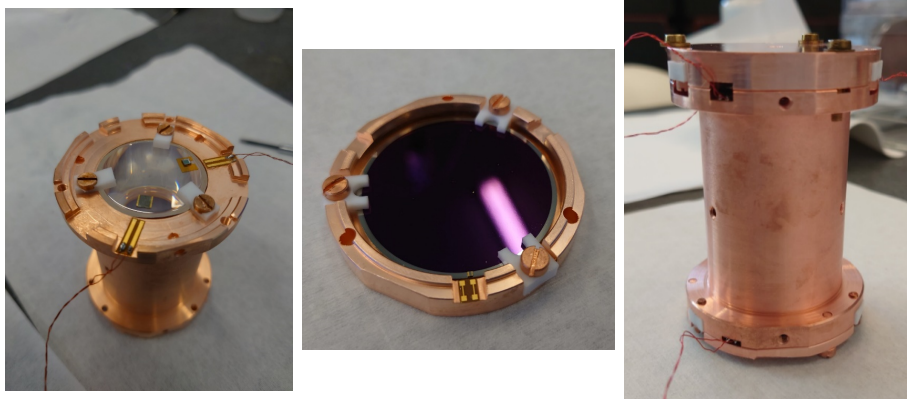


Figure 6.1 – *left*: The copper holder in which a cylindrical crystal is installed. *center*: The top cap in which a SiO-coated Ge light detector is mounted. *right*: The full assembly closed.

Both crystals were tested at 15 mK inside Ulysse cryostat in two different measurements. The first one performed was with the BGO crystal assembled inside the copper holder. We placed on the top a SiO-coated Ge wafer while a NbO-coated Ge wafer was installed on the bottom. The two light detectors had a different coating for a test of light collection out of the scope of this PhD thesis. Both of them had an NTD Ge glued on their surface for the temperature readout ($0.9 \times 0.9 \times 1$ mm³ for SiO LD and $3 \times 1 \times 1$ mm³ for NbO LD) with 3 epoxy glue spots. Moreover, to monitor the cooling down of the BGO crystal, we glued also on it a $4 \times 4 \times 1$ mm³ NTD with 9 glue spots and a Si heater with the usual procedure described in Chapter 3. The NTD bondings were done with $25 \mu\text{m}$ diameter gold wires and they were connected to the cryostat wiring with twisted copper cables after attaching the structure to the cryostat floating plate. Unfortunately, once at low temperature, we lost the contacts of the NbO-coated LD, ending up with only the SiO-coated LD to read the scintillation light.

After this measurement, we replaced the BGO with the ZWO crystal in the same assembly. We kept the light detectors exactly in the same configuration to have a fair comparison between the two scintillators. The contacts of the NbO were repaired to make the coating study. However, since in our case only the comparison between the scintillators matters and since we were able to study BGO performance only with the SiO-coated LD, the results presented here will only be the ones obtained with the latter even for the ZWO. We glued also on this crystal a $3 \times 3 \times 1$ mm³ NTD with 9 epoxy glue to monitor its cooling down and

potentially have a dual heat and light readout.

For the two measurements, the SiO LD was calibrated using the muon energy distribution maximum which is expected to be around 100 keV for a 0.175 mm wafer thickness. Moreover, during Th calibrations, it was possible to see in the light detector energy spectrum the peaks coming from γ interactions in the crystal thanks to the detected scintillation light. It allows also calibrating the BGO or ZWO and compiling the light yield. This feature is important, especially for the BGO crystal. Indeed, we confirmed that it is slow to cool down: it never reached the base temperature of the cryostat and its NTD never reached a resistance high enough to see any pulses and use the heat channel in coincidence with the light one to calculate the light yield. Right after the cooling down of the cryostat, the BGO NTD showed a resistance of 14 k Ω which increased to around 36 k Ω after one week of measurement. This last resistance value corresponds roughly to a temperature between 50 and 70 mK, well above the 15 mK of the cryostat. We did not observe such a slow cool down for the ZWO which had therefore the heat channel available. It is interesting to compare the behavior of the light detector in both runs: since we did not observe any major difference in the resistance of the SiO LD NTD at the same bias between the two measurements, it seems that the rather "hot" BGO was not affecting the temperature of the nearby materials. The results obtained and the performance of the SiO LD in both measurements are summarized in Table 6.1.

| Detector | Current (nA) | R_{NTD} (M Ω) | Sensitivity (μ V/keV) | FWHM _{bsl} (eV) | Light yield (keV/MeV) |
|---------------|--------------|-------------------------|----------------------------|--------------------------|-----------------------|
| SiO LD w/ BGO | 0.6 | 2.2 | 1.77 | 127 | 28.0 |
| SiO LD w/ ZWO | 0.6 | 1.7 | 1.73 | 145.5 | 13.6 |

Table 6.1 – Performance of the SiO LD in both measurements at 15 mK.

The energy spectrum of the light detector in both tests during a Th calibration is shown in Figure 6.2. The spectra were calibrated using the position of the muon bump for which the maximum is expected to be at 100 eV for that germanium thickness. We can also identify in the spectra the γ lines from the Th decay chain, labeled with dashed squares in Figure 6.2. They correspond to the scintillation light emitted when such an event interacts inside the crystal. By comparing their energy with the one at which they give a peak in the light detector spectrum, we can compute the crystal effective light yield presented in Table 6.1. The BGO showed a light yield almost more than two times better than the ZWO. This results seems in favor of the BGO but this difference could depend on the crystal quality (impurities can affect the scintillation yield). It might be possible to find ZWO crystals with higher light yields. We think however that the values obtained for both crystal would be already enough for the MINI-BINGO veto objectives.

On another topic, it seems that we see in the scintillation light spectrum of BGO a hint for a ^{207}Bi contamination: a tiny peak can be seen around 1634 keV, corresponding to the simultaneous detection of the γ at 569.7 and 1063.7 keV due to ^{207}Pb de-excitation. However, we just mention this as a "hint" since no other peak from this contamination can be clearly identified (the γ line at 570 keV, if present, is in any case hidden by the ^{208}Tl one as shown by the red square in Figure 6.2). This test didn't allow us to determine the amount of this contamination due to its too short duration and the too high rate of events even during background measurements. It affects a lot our selection efficiency since it induces pile-up events with an irregular pulse shape. To avoid this pile up effect, a contamination

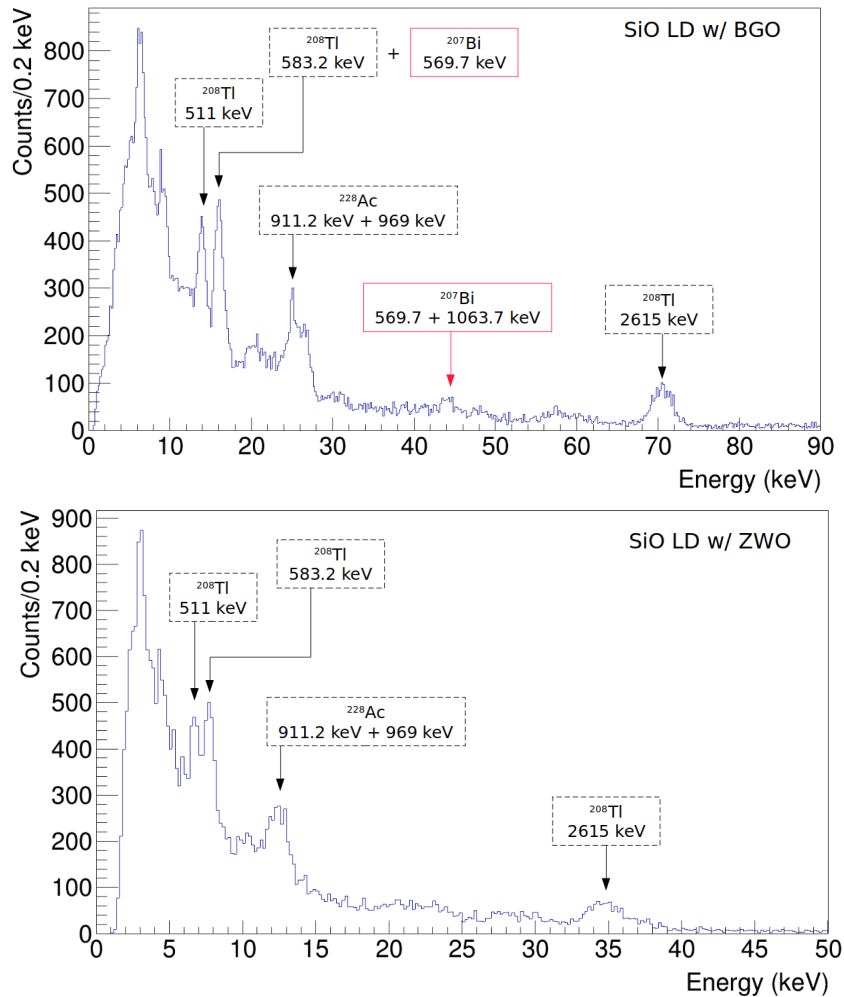


Figure 6.2 – Energy spectrum of the SiO light detector when it was facing a BGO crystal (top) and a ZWO one (bottom). The two spectra were acquired during an around 9h Th calibration at 15 mK. Further explanation can be found in the text.

measurement could be done in the future using smaller crystals and inside a setup with less background events, possibly underground.

We saw an interesting feature with BGO scintillation pulses in the SiO LD: they are slower than the pulses induced by direct ionization in the light detectors by muons for example. Therefore, by looking at the distribution of the pulse rise time as a function of the energy deposited in the BGO (calibrated using the light yield), we see two bands of events as shown in Figure 6.3. This characteristic is promising since it is a way, for example, to identify muon events and we used it in that case to calibrate the energy of the light detectors by isolating the muon distribution. We did not observe such a difference of pulse shape for the ZWO crystal.

Finally, this test allowed us to have a first comparison of the two candidates for the BINGO cryogenic veto. We have compared their behavior at low temperatures and have seen that both are showing a light yield high enough to reconstruct well the spectrum of events crossing them just by using the scintillation light detected by a Ge bolometric light detector.

Nevertheless, these first cryogenic measurements were not enough to definitely make a choice between the two candidates and deeper studies of for example the achievable energy threshold would have been required.

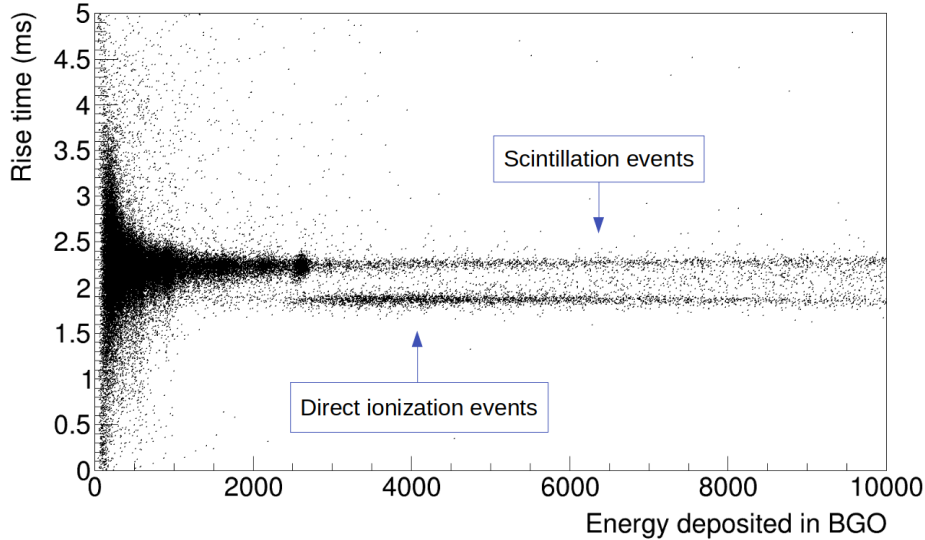


Figure 6.3 – Rise time distribution of the pulses in the SiO LD when it was facing the BGO crystal.

However, due to the conflict between Ukraine and Russia that started in February 2022, the procurement of ZWO became really complicated since the main producers were in these two countries. Moreover, as already mentioned, the growing of ZWO crystals in size that we require for the MINI-BINGO cryogenic veto has never been demonstrated. This has pushed the decision to continue the R&D for the MINI-BINGO demonstrator using only BGO crystals, exploring new producers and trying to find the most radiopure ones. However, ZWO crystals are not completely discarded since they are quite promising to be used as a low-radioactivity cryogenic active veto. Therefore, they could be envisaged in a longer time scale than MINI-BINGO one if the situation improves.

6.1.2 First veto prototype with two 12 cm high BGOs

In MINI-BINGO, the lateral BGO bars of the veto should have a height of 22.5 cm and be placed in a way to have a 2π coverage around the detector towers. In addition, a trapezoidal light detector should face each of them at the bottom or at the top to read the scintillation light (see Chapter 4). The idea is to have two circular copper structures (one at the top and one at the bottom) hosting the light detectors and keeping the BGOs well fixed in between. It has to be made of several modules that can be attached together in order to facilitate the assembly and bonding steps. We designed a first prototype of such a module to verify its mechanical robustness and we made a cryogenic test using it as an active veto for a small TeO_2 crystal to demonstrate the principle. The results are presented in this section.

Module assembly

Due to the limited experimental space in the Ulysse cryostat, we had to develop a smaller and simplified design that still includes the main features required to be tested. The module was made to host two trapezoidal BGO crystals next to each other, each facing two Ge light

detectors of the same dimension at the top and the bottom. The trapezoidal surface of BGOs considered is the same as the one foreseen for MINI-BINGO (3 cm for the small base and 5 cm for the large one) but we designed the assembly for 12 cm high crystals which is the maximum size that could be fitted inside the cryostat.

The module is composed of a top and a bottom copper piece which are a section of the full circle that will allow the 2π coverage around the towers. They contain three slots to place Teflon pieces that we can fix thanks to screws underneath. The PTFE pieces contain a slit allowing one to slide a light detector in it. Once done, BGOs can be placed on top of them, meaning that they share the same PTFE pieces with the LDs. The top copper piece with its mounted LDs can be put on the top of the BGOs and two copper bars are used on the sides to attach the top piece to the bottom one. In order to better fix the detectors, screws placed on the top Cu piece can be tightened to push its PTFE pieces downward, clamping top and bottom light detectors in the slits and fixing BGOs. The different part described in this paragraph can be seen in Figure 6.4.

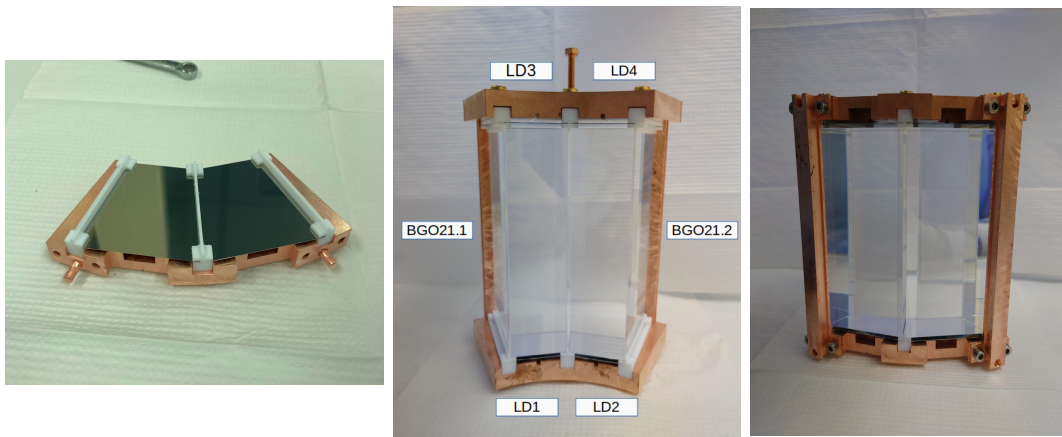


Figure 6.4 – *left*: Bottom copper piece with light detectors mounted in it. *center*: Front of the module once assembled. The name of each detector is shown. *right*: Back of the module.

We used two 12 cm high trapezoidal and polished BGO crystals grown by the Czochralski method by NIIC (ordered and received before the beginning of the conflict with Ukraine) on which we glued NTD Ge just to monitor their cooling down. We coupled to each a bottom and a top Ge light detector with also an NTD Ge glued for the readout using the usual gluing procedure with three Araldite epoxy glue spots. Among the four in total, three were SiO-coated and one bare germanium to see if we were observing a significant difference in the light collection. The NTD dimension and the coating of each LD are shown in Table 6.2 and their position with respect to the two BGOs and the module can be seen in Figure 6.4. The bonding of the NTDs was realized as usual with 25 μm Au wires to Kapton foils with gold pads on them. However, it appeared to be quite tricky: due to the weight of the assembly (each BGO is around 1.7 kg), it was difficult to manipulate under the bonding machine. Since even bigger crystals will be used in the MINI-BINGO veto, a modification of the module will have to be made in the future to allow the realization of the light detectors bonding before the mounting of the BGOs.

In order to realize some study on the coincidences of events, we decided to attach to the bottom copper piece a small $20\times 20\times 10\text{ mm}^3$ TeO_2 crystal facing the two BGOs. It had a Si heater and a $3\times 3\times 1\text{ mm}^3$ 41B NTD glued on it. In addition, we deposited on

| Detector | NTD batch | NTD dimensions | Coating |
|----------|-----------|--------------------------------------|------------|
| LD1 | 41B | $0.5 \times 1 \times 3 \text{ mm}^3$ | Not coated |
| LD2 | 41B | $0.5 \times 1 \times 3 \text{ mm}^3$ | SiO-coated |
| LD3 | 41B | $1 \times 1 \times 3 \text{ mm}^3$ | SiO-coated |
| LD4 | 41B | $0.7 \times 1 \times 3 \text{ mm}^3$ | SiO-coated |

Table 6.2 – Characteristics of each light detector.

the surface seen by the veto a drop of a liquid ^{238}U α source which had a 27 mBq activity to imitate surface contamination. The full assembly was placed in Ulysse cryostat, attached to the floating plate for which we optimized the anti-vibration system to support such a heavyweight. The structure can be seen in Figure 6.5. After closing the cryostat, we started the cooling down.

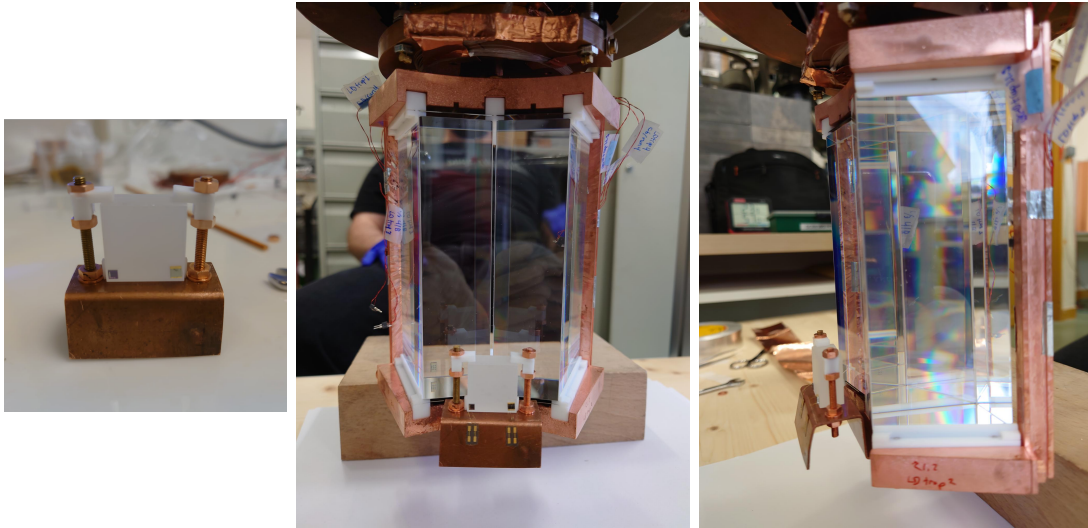


Figure 6.5 – *left*: Small $20 \times 20 \times 10 \text{ mm}^3$ TeO_2 assembled in an adaptation piece to attach it to our module. *center*: The full veto prototype inside the cryostat. *right*: Side view of the veto prototype in the cryostat. The liquid α source was deposited on the TeO_2 surface facing the two BGOs.

The cooling down of the prototype

We realized during the cooling down that the cryostat was slower to cool down than usual. Figure 6.6 shows the cooling down profile of the floating plate during the veto prototype run and compares it with the cooling profile for another run containing an assembly with four $45 \times 45 \times 45 \text{ mm}^3$ LMO crystals. Before 50 mK the rate is quite similar in both runs. However, it is clear that below this temperature, the cooling down in the case of the BGO assembly slows down, and the floating plate takes more than 60 hours to go from 40 mK to 25 mK instead of less than 2 hours in the case of the four LMOs run. It seems that, with such a mass of BGO, the difficulty to cool it down starts to affect the whole cryostat. This is an essential information for MINI-BINGO since, in that case, the mass of BGO will be much larger ($>100 \text{ kg}$), we can expect an extended cooling-down period. To have a first feedback on detector performance, we stabilized the temperature using the PID at 22.5 mK for the first measurement (plateau visible between 60 and 85 hours in 6.6). When we removed the

temperature stabilization, we observed a sudden drop of temperature and the cooling came back to its previous rate. It means that the heat load preventing the cryostat from cooling was becoming smaller and smaller (i.e. the BGO was still cooling down and was imposing the rate). A similar effect was observed after the second stabilization at 17 mK (between 140 and 160 hours). It is interesting to remark also that even if a perturbation induced a temperature rise (like an external cryostat vibration, represented by peaks in the temperature profile), the cryostat quickly recovered the temperature it had before the perturbation. This indicates that even though it is slow to cool down the BGOs, once they are cold, keep a certain "cooling momentum" and are not easy to heat up. It is encouraging because it means that a rise in temperature in the cryostat does not imply starting this slow cooling down again. It is not shown in Figure 6.6, but we were finally able after around eight days since the first measurement at 22.5 mK to stabilize the cryostat at 12.5 mK.

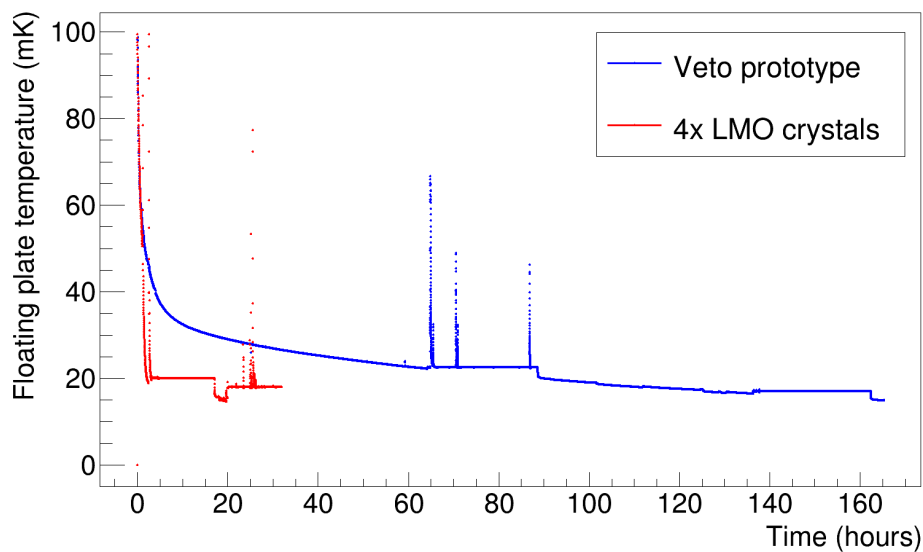


Figure 6.6 – Cooling down profile of the floating plate in the veto prototype run (blue) and in another run containing four $45 \times 45 \times 45 \text{ mm}^3$ LMO crystals (red). The starting time is taken when the temperature is equal to 100 mK. The different visible plateau corresponds to periods where the PID stabilized the temperature for measurements.

It is essential to notice that even when the floating plate was stabilized at 12.5 mK, it did not mean that the BGOs were at this temperature and they were continuously cooling down throughout the run. For example, the NTD of the BGO 21.2 showed a resistance below $10 \text{ k}\Omega$, which indicates that the crystal was still at a temperature between 50 and 70 mK if we roughly estimate using an $R(T)$ curve from the characterization of that NTD during a previous run. With such a low resistance, no pulses were observed in their heat channel. We observed similar behavior for the light detectors coupled to the BGOs which were continuously cooling down. However, they were cold enough for their NTD to reach a high resistance and get a reasonable sensitivity to measure the BGO scintillation light. To illustrate this, Table 6.3 shows the difference in resistance at 12.5 mK between two measurements separated by three days. It is clear that the resistance of the BGO and of the four light detectors increase, indicating that they are cooling down. We see, on the other hand, that the TeO_2 NTD stays at the same resistance and so it is not affected by BGOs. Therefore, it would be better

| Detector | Current (nA) | R_{NTD} | |
|------------------|--------------|---------------------------|----------------------------|
| | | 9 days after cooling down | 12 days after cooling down |
| LD1 | 19 | 152 k Ω | 170 k Ω |
| LD2 | 1.5 | 5.16 M Ω | 5.86 M Ω |
| LD3 | 19 | 221 k Ω | 252 k Ω |
| LD4 | 9.5 | 523 k Ω | 583 k Ω |
| BGO21.2 | 29 | 7.4 k Ω | 9.4 k Ω |
| TeO ₂ | 0.5 | 11.6 M Ω | 11.6 M Ω |

Table 6.3 – Resistance of the detector NTDs at 12.5 mK and its evolution after 3 days. Only one BGO is shown since, due to the wiring configuration, it was only possible to measure six channels at a time.

to modify the module design in the future and use independent PTFE pieces for the light detectors and the BGOs. It would thermally decouple them better and avoid such an effect.

Moreover, Table 6.3 allows us also to see that there was quite a discrepancy between the resistance of each light detector. It is probably due to a difference in the force that clamps them. It was confirmed during the disassembly where we discovered that LD1, the LD with the lower resistance, was not well fixed and was moving a lot when subject to vibrations. It also seems essential to find a better and more reproducible way to fix the LDs.

In any case, although BGO LDs were not at the base temperature of the cryostat, the resistances of their NTDs were high enough to see pulses which allowed us to make some measurements of BGO scintillation light and realize the studies we planned.

Detector calibration and performance

The data were acquired with a 5 kHz sampling frequency and processed in the first place with our usual MatLab-based software which applies an Optimum filter after building a mean pulse and a noise power spectrum.

The results that will be presented here have been obtained at 12.5 mK during a Th calibration. We chose the working point closest to the inversion point on the NTD load curves. Since some of them had a resistance quite low (below 300 k Ω), their load curves were not showing such a point within the range of bias we could put with our electronics. In those cases, we chose the maximum value available (19 nA). The working points used are the ones presented in Table 6.3 and the resistances as on the third column.

For the calibration of the light detectors, we took the benefit of the pulse shape difference between the scintillation events and the direct ionization events. We used a parameter depending on the pulse shape which we call PSD described in Ref. [153]. It gives information about how close the considered pulse shape (after optimum filtering) is to the mean pulse shape. The closer the two pulses are, the closer to 1 is this parameter. As shown in Figure 6.7 for LD2, the distribution obtained allowed us to identify the ²⁰⁹Bi X-rays K_α and K_β doublet emitted by BGO belonging to the direct ionization population of events (PSD \sim 1.02). We used the energy of these two peaks to calibrate the light detectors with a linear function.

To estimate the effective light yield of BGO measured by each Ge light detector, we used the same method as for the ZWO/BGO comparison: we identified the peaks corresponding to the Th source γ interactions in the BGO in the energy spectrum of the isolated scintillation

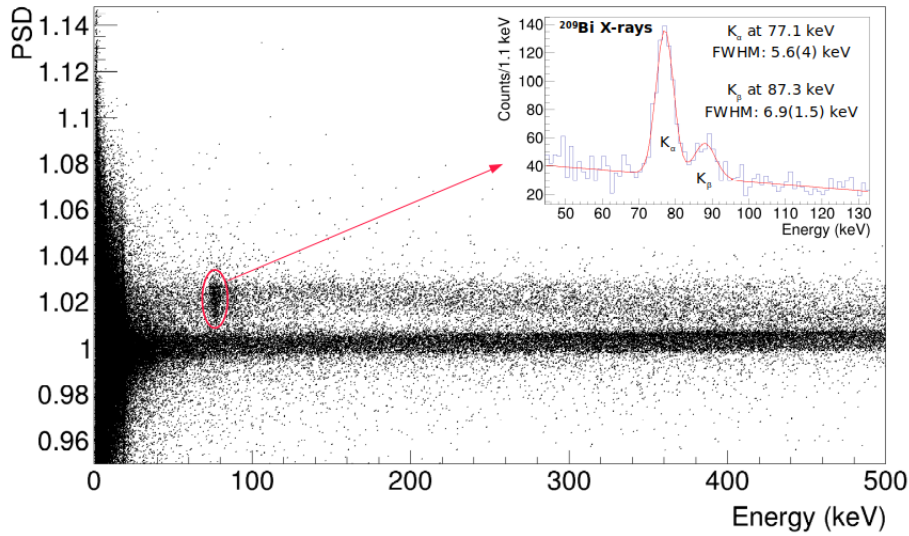


Figure 6.7 – PSD parameter as a function of the energy for LD2 during around 15 hours of Th calibration. The events in the red circle correspond to a ^{209}Bi X-ray doublet. A fit of the two peaks with two Gaussian functions and a linear background contribution is shown in the upper right corner of the figure.

events measured by the light detectors. We obtained the spectra as shown for example in the case of LD4 in Figure 6.8. By doing the ratio between the ^{208}Tl γ line at 2.615 MeV and the scintillation light peak energy measured by the light detector, we calculated the effective light yields reported in Table 6.4. All the light detectors measured a value of 7 keV/MeV and above except LD1, which was not coated with SiO. It confirms that this coating is efficient in enhancing BGO scintillation light collection. Concerning the slight differences observed in the value measured by the three other light detectors, we do not see a clear correlation with the wafer position in the assembly nor with the BGO faced and therefore, they remain unexplained.

| Detector | Sensitivity ($\mu\text{V}/\text{keV}$) | FWHM_{bsl} (eV) | FWHM @ 77.1 keV (keV) | Light yield (keV/MeV) | Rise-time (ms) | Decay-time (ms) |
|----------|--|--------------------------|--------------------------------|-----------------------|----------------|-----------------|
| LD1 | 0.19 | 992 | 4.5 | 5.0 | 1.4 | 5.5 |
| LD2 | 2.07 | 468 | 5.6 | 7.7 | 1.7 | 5.5 |
| LD3 | 0.24 | 440 | 6.5 | 8.8 | 1.3 | 3.7 |
| LD4 | 0.48 | 297 | 4.7 | 7.0 | 1.3 | 4.5 |

Table 6.4 – Performance of the LDs facing the BGOs during 15 hours of Th calibration

Table 6.4 shows that, due to their rather low resistance, LD3 and LD1 had a low sensitivity accordingly. LD1 showed also a particularly high noise compared to the other LDs, definitely due to its bad fixing that we observed during the dismounting of the structure. Since we saw two different populations of events with different pulse shapes, the rise times and decay times presented in this table correspond to the mean value calculated with both.

Concerning the TeO_2 crystal, we could stabilize the amplitudes of the pulses using heater events. We did the energy calibration by identifying different γ lines in its energy spectrum

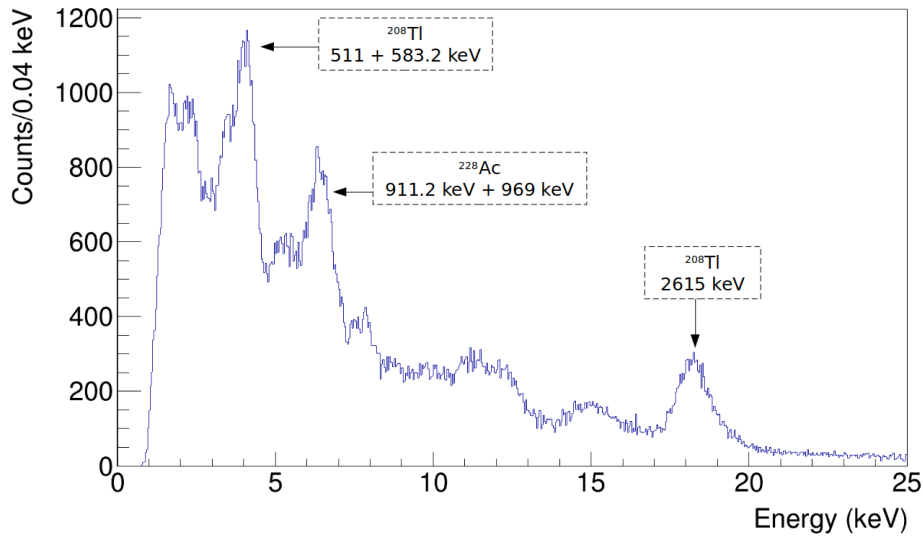


Figure 6.8 – Scintillation light energy spectrum measured by LD4 during this 15 hours Th calibration. The peak identified as scintillation light given by γ interaction in the BGO are labeled.

and using a second-order polynomial function to calibrate. During this measurement, the Th source was not in a position allowing the efficient irradiation of the small TeO_2 . As a consequence, we didn't see the corresponding γ lines in its energy spectrum. However, the γ lines coming from the environmental background (mostly from the ^{238}U decay chain) were clearly visible. The γ energy spectrum obtained can be found in the top plot of Figure 6.9. Moreover, we clearly see two peaks due to alphas present in the liquid source deposited on one of the surfaces. Both have a tail since the α particle can escape the crystal before depositing all its energy inside. The α region of the TeO_2 spectrum can also be found in the bottom plot of Figure 6.9. The sensitivity of this detector and its measured baseline FWHM are shown in Table 6.5.

| Detector | Sensitivity (nV/keV) | FWHM _{bsl} (keV) | FWHM @ 609 keV (keV) | Rise-time (ms) | Decay-time (ms) |
|----------------|----------------------|---------------------------|----------------------|----------------|-----------------|
| TeO_2 | 422 | 6.9 | 7.8 | 12.8 | 43 |

Table 6.5 – Performance of the TeO_2 crystal

The next step was to look at coincidences between the TeO_2 crystal and the BGOs through the light detectors. The presented results have been obtained during a 60 h background measurement at 12.5 mK acquired after the Th calibration already presented. Therefore, the detectors cooled down a bit between the two measurements, so their NTD resistance increased and their working points were changed accordingly.

Using the veto to reject surface radioactivity

The liquid source on the TeO_2 surface imitating surface contamination, we wanted to see if we were able to identify these events allowing their efficient rejection in the case of a real veto. Due to the size of the BGOs, we observed a relevant rate of events inside our light detectors as shown in Table 6.6, increasing the probability to have two signals overlapping. Argonaut,

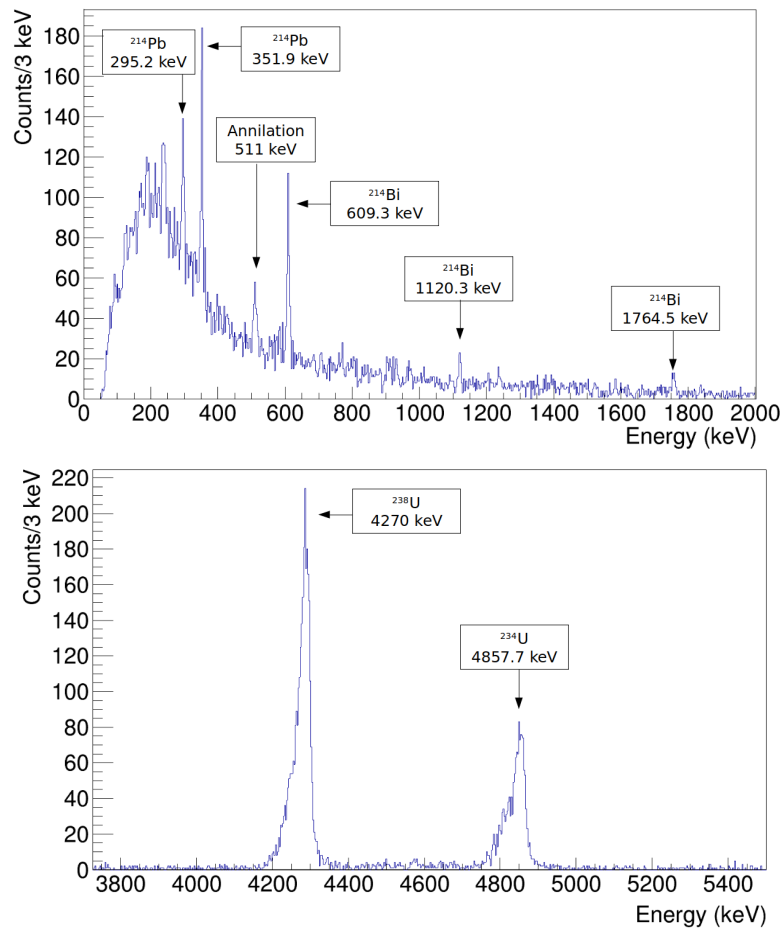


Figure 6.9 – *top*: γ region of the TeO_2 spectrum during the 15 hours Th calibration. The position of the source was apparently not optimal for the crystal to see the γ coming from it. The peaks from the environmental radioactivity used for the calibration are pointed out. *bottom*: α region of the TeO_2 spectrum. The two peaks from the liquid uranium source are visible.

our MatLab-based software applying an Optimum filter on the data stream, is not optimized for these measurement conditions. Indeed, it applies a filtered pulse shape cut based on the correlation parameter at the data triggering step (see section 3.3.3 in Chapter 3). Since the LD signals developed over around 20 ms even once filtered with the Gatti-Manfredi optimum filter, a lot of events will have their filtered pulse shape modified due to the presence of another signal within this time window. Therefore, we usually obtain a low reconstruction efficiency (see the next section). The goal for the veto being, on the contrary, to detect as many events as possible, we decided instead of trying to optimize the analysis using Argonaut to develop a new triggering algorithm to realize the coincidence and efficiency studies that will be presented here.

This algorithm is based on a derivative filter which, once applied to the data stream, gives sharper pulses as it can be seen in Figure 6.10 and give a baseline distributed around 0 less sensitive to low-frequency fluctuations. The triggering threshold is evaluated by taking a value around four times away from the filtered baseline RMS distribution mean value. An additional minimum energy threshold is applied to the total signal energy to avoid as much

| Detector | Rate of events >1.5 keV (Hz) |
|----------|------------------------------|
| LD1 | 3.4 |
| LD2 | 4.5 |
| LD3 | 5.3 |
| LD4 | 6.0 |

Table 6.6 – Event rate in each light detector.

as possible the triggers in the baseline. The values for each detector are reported in Table 6.7. This filter is less affected by pile-ups since it gives a shorter signal. Of course, this is true only if the second pulse of the pile-up has a high enough energy to be triggered, even if it lies in the negative part of the first pulse. In any case, since it doesn't imply any cut on the pulse shape, its efficiency is better than the one obtained with Argonaut. The position of the pulse is estimated as the intersection with the baseline of the tangent slope calculated at the point where the rise-time slope of the non-filtered pulse is maximum (i.e. where the filtered pulse is maximum). The amplitude is determined by integrating the filtered pulse from the triggered bin to the bin passing by 0. Since no optimum filter is applied, we lose some energy resolution which is acceptable here since it is not the most crucial parameter for the veto light detectors. We could implement it at the step of the amplitude determination in the future. To optimize the performance of the filter, the sampling frequency for TeO₂ signals was reduced offline to 1 kHz due to the rise time of its signals being of the order of tens of ms. It was not needed to do it for the light detectors.

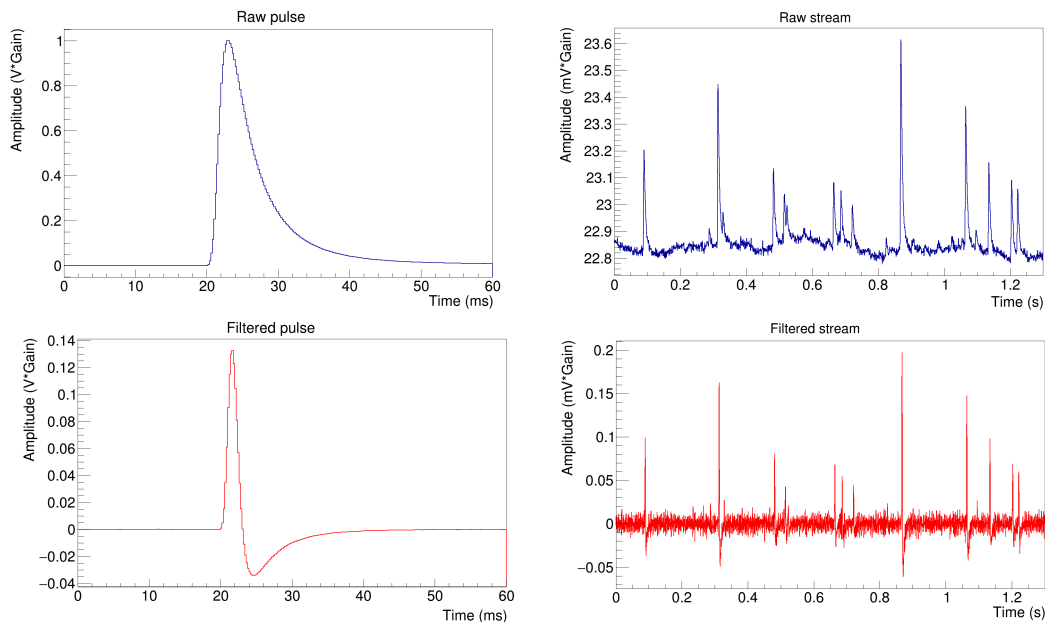


Figure 6.10 – *Top panels*: LD4 pulse normalized to 1 V*Gain and an insight of its data stream during the 60h background measurement. The gain was 1092 for this LD. *Bottom panels*: Same signal and data stream portion once filtered with the derivative filter.

When an event is triggered in the TeO₂ crystal, we look at the closest event in time

| Detector | RMS _{bsl} mean value (eV) | Derivative signal threshold (keV) | Total energy threshold (keV) |
|----------|--|--------------------------------------|---------------------------------|
| LD1 | 103 | 430 | 1.5 |
| LD2 | 111 | 450 | 1.5 |
| LD3 | 62 | 250 | 1.0 |
| LD4 | 48 | 190 | 1.0 |

Table 6.7 – Performance obtained and trigger values used after applying the derivative filter on the data stream of each LD.

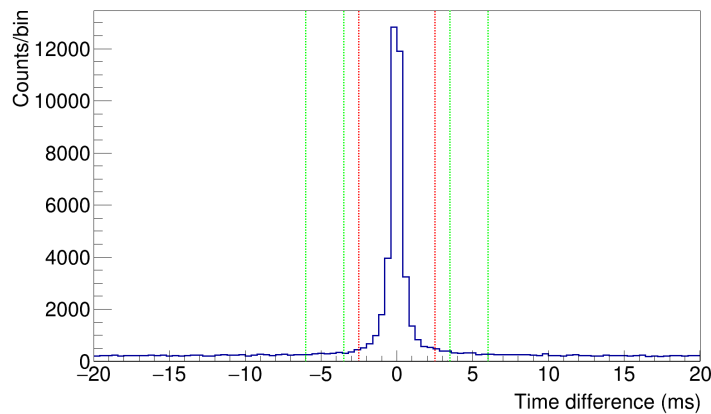


Figure 6.11 – Distribution of the time difference between the TeO₂ events and the events in the light detectors the closer to them. The red region is the real coincidences, while the green regions are the ones where we estimated the accidental coincidences distribution.

among the four light detectors. The time difference distribution is presented in Figure 6.11. One can see a peak appearing over an almost flat background. It corresponds to the in-time coincidence events between any light detector and the TeO₂ crystal. It is centered around 0 since an offset has properly been applied for each light detector to take into account the difference in time propagation between heat channel and light channels. We have considered as in-time coincidences the events within a 5 ms window around this peak (red region in Figure 6.11). On the other hand, the background corresponds to accidental coincidences. Since it is almost flat, we used the two green regions shown in the histogram to estimate their distribution under the peak. The energy spectrum of the events in TeO₂ in the 5 ms coincidence time window with the light detectors is shown in Figure 6.12 where a 15 keV energy threshold have been applied. One can also see the distribution of accidental coincidences estimated using the green regions. The two α peaks of the source at 4.2 MeV and 4.7 MeV correspond to events that deposit all their energy in the TeO₂ and nothing in the BGOs. Therefore, they should not be in coincidence with any light detectors, and as we can see, they are completely explained by the accidental coincidence distribution, demonstrating the validity of the method. Moreover, we can see in the lower energy region of the spectrum an excess of events peaking around 100 keV that is not due to accidental coincidences. We identify it as the nuclear recoils. Indeed, we expect daughter nuclei recoil energy for the α decay of ²³⁸U and ²³⁴U of around 72 and 83 keV respectively. It is coherent with our excess and the tail can be explained by the fact that some α particles are losing a bit of their energy

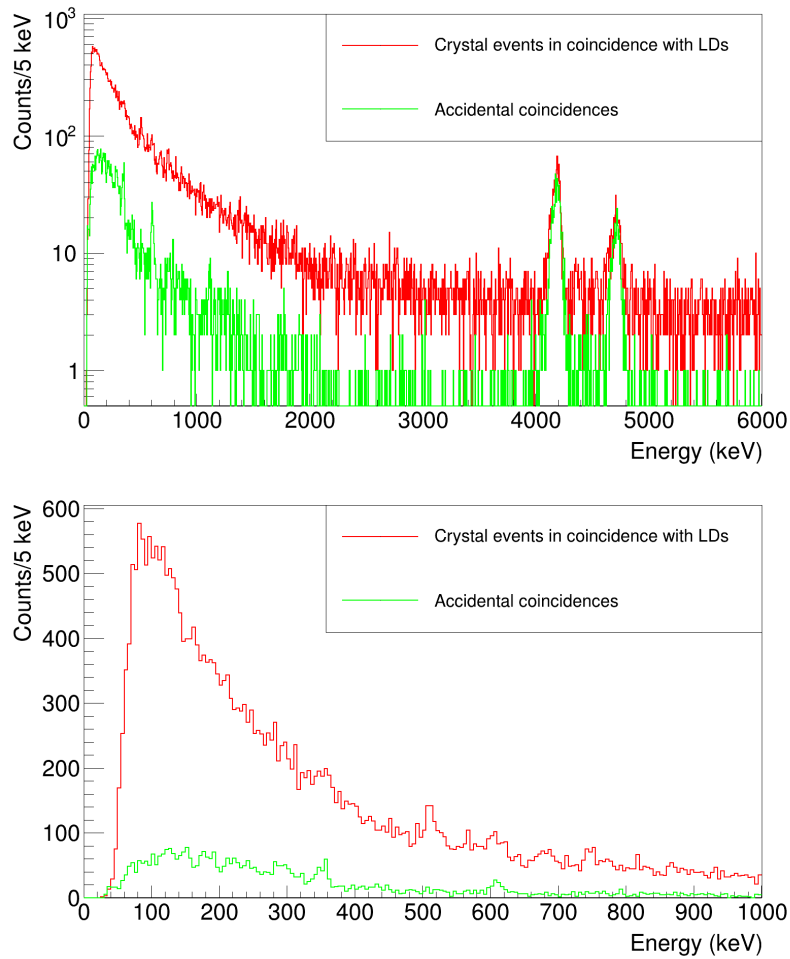


Figure 6.12 – Energy spectrum of the TeO_2 events in coincidences with the light detectors. The accidental coincidence distribution estimated with the method described in the text is shown in green.

in the TeO_2 before exiting it, giving an event with a slightly higher energy in total.

To verify this, we can look at what we obtain on the side of light detectors. Figure 6.13 presents the event in coincidence between LD4 and TeO_2 . One can see that in the region below 500 keV detected in the crystal, we distinguish two populations of events around 5 and 6 keV in the light detector not due to accidental coincidences. Since it corresponds to the energy region where we see nuclear recoils in the TeO_2 , it means that they correspond to the scintillation light emitted by the α particle that has deposited all its energy in the BGO. We can see that these events are distributed in such a way that the higher the energy in the TeO_2 , the lower the energy in the light detector. As already mentioned, this slope corresponds to a loss of energy of the α particle in the TeO_2 crystal before exiting it, resulting in less energy deposition in the BGO.

To make it clearer, we have applied a cut on the light detector energy using a descending first-order polynomial function (blue line in Figure 6.13), considering only the events below. We have removed the random coincidence contribution from the spectrum and we have calculated by slices of 100 keV deposited in the TeO_2 , the mean energy value of the remaining light detector events. We obtained the distribution shown in Figure 6.14 that we have fitted

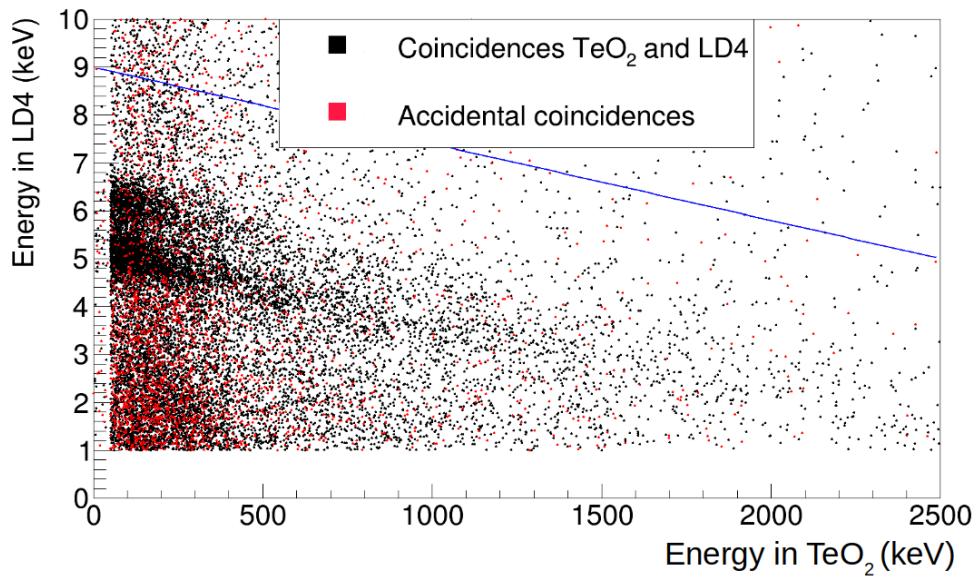


Figure 6.13 – Coincidences between the TeO_2 crystal and LD4. The blue line corresponds to the function used to isolate alpha events (see text).

with a first-order polynomial function. It is a way to approximate the slope of the alpha events corresponding to a conserved total energy. As we can see, it crosses the x-axis around 4.5 MeV, which is close to the mean energy of the two α peaks of the source, confirming the origin of these events.

Finally, we can isolate α 's that are depositing all their energy in the BGOs by taking the events with an energy deposition between 50 keV and 100 keV in the TeO_2 (basically just the energy of the daughter nuclear recoil). We obtain the energy spectrum shown in Figure 6.15 for LD4. One can see two peaks, centered at 5.1 and 6.1 keV respectively, corresponding to the two peaks of the source. Indeed, we can estimate the energy deposition inside the BGO with the light yield taking into account the scintillation quenching factor for α particles. We measured a light yield of 7.0 keV/MeV for LD4 and for energies between 4 and 5 MeV we can expect a quenching factor of around 17% according to Ref. [169]. For the first peak, we obtain $5.1/7.0/0.17=4.3$ MeV and for the second one, $6.1/7.0/0.17=5.1$ MeV. These values are really close to the α energies emitted during the decay of ^{238}U and ^{234}U (4.2 and 4.7 MeV). We saw these events in all light detectors, but the two peaks could be separated only for LD4 and LD3. It can be explained by the relatively high baseline fluctuation observed for LD1 and LD2 compared to LD4 and LD3 without the Optimum filtering which had a bad impact on their energy resolution (see Table 6.7).

In any case, we have evaluated the response of our veto prototype to a possible surface contamination of the bolometer it is facing. We have developed an algorithm to realize the coincidence between the BGOs and the crystal allowing an efficient rejection of these events by also estimating the distribution of accidental coincidences. This method can be applied also to identify the events originating from surface contamination that could lie in the ROI of bolometers by considering the conserved energy slope and tag the event following its trend.

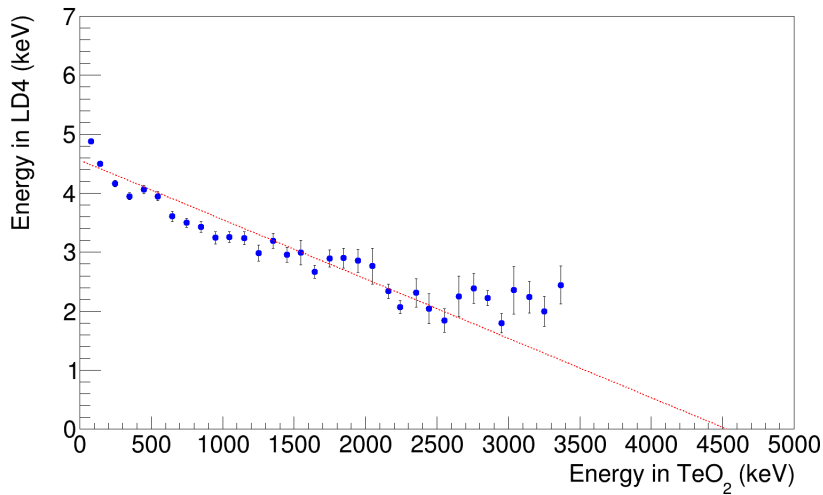


Figure 6.14 – Coincidences between the TeO_2 crystal and LD4 corrected from accidental coincidences. The points represent the mean energy value of the events in LD4 each 100 keV window of energy deposited in the TeO_2 crystal. The red dashed line is the first-order polynomial function that we used to fit the slope.

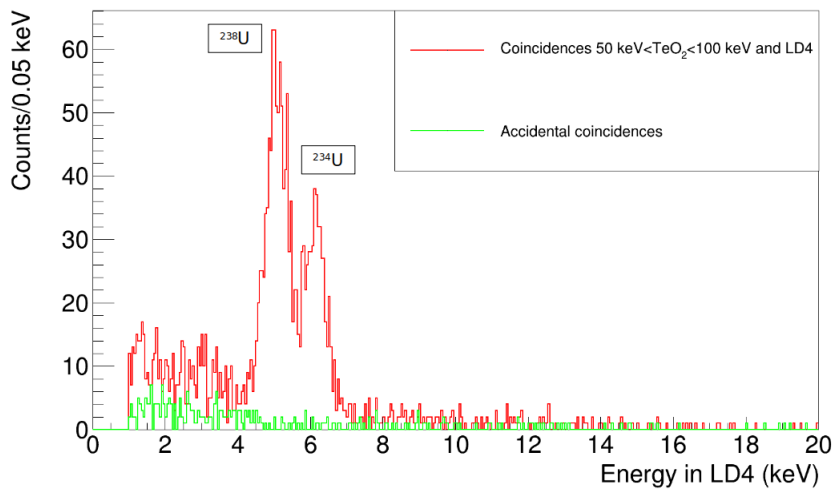


Figure 6.15 – Energy spectrum of LD4 for the events in coincidence with the TeO_2 crystal that have deposited in it an energy between 50 and 100 keV.

Energy threshold estimation

One of the crucial point to ensure a good external γ rejection with our veto is to detect the lowest possible energy deposition in the BGO with the scintillation light. Our objective is to reach a 50 keV energy deposition threshold in the BGO (see Chapter 4). This feature depends on the light collection of our light detectors, and this part will be discussed in the next section, but it depends also on their intrinsic performance. We tried to evaluate the energy threshold reached by our light detectors in the veto prototype.

To do so, we have done an offline reconstruction efficiency study: we have injected synthetic pulses using an average pulse at different energies in the data stream of each

light detectors. We checked how many we were recovering after data processing and all selection cuts. We considered that an overlay event was detected as long as it was triggered, independently of the reconstructed energy value since adding this constraint is lowering the measured efficiency. We obtained the efficiency plots presented in Figure 6.16. First of all, one can see the difference between the derivative filter and the Argonaut software. With Argonaut, the maximum efficiency stays around 90% due to the threshold algorithm depending on the pulse shape which, in the case of high rates of event, is quite affected by pile-ups. It is not the case for the derivative filter algorithm which reaches quickly values close to 100% reconstruction efficiency. Therefore, the latter seems to definitely be the best threshold algorithm to use in order to get the best veto efficiency. However, further tests will have to be done to confirm this, especially in low background environment, to verify that it is the case also in a low rate of events configuration.

Using the derivative filter results, we can estimate the threshold of each light detector as the energy value for which the reconstruction efficiency becomes higher than 90% (horizontal dashed lines in Figure 6.16). The estimated values can be found in Table 6.8. If we consider that the required energy threshold is 50 keV in the BGO, we can translate this value to a light channel threshold for each light detector using their light yield. We obtain the values presented the third column of the table. One can see that none of the light detectors reached such low energy thresholds. Even if their performance were better, it seems challenging to consider that these values are possible with these kind of light detectors since it implies an improvement by more than a factor 5 compared to what we obtained even for the best LD.

| Detector | Estimated energy threshold @ 90%(keV) | Required energy threshold (keV) | Effective energy threshold w/ a x10 NTL Gain (keV) |
|----------|---------------------------------------|---------------------------------|--|
| LD1 | 5 | 0.25 | 2.5 |
| LD2 | 5 | 0.385 | 3.85 |
| LD3 | 2.3 | 0.44 | 4.4 |
| LD4 | 2.4 | 0.35 | 3.5 |

Table 6.8 – Estimated energy threshold of each lighth detector.

This is why BINGO plans to read the scintillation light of BGOs with NTL light detectors as explained in Chapter 4. Thanks to the amplification of the light signal they provide, we should be able to reach the threshold objective. To show it, we can consider that the light detectors of the prototype were NTL ones with a gain of 10 on their signals. This gain value was demonstrated already as reachable by NTL Ge light detectors [149] and can be taken as an objective for BINGO veto light detectors. In that case, the signal-to-noise (S/N) ratio of the light channels would be 10 times higher. It means that a 1 keV signal would have the same S/N than a 10 keV signal detected with the not amplified Ge wafers of the veto prototype, and so the same reconstruction efficiency. Therefore, we can estimate an effective energy threshold (vertical lines in in Figure 6.16)) which takes into account this boost of S/N and see if it would have been reached with this veto prototype. We see that it is the case for LD3 and LD4 while for LD1, the lower light collection due to its not coated surface and its high noise prevents it to reach it. LD2 showed also higher noise fluctuations than LD3 and LD4, which has naturally affected its reconstruction efficiency at low energies. Therefore, if we work on the noise of our LDs, by for example fixing them better, and if all the detectors are coated with SiO₂, the 50 keV energy threshold objective in the BGOs could be achieved. Of course, it is only a preliminary rough estimation and a veto prototype with NTL light

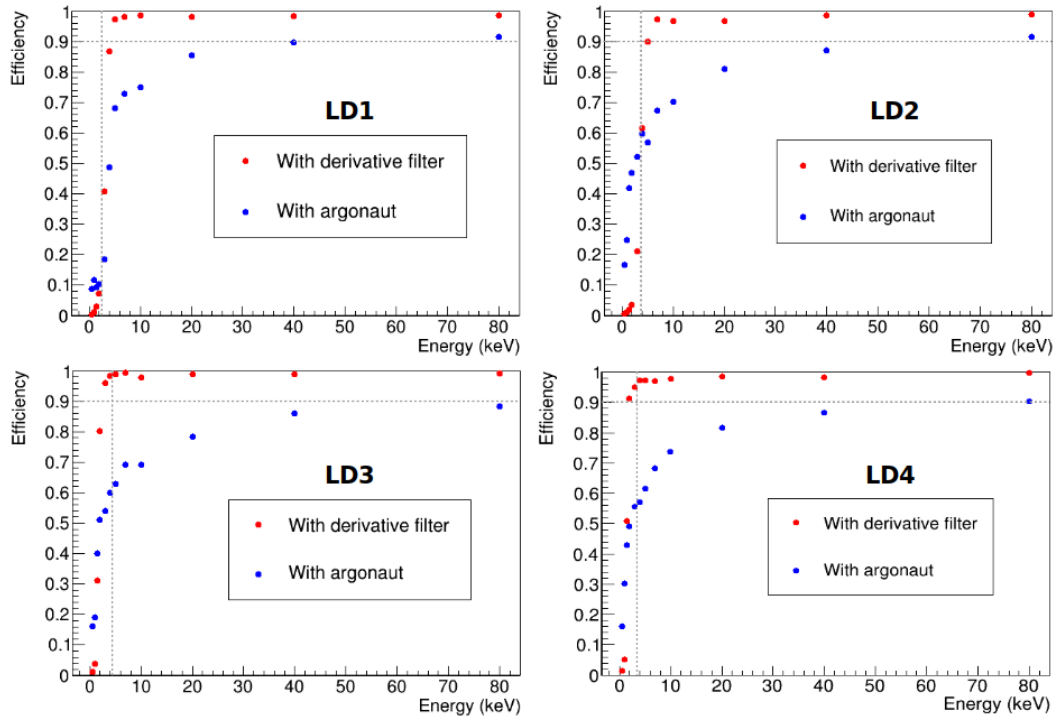


Figure 6.16 – Reconstruction efficiency as a function of the energy for the four light detectors. The horizontal dashed lines represent the 90% efficiency while the vertical ones is the effective energy threshold in the case of a NTL light detector with a gain of 10 (see text).

detectors has to be tested in the future to confirm this hypothesis.

Conclusion

This first cryogenic test of the BINGO-like BGO veto has given us precious information. Firstly on the mechanical structure, we saw that it is important to design it in a way that it is easy to handle due to the weight of BGOs. In addition, since BGOs are slow to cool down, which also affects the environment, it seems crucial to well decouple the light detectors from them so they can obtain the best performance possible. Therefore, a new assembly is now under study in which the bonding of light detectors NTDs can be done before mounting the BGO. We will use also a new way to hold the wafers using PTFE pieces different from the ones on which the scintillators are resting. Secondly, thanks to a small TeO_2 crystal on which a liquid U source was deposited, we have studied and developed a coincidence algorithm using a derivative filter. We obtained good results with the possibility to identify the events coming from such origin. Finally, we did a preliminary light detector threshold estimation confirming that NTL light detectors are mandatory also for the veto. In principle, such LDs with a gain of 10 should allow to reach a 50 keV threshold in the BGOs.

The veto tests will continue, including a new prototype using NTL light detectors and some of the potential light collection improvements discussed in the next section.

6.1.3 Room temperature BGO light output measurements

In the configuration foreseen for the MINI-BINGO cryogenic veto, presented in Chapter 4, the 4π coverage will allow a high interaction probability of external γ background within it. However, the efficiency of our active vetoing will depend a lot on how well we will be able to detect these interactions thanks to the scintillation light emitted by the BGOs. This implies working on light detectors' performance by using NTL ones for example but also on their light collection. In order to enhance it, one way would be to put on the veto external side a reflective foil that would prevent the scintillation light from escaping. The same reflective material could also be put in between each BGO crystal, ensuring even better confinement of the light but also preventing cross-talks between light detectors belonging to different BGOs. However, the same technique can not be applied on the inner face of the veto facing TeO₂ and LMO crystals. The contamination of the reflecting foil could be a problem and putting a "dirty" material close to the bolometer would be against BINGO objectives. It would also prevent the use of the BGOs to reject the surface radioactivity of bolometers since it would be stopped by the foil before reaching the BGO crystals. On the other hand, keeping this surface bare also has some drawbacks. It gives to the BGO scintillation light a way to escape it, reducing the light collection of their Ge LDs and potentially at the same time induce spurious signals in the bolometers. The other way is also true, we could lose some of the scintillation light of LMO and Cerenkov one of TeO₂ which could impact our α and β/γ discrimination. The way to overcome these challenges is to evaporate directly on that surface of the BGO a thin layer (~ 200 nm) of a material, such as Al or Au, in order to reflect the scintillation light of BGOs and keep the one from bolometers inside their area while not stopping the α or β radiation allowing still an efficient surface radioactivity rejection.

Before implementing such methods, we decided to realize some tests to find out which would be the best reflecting foil to enhance the light collection but also how a surface coating would affect it, for example. However, cryogenic measurements are not suitable for the study of many different configurations since a run, in general, lasts at least two weeks, including the time of the cooling down and warming up of the cryostat. Therefore, we decided to develop a room-temperature test bench where the scintillation light of BGOs is measured using a photo-multiplier tube (PMT). This installation allowed us to compare the efficiency of different materials used as reflecting foil more easily and more effectively. We also took benefit of it to compare BGOs coming from different producers. The results are presented in this section.

The PMT test bench

For these room temperature scintillation light measurements, we decided to use as a light detector a PMT. It is a highly sensitive device used to detect and amplify very low levels of light. It consists of a photocathode that converts incident photons into electrons, which are accelerated by a series of dynodes through a high-voltage potential. As the electrons strike each dynode, a cascade effect occurs, resulting in an exponential increase in the number of electrons. This multiplication process produces a measurable current that is proportional to the incident light intensity. A schema of the working principle can be seen in Figure 6.17. In our case, we worked with a Philips 56 AVP model [170] that we recovered from a PMT stock available at CEA and which is a cylinder with a 4.2 cm diameter photo-cathode.

We designed a support optimized for this PMT model which was made for the measure of small cylindrical 3 cm diameter and 6 cm height crystals since we already had some crystals of this size (see section 6.1.1). We chose a PMT high-voltage (HV) base with a larger diameter

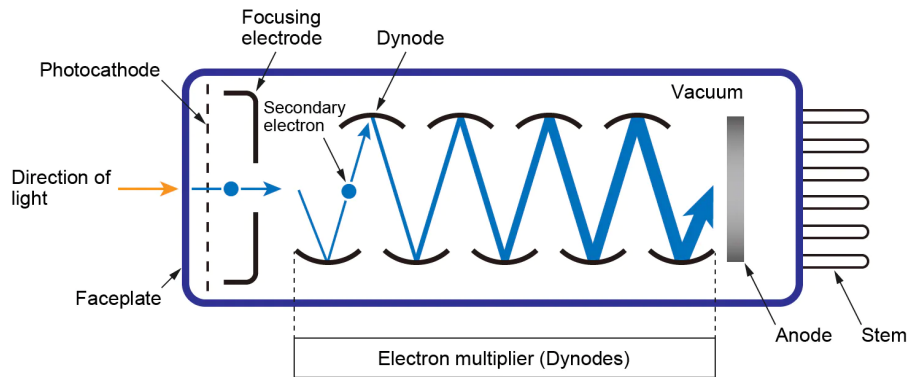


Figure 6.17 – Photo-multiplier tube working principle. Drawing taken from [171]

than the PMT in which it is possible to screw a metallic tube in order to encapsulate the PMT. This base also has springs within it. Therefore, when the PMT is connected, it can be pushed against the springs and move a bit along their axis. Moreover, we put inside the metallic tube a smaller tube made of mu-metal around the PMT to shield it against magnetic field effects. We designed a support for the cylindrical BGO that can be seen in the top photo of Figure 6.18. It is a cylindrical metal piece that fits perfectly in the main tube and on which there is a slot to place the BGO. The latter can be fixed thanks to a collar that can be tightened with a screw. The collar has a PTFE ring within it which is the part touching the crystal, avoiding damaging it when tightening. Once the BGO is well fixed, we deposit on its top surface some EJ-550 Si optical grease which avoids having air between the crystal and the PMT and so optimizes the optical coupling. This piece can be placed inside the tube and pushed against the PMT, compressing the springs. This action ensures to spread the optical grease between the BGO and the PMT surfaces uniformly. Finally, we use a cap that we can screw into the main tube to keep the pressure. When screwed, the cap pushes the crystal adaptation piece, and so the BGO, against the PMT while an opposite force due to the springs push the PMT against the BGO, ensuring a good mechanical coupling between the two surfaces. A simplified drawing of the full mechanics is also presented in Figure 6.18. Moreover, to make sure that the setup is completely isolated from external light, we used an additional rubber cap.

The assembly was mounted inside a metallic bench in a horizontal position. The latter had a slot to place a source collimator in which we could place a ^{60}Co source which produces two main γ lines at 1.17 and 1.33 MeV. On the electronics side, the PMT was powered by a CAEN HV power supply. The signals were passing through a timing filter amplifier allowing us to integrate and amplify them before being acquired by a Red Pitaya STEMLab 125-14 card [172] which has a sampling frequency of 125 MHz and a 14-bit ADC resolution. All these elements can be seen in the photos of Figure 6.19. For the data processing, we used a software called mcpha [173]. It applies to the input signal a cascaded integrator-comb (CIC) and a Finite Impulse Response filter (FIR), reducing the sampling frequency to 31.25 MHz. It is determining the height of each signal subtracting the value of the baseline estimated as the minimum value just before the rising edge of the analyzed pulse. The user can also put a manual value for the threshold and indicates the wanted measurement duration. After starting the acquisition, the software stocks the amplitude of each triggered pulse in a histogram that we can save as an ASCII file containing the number of counts in each bin.

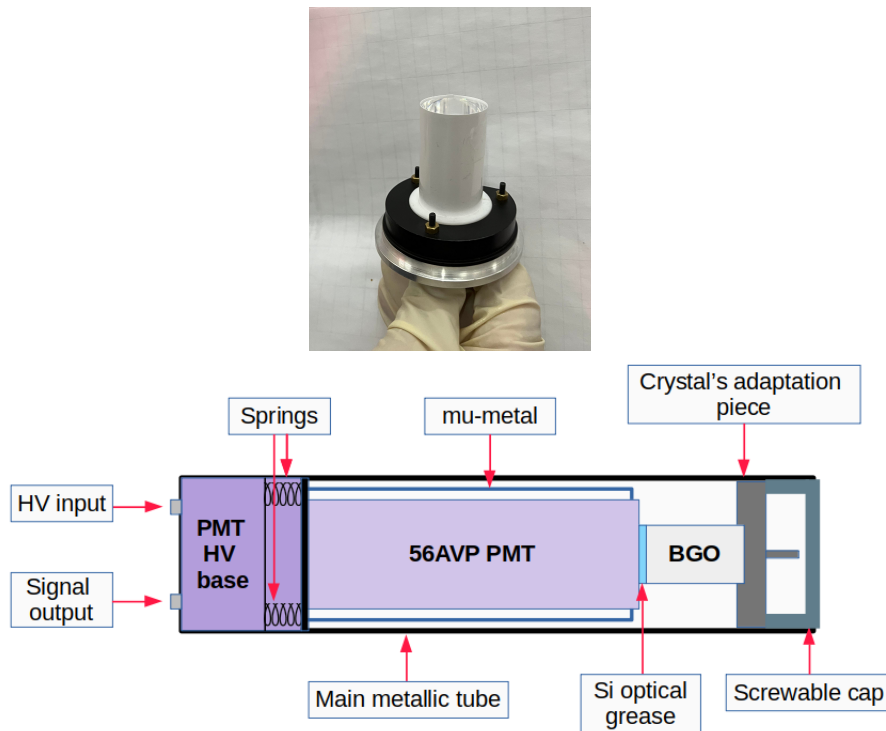


Figure 6.18 – *top*: Photo of the crystal's adaptation piece with a BGO covered by a reflecting material mounted inside. *bottom*: Simplified drawing of the PMT mechanic.

We tried different sets of parameters for the setup and we obtained the best results with 1700 V applied through the PMT, and a 20 ns integration of the signal with a gain of 5 applied with the amplifier module. Therefore, all the results presented here were acquired with this combination of parameters.

Configurations tested

With the test bench finalized, we were ready to test different BGO configurations facing the PMT. We had at our disposal two different reflecting foils to wrap the cylindrical BGOs and compare their performance. The first one is the 3M[®] Enhanced Specular Reflector (ESR) Film with a 65 μm thickness which was used for example in the CUPID-Mo experiment [101] and is well-known to work at low temperature. Its reflectivity is larger than 98% across the visible spectrum which fits the BGO light emission spectrum. The second one is a polyester (PET) Melinex[®]339 white polished film of 175 μm thickness. It has only 4% total light transmission and good reflectivity properties.

Moreover, we took benefit of the setup to test the light output of BGOs coming from different producers. We had two polished BGOs produced by NIIC in Russia ordered before the conflict. One was tested in the cryogenic measurement presented in section 6.1.1. We coated the lateral surface of the second one with a 120 nm Al layer by evaporation in Orsay. The latter was also tested during a cryogenic measurement, which is not described in this thesis, and we observed a severe diminution of the light output. We wanted to cross-check this result with our room temperature setup. In addition, we had three BGOs produced by SICCAS in China which could be a potential producer for the MINI-BINGO cryogenic

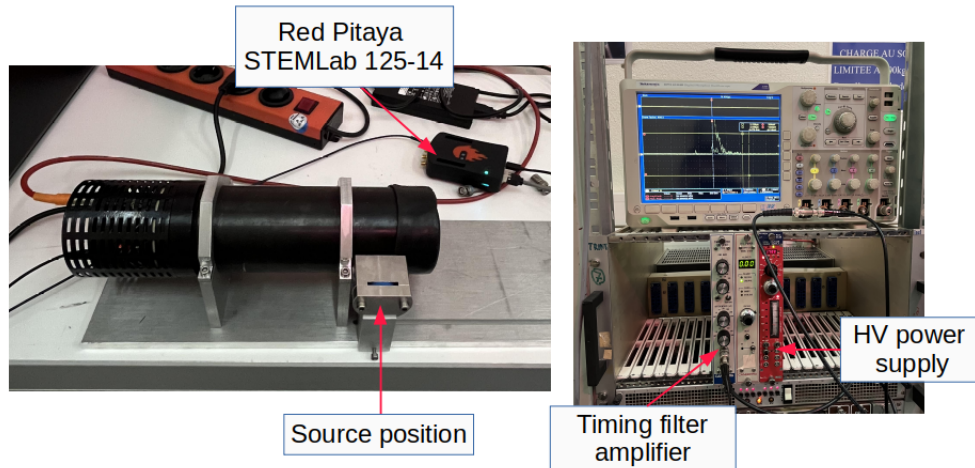


Figure 6.19 – *left*: Photo of the PMT test bench. The source collimator can be seen as well as the acquisition card. *right*: Photo of the electronic crate. One can see the HV power supply used for the PMT, the timing filter amplifier used to integrate and amplify its output signal, and the oscilloscope utilized for looking at the signals.

veto. The first one is not optically polished, the second one has only its top and bottom surface polished (half-polished) while the third one is totally polished. It allowed us to test which polishing was giving the best result. Finally, we had also a BGO crystal produced by ISMA in Ukraine. Photos of different configurations that we tested can be found in Figure 6.20. One can notice that the Al coating of the NIIC BGO was damaged. After the evaporation, it was homogeneous on the whole surface and was tested like that during the cryogenic measurement. After this measurement, the crystal was stored under nitrogen until we recovered it for this room-temperature test. It is at that moment that we realized the damage on the coating. Therefore, it seems only due to the time elapsed during the two measurements (around 5 months). If the coating is selected as a solution for the inner part of the MINI-BINGO cryogenic veto, this problem will have to be investigated. For our test, we decided to proceed in any case since still a non-negligible percentage of the surface was covered. The results will be presented in the next section.



Figure 6.20 – Photos of different BGO configurations that we tested. (1) Polished BGO. (2) Half-polished BGO. (3) Not polished BGO. (4) Al-coated BGO. (5) BGO wrapped in the ESR film. (6) BGO wrapped in the PET film.

Results and discussion

The first thing that we did was to check the effect of the source on the measured energy spectrum. We used for that the polished NIIC BGO wrapped in the ESR film. We took a 10 min acquisition with and without the ^{60}Co source. We obtained the two spectra shown in Figure 6.21. When the source is placed inside the collimator, the rate of events becomes much larger and we see appearing two bumps of events at a different range of energy. We can see that the one in the larger region of energy seems to split in two. We identified this as the two γ lines of ^{60}Co at 1.17 and 1.33 MeV. This is the only configuration where it is possible to distinguish the two peaks as it will be presented later. We fitted them using a convolution of two Gaussian functions and used the position of the two mean values obtained to calibrate the energy spectrum. Using the calibration, we see that the first bump is around 200 keV. Our hypothesis is that it is due to back-scattered photons: the photons from the source that are Compton scattered in the surrounding material around the BGO before reaching it with an angle superior at 120° have almost constant energy. The mean value of the back-scattered photons of the two γ lines of ^{60}Co is 212 keV [174], coherent with the mean value of our bump. In any case, for the purpose of our test, we did not calibrate the spectra since what interests us is to compare relatively the position of the ^{60}Co photopeak bump between each configuration.

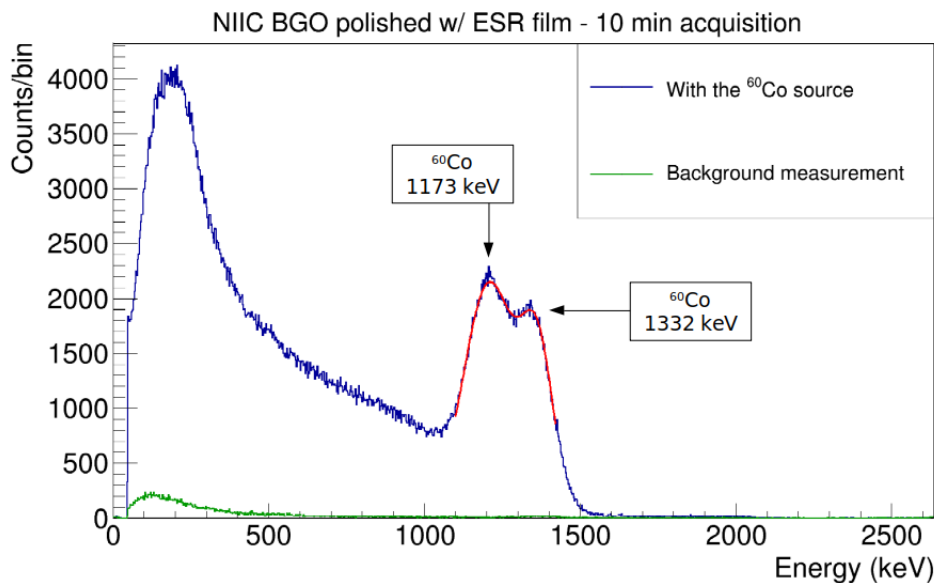


Figure 6.21 – Calibrated energy spectra of the NIIC polished BGO wrapped in an ESR film during a 10 min acquisition with and without the ^{60}Co source. The two peaks of the source were fitted using the sum of two Gaussian functions (red solid line) and the spectrum was calibrated according to the result with a second-order polynomial function.

The relative comparison of the position of this bump is valid only if our setup is giving reproducible results (i.e. the position of the bump doesn't change between two measurements for the same configuration). In order to check this, we reproduced the same test with the polished NIIC crystal wrapped in the ESR film three times throughout our room-temperature measurement campaign. It allowed us to make sure that the HV power supply and PMT were stable, but also that the results were not depending on the amount of optical grease

(it was put by hand so without a clear set amount) and on the way the wrapping in the reflecting material was done (we used a different sheet of ESR film each time). The spectra obtained are shown in Figure 6.22. We observed only a really slight difference smaller than 1% between the position of the bumps in the reproducibility measurements, ensuring good stability of our setup.

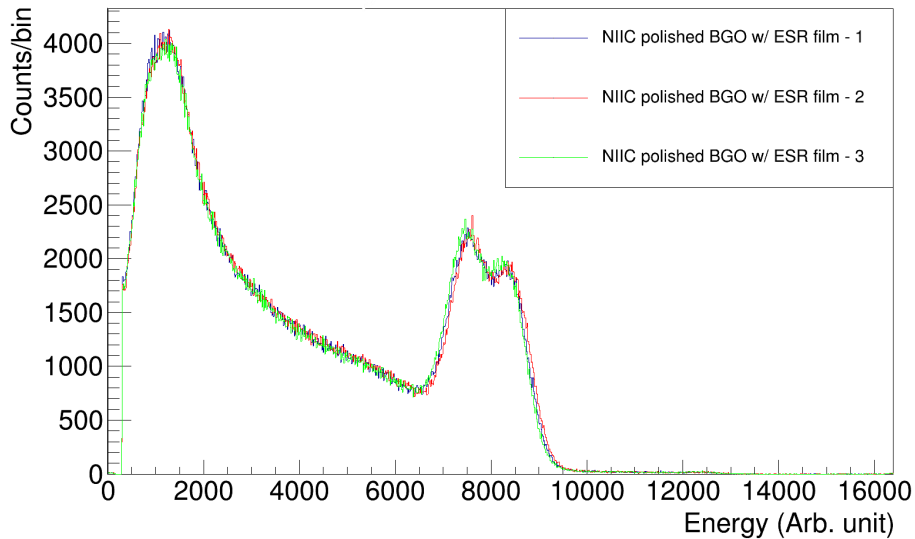


Figure 6.22 – Test bench reproducibility test. The three plotted measurements were done at different moments during the measurement campaign with different ESR film sheets and amounts of optical grease.

With that being said, we can now focus on the real comparison between each setup. We evaluated the position of the bump by fitting it with a Gaussian function for each configuration to relatively compare their light output. We started by comparing the light output of polished BGOs wrapped in the two different reflecting materials with respect to when they are naked. For NIIC BGO, we tested also the Al-coated crystal. The energy spectra obtained with NIIC and SICCAS crystals are shown in Figure 6.23. The first thing to notice is that when the crystals are naked, the two γ peaks of the source are completely overlapping. For both BGOs, one can see that wrapping the crystal in the ESR film give the best light output with an increase of around 53% for the NIIC BGO and of 20% for the SICCAS one compared to when it is naked. This difference between the two crystals could be explained by different light emission spectra due to a different composition of the crystal (for example due to a different level of impurities). Moreover, we see that for the NIIC crystal wrapped in the ESR film, we start to well distinguish the two γ lines of ^{60}Co while only a sort of shoulder appears in the bump for the SICCAS one. The PET film is the second best configuration with an 18% light output increase for the NIIC crystal but of only 4% in the case of the SICCAS BGO. We see also that, as already observed during the cryogenic measurement, the Al-coated BGO is giving a really low light yield with a reduction of around 67% compared to the naked one. This could be explained by the fact that the coating is absorbing a large part of the scintillation or that it stays trapped inside the BGO. Hence, this test is in disfavor of the coating solution. However, here all the lateral surface of the BGO is coated which represents 80% of the total surface. Maybe coating a smaller surface (i.e. only the inner surface of the trapezoidal BGO for MINI-BINGO) could have a minor impact and still work well, coupled

with a wrapping of reflecting material. Further tests will have to be done to test this case.

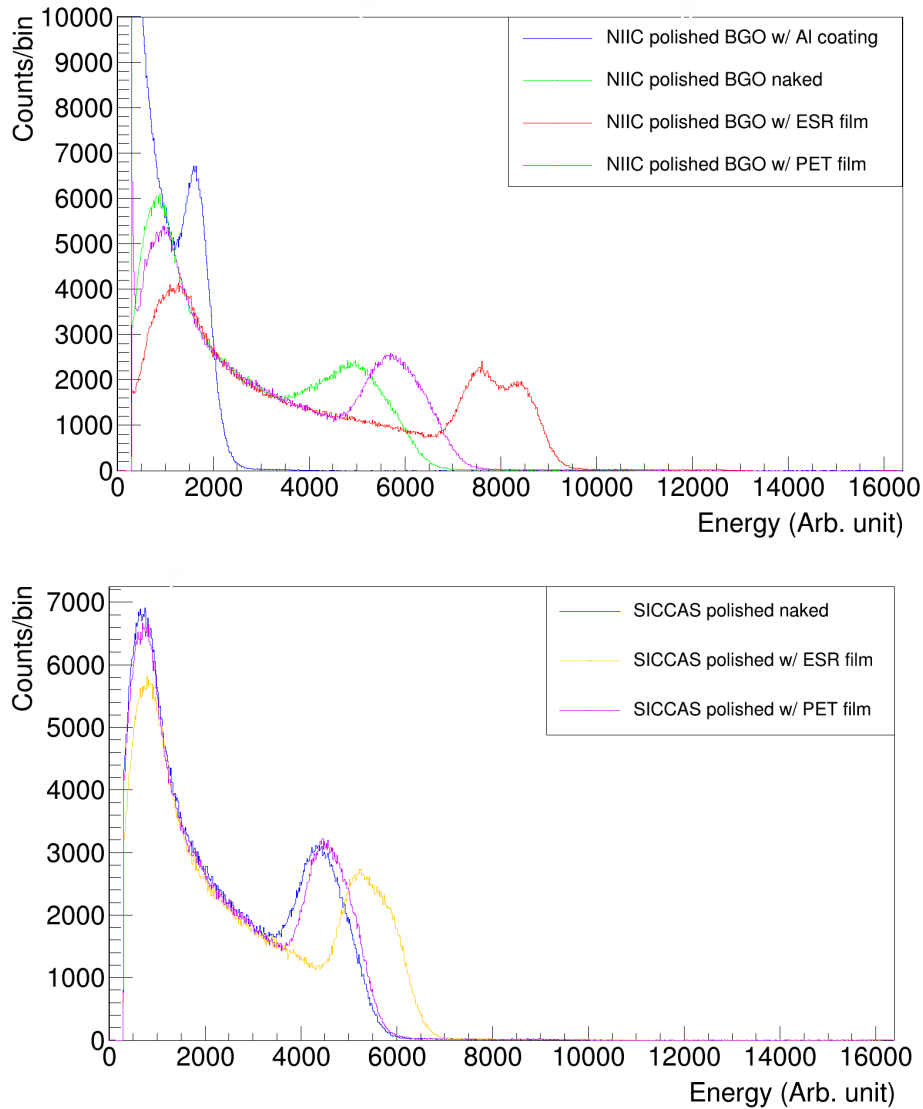


Figure 6.23 – *top*: Comparison of the NIIC polished BGO wrapped in different materials and with the one coated with Al. *bottom*: Comparison of the SICCAS polished BGO wrapped in different materials

In addition, we compared the effect of the different polishing on the light yield and try to estimate which one would be the best for the cryogenic veto. We had three SICCAS BGOs with different types of polishing that can be seen in Figure 6.20. The results are presented in Figure 6.24. One can see that the more polished the surface the better the light output. The bump position is 30% lower in the case of the half-polished crystal compared to the completely polished while is it 36% lower in the case of the not polished crystal.

Finally, Figure 6.25 presents the difference between the BGOs from the three different producers when they are wrapped with the ESR film. One can clearly see that the crystal from NIIC has the best light output while the one from ISMA is the worst. We measure for the ISMA crystal in this configuration a light yield almost 50% smaller than the NIIC crystal one. As already mentioned, these discrepancies could be due to a difference in the composition of

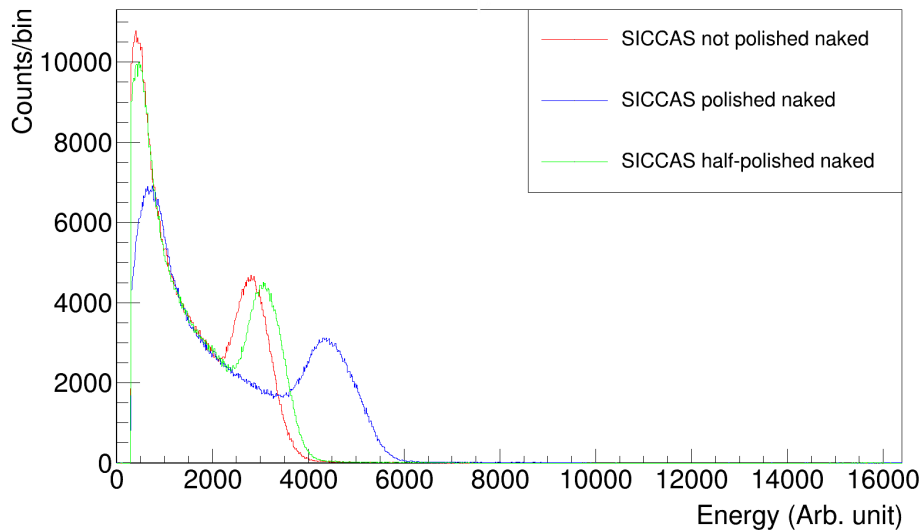


Figure 6.24 – Comparison of the spectra obtained for the SICCAS crystals with a different surface polishing.

each crystal and the level of impurities that could influence the scintillation yield. Therefore, this parameter seems to play an important role for the MINI-BINGO cryoveto in addition to the choice of the reflecting material. It will be crucial to investigate the reason for these differences and to check if other producers could make crystals of the same quality as the NIIC ones.

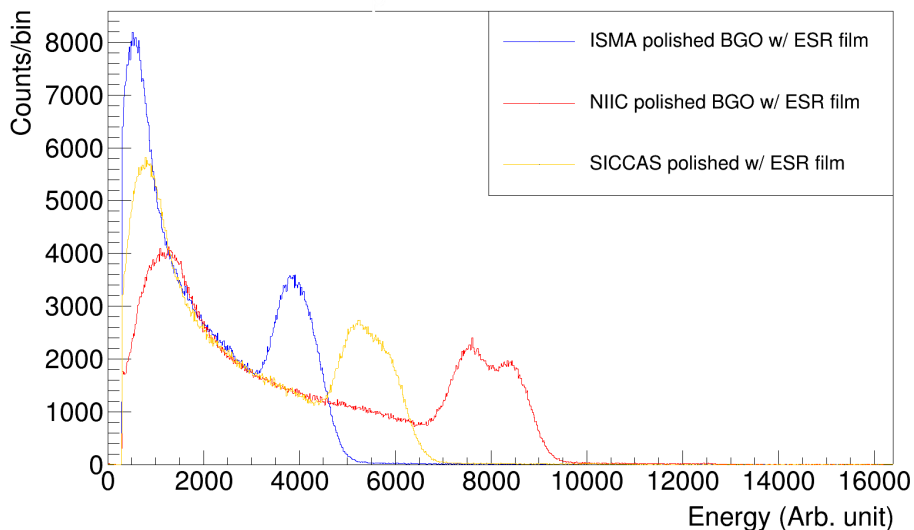


Figure 6.25 – Comparison of the spectra obtained for the crystal of each producer when wrapped in the ESR film.

Table 6.9 is summarizing all the results we have obtained. It compares the light output (LO) of each configuration with the polished and naked configuration for the same producer but also in general with the polished and naked configuration of the NIIC BGO. One can see that the best configuration was obtained with the NIIC polished BGO wrapped in the ESR

film which gathers all the best features between each comparison: the best producer, the best surface treatment, and the best reflecting foil. The ESR film which was widely used in bolometric experiments is now considered as the one to be used for the external part and in between the BGOs for the MINI-BINGO cryogenic veto. However, it is possible that another better reflecting foil can be commercially available. Now that the test bench is working well, more tests will definitely be done with other materials. Moreover, it is straightforward to adapt the setup to longer and trapezoidal crystals, as the one of section 6.1.2, which is the shape foreseen for MINI-BINGO. It means that it should be possible to test the Al coating on the inner surface, but also other coatings like Au or MgO since they can be done locally with the IJCLab evaporator in Orsay. We have seen also that the light output depends on the crystal origin. Therefore, it adds a requirement for the producer that will be chosen: in addition to a ^{207}Bi contamination smaller than 100 mBq/kg, the BGOs should have the best scintillation yield possible. This is why the development of this room-temperature test bench was also crucial for MINI-BINGO. It allows us to have fast feedback and comparisons on crystal performance. The work will be pursued to, in the end, choose the best combinations for MINI-BINGO and have the cryogenic veto with the lowest possible energy threshold.

| Producer | Surface treatment | Reflecting material | LO difference w/ polished + naked | LO difference w/ polished + naked NIIC BGO |
|----------|-------------------|---------------------|-----------------------------------|--|
| NIIC | Polished | Naked | - | - |
| NIIC | Polished | PET film | +17% | +17% |
| NIIC | Polished | ESR film | +53% | +53% |
| NIIC | Polished | Al coating | -67% | -67% |
| SICCAS | Polished | Naked | - | -10% |
| SICCAS | Half-polished | Naked | -30% | -37% |
| SICCAS | Not polished | Naked | -36% | -43% |
| SICCAS | Polished | PET film | +4% | -7% |
| SICCAS | Polished | ESR film | +20% | +8% |
| ISMA | Polished | Naked | - | -32% |
| ISMA | Polished | PET film | +9% | -26% |
| ISMA | Polished | ESR film | +17% | -21% |

Table 6.9 – Summary of the relative light output measurement with the different BGO configurations

6.2 Second part: Lead screening with bolometric measurements

As explained in Chapter 4, the MINI-BINGO demonstrator will take place in a brand new dry dilution cryostat. The success of that experiment in demonstrating that BINGO technologies are the key for pushing the boundaries of background rejection in bolometric experiments also requires operating it in a really low background environment. This is why the cryostat will be installed in the underground laboratory of Modane which, thanks to its 4800 m.w.e depth, ensures a reduction of the muon flux to around 5 muons/m²/day [175]. However, other environmental radioactivity is expected [176] and has to be mitigated at the level of the cryostat installation.

This external flux includes γ s coming from surrounding laboratory materials or wall concrete and to reduce it a lead shield will be deployed all around the cryostat in ideally a 4π coverage. The design is still under study with the help of Monte-Carlo simulations to ensure to use of the best geometry, but it should have, in principle, a thickness of at least 23 cm to get the best γ stopping power. In addition, another internal shield made of two 5 cm thickness lead plates will be installed inside the cryostat, just above the experimental area, to shield the latter from the radioactivity of the cryostat components. Figure 6.26 shows a possible geometry for the MINI-BINGO lead shield where external and internal parts are visible.

Naturally, a careful lead selection is required since it is close to the detectors. It is quite common to find commercial lead with low contamination of long-lived isotopes such as ^{232}Th , ^{238}U and ^{235}U . However, the secular equilibrium is broken for ^{210}Pb , which can harm our low-background objectives. This isotope can undergo a β decay with a half-life of 22.3 years and a Q-value of 64 keV. The resulting isotope, ^{210}Bi , can undergo β decay with a half-life of only 5.013 days and a transition energy of 1.163 MeV, forming ^{210}Po . The latter can decay through α decay to stable ^{206}Pb with a half-life of 138.376 days and a Q-value of 5.407 MeV. This chain is relatively short, and in our case, the β decays, especially the one above 1 MeV from ^{210}Bi , are the problem since they can induce a continuous background contribution by bremsstrahlung emission, saturating our cryogenic veto. It is then crucial to control this ^{210}Pb contamination in our shield. For MINI-BINGO, it is planned to use a 2 cm layer of ultra-low radioactivity lead in the external shield part, the closest to the cryostat, and to use this type of lead for the internal one.

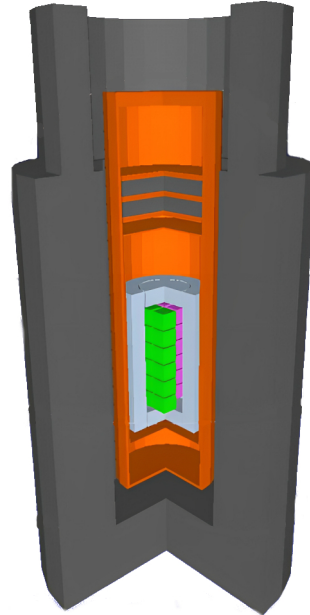


Figure 6.26 – Example of geometry for the MINI-BINGO lead shield implemented in a Geant4 simulation to study the γ background. The grey parts are made of lead, the orange ones are made of copper, the white ones represent the BGO veto, while green cubes are the TeO_2 crystals and the pink ones are LMO ones.

A precise contamination measurement of an ultra-low radioactivity lead using the bolomet-

ric technique has been done in the framework of this thesis and the results will be presented in this part of the Chapter.

6.2.1 Context of the measurement

We have a large stock of $100 \times 200 \times 50$ mm³ lead bricks at CEA used in the past by low background experiments and the plan is to use part of them for the MINI-BINGO lead shield, limiting the cost of such an infrastructure. We were able to identify for some of the bricks the foundries where they were produced thanks to a label inscribed on their surface. Table 6.10 shows the number of bricks we have from each producer.

| Foundry label | Number of bricks | Estimated total weight |
|---------------|------------------|------------------------|
| FG | 356 | 3987 kg |
| Roussel | 58 | 650 kg |
| PN | 42 | 470 kg |
| S | 10 | 112 kg |
| Vitry | 9 | 101 kg |
| Nantes | 1 | 11.2 kg |
| Unknown | 452 | 5062 kg |

Table 6.10 – Lead stock at CEA available to be used for the MINI-BINGO lead shield.

In order to select which potential batch of bricks we could use for the MINI-BINGO shield, we sent to the underground laboratory of Modane small, approximately $50 \times 50 \times 5$ mm³, cleaned (the procedure is explained later) samples, cut directly from a brick of each foundry to measure their radioactivity. They were measured using a closed-end coaxial HP-Ge detector called Gentiane, in an ultra-low background environment. The results obtained regarding the ²¹⁰Pb contamination are shown in Table 6.11. The values presented in this table were obtained using two different analyses. The full peak analysis considers a window around the peak and counts the number of events in it, while the full spectrum analysis takes into account the whole spectrum and the full decay chain. In general, the latter is more precise; in our case, we will consider both analyses since our approach to measuring the contamination is closer to the full peak analysis. According to these measurements, the FG batch is interesting for the external part of the shielding since it is showing a ²¹⁰Pb activity inferior at 30 Bq/kg and we have a good amount of bricks. For the internal part, the Roussel lead is really promising with an ultra-low ²¹⁰Pb activity, below 2 Bq/kg. The quantity available would be, in principle, more than 70% of what is required to build the geometry of Figure 6.26, reducing the cost since this is the most expensive type of lead.

In order to get a confirmation of the low radioactivity of the Roussel batch but also to obtain a more precise estimation, we decided to perform a cryogenic measurement of this lead. The latter offers a much bigger detection efficiency than HP-Ge detectors due to the fact that the source is also the detector. Indeed, HP-Ge detectors are measuring the 46 keV γ and the beta decay spectra of the ²¹⁰Pb decay chain to estimate the activity. Hence, the detection is impacted a lot by self-absorption, the geometry of the sample, and branching ratios (the 46 keV γ has only a 4% branching ratio). On the contrary, a lead bolometer could measure directly the α from the ²¹⁰Po decay which has a low probability to escape, a branching ratio of almost 100% and a high energy, around 5.4 MeV, ensuring to get a signal in a high signal to noise ratio region with a moderated background. In addition, pure

| Sample | mass (g) | ^{210}Pb activity full spectrum analysis (Bq/kg) | ^{210}Pb activity full peak analysis (Bq/kg) |
|---------|----------|---|---|
| FG | 213.87 | 19.73(225) | 19.10(272) |
| S | 222.55 | 14.95(170) | 16.68(260) |
| PN | 239.72 | 30.70(195) | 24.14(372) |
| Roussel | 235.64 | 0.73(37) | 1.42(45) |
| Vitry | 205.87 | 53.44(480) | 53.28(775) |
| Unknown | 221.32 | 52.01(329) | 50.59(768) |

Table 6.11 – ^{210}Pb contamination for each sample measured by the Gentiane detector at LSM. The error written are only statistical and an additional systematical error of around 10% is estimated.

lead bolometers have already been successfully operated in the past to measure their ^{210}Pb contamination [177] and recently, the best limit ever obtained on that contamination for an archeological lead has been put using this kind of detectors [64]. We were then quite confident that even with our above-ground cryostat, we would get a sensitivity high enough to estimate the contamination of our samples considering the ones measured by the HP-Ge detector.

6.2.2 Samples preparation

We cut four small samples from a Roussel brick using a metallic saw with the goal of obtaining a dimension of approximately $20 \times 10 \times 10 \text{ mm}^3$. We cleaned their surface with a well-defined procedure. It consisted of dipping and rubbing the samples in different chemical baths for 3 minutes each. The first one contained a 1% diluted acetic acid water solution to remove the oxide layer. The samples were then put in a bath of a water solution containing 1% of nitric acid and 3% of hydrogen peroxide, which removes a significant surface layer. These two steps were repeated two times before moving to two new baths containing water and 3% of hydrogen peroxide. Finally, the samples were dried, and we used ethanol for the final wipe. Once all the samples cleaned, we selected the two with dimensions the closest to our goal to be sure that they would fit in our assembly. They were called Pb#1 and Pb#3 and had a mass of 23.76 g and 25.28 g, respectively.

We glued on each of them a 41B $3 \times 3 \times 1 \text{ mm}^3$ NTD Ge using a matrix of 9 Araldite® Rapid glue spots and one Si heater. We mounted them in a small assembly that can be seen in the photo on the left of Figure 6.27. It is composed of a copper plate covered by a reflecting foil (not relevant in this test). The samples are sitting respectively on two PTFE pieces while two others are pressing against them on the top thanks to nuts screwed on screw rods. The bonding of the NTDs was done with 25 μm Au wires on the gold pads of a Kapton foil glued on copper adaptation pieces, ensuring that they are at the same height. We soldered twisted Cu cables at the other end for the connection to the cryostat wiring. Another copper plate was finally put on the top and the assembly was attached to another one, for the CROSS R&D, before being mounted to the cryostat floating plate (photo on the right of Figure 6.27).

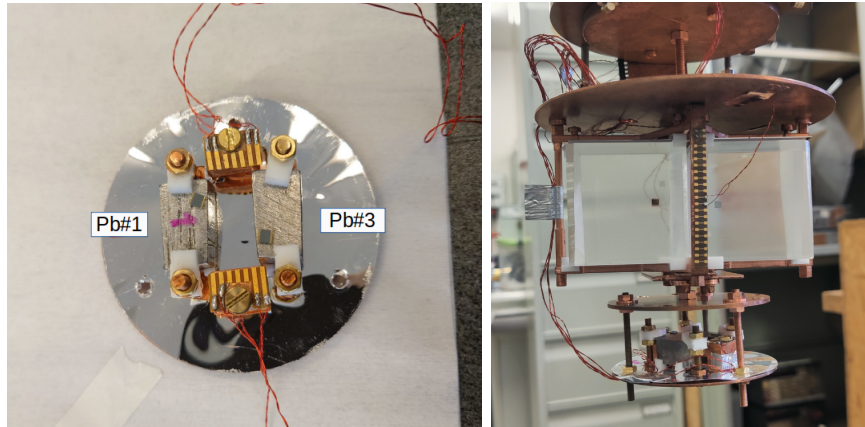


Figure 6.27 – *left*: The two Roussel lead samples mounted in a bolometric assembly. Their respective NTD Ge can be seen but not the Si heater since they were not glued yet at that point. *right*: The assembly once installed inside the Ulysse cryostat. It is at the bottom of another assembly related to the R&D work for the CROSS project.

6.2.3 Cryogenic measurements and ^{210}Pb contamination estimation

We cooled down the cryostat and we performed background measurements at three different temperatures: 16 mK, 22 mK and 25 mK. The results that will be presented here were obtained at 22 mK, but all the background data acquired were used to determine at the end the ^{210}Pb contamination. The data were acquired with the already presented CUORE-like electronics with a sampling frequency of 5kHz and a Bessel cut-off frequency of 675 Hz. The data were finally processed with our MatLab-based software applying the Gatti-Manfredi optimum filter to the data stream. We used a γ peak or heater events for the data stabilization, depending on which method was giving the best results.

The calibration of the two lead bolometers was rather simple: even during background measurements, we could identify γ peaks from the natural ambient radioactivity, allowing us to realize a calibration using a linear function. The energy spectrum measured with Pb#1 is presented in Figure 6.28. The γ lines from ^{214}Bi are clearly visible and are usual in our above-ground setup (see other measurements realized in this cryostat already presented in this thesis). Moreover, one can see the α peak around 5.4 MeV due to ^{210}Po decay and so directly related to the ^{210}Pb contamination of the sample. One can notice that it has a strange shape which will be discussed later.

The performance of our two bolometers during this measurement is summarized in Table 6.12. The working points were chosen as the ones with the maximum heater amplitude. The sensitivities and baseline FWHM obtained appear to be relatively good if we consider that we just cut the samples from an ingot without further preparation. This confirms the high potential of this method to measure the internal radioactivity of lead.

| Detector | Bias (nA) | NTD resistance (M Ω) | Sensitivity (nV/keV) | FWHM _{bsl} (keV) | FWHM @ 609 keV (keV) |
|----------|-----------|------------------------------|----------------------|---------------------------|----------------------|
| Pb#1 | 2.15 | 1.95 | 10.8 | 26 | 38.6 |
| Pb#3 | 2.5 | 1.66 | 8.4 | 30 | 45.3 |

Table 6.12 – Performance of the lead bolometers at 22 mK

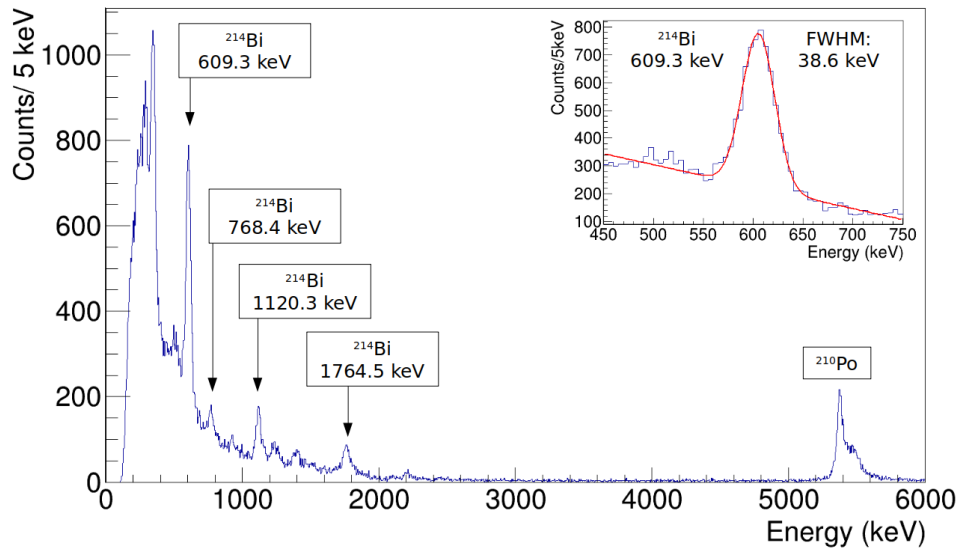


Figure 6.28 – Energy spectrum obtained with Pb#1 during a 64h background measurement at 22 mK. The γ peaks used for calibration are labeled with an arrow. The ^{214}Bi line at 609.3 keV has been fitted using a Gaussian with a linear background contribution.

As already mentioned, the ^{210}Po α peak around 5.4 MeV was showing a strange shape with a sort of a tail (see Figure 6.28). This behavior was observed for both samples and in all measurements we did but also in the measurements done in the past with pure lead bolometers [64, 177]. We investigated the origin of this tail by looking at the shape of the signals forming the peak. Figure 6.29 shows the PSD parameter as the function of the energy of Pb#1. We can see that the tail is due to a drift of the event pulse shape leading to a bad estimation of the amplitude by our data processing software and to a tail in the final energy spectrum. This effect is quite pronounced at 5.4 MeV but we can see some hint of similar behavior at lower energy on the 609.3 keV ^{214}Bi γ line (and it was observed in Ref. [64] for the 2615 keV ^{208}Tl γ line with the appearance of a tail in their energy spectrum). Therefore, it seems that it depends on the event energy. Figure 6.29 also presents the shape of the pulses at different positions in the tail. We can see the presence of a fast component in the pulse. The higher the estimated energy in the tail, the higher this component, but also the lower the density of events. A dependence of the detector response on the position of the energy deposition in the sample could explain this feature. Indeed, the lead had a polycrystalline structure, and the high energy γ can undergo multi-Compton scattering in the absorber.

In order to estimate the number of events in the ^{210}Po α peak and determine the ^{210}Pb contamination, we corrected this "drift" effect by fitting it using a second-order polynomial function and stabilizing the energy of the events to the energy of the α decay (see Figure 6.30). It allows us to fit the stabilized data using a Gaussian function and determine more easily the number of counts under it. To do so, we integrated the number of events in a range of $\pm 5\sigma$ around the mean value of the fitted Gaussian. We estimated the number of background events by looking at 5.65–5.75 and 5.85–5.95 MeV energy intervals where no α s from U or Th decay chains are expected. Moreover, we estimated our reconstruction efficiency by injecting synthetic pulses around 5.4 MeV, constructed using a mean pulse, in the data stream. We were looking at how many we were able to recover after our data processing and analysis cut. We found for this measurement a 88(2)% reconstruction efficiency. Putting

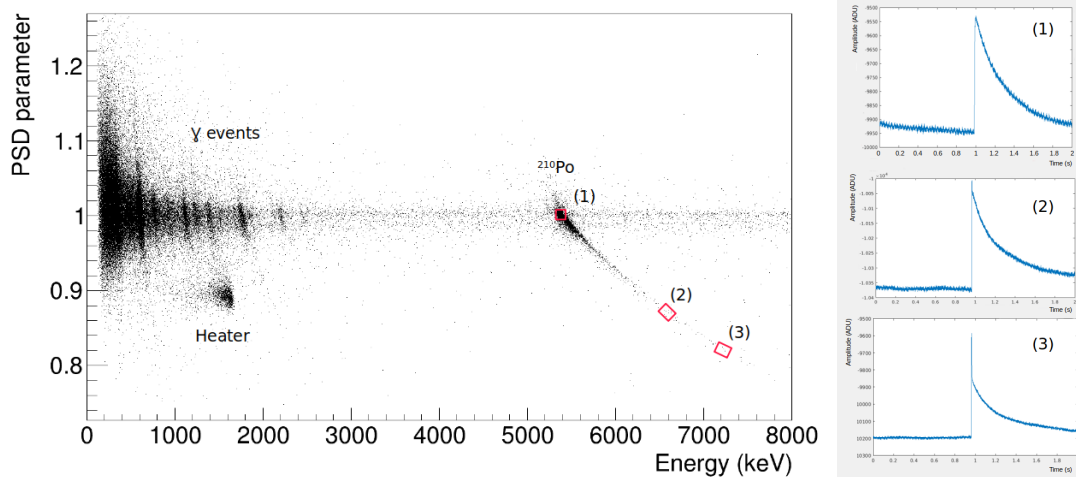


Figure 6.29 – *left*: PSD parameter as a function of the energy for Pb#1. *right*: Characteristic shapes of the pulses in the regions (1), (2) and (3) indicated on the PSD plot.

this together, we were able to evaluate the ^{210}Pb contamination of our samples. The values we found in all our background measurements are summarized in Table 6.13.

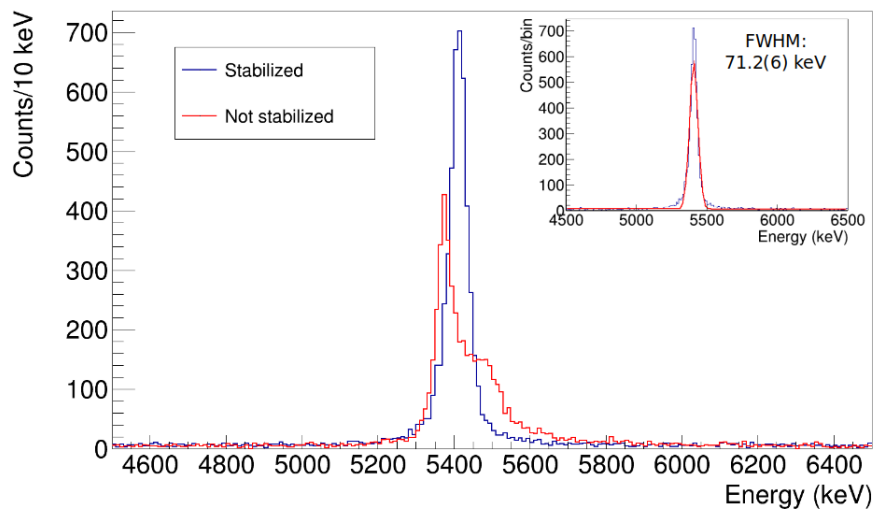


Figure 6.30 – The ^{210}Pb alpha peak before and after the stabilization process using the PSD parameter. Once stabilized, it was fitted using a Gaussian function with a linear contribution of the background.

The mean values obtained are 0.94(3) Bq/kg for Pb#1 and 0.89(3) Bq/kg for Pb#3. The error presented are only due to statistics and could be underestimated since we did not include systematics on the sample mass measurement or the detection efficiency. These results are compatible with the value obtained by the gamma screening done by the HP-Ge detector as it is shown in Figure 6.31, and confirm the low activity of the Roussel bricks. This level of contamination is acceptable for the internal part of the MINI-BINGO lead shielding.

We have demonstrated that we can realize lead radiopurity measurement in our above-

| Measurement temperature | Duration | Sample | ^{210}Pb contamination (Bq/kg) |
|-------------------------|----------|--------|---|
| 16 mK | 9h15min | Pb#1 | 0.94(5) |
| | | Pb#3 | 0.89(4) |
| 22 mK | 63h45min | Pb#1 | 0.98(3) |
| | | Pb#3 | 0.90(3) |
| 25 mK | 14h10min | Pb#1 | 0.91(4) |
| | | Pb#3 | 0.88(4) |

Table 6.13 – ^{210}Pb contamination measured in the different background measurements.

ground setup using samples directly cut from a brick. We are sensitive to low level of contamination which is promising since this method is a good alternative to the HP-Ge measurement and provides even more precise measurements. Finally, the same kind of bolometric measurements could be performed also on small BGO samples to evaluate for example their ^{207}Bi contamination level.

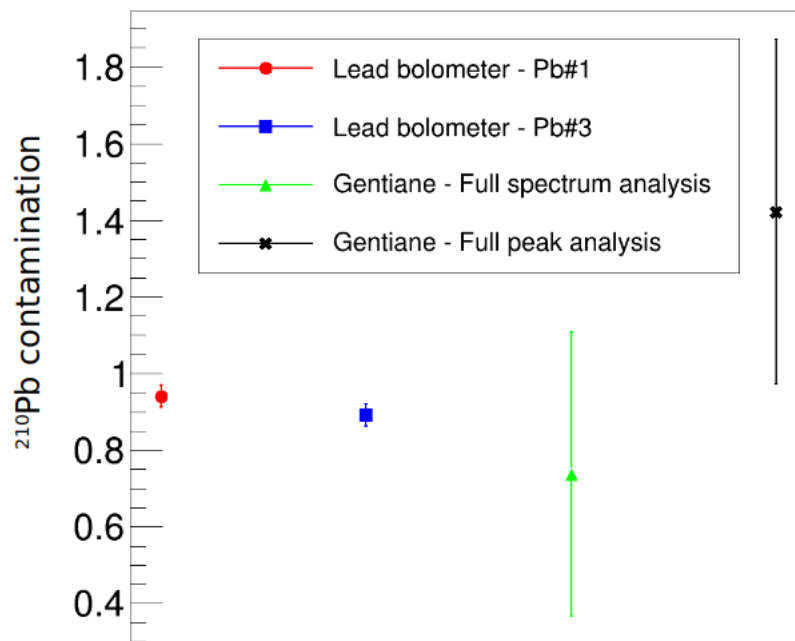


Figure 6.31 – Roussel brick mean contamination measured with lead bolometers and compared with the measurement of the Gentiane HP-Ge detector at LSM.

Chapter 7

Neganov-Trofimov-Luke light detectors

Neganov-Trofimov-Luke Ge light detectors are at the center of BINGO innovations. On the bolometer performance side, the light signal amplification they provide will allow the detection of Cerenkov light emitted by TeO_2 crystals and their use as scintillating bolometers. Moreover, a higher signal-to-noise ratio in the light channel is a desirable feature to reject the random coincidences from $2\nu 2\beta$ of ^{100}Mo in LMO crystals. The active veto will also benefit from the NTL light detector performance since it will help to reach the low energy threshold needed to achieve an efficient external γ rejection.

This Chapter will present the R&D campaign done in the framework of BINGO. It will start with a description of how they are fabricated and how they are usually characterized. Then, the results of new prototypes will be presented.

7.1 Preliminary considerations

As already mentioned in Chapter 4, NTL Ge light detectors coupled to TeO_2 bolometers were already successfully operated [151]. Moreover, another study developed a fabrication process and showed that it was giving reproducible and well-performing detectors [150], that could potentially be used in a large-scale bolometric experiment. The latter was done with five high-purity 44 mm diameter and 0.175 mm thickness circular Ge wafers with five 100 nm thick annular concentric electrodes deposited on the surface and separated by a 3.8 mm pitch (shown in Figure 4.3). They were operated with a voltage difference between 50V and 90V, giving an NTL gain of 10 for all of them.

The objective of BINGO is to demonstrate that, at least, such performance can be obtained on other shapes of wafers like square or trapezoidal ones. This implies studying different electrode geometry in order to optimize the charge collection and avoid as much as possible the trappings, with the goal also of getting an even higher gain. In parallel, the repeatability and robustness of the fabrication process with such wafers must be shown since more than 60 will have to be produced for MINI-BINGO.

With that in mind, we can now focus on what characterizes an NTL light detector. Two parameters are crucial for obtaining good performance. The first one is the maximum voltage difference that is possible to put through the electrodes before the appearance of a current, usually called a leakage current. Indeed, according to equation 4.1, the NTL gain is scaling linearly with the voltage difference. However, the amplification efficiency (η in the equation), which is the second parameter of importance, can influence the gain obtained at

each voltage. Therefore, it is also important to make sure that as much as possible charges are collected and are not being trapped by impurities. This is why NTL Ge LD are fabricated using high-purity Ge wafers. A common way to illustrate the performance of an NTL LD is by plotting the gain as a function of the voltage difference, as shown in Figure 7.1, also called a gain curve. It can be obtained by using an LED to inject light into the wafer at a low temperature through optical fibers reaching it. One can check how the amplitude of the given signal varies with the voltage difference through the electrodes. The slope of the gain increase is proportional to the amplification efficiency. Of course, the gain measured depends on the wavelength of the source [147]. Therefore, it does not represent the effective gain obtained for the scintillation light of a crystal to which it could be coupled if the LED does not have the same wavelength. Another way of determining it will be explained later. This method gives anyway a good estimation of the overall performance of the LD.

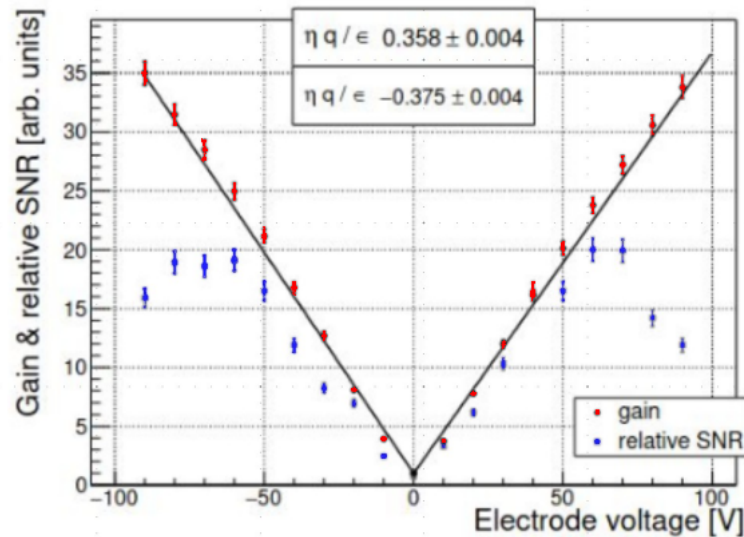


Figure 7.1 – Gain as a function of the voltage difference through the electrodes of an NTL LD tested in Ref. [150]. The SNR at each point is also shown.

Moreover, one can also see that there is usually an optimum voltage difference where the signal-to-noise ratio is the highest. This behavior is more related to the setup as it was demonstrated in Ref. [150]. It is, therefore, important to monitor also the baseline RMS while choosing the voltage difference to ensure the best performance for the detector.

The best electrode geometry would be the one maximizing the surface covered by electrodes that can handle the highest possible voltage difference without showing a leakage current and that maximizes the charge collection. In addition, in our case, other points can be important such as the easiness of the electrode deposition for mass production, the easiness of their bondings, and the reproducibility of the detectors.

7.2 NTL light detector fabrication

The high-purity Ge substrates (impurity of the order of $10^{11}/\text{cm}^3$) used for the fabrication of the NTL LD tested in this thesis have been produced by Umicore. They are circular wafers available in different thicknesses and diameters in which we cut the shapes needed for our detectors. The deposition of Al electrodes can be done on the obtained Ge detector. In this

thesis, two methods were used and they will be described here below:

The shadow mask method - This method is the one that was used in the past on circular wafers with circular electrodes mentioned earlier. The Ge wafer is placed in an evaporator under a vacuum with a mechanical mask on it covering the parts where we do not want electrodes. Before electrode evaporation, a surface treatment is done. The surface is bombarded with Ar ions in order to remove the oxidized Ge layer and improve the adherence of the subsequent depositions. Following that, the deposition of a 50 nm thick layer of amorphous germanium and hydrogen (a-Ge:H) is done. It will act as an insulation layer, reducing the risk of an apparition of a leakage current [178]. Finally, the 100 nm thick Al electrodes can be evaporated. Depending on the shape of the electrodes, the mechanical mask can need to be rotated manually to obtain the desired pattern (Figure 7.2). It implies breaking the vacuum of the evaporator and realizing an additional small Ar bombardment each time, increasing the number of steps and production time. At the end, a SiO coating can be realized on the whole surface to enhance the light collection. This method has already proven its suitability for obtaining robust detectors achieving good performance with a high gain and high voltage handling. However, it requires producing a mechanical mask for each electrode pattern we would like to test. It has to be commercially ordered and take time (~2 months) to be fabricated. We decided to try a new way to make the electrodes that was easier and faster to try new geometries for our R&D purpose.

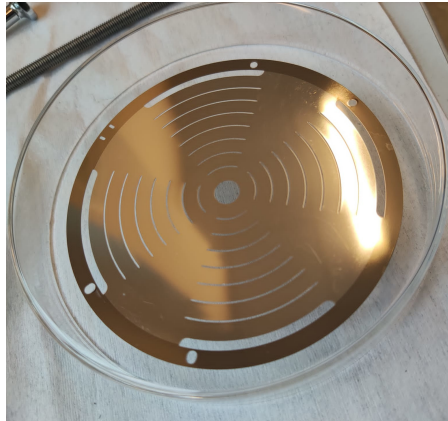


Figure 7.2 – Mechanical mask used with the shadow mask method to evaporate annular electrodes of the wafer surface. It has to be rotated in order to complete the electrode rings and so the evaporation has to be done in 3 steps: (1) Ar bombardment + a-Ge:H evaporation. (2) Rotate the mask, then Ar bombardment, a-Ge:H evaporation and Al evaporation. (3) Rotate the mask, slight Ar bombardment + Al evaporation.

Photo-lithography with lift-off - With this method, the wafer is first completely covered with a photo-sensitive resin layer. The parts where we want electrodes are exposed to light thanks to a commercial mask that is way quicker to get than the one of the previous method (~1 week), removing the resin at the electrode positions. The wafer is placed in the evaporator under vacuum and the same surface treatment (as the one of the shadow mask method) is done before evaporating the Al. Finally, the remaining resin can be removed with an acetone bath, revealing the electrode pattern. All the steps are summarized in Figure 7.3. A SiO coating can also be done afterward. This method is really promising since evaporation can be done in one step, reducing the production time. Moreover, it is more convenient to

test new electrode geometries since the delay in getting a new mask is smaller. Moreover, it allows us to make electrode patterns with a resolution of $1\ \mu\text{m}$ against $20\text{-}30\ \mu\text{m}$ with the shadow mask method. However, since it was the first time that such a method was used for thin Ge wafers, its suitability needed to be confirmed.

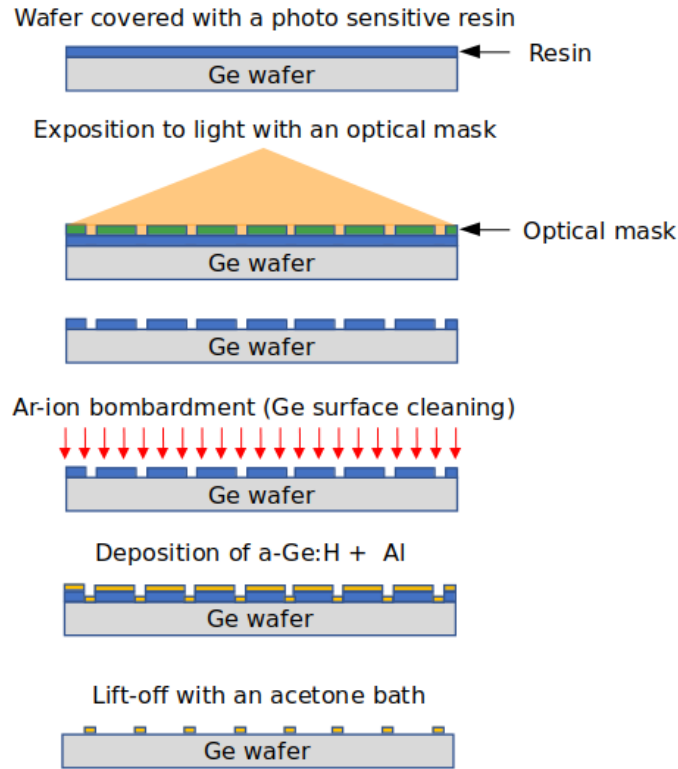


Figure 7.3 – Schematic view of the photo-lithography with lift-off method to evaporate the electrodes on the wafer.

Once the electrodes are deposited, they are bonded between each other to form two sets allowing us to apply a voltage difference. It is done with $25\ \mu\text{m}$ Al wires. A small NTD Ge is similarly glued on the surface as for standard Ge LD. However, it must not be glued directly on an electrode but on a bare part of the wafer, preferably at a reasonable distance of the last electrode to avoid leakage current through it. Finally, the detector is mounted in its assembly, the NTD is bonded as usual and the most external electrode of each set is connected to gold pads situated on a kapton foil glued on the holder, similarly to the NTD bondings. From there, Cu wires are soldered to connect the sets to the cryostat wiring.

7.3 Three new electrode designs

As already stated, we need to find the best electrode geometry for our square and trapezoidal light detectors. We decided to start with the square wafers and we came up with three new electrode geometries, each with its own specificity, with the goal in mind to get the best performance from our NTL LDs. They were all produced with the lift-off photo-lithography and so were also the first tests of this method.

7.3.1 Edge geometry

With this design, the Al electrodes are deposited on the two lateral edges of a square $45 \times 45 \times 0.3 \text{ mm}^3$ Ge wafer. Since the two electrodes are separated by 45 mm, we expected a low electric field throughout the Ge and so to be able to put a high voltage difference. Of course, this distance increases also the probability of having charge trappings with eventually a negative impact on the gain. However, if the voltage difference is high enough, gain values within BINGO requirements could be obtained. Another advantage of this geometry is the simplicity of the electrode design: it does not require any complicated mask but just to cover the two wafer surfaces during the evaporation. Several samples could be put against each other in the tool used to hold the wafers during evaporation (see Figure 7.4), making mass production easier and faster. A preliminary test not reported in this thesis showed that to prevent leakage currents from the two not-coated edges, an additional step was required in the fabrication procedure: a chemical etching of the four edges done as the first step. It removes a $10 \mu\text{m}$ Ge layer which contains more impurities due to cutting and surface contamination implying charge transport and leakage current development.

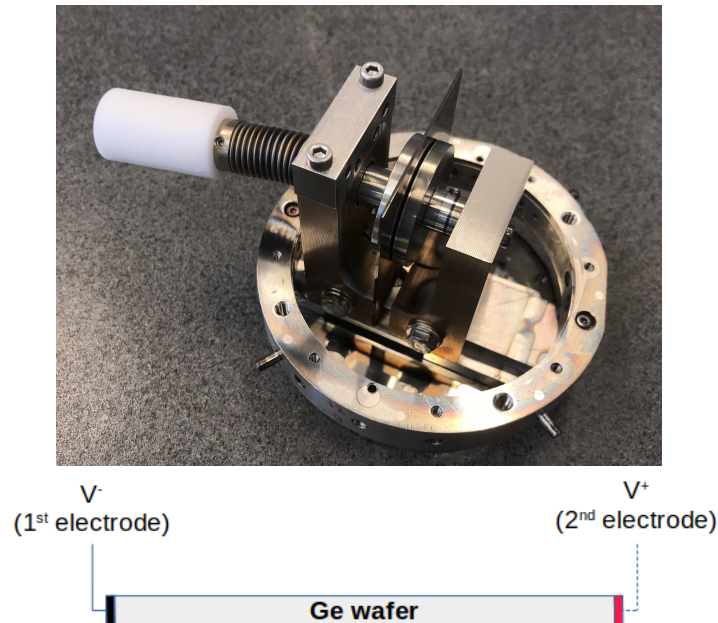


Figure 7.4 – *top*: Photo of the wafer mounted in the tool used for the evaporation of the Al on the two edges. The planar surfaces are covered with resin. *bottom*: Schematic view of the electrode bonding for the edge geometry.

7.3.2 Concentric geometry

This geometry is the most straightforward way to adapt the annular geometry to square $45 \times 45 \times 0.3 \text{ mm}^3$ wafers. There are five square electrodes with rounded angles and a circular central one allowing an efficient coverage of the wafer surface. We kept the same pitch of 3.8 mm between the center of each $200 \mu\text{m}$ thick electrode, with the most external electrode being a 2 mm grid, as it can be seen on the top photo in Figure 7.5. The bondings are done to form two sets of electrodes, as it is shown in the bottom part of the same figure.

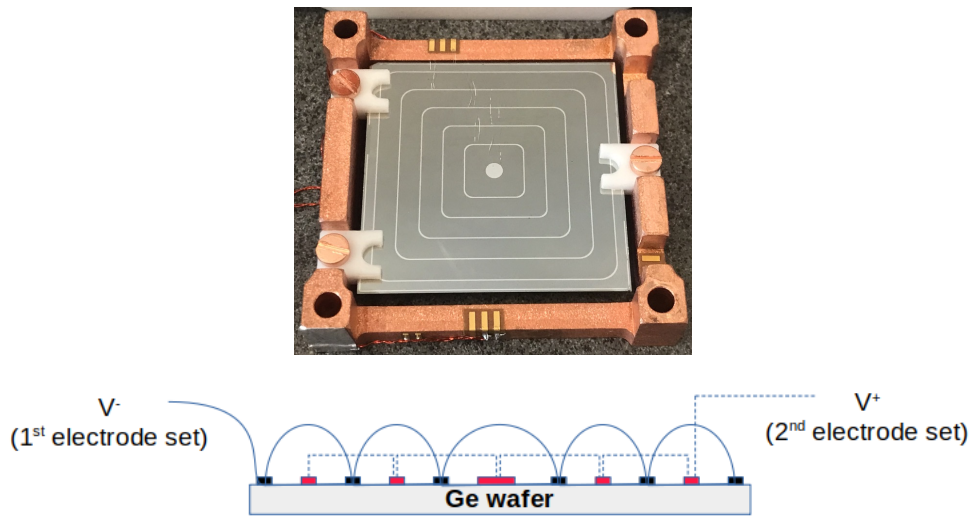


Figure 7.5 – *top*: NTL LD with a concentric electrode geometry inside a copper holder. *bottom*: Schematic view of the electrode bonding for the concentric geometry.

7.3.3 Meander geometry

Finally, the last electrode geometry consists of two 200 μm thick electrodes meandering in a sort of spiral shape on the $45 \times 45 \text{ mm}^2$ Ge surface (see Figure 7.6). The main advantage of this design is that only two bondings are required since only two electrodes are present while keeping the spirit of the concentric geometry and a similar electric field. It quite simplifies the assembly procedure. The distance between the two electrodes is 3.8 mm everywhere, and the most external one becomes a 2 mm grid at the edge of the wafer.

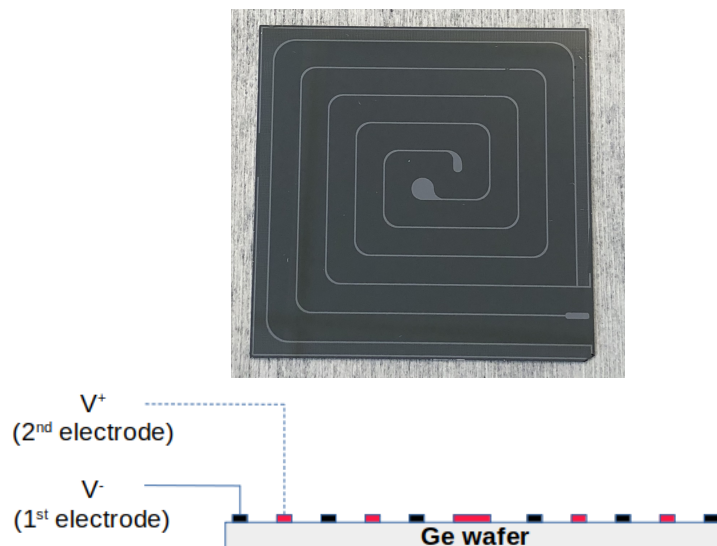


Figure 7.6 – *top*: NTL LD with the meander design for the electrode *bottom*: Schematic view of the electrode bonding for the meander geometry.

7.4 Cryogenic test and results

Detector assembly

We realized a measurement at low temperatures of NTL LDs with these three new electrode designs. We mounted them in two different assemblies in which they were facing LMO crystals. The first one is a BINGO nylon assembly described in Chapter 5, where an edge vertical $45 \times 45 \times 0.3 \text{ mm}^3$ Ge NTL LD was placed on one side and a concentric NTL LD of the same dimensions, called here Concentric2, was placed on the other side. The second assembly is a CROSS-like one, where the two light detectors are in a horizontal position at the top of the crystal, clamped by PTFE pieces. In this one, a second concentric $45 \times 45 \times 0.3 \text{ mm}^3$ NTL LD, called Concentric1, was assembled along with a meander NTL LD of the same dimensions facing the second LMO crystal. The two assemblies were attached together, with a copper plate separating them, before being screwed to the floating plate of the Ulysse cryostat (Figure 7.7).

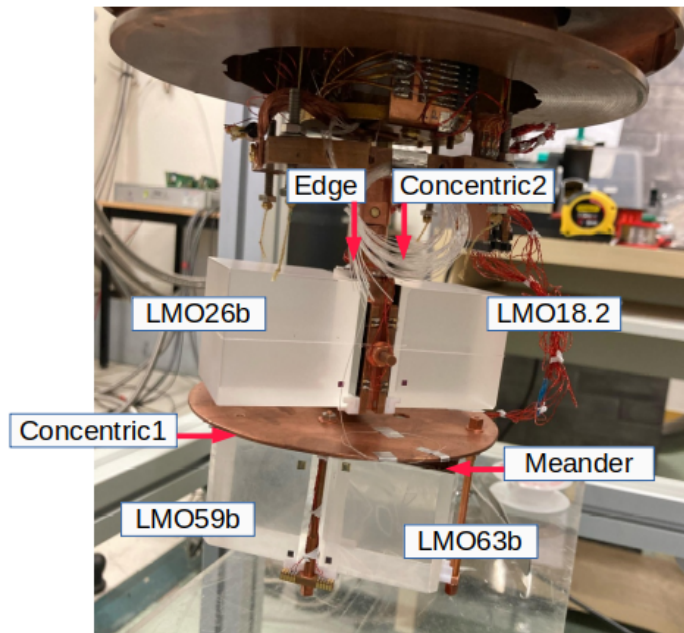


Figure 7.7 – The assembly used to test the three new electrode geometry attached to the Ulysse floating plate. It is composed of a BINGO module (top) and a CROSS one (bottom).

Each LD was equipped with an NTD Ge with dimensions of $3 \times 1 \times 1 \text{ mm}^3$ except for Edge which had a smaller one of $3 \times 0.5 \times 1 \text{ mm}^3$. All the crystals also had on their surface an NTD Ge glued for the dual heat and light readout, but we will not discuss their performance here since our main interest is NTL light detectors.

In addition, an LED placed outside the cryostat at room temperature could also shine with an 820 nm light all the detectors through an optical fiber reaching the floating plate stage. It was used periodically for space charge neutralization and to check NTL gain depending on the voltage difference applied through the electrodes. Its wavelength is a bit shifted compared to LMO scintillation light which is at around 630 nm.

Gain curves

The cryostat was first cooled down at 18 mK. The first thing we realized is the determination of the maximum voltage each detector could handle before the apparition of a leakage current and we drew gain curves shown in Figure 7.8 using pulses injected with the LED at that temperature.

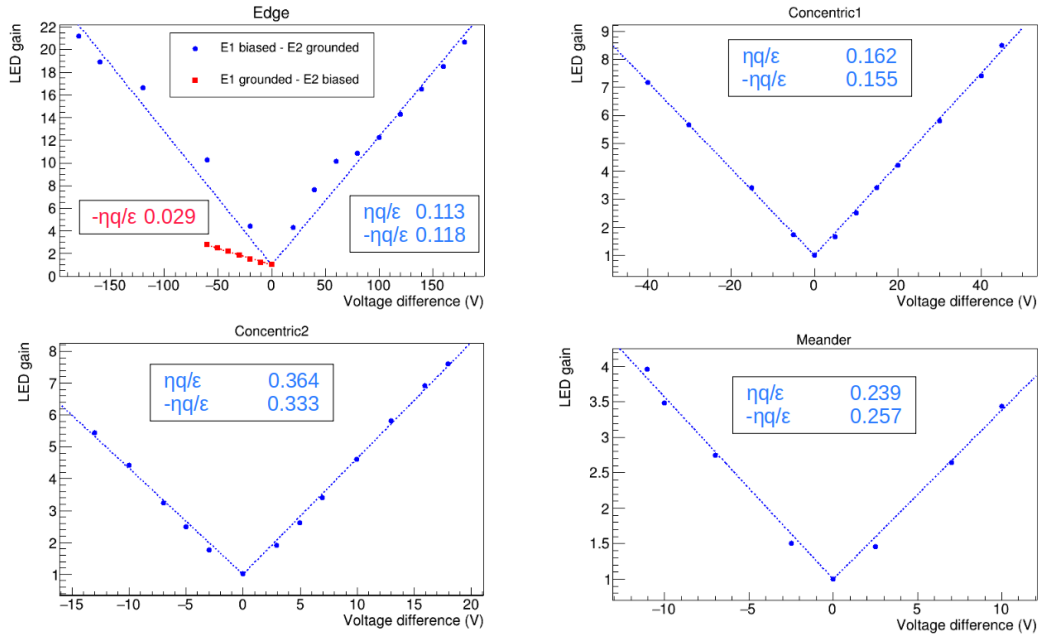


Figure 7.8 – Gain curves obtained at 18 mK using the LED. Positive and negative bias sides have been fitted independently using a linear function passing by 1. The slope corresponding to the factor $\eta q/\epsilon$ in equation 4.1 is shown.

Before discussing the gain curves obtained, it is important to underline that the measured gain using the LED is not representative of the effective gain that can be obtained for the crystal scintillation light. Indeed, here, the optical fiber bringing the LED light to the floating plate level was placed in such a way that all the LDs saw it. However, its position did not ensure that their surface was shined homogeneously and we saw that some of the LDs saw more the LED light than others. It impacts both the parameters η and ϵ , giving a wrong estimation of the real gain that can achieve the LD. A more reliable procedure could consist in diffusing the LED light to ensure that it reaches all the detectors homogeneously. Moreover, we could consider having one optical fiber per LD.

This study using the LED is interesting in our case since we can see how the slope changes depending on how the bias is applied between the sets of electrodes. For all the LDs, the voltage difference was applied by grounding one of the two sets of electrodes while connecting the other one to a DC power supply. For Concentric1, Concentric2 and Meander, we observed just a slight difference - not reported in Figure 7.8 - between the gain measured when putting the bias on the first set and grounding the second one and doing the opposite. However, for Edge, we saw a big difference depending on which electrode was biased, as can be seen on its gain curve. For the first configuration, we were able to put high positive and negative voltage differences and observe a gain. However, when we swapped which electrode was biased, the behavior changed completely: we observed a leakage current when putting

any positive voltage difference, while for negative values, a leakage current appeared around -60V with a poor gain obtained. We think that this could be due to the position of the NTD on the wafer. Since it is glued closer to one of the two electrodes, the leakage current could appear directly through it. We did not keep track of the electrode which was the closest to the NTD. However, regarding the results, we think that it was E2. In addition, observed a difference in the obtained gain between positive and negative bias values for all the LDs. This behavior is common and was already observed in the past.

Another important piece of information obtained with this study is the maximum voltage difference that can be applied through the electrodes before seeing a leakage current. The latter is, in general, easy to recognize. After passing a critical voltage difference, a flow of electrons starts to circulate in the wafer. We observe then a sudden rise of temperature of the detector but also of the cryostat in most cases due to the power dissipation. For each light detector, the critical measured value is reported in Table 7.1. As expected, the edge geometry allows us to put a really high voltage difference through the electrodes. We tried up to 200 V, which was the maximum of our power supply. We did not see any leakage current even at this value, meaning that, in principle, it could handle higher values. For the concentric geometry, one could handle 55 V before seeing a leakage current for higher values, while it was possible to put at maximum 23 V on the other one. This difference is quite puzzling since these two LDs were fabricated following exactly the same procedure. Although the statistic is really low, it can raise questions about the repeatability of the method. Finally, we were able to put through the two electrodes of the meander LD only a maximum of 15 V. In any case, the measurement of the effective gain for the LMO scintillation is required to have a complete picture of their performance. By monitoring the noise level at each point, we chose a voltage difference where it was minimum to operate them. These values are also shown in Table 7.1.

| Detector | Max voltage difference (V) | Best voltage difference (V) |
|-------------|----------------------------|-----------------------------|
| Edge | >200 / <-200 | 190 |
| Concentric1 | 55 / -50 | 35 |
| Concentric2 | 23 / -22 | 16 |
| Meander | 15 / -15 | 10 |

Table 7.1 – Maximum voltage difference applicable before seeing a leakage current for each detector. The voltage difference at which we operated the detectors is also shown.

Measurement results

We determined the best working point for the NTD bias of each LD by looking at the bias where the LED pulse was maximum. Since the NTD of Edge was smaller than the others, it showed a really high resistance. Hence, it was necessary to operate it at 18 mK and overbias it to obtain the best performance. For the others, the results presented here have been obtained at 14 mK.

For each detector, we performed a measurement without and with biasing the electrodes to compare the performance. In the former case, the energy calibration was realized using the muon distribution for which the maximum is at 200 keV for 0.3 mm thick wafers in a horizontal position and at 260 keV for those in a vertical position. However, when the electrodes are

biased, the muon bump tends to enlarge due to some events with partial amplification. Thus, it is more precise in that case to realize the calibration using the light yield value of the γ/β band measured during the measurement at 0 V thanks to the heat/light coincidence with the LMO crystals they were facing. The light yield plot of Concentric1 not biased and with 35 V through the electrodes is shown in Figure 7.9. We measured for all the detectors a light yield of 0.13 keV/MeV, which is relatively weak since none of the LD was coated with SiO. In comparison, when the LDs are SiO coated, we usually measure a light yield of around 0.24 keV/MeV (see Chapter 5). However, one can clearly see the amplification of the signal thanks to the NTL effect when bias is applied through the electrodes. It improves the signal-to-noise ratio and so the discrimination power, allowing a better α rejection although the light yield is low. We can compute it for the events with energy superior at 3 MeV and we found 1.91 for Concentric1 when not biased while it becomes 5.12 with 35 V, allowing in the latter case an α rejection higher than 99%.

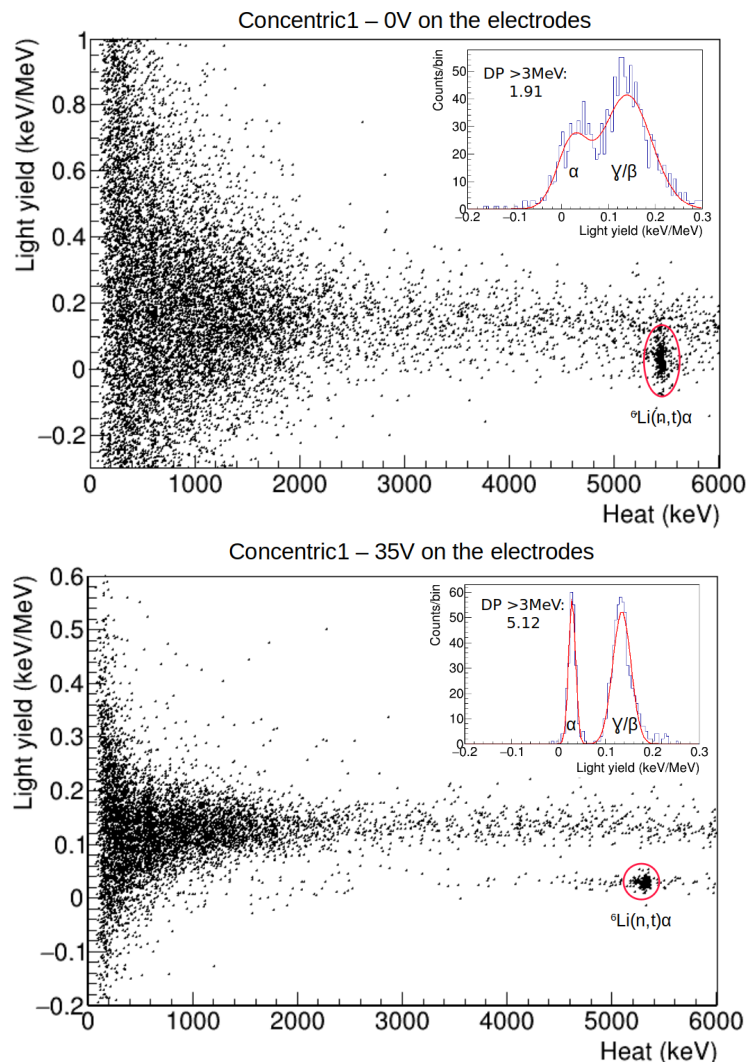


Figure 7.9 – *top*: Light yield measured by Concentric1 with 0V through the electrodes as a function of the heat measured in LMO59b, the crystal it is facing. *bottom*: Same plot but with 35 V applied through the Concentric1's electrodes.

We can define the effective gain, which corresponds to the boost of the SNR, as the ratio between the baseline FWHM during the measurement with the electrodes off and the one with the electrodes on. All the results obtained for each LD are summarized in Table 7.2.

| Detector | Temperature (mK) | Current (nA) | Electrode bias (V) | Sensitivity ($\mu\text{V}/\text{keV}$) | FWHM _{bst} (eV) | Effective gain | DP >3 MeV |
|-------------|------------------|--------------|--------------------|--|--------------------------|----------------|-----------|
| Edge | 18 | 5 | 0 | 1.1 | 508 | - | 1.8 |
| | | | 190 | 13.1 | 82 | 6.2 | 3.1 |
| Concentric1 | 14 | 1 | 0 | 1.8 | 404 | - | 1.9 |
| | | | 35 | 12.3 | 56 | 7.2 | 5.1 |
| Concentric2 | 14 | 0.46 | 0 | 1.1 | 1172 | - | 0.2 |
| | | | 16 | 5.4 | 262 | 4.5 | 2.6 |
| Meander | 14 | 1 | 0 | 1.6 | 686 | - | 0.2 |
| | | | 10 | 5.4 | 219 | 3.1 | 2.1 |

Table 7.2 – Comparison of the performance of each NTL light detector with and without bias through the electrodes.

Despite the high voltage difference put through the Edge electrodes, we see that we obtain an effective gain of only 6.2. It confirms that this geometry is subject to a lot of charge trapping, leading to incomplete signal amplification. It also explains another observation that we made: this LD was really long to regenerate using the LED and this procedure could take around half an hour, while for the others, it was taking less than 5 minutes on average. Since we didn't observe any leakage current up to 200V, it seems that, in principle, we could reach higher gain values by increasing the bias. However, having such high voltage value on many detectors in the cryostat environment could be risky and difficult to handle.

The detector that obtained the best effective gain value is without any surprise Concentric1. Indeed, it has a geometry that allows a similar electric field to the annular electrode one, which obtained good results in the past. In addition, it was the detector of this kind that was operated at the highest voltage difference. Unfortunately, being limited by a leakage current at 55 V, the gain obtained is lower than 10, which was our main objective for this batch of detectors. Moreover, we can see that for the second concentric detector produced using exactly the same fabrication protocol, we observed a leakage current at a much lower value, and we had to operate it at only 16 V. Its effective gain is accordingly impacted and so is lower than 5. It's a pity since if we consider that the gain scale linearly with the voltage difference, we could have expected a gain close to 10 at 35 V, so even higher than Concentric1 measured one. This reproducibility issue is a problem for ton-scale experiments and has to be investigated further. On a brighter side, these two LDs are a good example of how powerful is the NTL amplification for bolometric light detectors: due to the low light yield and its high noise before amplification, Concentric2 did not reach any α discrimination ($(\text{DP}<1)$) before amplification while afterward, at least a partial one was achieved ($(\text{DP}>2.5)$). For Concentric1, we went from a partial identification ($(\text{DP}<2)$) to a complete alpha rejection after amplification ($(\text{DP}>3.1)$). It confirms what was already stated for the underground test of the BINGO tower in Chapter 5: with a minimal NTL amplification, all the detectors would have reached a complete α rejection. Finally, the Meander geometry showed a small effective gain of 3.1 due to the small bias at which it was possible to operate its electrode.

In general, none of the detectors of this batch reached our performance objective and were able to reproduce the results obtained on circular wafers with annular electrodes. Although the concentric and meander geometries are supposed to allow a similar electric field, they showed

a leakage current at a way lower voltage difference than the latter, limiting their reachable effective gain. This result raised doubt about the photo-lithography with the lift-off process to make the electrodes. Even if the surface treatment done before the Al evaporation is the same as for the shadow mask method and although we kept the same distance between the electrodes, it seems that the photo-resin coverage is somehow impacting the Ge surface, which leads to leakage currents at lower bias values. Of course, this conclusion is not definitive since the amount of LDs made with this method is rather small. The procedure could be studied and improved in the future. Nevertheless, in order to have some answers and also more results for the BINGO R&D, we decided to move on to the production of a new batch of detectors using, this time, the old shadow-mask method and see if, at least, better performance could be obtained.

7.5 Back to the basics

The shadow-mask method requires a mechanical mask containing the electrode geometry. At that time, we only had the one shown in Figure 7.2 with 100 μm -thick annular electrodes separated by 3.8 mm. We produced as a reference three new 45 mm diameter and 0.175 mm thickness circular NTL light detectors to cross-check the performance obtained in the past. We evaporated this pattern also on three square wafers. This geometry is not optimized for square wafers since the two most external electrodes are not fitting on the surface and are therefore not bonded. It means that at the end, the square NTL has only four annular electrodes plus the central one bonded instead of five rings and the central one as for the circular ones. However, this test is a good preliminary determination of the difference between the performance obtained with the photolithography and shadow mask methods. In addition, all the wafers were coated with SiO on the surface where the electrodes are. Only a small band across the surface was left bare to avoid bonding the electrodes through the SiO.

For this measurement, it was decided not to couple the LD with a crystal. The circular wafers were mounted inside circular copper holders, clamped by three PTFE pieces which is exactly the same configuration as in Ref. [150] that is closed with a copper cap. For square wafers, similar square holders were made where three PTFE pieces also clamp the detectors and that can also be closed with a copper cap. The two types of detectors inside their respective holders are shown in Figure 7.10.

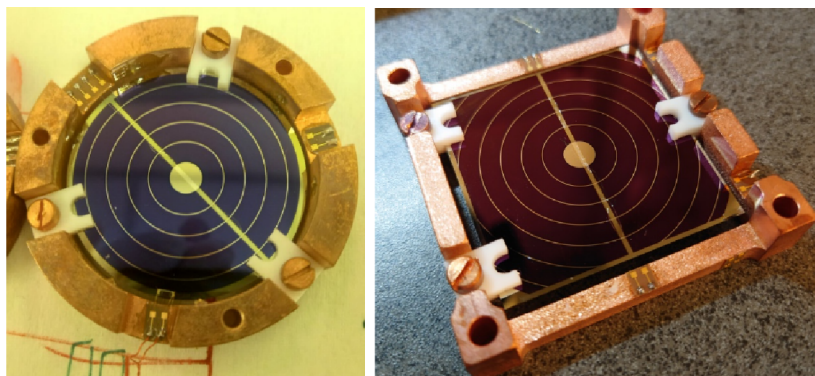


Figure 7.10 – *left*: Circular NTL light detector with annular electrodes mounted in its copper holder. *right*: Square NTL light detector with annular electrodes mounted in its copper holder. For both, the central band corresponds just to the bonding part where there isn't any SiO coating.

We glued on each LD a 41B $3 \times 1 \times 1$ mm³ NTD and we stacked the holders in a tower that we attached to the Ulysse floating plate, with square LDs on the top and circular ones on the bottom as shown in Figure 7.11. During this test, three other LDs were placed in the tower but they will not be discussed here since the purpose of their measurement is out of the scope of the present work.

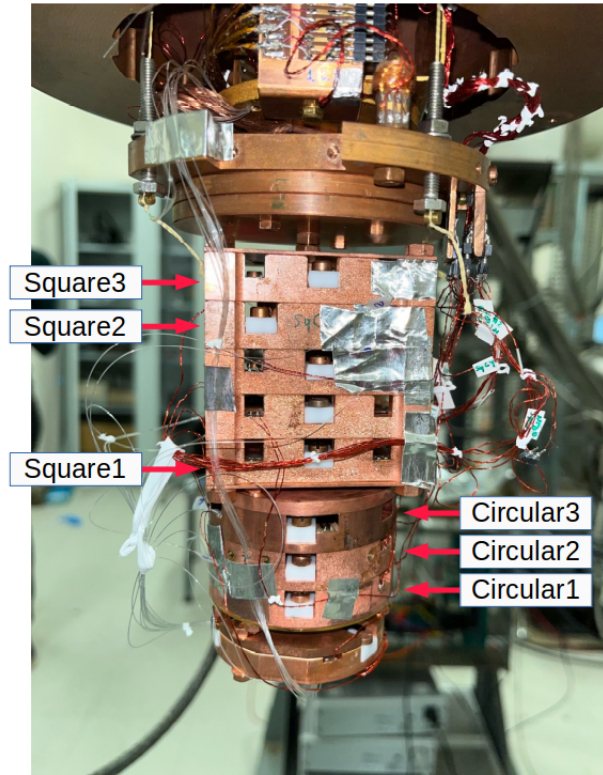


Figure 7.11 – The NTL LDs tower attached to the Ulysse floating plate.

In addition, we put an optical fiber in each detector assembly which brought the light of the room-temperature LED. We changed the model of the latter to use a new one with an emission wavelength of 610 nm, much closer to the LMO scintillation light wavelength. In this configuration, all the LDs are shined homogeneously with a light similar to LMO scintillation light. The gain curve can give this time more accurate information about the signal gain and can allow a relative comparison between each electrode geometry.

The cryostat was finally cooled down at 20 mK, the temperature at which we did the gain curves. Unfortunately, the NTD contacts of Square2 were lost at low temperatures and it was not possible to measure it. Thus, we just estimated its maximum voltage difference value by looking at starting which bias put through the electrodes the cryostat mixing chamber was suddenly rising in temperature. Moreover, Circular3 showed an unusual behavior for not yet explained reason: its baseline was a lot affected by voltage variation through its electrode, shifting each time and never recovering to its value before voltage application. It was also really long to regenerate using the LED. We decided not to do the gain study for this LD but just to evaluate its leakage current value. For all the four other LDs, the gain curves were done in three different bias configurations: both set of electrodes bias at an opposite value, only one set biased and the other one grounded, and the mirror configuration. We observed a difference as in the previous test for the two last configurations with one better

than the other while it appeared that the two sets biased configuration was actually showing the average gain value of the two others. The curves presented in Figure 7.12 were obtained with the best bias configuration. The maximum voltage value of each LD and, in the case where it was possible to determine it, the best bias where the highest signal-to-noise ratio was obtained are reported in Table 7.3. The gain values reported in this table correspond to the LED gain and not to the effective gain defined earlier. While looking at them, it is important to remember that the latter could be lower, being limited by detectors' intrinsic baseline resolution. However, it is a good approach for preliminary performance estimation.

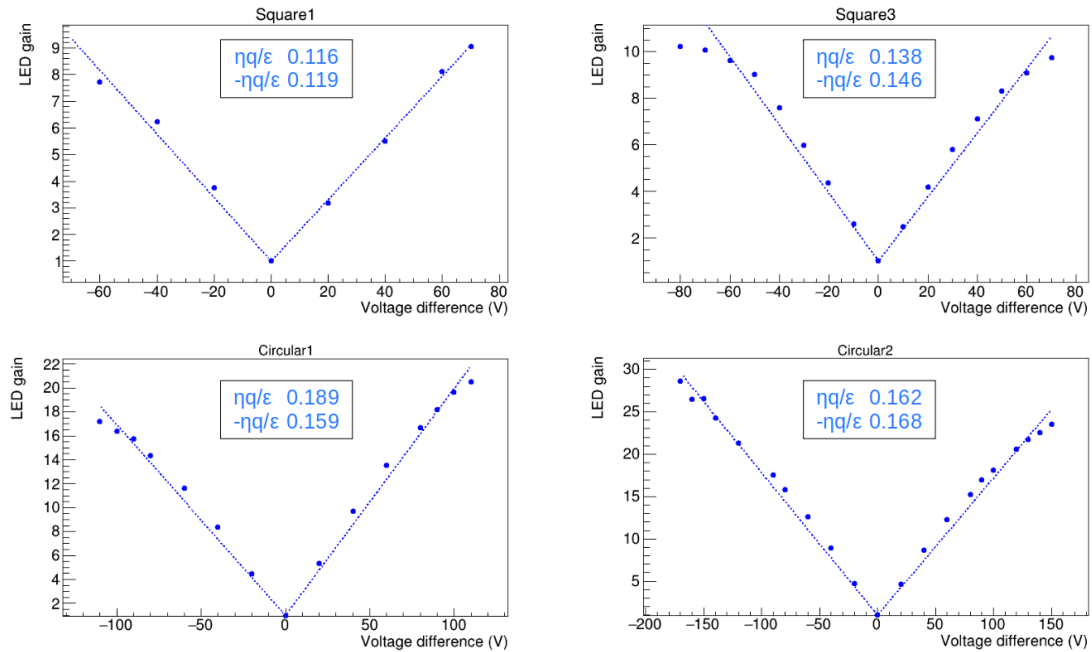


Figure 7.12 – Gain curves of the two square NTL LDs with annular electrodes (top) and of the two circular ones with annular electrodes (bottom). The positive and negative sides have been fitted independently using a first-order polynomial function passing by 1. The values for the coefficient of the slope obtained are shown.

The first important result from this study is that compared to the previous test with photolithography-made NTL LDs, we were able here to put a larger bias difference through the electrodes of each LDs. It seems to confirm that the shadow mask method works better for electrode evaporation. For circular wafers, one can see that leakage currents appeared at really high bias values, even higher than 150 V while for square ones, it was around 100 V. Regarding the LED gain, thanks to the high voltage difference at which it was possible to operate them, the circular LDs have obtained really high amplification confirming the excellent performance they can reach. For square wafers, since the electrodes cover only 56% of the total Ge surface, we were accordingly expecting a smaller gain for the same voltage difference. This is what we observed with a gain of 9 for both at maximum. However, this is already quite promising since, in the future, we could order new mechanical masks and test, for example, the concentric electrode geometry. The latter should get better results since it allows complete signal amplification on the whole wafer surface. If we now consider the reproducibility, we can see that for the same wafer shape, the leakage current appears at around the same voltage difference value, with some exceptions depending on the bias

| Detector | Max voltage difference (V) | Best voltage difference (V) | Gain |
|-----------|----------------------------|-----------------------------|------|
| Square1 | 83 / -83 | 70 | 9 |
| Square2 | 100 / -100 | - | - |
| Square3 | 100 / -100 | -50 | 9 |
| Circular1 | 190 / -120 | 90 | 18 |
| Circular2 | 190 / -190 | -170 | 28.5 |
| Circular3 | 180 / -180 | - | - |

Table 7.3 – Maximum voltage difference applicable before seeing a leakage current for each detector. The voltage difference at which we operated the detectors is also shown.

configuration. This is encouraging, but of course, a larger statistic will be required before drawing a definitive conclusion.

This measurement was a preliminary study of the shadow mask made annular electrodes on square wafers and the performance investigation was not pushed further. Instead, we focused on the production of a batch of 10 square NTL LD using exactly the same procedure. This batch is under test during the writing of this thesis in the LSC underground laboratory in a tower with each detector coupled to a LMO crystal. The reproducibility of the detector performance will be studied, as well as their behavior when they are coupled to crystals regarding, for example, the α rejection. It is an important test for BINGO that will, in principle, definitely state the method that will be used for electrode evaporation for the MINI-BINGO demonstrator. Moreover, an order has been made for new mechanical masks with concentric geometry and the meander one. These geometries, coupled with the shadow-mask method, will be tested in the coming months. The work done in this thesis was only the beginning of the R&D campaign regarding NTL LDs for bolometric measurements, and the work will be pursued to obtain the best ones possible and reach all the ambitious BINGO objectives.

7.6 Discussion on random coincidences rejection using NTL light detectors

One of the limitations of bolometers operated with NTD Ge is their relatively slow response to an energy deposition. As already mentioned, it can induce a source of background when using crystals embedding ^{100}Mo . Indeed, due to the fast $2\nu 2\beta$ half-life of this isotope, the probability of having a random coincidence between two events of that nature is rather high and can lead to a misinterpretation of these two signals as a single one landing in the ROI. We can estimate the number of expected pile-up events I_{PU} in an energy interval $\Delta E=1\text{keV}$ around the Q-value of ^{100}Mo (3034 keV). Starting from a Poisson law, we can write:

$$I_{PU} = \tau \times I_0^2 \times \epsilon = \tau \times \left(\frac{\ln 2 \times N}{T_{1/2}^{2\beta}} \right)^2 \times \epsilon \quad (7.1)$$

With I_0 the rate of $2\nu 2\beta$ events, N the number of ^{100}Mo nuclei, ϵ the probability that the sum of the two $2\nu 2\beta$ events involved in the pile-up is equal to $Q_{\beta\beta}$, and τ the time resolution of the detector. Finally, we can deduce the background index b_{PU} that this represents:

$$b_{PU} = I_{PU} \times \frac{T_0}{m} = \tau \times I_0^2 \times \epsilon \times \frac{T_0}{m} \quad (7.2)$$

where T_0 is the number of seconds in one year and m is the mass of the crystal.

For a 95% enriched LMO crystal with a mass of 280 g, we have $N = 9.215 \cdot 10^{23}$ ^{100}Mo nuclei, leading to a $2\nu 2\beta$ decay activity of $I_0 = 2.84 \cdot 10^{-3}$ Bq. We can determine ϵ by performing the convolution of two energy spectra of the $2\nu 2\beta$ decay, giving us the energy spectrum of the pile-ups and thus the probability of having an energy of 3034 ± 1 keV. We find $\epsilon = 3.3 \cdot 10^{-4}$ [179]. We obtain a rough estimation of the pile-up contribution to the background as a function of the detector time resolution:

$$b_{PU} = 3 \cdot 10^{-4} \times \left(\frac{\tau}{1 \text{ ms}} \right) \quad [\text{ckky}] \quad (7.3)$$

To be more exact, we should take into account that for pile-up signals the optimal filtering slightly changes the energy as it is shown in Ref. [153] which would slightly change the above formula. In bolometers, the time resolution depends on the rise time of the signal but can be improved thanks to off-line analysis cut based on, for example, the pulse-shape. It was shown in Ref. [152] by using the heat channel, which has a rise-time of the order of 15 ms, a 90% rejection of pile-up events separated by more than 2 ms was feasible. It gives a background contribution at the level of $6 \cdot 10^{-4}$ ckky in the ROI, which is of course really worrying for BINGO, but also and especially for CUPID, since it would already prevent it from reaching its objective of 10^{-4} ckky in the ROI.

Since Ge light detectors have a signal rise time around one order of magnitude lower than the crystals, it seems that they are the key to reaching a better time resolution and so reduce the pile-up contribution. With their rise-time around 1 ms, we can expect a background contribution of $3 \cdot 10^{-4}$ ckky, which is still too high for CUPID, but pulse-shape cuts could reduce it in the same manner as for the heat channel. However, the limitation of the light channel lies in its signal-to-noise ratio, which is much lower than the heat channel one. It makes these cuts way more complicated and less efficient. The problem is that for CUPID, the pile-up contribution objective is of the order of $0.5 \cdot 10^{-4}$ ckky which needs roughly a time resolution of around 0.17 ms. This value seems out of reach with the current Ge LD configuration and an improvement of the baseline design is definitely required.

This is why the NTL Ge LD technology developed for BINGO should also have a huge impact on CUPID. Thanks to the SNR boost it provides and if we manage to demonstrate their suitability for large experiments, it could be considered for the CUPID baseline design. A recent work described in Ref. [153] has studied the impact of the signal-to-noise ratio on the pile-up rejection in the light channel using the current performance reached by NTL light detectors. They obtained the plot shown in Figure 7.13. It represents the pile-up background contribution as a function of the SNR for different rise time values. One can see that the larger the SNR, the better the pile-up rejection capability until a sort of plateau. The current simple Ge LDs reach an SNR of 10 with a rise-time of the order of 1.2 ms. Therefore, if we consider an NTL LD with an amplification factor of 10, as it was already obtained and which gives an SNR of 100, the background contribution would be of the order of $1 \cdot 10^{-4}$ ckky. It is still a bit high for CUPID but reducing the rise time by for example, optimizing the NTD geometry or their resistance could help to reach a background value within CUPID requirements.

In any case, for the BINGO objective of background around 10^{-5} ckky, an improvement of the NTL light detectors SNR is mandatory compared to what is currently reachable. Different strategies can be explored in parallel, including:

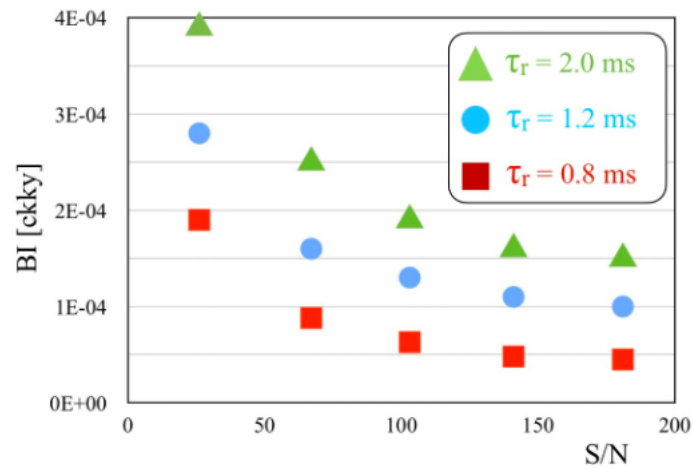


Figure 7.13 – Pile-up background contribution as a function of the SNR in the light channel after optimal filtering and pulse-shape cuts. The study was made with different signal rise times τ_r . Figure from [153].

- **Working on the light detector’s intrinsic baseline resolution:** Applying a gain of 10 on a light detector having already a better signal-to-noise ratio than 10 before amplification can allow achieving, in the end, a way higher SNR. It can be done by working on the noise conditions of the setup, on how the LD is fixed and so on.
- **Obtaining better NTL amplification:** So far, the gain of 10 is considered to be obtained by circular LDs with annular electrodes and is expected to be demonstrated for square wafers with new geometries as the concentric one, for example. However, we can think that other geometries can be studied in order to try to obtain an even better amplification and stronger electric field through the wafer. Some work has been done in this direction in this thesis. The results were inconclusive due to the new photolithography method tested for electrode evaporation which seemed to prevent the NTL LD from being operated with a high voltage difference. It will be pursued, but this time by using the shadow mask method.
- **Improving the speed of the detector response:** As it was already stated, the signal rise time has a strong influence on the pile-up rejection capability. Therefore, having faster detectors could help to reduce this source of background. Some preliminary studies have shown that choosing the right working point for the NTD bias could help to obtain a rise time of the order of 0.8 ms. Moreover, new NTD geometries and ways to couple it to the LD will be tested in the coming months. It is also worth mentioning that, in principle, the NTL technology is compatible with other types of thermistors like TES, which give a much faster signal ($O(100 \mu\text{s})$). This is also a path that could be explored to reach BINGO objectives, although it requires a completely new R&D program.

All these considerations point toward the necessity of the NTL Ge light detector technology for the future of bolometric experiments. Understanding better their behavior and the performance they can reach is crucial. The current pile-up challenge that CUPID is facing will for sure push the R&D further and could allow the work realized in the framework of BINGO to have an impact on bolometric experiments sooner than expected.

Conclusions and perspectives

The goal of the next-generation experiment CUPID is to reach a background index of 10^{-4} ckky in ^{100}Mo , thanks to the use of scintillating bolometers. It will allow it to explore completely the region of possible values for $m_{\beta\beta}$ in the case of the inverted hierarchy for neutrino mass. If no discovery is made, the experimental sensitivity will have to be pushed further and one of the keys to do so is to reduce the background. The BINGO project prepares this eventuality and aims to reach a background index of 10^{-5} ckky in the ROI of ^{130}Te and ^{100}Mo , respectively embedded inside TeO_2 and LMO crystals. It is based on three innovations to reduce the background: a new detector assembly that reduces the passive material around the detectors, a cryogenic active veto that will help to reject the external γ background, and finally, more efficient light detectors where we take benefit of the NTL effect to amplify the signals, mandatory to use TeO_2 as scintillating crystals. The work realized and presented in this thesis has been focused on the first development and experimental studies of these three innovations in the framework of the construction of a demonstrator MINI-BINGO, that will demonstrate their potential in background rejection for next-next generation of bolometric experiments.

The current component dominating the background of the CUORE experiment are the α events coming from crystal internal contamination and surface radioactivity of the surrounding material. The dual heat and light readout provided by scintillating bolometers allows their identification and their rejection. It was shown that this technology can be used with TeO_2 given the use of NTL light detectors that are able to detect the Cerenkov light emitted by these crystals. For BINGO, square NTL light detectors will be used for that purpose and the demonstration of their performance had to be done. We have produced a new batch of NTL LDs testing a new method to evaporate the electrodes with three different geometries. The lithography was appealing since it is more flexible and allows faster prototyping of new electrode arrangements compared to the shadow mask method. However, it appeared that it was giving NTL light detectors with worst performance preventing us from really comparing each geometries. We decided to try out the shadow mask method with annular electrodes, reproducing the geometries already tested in the past on circular wafers that obtained an SNR amplification of around 10. We showed that time that this method is better and gives LDs with comparable performance if we consider that the electrodes did not completely cover their surface due to the unoptimized geometry. Thus, the work will be pursued with the shadow mask method and a determining test is currently ongoing at the LSC with 10 square wafers of this kind. It will be a way to test their reproducibility which is one of the main criteria to implement this technology in large-scale experiments. The electrode geometry optimization will be pursued with the goal in mind to reach the highest NTL gain possible. Some of the geometries considered in this thesis could be really promising with the shadow mask method and will be envisaged for the future tests. The work presented here about NTL LDs was the beginning of an exciting R&D campaign surrounding this technology, and due to the already good performance obtained with circular wafers, we are confident that

they are the key to achieving an efficient α rejection even with TeO_2 crystals. Moreover, with the pile-up challenge that has to be faced when using bolometers embedding ^{100}Mo , it could have, for sure, consequences even of the next generation experiment CUPID. The high SNR these detectors can reach can be exploited to reject this source of background which is currently the most worrying one in CUPID.

Since the surface α s are no longer considered a problem, the most harmful contribution coming from the surrounding material becomes the surface β s. Against them, BINGO proposes a bolometer assembly, where the amount of passive materials around the crystals is minimized. The innovation lies in the use of a nylon wire to hold the crystals to a small copper holder, with the light detector placed in between. The wire ensures a minimum passive surface against the crystal, while the LD serves as an active shielding against the copper surface radioactivity. In this thesis, the first prototypes of this concept were cryogenically tested at different scales. We started with a small assembly to check the nylon wire properties at low temperatures, resulting in a confirmation of its suitability to keep the detectors well-fixed without preventing them from obtaining good performance. Indeed, we have even obtained an impressive energy resolution of 6 keV for the neutron capture peak of ^6Li for one of the crystals. We pursued our journey by testing a nylon wire assembly with CUPID-size LMO crystals in our above-ground cryostat. It was the occasion to develop an assembling tool allowing an easy and reproducible mounting of the detectors. Moreover, we cooled down this module along with a more standard one used for the CROSS R&D, also containing two LMO crystals. We didn't observe any relevant difference in terms of performance or noise between the two assemblies, demonstrating that this new way to hold the detectors gives similar results compared to the old-fashioned ones. It is really promising since it significantly reduces the crystal surface exposed to the passive material compared to the CUPID baseline module, ensuring a drastic reduction of the surface radioactivity contribution while keeping the same performance for the detectors. Finally, we realized an underground measurement of the first BINGO tower prototype, composed of two nylon wire modules at LSC. The copper holder was modified to allow a stacking of the modules in a tower and its mass was reduced with respect to the previous test. Once again, we obtained good performance for all the detectors in the tower. The average baseline FWHM of the four crystals is 2.3 keV which is similar to the crystal performance in the CUORE experiment. For the light detectors, we measure only for two of them a $\text{DP} > 3.1$, allowing a more than 99% alpha rejection. For the two others, we can expect to reach this performance with the signal amplification provided by the NTL light detectors that will be used in fine. In any case, these tests have validated the nylon-wire assembly for LMO crystals with a final copper holder design and a robust assembly procedure. On the way to MINI-BINGO, it will be tested in the future with TeO_2 crystals, which are bigger and heavier than LMOs. Before the definitive validation, the same modules will be tested with NTL light detectors. If these future tests confirm the good results obtained already with the ones realized in this thesis, we can expect that this assembly concept will become a standard for low radioactivity bolometric measurements due to the surface radioactivity suppression it provides.

The last background contribution BINGO aims to fight is the one of external γ radioactivity. It is particularly dominant in the ROI of ^{130}Te due to its non-favorable $Q_{\beta\beta}$, below the natural γ radioactivity endpoint. The idea here is to implement a cryogenic active veto in a 4π coverage of this bolometric area. It will be composed of scintillators, for which the scintillation light emitted after the interaction of this type of event within it will be detected by NTL light detectors. The ones in coincidence with a bolometer can therefore be easily rejected to reach the background objectives of BINGO. In this thesis, we identified two suitable scintillator candidates, the ZWO and BGO but most of the R&D was realized with BGO

due to the procurement difficulties of ZWO. A cryogenic veto implies many challenges, such as a high radiopurity, a mechanical holder keeping the internal part as much as possible free from any passive materials, and the cooling down of an additional mass beside the detectors. It was then crucial to test a small-scale prototype of a BGO veto cryogenically. We designed a mechanical assembly capable of hosting two 12 cm height trapezoidal BGOs, each faced by two regular Ge light detectors. We placed in front of it a small TeO_2 crystal, where we deposited on its surface facing the scintillators a drop of a liquid U source to imitate surface contamination. We obtained quite inhomogeneous light detector performance, probably because we observed that they were not at the same temperature. Indeed, the BGO is slow to cooldown and it had an impact on LDs cooling down since they were sharing the same PTFE pieces in this assembly, thermally coupling them too strongly. We, therefore, know for the future that an independent way to fix the light detectors and the BGO has to be implemented. It didn't prevent us, however, from realizing a coincidence study between the TeO_2 and the BGOs. We developed a coincidence algorithm that allowed us to efficiently identify the α events coming from the source, demonstrating the utility of the veto against this type of events also. Finally, we also estimated the energy threshold of our light detectors thanks to a reconstruction efficiency. We saw that, given that NTL LDs will be used to read the scintillation light and that they provide an amplification of the SNR of at least 10, an energy threshold lower than 50 keV in the BGO could be reached, fulfilling the requirements for an efficient external γ rejection. In the future, the mechanical assembly will be improved thanks to the precious information obtained with this measurement, and a new prototype will be tested with this time NTL LDs to confirm the energy threshold assumption. We also worked on the light collection of the LDs since it is one of the factors on which the energy threshold depends. To do so, we have elaborated a PMT room temperature bench to compare the light output of different BGO configurations, like different reflecting materials or polishing. Thanks to it, we can find the best combination of reflecting material, BGO provider and polishing, allowing us to get the highest light output from the crystals. So far, we have seen that a completely polished crystal wrapped inside a 3M[®] ESR film was giving the best results. Now that the setup is working well, other configurations will be tested to choose the best one to be implemented in the MINI-BINGO cryo-veto.

In prospect of these activities and to support our claims, a multi-pronged simulation effort has been started, investigating the MINI-BINGO demonstrator, the BINGO geometry within the CUORE cryostat to provide a comparison against the CUPID baseline strategy and an optimization study for a future tonne-scale experiment. For the context of this conclusion, I will provide a quick outlook on the ongoing work for the comparison against the CUPID baseline geometry. We are simulating the BINGO innovations inside the CUORE infrastructure in GEANT4. Our objective is to understand what are the crucial points to understand how to achieve our background objective in a CUORE-size experiment. Thanks to CUORE/CUPID simulations, we have a very detailed picture of radioactive contaminations from the cryostat and the shields. We implemented inside simplified BINGO-like towers that accurately reproduce the ratio between the passive and active materials and in particular, maintains the exposed surface area as close as possible to the reality of the nylon-wire assembly. If we consider $45 \times 45 \times 45 \text{ mm}^3$ LMO crystals, it is possible to fit in total 1612 crystals densely arranged in 62 towers of 13 floors. To simulate the LDs, we assume that each event in a LMO leads to a light signal with a LY of 0.3 keV/MeV, an α quenching of 20% and a baseline FWHM of 100 eV. The 5 cm thick BGO cryo-veto is implemented in a simple way by considering a perfect 4π coverage around the towers thanks to a cylindrical shape representing around 1.2 tons of material. The copper for the mechanical support of the veto and further details like cabling or the LDs were neglected in this first implementation. A 3D rendering of

BINGO inside the CUORE cryostat can be seen in Figure 7.14. We use as radioactive sources the same ones as in CUPID simulations (for example, for copper contamination) in order to have a fair comparison between the two reachable background indexes. For the sources not present in CUPID simulations, like the nylon wire, they will be added using dedicated radiopurity measurements that will be done in the future.

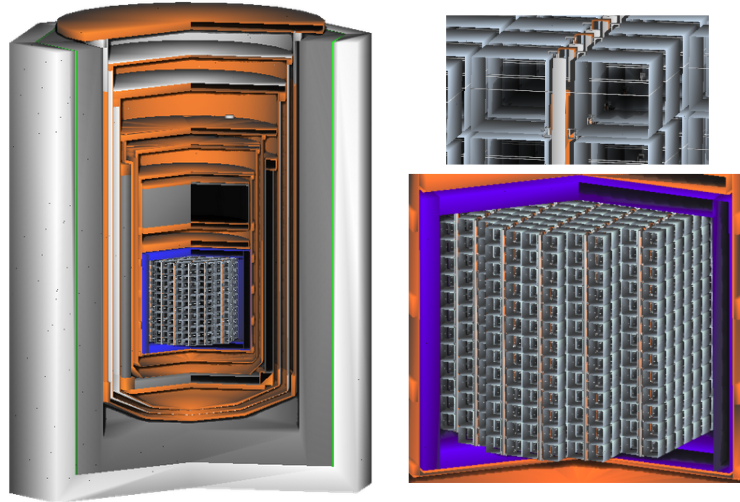


Figure 7.14 – 3D renderings of BINGO innovations inside the CUORE cryostat simulation. One can see the cryo-veto in blue.

To understand which type of info this simulation can bring us, we can have a look for example to the preliminary energy spectrum produced by the Th contamination in the Teflon - a material really close to the LMO crystals - and the one produced by the Th contamination of the Roman lead shield, far from the crystals. The activities used are the ones coming from the CUORE background model. The cuts applied on the spectra are summarized in Table 7.4. They are typical and were, for example, used for the CUPID-Mo demonstrator [101], except for the cryo-veto cut which comes with BINGO innovations. We considered a 10 keV threshold in the LMOs, 3 keV in the LD as a particle veto and 50 keV for the cryo-veto. The two simulated LMO energy spectra obtained are shown in Figure 7.15.

| Cut | Description |
|---------|---|
| M1 | Keep events detected only in one crystal |
| LD0 | Cut the events passing in an LD (particle veto) |
| GammaLY | Keep only the events with an LY inside the γ/β LY band |
| DC | Rejection of any ^{208}Tl β decay candidate within 10 half-lives (~ 30 min) after a primary ^{212}Bi α decay candidate |
| Veto | Rejection of the events interacting in the cryo-veto |

Table 7.4 – Simple cuts applied for the simulation.

Our interest here is to look at the effect of the veto cut on the energy spectra. Although they are not normalized in cky, we can see the relative difference before and after this cut in the number of counts per bin. As expected, it is most effective for ^{130}Te ROI cleaning but still allows a factor of a few improvements in the ^{100}Mo one. For the spectrum of events coming from the PTFE, we see that the cut allows a decrease by one order of magnitude of the background while it is less impacting for external γ . It seems that in the end, the active

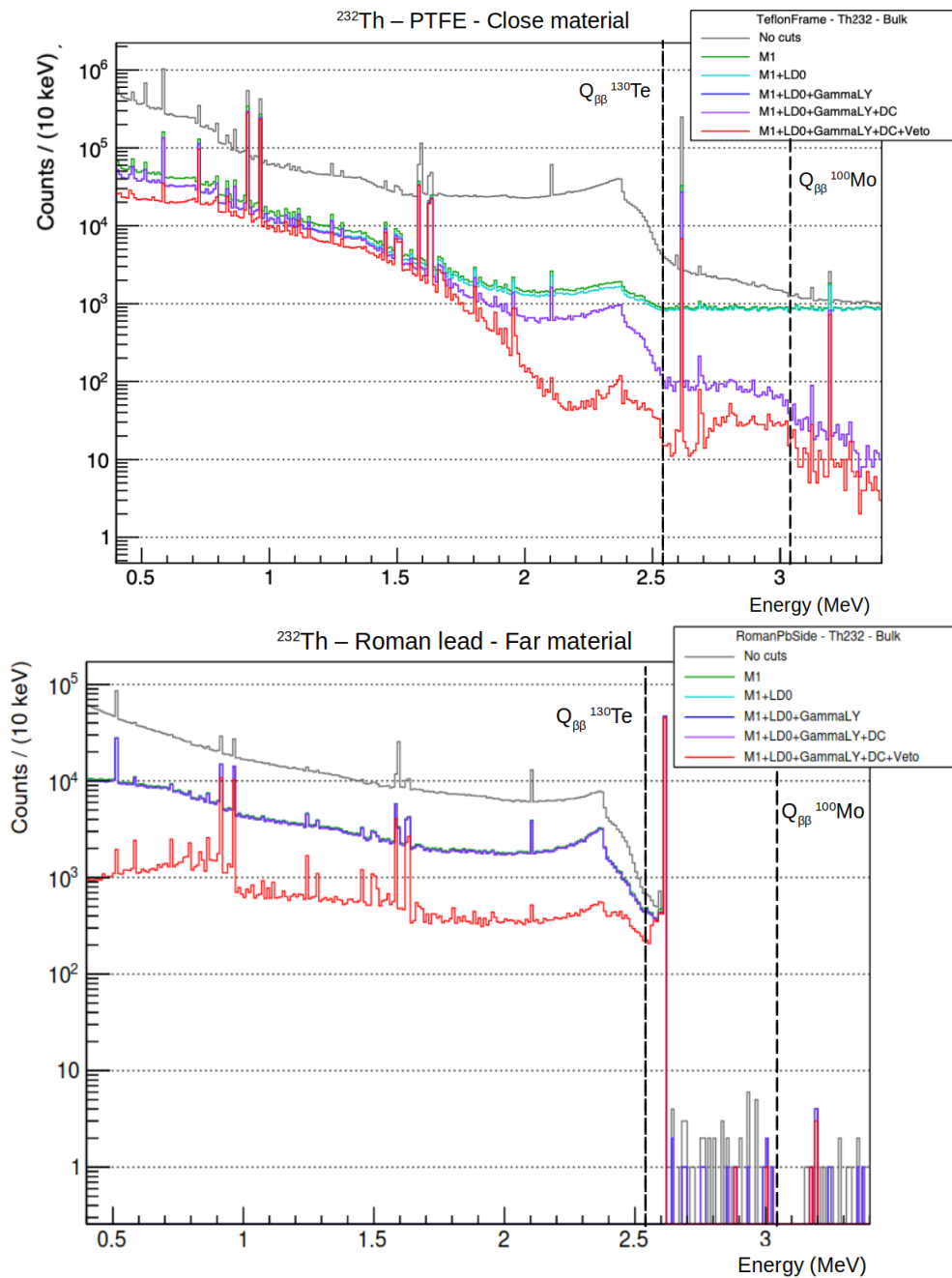


Figure 7.15 – *top*: Simulated LMOs energy spectrum of the Th decay chain induced by a bulk contamination in PTFE pieces used in the nylon wire assembly. *bottom*: Simulated LMOs energy spectrum of the Th decay chain induced by a bulk contamination in one of the cryostat copper screen.

veto cut will have a stronger effect on rejecting the background coming from the internal components rather than from the external one, already shielded passively by the scintillators but also by the Roman lead and other material layers. This is exactly the type of study that this simulation will provide. We can think, as another example, the try of different cryo-veto thicknesses to see what could be the effect and if a thicker veto would allow a more efficient vetoing. This simulation is still at a preliminary stage and will be improved and completed

in the future. In the end, once all the background components are simulated, we will get an estimation of the background index that we expect to obtain with BINGO innovations and fairly compare it with the one obtained by CUPID simulations.

With the results obtained in the framework of this thesis, we are now roughly halfway to the construction of MINI-BINGO. They have provided important validations of the concept and significant advancements in the design of the three BINGO innovations for background rejection. From the genesis of this project to its current status, the path has been opened towards a background index of 10^{-5} ckky. The efforts will be pursued to reach all the ambitious objectives of the MINI-BINGO demonstrator, which could definitely have a determinant impact on the future of ton-scale bolometric experiments searching for $0\nu 2\beta$.

Bibliography

- [1] C.D. Ellis and W.A. Wooster. The average energy of disintegration of radium E. *Proc. R. Soc. Lond. A*, 117:109–123, 1927. <https://doi.org/10.1098/rspa.1927.0168>.
- [2] W. Pauli. Letter to L. Meitner and her colleagues (letter open to the participants of the conference in Tübingen). 1930.
- [3] J. Chadwick. Possible existence of a neutron. *Nature*, 129(3252):312–312, Feb 1932.
- [4] E. Fermi. Tentativo di una teoria dei raggi β . *Il Nuovo Cimento (1924-1942)*, 11:1, 1934. doi:10.1007/BF02959820.
- [5] H. Bethe and R. Peierls. The “Neutrino”. *Nature*, 133(3362):532–532, Apr 1934.
- [6] B. Pontecorvo. Report pd-205. *Chalk River Laboratory*, 1946.
- [7] F. Reines and C. L. Cowan. Detection of the free neutrino. *Phys. Rev.*, 92:830, 1953. doi:10.1103/PhysRev.92.830.
- [8] F. Reines and C.L. Cowan. The Neutrino. *Nature*, 178(4531):446–449, Sep 1956.
- [9] C. S. Wu et al. Experimental test of parity conservation in beta decay. *Phys. Rev.*, 105:1413–1415, Feb 1957.
- [10] L.M. Lederman R.L. Garwin and M. Weinrich. Observations of the failure of conservation of parity and charge conjugation in meson decays: the magnetic moment of the free muon. *Phys. Rev.*, 105:1415–1417, Feb 1957.
- [11] T. D. Lee and C. N. Yang. Question of parity conservation in weak interactions. *Phys. Rev.*, 104:254–258, Oct 1956.
- [12] M. Goldhaber et al. Helicity of Neutrinos. *Phys. Rev.*, 109:1015–1017, Feb 1958.
- [13] G. Danby et al. Observation of high-energy neutrino reactions and the existence of two kinds of neutrinos. *Phys. Rev. Lett.*, 9:36–44, Jul 1962.
- [14] K. Kodama et al. (DONUT collaboration). Observation of tau neutrino interactions. *Physics Letters B*, 504(3):218–224, 2001.
- [15] D. Decamp et al. (ALEPH collaboration). Determination of the number of light neutrino species. *Physics Letters B*, 231(4):519–529, 1989.
- [16] P. Aarnio et al. (DELPHI collaboration). Measurement of the mass and width of the Z^0 -particle from multihadronic final states produced in e^+e^- annihilations. *Physics Letters B*, 231(4):539–547, 1989.

- [17] B. Adeva et al. (L3 collaboration). Measurement of Z^0 decays to hadrons, and a precise determination of the number of neutrino species. *Physics Letters B*, 237(1):136–146, 1990.
- [18] R. Davis et al. Search for neutrinos from the sun. *Phys. Rev. Lett.*, 20:1205–1209, May 1968.
- [19] K.S. Hirata et al. Observation of ^8B solar neutrinos in the Kamiokande-II detector. *Phys. Rev. Lett.*, 63:16–19, Jul 1989.
- [20] P. Anselmann et al. (GALLEX collaboration). Solar neutrinos observed by GALLEX at Gran Sasso. *Physics Letters B*, 285(4):376–389, 1992.
- [21] J.N. Abdurashitov et al. Results from SAGE (the Russian-American gallium solar neutrino experiment). *Physics Letters B*, 328(1):234–248, 1994.
- [22] V. Gribov and B. Pontecorvo. Neutrino astronomy and lepton charge. *Physics Letters B*, 28(7):493–496, 1969.
- [23] B. Pontecorvo. Inverse beta processes and nonconservation of lepton charge. *Zh. Eksp. Teor. Fiz.*, 34:247, 1957.
- [24] B. Pontecorvo. Neutrino Experiments and the Problem of Conservation of Leptonic Charge. *Zh. Eksp. Teor. Fiz.*, 53:1717–1725, 1967.
- [25] K.S. Hirata and al. Experimental study of the atmospheric neutrino flux. *Physics Letters B*, 205(2):416–420, 1988.
- [26] D. Casper et al. Measurement of atmospheric neutrino composition with the IMB-3 detector. *Phys. Rev. Lett.*, 66:2561–2564, May 1991.
- [27] Y. Fukuda et al. Evidence for oscillation of atmospheric neutrinos. *Phys. Rev. Lett.*, 81:1562–1567, Aug 1998.
- [28] Q. R. Ahmad et al. Direct evidence for neutrino flavor transformation from Neutral-Current interactions in the Sudbury Neutrino Observatory. *Phys. Rev. Lett.*, 89:011301, Jun 2002.
- [29] M.A. Acero et al. (the $\text{NO}\nu\text{A}$ collaboration). Improved measurement of neutrino oscillation parameters by the $\text{NO}\nu\text{A}$ experiment. *Phys. Rev. D*, 106:032004, Aug 2022.
- [30] K. Abe et al. (T2K collaboration). Improved constraints on neutrino mixing from the T2K experiment with 3.13×10^{21} protons on target. *Phys. Rev. D*, 103:112008, Jun 2021.
- [31] Changdong Shin (for the RENO collaboration). Recent Results from RENO. *PoS, ICHEP2020*:177, 2021.
- [32] The JUNO collaboration. JUNO physics and detector. *Progress in Particle and Nuclear Physics*, 123:103927, 2022.
- [33] C. Palomares and the DUNE Collaboration. Dune physics program and status. *Journal of Physics: Conference Series*, 2156(1):012107, Dec 2021.

- [34] P.F. de Salas et al. 2020 global reassessment of the neutrino oscillation picture. *Journal of High Energy Physics*, 2021(2):71, Feb 2021.
- [35] S.F. King. Neutrino mass models. *Reports on Progress in Physics*, 67(2):107, dec 2003.
- [36] A.S. Dighe and A.Y. Smirnov. Identifying the neutrino mass spectrum from a supernova neutrino burst. *Phys. Rev. D*, 62:033007, Jul 2000.
- [37] S. Hannestad and T. Schwetz. Cosmology and the neutrino mass ordering. *Journal of Cosmology and Astroparticle Physics*, 2016(11):035, nov 2016.
- [38] I. Esteban et al. The fate of hints: updated global analysis of three-flavor neutrino oscillations. *Journal of High Energy Physics*, 2020(9):178, Sep 2020.
- [39] A. Cabrera et al. Synergies and prospects for early resolution of the neutrino mass ordering. *Scientific Reports*, 12(1):5393, Mar 2022.
- [40] E. Majorana. Teoria simmetrica dell'elettrone e del positrone. *Il Nuovo Cimento (1924-1942)*, 14(4):171–184, Apr 1937.
- [41] J. Angrik et al. (KATRIN collaboration). KATRIN design report 2004. 2 2005.
- [42] M. Aker et al. (KATRIN collaboration). Direct neutrino-mass measurement with sub-electronvolt sensitivity. *Nature Physics*, 18(2):160–166, Feb 2022.
- [43] Project 8 Collaboration. Tritium beta spectrum and neutrino mass limit from cyclotron radiation emission spectroscopy, 2022.
- [44] M. Kaplinghat et al. Determining neutrino mass from the cosmic microwave background alone. *Phys. Rev. Lett.*, 91:241301, Dec 2003.
- [45] N. Palanque-Delabrouille et al. Neutrino masses and cosmology with Lyman- α forest power spectrum. *Journal of Cosmology and Astroparticle Physics*, 2015(11):011, nov 2015.
- [46] T. M. C. Abbott et al. (DES collaboration). Dark Energy Survey Year 3 results: Cosmological constraints from galaxy clustering and weak lensing. *Phys. Rev. D*, 105:023520, Jan 2022.
- [47] A. Lokhov et al. Probing the neutrino-mass scale with the katrin experiment. *Annual Review of Nuclear and Particle Science*, 72(1):259–282, 2022.
- [48] M. Goeppert-Mayer. Double Beta-Disintegration. *Phys. Rev.*, 48:512–516, Sep 1935.
- [49] R. Saakyan. Two-Neutrino Double-Beta Decay. *Annual Review of Nuclear and Particle Science*, 63(1):503–529, 2013.
- [50] M.G. Inghram and J.H. Reynolds. Double Beta-Decay of Te^{130} . *Phys. Rev.*, 78:822–823, Jun 1950.
- [51] A. Barabash. Precise Half-Life Values for Two-Neutrino Double- β Decay: 2020 Review. *Universe*, 6(10), 2020.
- [52] W.H. Furry. On transition probabilities in double beta-disintegration. *Phys. Rev.*, 56:1184–1193, Dec 1939.

- [53] J. Schechter and J. W. F. Valle. Neutrinoless double- β decay in $SU(2)\times U(1)$ theories. *Phys. Rev. D*, 25:2951–2954, Jun 1982.
- [54] P. Stöcker et al. Strengthening the bound on the mass of the lightest neutrino with terrestrial and cosmological experiments. *Phys. Rev. D*, 103:123508, Jun 2021.
- [55] A. Babič et al. Bound-state double- β decay. *Phys. Rev. C*, 98:065501, Dec 2018.
- [56] J.T. Suhonen. Value of the Axial-Vector Coupling Strength in β and $\beta\beta$ Decays: A Review. *Frontiers in Physics*, 5, 2017.
- [57] M. Agostini et al. Toward the discovery of matter creation with neutrinoless double-beta decay, 2022.
- [58] J.J. Gómez-Cadenas et al. Sense and sensitivity of double beta decay experiments. *Journal of Cosmology and Astroparticle Physics*, 2011(06):007, jun 2011.
- [59] G.J. Feldman and R.D. Cousins. Unified approach to the classical statistical analysis of small signals. *Phys. Rev. D*, 57:3873–3889, Apr 1998.
- [60] A. Giuliani and A. Poves. Neutrinoless Double-Beta Decay. *Advances in High Energy Physics*, 2012:857016, Dec 2012.
- [61] M. Agostini et al. (GERDA collaboration). Final Results of GERDA on the Search for Neutrinoless Double- β Decay. *Phys. Rev. Lett.*, 125:252502, Dec 2020.
- [62] The CUPID Interest Group. Cupid pre-cdr, 2019.
- [63] R.L. Brodzinski, H.S. Miley, J.H. Reeves, and F.T. Avignone. Further reduction of radioactive backgrounds in ultrasensitive germanium spectrometers. *Nuclear Instruments and Methods in Physics Research Section A: Accelerators, Spectrometers, Detectors and Associated Equipment*, 292(2):337–342, 1990.
- [64] L. Pattavina et al. Radiopurity of an archaeological roman lead cryogenic detector. *The European Physical Journal A*, 55(8):127, Aug 2019.
- [65] R.J. Cooper et al. A novel HPGe detector for gamma-ray tracking and imaging. *Nuclear Instruments and Methods in Physics Research Section A: Accelerators, Spectrometers, Detectors and Associated Equipment*, 665:25–32, 2011.
- [66] M. Agostini et al. (GERDA collaboration). Production, characterization and operation of ^{76}Ge enriched BEGe detectors in GERDA. *The European Physical Journal C*, 75(2):39, Feb 2015.
- [67] M. Agostini et al. (GERDA collaboration). Pulse shape discrimination for Gerda Phase I data. *The European Physical Journal C*, 73(10):2583, Oct 2013.
- [68] D. Budjáš et al. Pulse shape discrimination studies with a Broad-Energy Germanium detector for signal identification and background suppression in the GERDA double beta decay experiment. *Journal of Instrumentation*, 4(10):P10007, oct 2009.
- [69] P.N. Luke et al. Low capacitance large volume shaped-field germanium detector. *IEEE Transactions on Nuclear Science*, 36(1):926–930, 1989.

- [70] E.W. Hoppe et al. Reduction of radioactive backgrounds in electroformed copper for ultra-sensitive radiation detectors. *Nuclear Instruments and Methods in Physics Research Section A: Accelerators, Spectrometers, Detectors and Associated Equipment*, 764:116–121, 2014.
- [71] I.J. Arnquist et al. (MAJORANA collaboration). Final Result of the Majorana Demonstrator’s Search for Neutrinoless Double- β Decay in ^{76}Ge . *Phys. Rev. Lett.*, 130:062501, Feb 2023.
- [72] N. Abgrall et al. The Majorana Demonstrator radioassay program. *Nuclear Instruments and Methods in Physics Research Section A: Accelerators, Spectrometers, Detectors and Associated Equipment*, 828:22–36, 2016.
- [73] N. Abgrall et al. (LEGEND collaboration). The Large Enriched Germanium Experiment for Neutrinoless $\beta\beta$ Decay: LEGEND-1000 Preconceptual Design Report. 7 2021.
- [74] A. Domula et al. Pulse shape discrimination performance of inverted coaxial Ge detectors. *Nuclear Instruments and Methods in Physics Research Section A: Accelerators, Spectrometers, Detectors and Associated Equipment*, 891:106–110, 2018.
- [75] R. Neilson et al. Characterization of large area APDs for the EXO-200 detector. *Nuclear Instruments and Methods in Physics Research Section A: Accelerators, Spectrometers, Detectors and Associated Equipment*, 608(1):68–75, 2009.
- [76] E. Conti et al. Correlated fluctuations between luminescence and ionization in liquid xenon. *Phys. Rev. B*, 68:054201, Aug 2003.
- [77] Search for Neutrinoless Double- β Decay with the Complete EXO-200 Dataset. *Phys. Rev. Lett.*, 123:161802, Oct 2019.
- [78] G. Adhikari et al. (nEXO collaboration). nEXO: neutrinoless double beta decay search beyond 10^{28} year half-life sensitivity. *Journal of Physics G: Nuclear and Particle Physics*, 49(1):015104, dec 2021.
- [79] D. Nygren. High-pressure xenon gas electroluminescent TPC for $0\nu\beta\beta$ search. *Nucl. Instrum. Meth. A*, 603:337–348, 2009.
- [80] J. Renner et al. (the NEXT collaboration). Energy calibration of the NEXT-White detector with 1% resolution near $Q_{\beta\beta}$ of ^{136}Xe . *Journal of High Energy Physics*, 2019(10):230, Oct 2019.
- [81] Simón, A. et al. (the NEXT collaboration). Boosting background suppression in the NEXT experiment through Richardson-Lucy deconvolution. *Journal of High Energy Physics*, 2021(7):146, Jul 2021.
- [82] J. Martín-Albo et al. (the NEXT collaboration). Sensitivity of next-100 to neutrinoless double beta decay. *Journal of High Energy Physics*, 2016(5):159, May 2016.
- [83] R. Felkai et al. Helium–xenon mixtures to improve the topological signature in high-pressure gas xenon tpcs. *Nuclear Instruments and Methods in Physics Research Section A: Accelerators, Spectrometers, Detectors and Associated Equipment*, 905:82–90, 2018.

- [84] C. Adams et al. (the NEXT collaboration). Sensitivity of a tonne-scale NEXT detector for neutrinoless double-beta decay searches. *Journal of High Energy Physics*, 2021(8):164, Aug 2021.
- [85] I. Rivilla et al. Fluorescent bicolour sensor for low-background neutrinoless double β decay experiments. *Nature*, 583(7814):48–54, Jul 2020.
- [86] K. Eguchi et al. (KamLAND collaboration). First Results from KamLAND: Evidence for Reactor Antineutrino Disappearance. *Phys. Rev. Lett.*, 90:021802, Jan 2003.
- [87] S. Abe et al. (KamLAND-Zen collaboration). Search for the Majorana Nature of Neutrinos in the Inverted Mass Ordering Region with KamLAND-Zen. *Phys. Rev. Lett.*, 130:051801, Jan 2023.
- [88] J. Shirai for the KamLAND-Zen Collaboration. Results and future plans for the kamland-zen experiment. *Journal of Physics: Conference Series*, 888(1):012031, sep 2017.
- [89] J Boger et al. (. The Sudbury Neutrino Observatory. *Nuclear Instruments and Methods in Physics Research Section A: Accelerators, Spectrometers, Detectors and Associated Equipment*, 449(1):172–207, 2000.
- [90] M. Anderson et al. (SNO+ collaboration). Measurement of the ^8B solar neutrino flux in SNO+ with very low backgrounds. *Phys. Rev. D*, 99:012012, Jan 2019.
- [91] M. Anderson et al. (SNO+ collaboration). Search for invisible modes of nucleon decay in water with the SNO+ detector. *Phys. Rev. D*, 99:032008, Feb 2019.
- [92] A. Allega et al. (SNO+ collaboration). Improved search for invisible modes of nucleon decay in water with the SNO + detector. *Phys. Rev. D*, 105:112012, Jun 2022.
- [93] M. Anderson et al. (SNO+ collaboration). Development, characterisation, and deployment of the SNO+ liquid scintillator. *Journal of Instrumentation*, 16(05):P05009, may 2021.
- [94] C. Grant. Results from KamLAND-ZEN and SNO+, July 2020.
- [95] C. Alduino et al. The CUORE cryostat: An infrastructure for rare event searches at millikelvin temperatures. *Cryogenics*, 102:9–21, 2019.
- [96] N. Wang et al. *Properties of NTD Ge and implantation of NTD Ge sensors in a large composite phonon detector*. Editions Frontieres, France, 1992.
- [97] D.Q. Adams et al. (The CUORE collaboration). Search for Majorana neutrinos exploiting millikelvin cryogenics with CUORE. *Nature*, 604(7904):53–58, Apr 2022.
- [98] O. Azzolini et al. Background model of the CUPID-0 experiment. *The European Physical Journal C*, 79(7):583, Jul 2019.
- [99] O. Azzolini et al. Final Result on the Neutrinoless Double Beta Decay of ^{82}Se with CUPID-0. *Phys. Rev. Lett.*, 129:111801, Sep 2022.
- [100] C. Augier et al. (CUPID-Mo collaboration). Final results on the $0\nu 2\beta$ decay half-life limit of ^{100}Mo from the CUPID-Mo experiment. *The European Physical Journal C*, 82(11):1033, Nov 2022.

- [101] E. Armengaud et al. (CUPID-Mo collaboration). The CUPID-Mo experiment for neutrinoless double-beta decay: performance and prospects. *The European Physical Journal C*, 80(1):44, Jan 2020.
- [102] A. Fleischmann et al. Metallic magnetic calorimeters. *AIP Conference Proceedings*, 1185(1):571–578, 2009.
- [103] M.H. Lee. AMoRE: a search for neutrinoless double-beta decay of ^{100}Mo using low-temperature molybdenum-containing crystal detectors. *Journal of Instrumentation*, 15(08):C08010, aug 2020.
- [104] H.B. Kim et al. Status and Performance of the AMoRE-I Experiment on Neutrinoless Double Beta Decay. *Journal of Low Temperature Physics*, 209(5):962–970, Dec 2022.
- [105] V. Alenkov et al. First results from the AMoRE-Pilot neutrinoless double beta decay experiment. *The European Physical Journal C*, 79(9):791, Sep 2019.
- [106] R. Arnold et al. Technical design and performance of the NEMO 3 detector. *Nuclear Instruments and Methods in Physics Research Section A: Accelerators, Spectrometers, Detectors and Associated Equipment*, 536(1):79–122, 2005.
- [107] R. Arnold et al. (NEMO-3 collaboration). Results of the search for neutrinoless double- β decay in ^{100}Mo with the NEMO-3 experiment. *Phys. Rev. D*, 92:072011, Oct 2015.
- [108] M. Bongrand. Latest NEMO-3 Results and Status of SuperNEMO. *Physics Procedia*, 61, 12 2015.
- [109] H. Ohsumi (on behalf of the NEMO and SuperNEMO Collaboration). Supernemo project. *Journal of Physics: Conference Series*, 120(5):052054, jul 2008.
- [110] Thibaud Le Noblet, on behalf of the NEMO 3, and SuperNEMO collaborations. Latest results from nemo-3 and commissioning status of the supernemo demonstrator. *Journal of Physics: Conference Series*, 1342(1):012029, jan 2020.
- [111] A. Giuliani et al. Double Beta Decay APPEC Committee Report. 2019. arXiv:1910.04688.
- [112] E. Caden. Status of the SNO+ Experiment. *Journal of Physics: Conference Series*, 1342(1):012022, jan 2020.
- [113] S. P. Langley. The Bolometer and Radiant Energy. *Proceedings of the American Academy of Arts and Sciences*, 16:342–358, 1880.
- [114] F. SIMON. Application of Low Temperature Calorimetry to Radioactive Measurements. *Nature*, 135(3418):763–763, May 1935.
- [115] D.H. Andrews, and R.D Fowler, and M.C. Williams. The Effect of Alpha-particles on a Superconductor. *Phys. Rev.*, 76:154–155, Jul 1949.
- [116] E. Fiorini. and T.O. Niinikoski. Low Temperature Calorimetry for Rare Decays. *Nucl. Instrum. Meth. A*, 224:83, 1984.
- [117] P. A. Puiu. *Transition Edge Sensor Calorimeters for HOLMES*. PhD thesis, Milan Bicocca U., 2017.

- [118] D. Kent Irwin. SQUIDs and Transition-Edge Sensors. *Journal of Superconductivity and Novel Magnetism*, 34(6):1601–1606, Jun 2021.
- [119] V. Singh et al. Large area photon calorimeter with Ir-Pt bilayer transition-edge sensor for the CUPID experiment, 2022.
- [120] P.W. Anderson. Absence of diffusion in certain random lattices. *Phys. Rev.*, 109:1492–1505, Mar 1958.
- [121] N.F. Mott and W.D. Twose. The theory of impurity conduction. *Advances in Physics*, 10(38):107–163, 1961.
- [122] I.B. Shklovskii and A.L. Efros. *Variable-Range Hopping Conduction*, pages 202–227. Springer Berlin Heidelberg, Berlin, Heidelberg, 1984.
- [123] A.L. Efros and B.I. Shklovskii. Coulomb gap and low temperature conductivity of disordered systems. *Journal of Physics C: Solid State Physics*, 8(4):L49, feb 1975.
- [124] E. Haller, K. Itoh, and J. Beeman. Neutron Transmutation Depot (NTD) Germanium Thermistors for Submillimetre Bolometer Applications. 388:115, 11 1996.
- [125] C. Alduino et al. CUORE-0 detector: design, construction and operation. *Journal of Instrumentation*, 11(07):P07009, jul 2016.
- [126] D.L. Helis. *Searching for neutrinoless double-beta decay with scintillating bolometers*. Theses, Université Paris-Saclay, September 2021.
- [127] C. Arnaboldi et al. A front-end electronic system for large arrays of bolometers. *Journal of Instrumentation*, 13(02):P02026, feb 2018.
- [128] Michele Mancuso. *Development and optimization of scintillating bolometers and innovative light detectors for a pilot underground experiment on neutrinoless double beta decay*. Theses, Université Paris Saclay (COmUE) ; Università degli studi dell’Insubria (Varese, Italie), February 2016.
- [129] S.H. Moseley, J.C. Mather, and D. McCammon. Thermal detectors as x-ray spectrometers. *Journal of Applied Physics*, 56(5):1257–1262, 09 1984.
- [130] R. Maisonobe et al. Vibration decoupling system for massive bolometers in dry cryostats. *Journal of Instrumentation*, 13(08):T08009, aug 2018.
- [131] Vibrations on pulse tube based Dry Dilution Refrigerators for low noise measurements. *Nuclear Instruments and Methods in Physics Research Section A: Accelerators, Spectrometers, Detectors and Associated Equipment*, 858:73–79, 2017.
- [132] E. Gatti and P.F. Manfredi. Processing the signals from solid-state detectors in elementary-particle physics. *La Rivista del Nuovo Cimento (1978-1999)*, 9(1):1–146, Jan 1986.
- [133] E. Andreotti et al. Production, characterization, and selection of the heating elements for the response stabilization of the CUORE bolometers. *Nuclear Instruments and Methods in Physics Research Section A: Accelerators, Spectrometers, Detectors and Associated Equipment*, 664(1):161–170, 2012.

- [134] A. Alessandrello et al. Methods for response stabilization in bolometers for rare decays. *Nuclear Instruments and Methods in Physics Research Section A: Accelerators, Spectrometers, Detectors and Associated Equipment*, 412(2):454–464, 1998.
- [135] J.B. Birks. Scintillations from Organic Crystals: Specific Fluorescence and Relative Response to Different Radiations. *Proceedings of the Physical Society. Section A*, 64(10):874, oct 1951.
- [136] S. Nagorny et al. Quenching factor for alpha particles in ZnSe scintillating bolometers. *IOP Conference Series: Materials Science and Engineering*, 169(1):012011, feb 2017.
- [137] C. Bobin et al. Alpha/gamma discrimination with a CaF₂(Eu) target bolometer optically coupled to a composite infrared bolometer. *Nuclear Instruments and Methods in Physics Research Section A: Accelerators, Spectrometers, Detectors and Associated Equipment*, 386(2):453–457, 1997.
- [138] *An experimental study of antireflective coatings in Ge light detectors for scintillating bolometers*, number 65 in RPSCINT 2013 - INTERNATIONAL WORKSHOP ON RADIOPURE SCINTILLATORS, Kyiv, Ukraine, 2014.
- [139] A. Zolotarova. *Study and selection of scintillating crystals for the bolometric search for neutrinoless double beta decay*. Theses, Université Paris Saclay (COMUE), September 2018.
- [140] PT405 cryocoolers. <https://www.cryomech.com/products/pt405/>. Accessed: 2023-06-19.
- [141] T. Prouvé et al. Pulse-Tube Dilution Refrigeration Below 10 mK. *Journal of Low Temperature Physics*, 148:909–914, 09 2007.
- [142] C. Alduino et al. (CUORE collaboration). CUORE sensitivity to $0\nu\beta\beta$ decay. *The European Physical Journal C*, 77(8):532, Aug 2017.
- [143] G. Benato. Status and results of the CUORE experiment. In *Matrix Elements for the Double beta decay EXperiments 2019 (MEDEX'19)*, May 27 - May 31 2019.
- [144] T. Tabarelli de Fatis. Cerenkov emission as a positive tag of double beta decays in bolometric experiments. *The European Physical Journal C*, 65(1):359–361, Jan 2010.
- [145] B.S. Neganov and V.N. Trofimov. Colorimetric method measuring ionizing radiation. *Otkryt. Izobret.*, 146:215, 1985.
- [146] P.N. Luke. Voltage-assisted calorimetric ionization detector. *Journal of Applied Physics*, 64(12):6858–6860, Dec 1988.
- [147] S. Koc. The quantum efficiency of the photo-electric effect in germanium for the 0.3–2 μ wavelength region. *Czechoslovakij fiziceskij zurnal*, 7(1):91–95, Jan 1957.
- [148] E. Olivieri et al. Space-and-surface charge neutralization of cryogenic Ge detectors using infrared LEDs. *AIP Conference Proceedings*, 1185, 12 2009.
- [149] M. Tenconi. *Development of luminescent bolometers and light detectors for neutrinoless double beta decay search*. PhD thesis, U. Paris-Sud 11, Dept. Phys., Orsay, 2015.

- [150] V. Novati. *Sensitivity enhancement of the CUORE experiment via the development of Cherenkov hybrid TeO₂ bolometers*. PhD thesis, CSNSM, Orsay, 2018.
- [151] L. et al. L. Bergé. Complete event-by-event $\alpha/\gamma(\beta)$ separation in a full-size TeO₂ CUORE bolometer by Neganov-Luke-magnified light detection. *Phys. Rev. C*, 97:032501, Mar 2018.
- [152] A. Armatol et al. (CUPID collaboration). Novel technique for the study of pileup events in cryogenic bolometers. *Phys. Rev. C*, 104:015501, Jul 2021.
- [153] A. Ahmine et al. Enhanced light signal for the suppression of pile-up events in Mo-based bolometers for the $0\nu\beta\beta$ decay search. *The European Physical Journal C*, 83(5):373, May 2023.
- [154] C. Alduino et al. The projected background for the CUORE experiment. *The European Physical Journal C*, 77(8):543, Aug 2017.
- [155] E. Armengaud et al. Development of ¹⁰⁰Mo-containing scintillating bolometers for a high-sensitivity neutrinoless double-beta decay search. *The European Physical Journal C*, 77(11):785, Nov 2017.
- [156] I.C. Bandac et al. (CROSS collaboration). The $0\nu 2\beta$ -decay CROSS experiment: preliminary results and prospects. *Journal of High Energy Physics*, 2020(1):18, Jan 2020.
- [157] H. Khalife. *CROSS and CUPID-Mo : future strategies and new results in bolometric search for $0\nu\beta\beta$* . Theses, Université Paris-Saclay, January 2021.
- [158] W. Trzaska and al. Cosmic-ray muon flux at Canfranc Underground Laboratory. *Eur. Phys. J. C*, 79(8):721, 2019.
- [159] E. Olivieri et al. (CROSS collaboration). The new CROSS Cryogenic Underground (C2U) facility: an overview. In *XXIX International (online) Conference on Neutrino Physics and Astrophysics (Neutrino 2020)*, June 22 - July 02 2020.
- [160] "ultra-quiet technology".
<https://cryoconcept.com/product/the-ultra-quiet-technology/>.
- [161] G. Buşe et al. First scintillating bolometer tests of a CLYMENE R&D on Li₂MoO₄ scintillators towards a large-scale double-beta decay experiment. *Nuclear Instruments and Methods in Physics Research Section A: Accelerators, Spectrometers, Detectors and Associated Equipment*, 891:87–91, 2018.
- [162] K. Alfonso et al. (CUPID collaboration). Optimization of the first cupid detector module. *The European Physical Journal C*, 82(9):810, Sep 2022.
- [163] K. Alfonso et al. (CUPID and CROSS collaboration). Twelve-crystal prototype of Li₂MoO₄ scintillating bolometers for CUPID and CROSS experiments, 2023.
- [164] R. Cerulli. Low background techniques toward a znwo4 directionality experiment. *International Journal of Modern Physics A*, 32(30):1743009, 2017.
- [165] D. Poda. Scintillation in Low-Temperature Particle Detectors. *Physics*, 3(3):473–535, 2021.

- [166] P. Belli et al. New development of radiopure ZnWO_4 crystal scintillators. *Nuclear Instruments and Methods in Physics Research Section A: Accelerators, Spectrometers, Detectors and Associated Equipment*, 935:89–94, 2019.
- [167] Trevor A. Lewis. The reduction of background signal in bismuth germanate scintillators. *Nuclear Instruments and Methods in Physics Research Section A: Accelerators, Spectrometers, Detectors and Associated Equipment*, 264(2):534–535, 1988.
- [168] F.A. Danevich and V.I. Tretyak. Radioactive contamination of scintillators. *International Journal of Modern Physics A*, 33(09):1843007, 2018.
- [169] L. Cardani et al. A BGO scintillating bolometer for γ and α spectroscopy. *Journal of Instrumentation*, 7(10):P10022, oct 2012.
- [170] PHILIPS Photomultiplier 56 AVP. <https://frank.pocnet.net/sheets/084/5/56AVP.pdf>. Accessed: 2023-05-26.
- [171] Photomultiplier Tube (PMT). https://www.matsusada.com/application/ps/photomultiplier_tubes/. Accessed: 2023-05-26.
- [172] STEMLab 125-14. <https://redpitaya.com/rtd-iframe/?iframe=https://redpitaya.readthedocs.io/en/latest/developerGuide/hardware.html>. Accessed: 2023-05-27.
- [173] Multichannel Pulse Height Analyzer. <http://pavel-demin.github.io/red-pitaya-notes/mcpha/>. Accessed: 2023-05-27.
- [174] N. Rashid. Gamma Ray Spectroscopy of Co-60 Radioactive Source. 2018.
- [175] B. Schmidt et al. Muon-induced background in the EDELWEISS dark matter search. *Astroparticle Physics*, 44:28–39, 2013.
- [176] V. Palušová et al. Natural radionuclides as background sources in the Modane underground laboratory. *Journal of Environmental Radioactivity*, 216:106185, 2020.
- [177] A. Alessandrello et al. Measurements of internal radioactive contamination in samples of Roman lead to be used in experiments on rare events. *Nuclear Instruments and Methods in Physics Research Section B: Beam Interactions with Materials and Atoms*, 142(1):163–172, 1998.
- [178] T. Shutt et al. A solution to the dead-layer problem in ionization and phonon-based dark matter detectors. *Nuclear Instruments and Methods in Physics Research Section A: Accelerators, Spectrometers, Detectors and Associated Equipment*, 444(1):340–344, 2000.
- [179] D.M. Chernyak et al. Random coincidence of $2\nu 2\beta$ decay events as a background source in bolometric $0\nu 2\beta$ decay experiments. *The European Physical Journal C*, 72(4):1989, Apr 2012.